
Controlling and Reshaping Biological Reaction-Diffusion

Philipp Glock



München 2019

Controlling and Reshaping Biological Reaction-Diffusion

Philipp Glock

Dissertation
an der Fakultät für Biologie
der Ludwig-Maximilians-Universität
München

vorgelegt von
Philipp Glock
aus Schwäbisch Hall

München, den 22.01.2019

dedicated to Friedrich Busch

Erstgutachterin: Prof. Kirsten Jung
Zweitgutachter: Prof. Marc Bramkamp
Tag der Abgabe: 22.01.2019
Tag der mündlichen Prüfung: 08.05.2019

Eidesstattliche Erklärung

Hiermit versichere ich an Eides statt, dass die vorliegende Dissertation von mir selbstständig und ohne unerlaubte Hilfe angefertigt wurde. Des Weiteren erkläre ich, dass ich nicht anderweitig ohne Erfolg versucht habe, eine Dissertation einzureichen oder mich der Doktorprüfung zu unterziehen. Die Dissertation liegt weder ganz, noch in wesentlichen Teilen einer anderen Prüfungskommission vor.

München, 20. Januar 2019

Philipp Glock

Contents

Eidesstattliche Erklärung	v
List of Publications	xi
Summary	xiii
1 Introduction	1
1.1 Pattern formation via reaction and diffusion	1
1.2 Model systems for reaction-diffusion and control schemes	2
1.3 The Min system of <i>Escherichia coli</i>	5
1.3.1 The Min system <i>in vivo</i>	5
1.3.2 Bottom-up reconstitution of the Min system	9
1.3.3 Controlling self-organization in the Min system	10
1.4 Objective of this thesis	12
2 Publications	15
2.1 Optical Control of a Biological Reaction-Diffusion System	16
2.1.1 Supplement to Optical Control of a Biological Reaction-Diffusion System	21
2.2 <i>In Vitro</i> Reconstitution of Self-Organizing Protein Patterns on Supported Lipid Bilayers	29
2.2.1 Supplement to <i>In Vitro</i> Reconstitution of Self-Organizing Protein Patterns on Supported Lipid Bilayers	42
2.3 Stationary Patterns in a Two-Protein Reaction-Diffusion System	45
2.3.1 Supplement to Stationary Patterns in a Two-Protein Reaction-Diffusion System	55
2.4 The MinDE system is a generic spatial cue for membrane protein distribution in vitro	81
2.4.1 Supplement to The MinDE system is a generic spatial cue for mem- brane protein distribution in vitro	97
2.5 Switching Protein Patterns on Membranes	135

3 Outlook	143
3.1 Manuscript: Building minimal biochemical interaction networks for pattern formation	143
4 Discussion	153
A Appendix	159
A.1 Discontinued approaches to photocontrol the Min system	159
A.2 Programs and additional code	161
A.2.1 CoolLED-control	161
A.2.2 Visualization of spectra	161
A.2.3 ImageJ/Fiji code	162
Bibliography	167
Abbreviations	173
Image Credits	175
Acknowledgments	177

List of Figures

1.1	Examples of Patterns	2
1.2	Belousov-Zhabotinsky Reaction and CO oxidation on platinum	3
1.3	Resonant patterns in the BZ reaction	4
1.4	Min and nucleoid occlusion	6
1.5	MinD crystal structure	7
1.6	MinE conformations	8
1.7	Min oscillations in vivo	9
1.8	Comparison flow cell - well setup	10
1.9	Schematic of Min mechanism on SLB	14
A.1	Photocontrol based on LOV-domain dimerizers	160
A.2	Photocontrol based on LOV-domain caging a MinE peptide	160

List of Publications

The following publications are included in this thesis:

My Role	Title	Journal
first author	Optical Control of a Biological Reaction-Diffusion System	<i>Angewandte Chemie intl. ed.</i>
first author	Stationary Patterns in a Two-Protein Reaction-Diffusion System	<i>ACS Synthetic Biology</i>
first author, shared	<i>In Vitro</i> Reconstitution of Self-Organizing Protein Patterns on Supported Lipid Bilayers	<i>Journal of Visualized Experiments</i>
second author	The MinDE system is a generic spatial cue for membrane protein distribution in vitro	<i>Nature communications</i>
first author, review article	Switching Protein Patterns on Membranes	<i>Current Opinion in Colloid & Interface Science</i>

Additionally, one unpublished manuscript is provided in section 3.1.

Summary

Pattern formation by reaction-diffusion mechanisms is of crucial importance for the development and sustenance of all living beings. However, biological model systems so far lack the tools and versatility of the established chemical models. In this thesis, we set out to develop and expand the Min system of *Escherichia coli* towards becoming a universal model for biological reaction-diffusion in an *in vitro* setting.

To this end, we firstly developed a strategy to control the Min reaction *in situ*. This was facilitated by incorporating a chemically synthesized azobenzene-moiety into a peptide derived from MinE. This MinE-peptide is capable of stimulating hydrolysis of ATP by MinD. Photoswitching the azobenzene crosslinker allows to also switch α -helicity of the peptide and therefore its activity. By periodically activating this peptide photoswitch we found resonance phenomena in the Min reaction. The photoswitch described here could thus be used in many synthetic biology scenarios, but also to learn about Min and biological reaction-diffusion systems. Secondly, we discovered that the Min system can form stationary patterns, which greatly expands the pattern diversity and therefore the phenomena which the Min model can help us understand. Especially when it comes to important decisions in development, such as cell fate or macroscopically visible effects such as fur patterns, stationary patterns are much more prominent than oscillations and waves. The discovery of these patterns also creates many opportunities for applications, especially when combined with the newly found ability of Min proteins to position arbitrary membrane-bound factors. Thirdly, this thesis shows that the Min system's complexity can be reduced even more by substituting MinE with small peptides. A combined theory-experiment approach outlines how pattern forming capabilities are restored in a small MinE-derived peptide either by adding membrane binding or by dimerizing it. This study further highlights how peptides and proteins excel as model morphogens due to their modularity and mutability. Lastly, protocols and resources are more easily available due to a combined method-paper and video that was published in open access.

In conclusion, by adding tools and versatility, this thesis introduces great progress towards establishing the *in vitro* Min system as the ideal model for biological reaction-diffusion.

Introduction

1.1 Pattern formation via reaction and diffusion

Patterns are one of the defining hallmarks of all things living. From very small, e.g. the internal organization of bacterial cells, to very large, like the hierarchical distribution of branches and leaves on a tree, nature and life is patterned. There are, however, also patterns found in the non-living, such as hexagonal columns of basalt formations or ripples in desert sands. The striking similarities between patterns in both the biosphere and the non-living can be explained by the fact that many patterns rely on the same basic physical principles. Reaction-diffusion (RD) is one mechanism by which many such patterns arise. But no matter the specific mechanism - we can already state based on the second law of thermodynamics that the installment of order, which is necessary for a pattern, will require energy. Figure 1.1 shows examples of Patterns observed both in living and non-living systems. While many mechanisms can be responsible for patterns in the non-living, such as ripples in sand dunes or on ocean floors, two models are most commonly used to explain patterning in cells, tissues or organisms. These two models are the French Flag model and RD [1, 2]. In the French Flag model, introduced first by Lewis Wolpert [3], a gradient of a morphogen is externally deposited. The final pattern is then derived by thresholds referring to this gradient, resulting, for example, in three consecutive vertical regions as in a French flag. It is known that such a mechanism is at work e.g. during development of *Drosophila melanogaster* embryos [4]. RD patterning, on the other hand, is truly self-organized and does not rely on any external information. The concept was introduced and derived mathematically by Alan Turing as early as 1952 [5], but went mostly unnoticed for a time and gained general attention only later. One of the reasons for this delayed reception is that RD is counter-intuitive at first. Diffusion generally distributes particles and molecules evenly, thereby increasing entropy and equalizing the regular fluctuations in concentration that constitute any pattern. When combined with specific ‘reactions’, however, patterns can emerge in a self-organized manner. Here, it is important to note that reactions can refer to actual chemical reactions involving the morphogen substances, but can also be conformational changes of macromolecules or even their reversible associations [6]. The work presented in this thesis focuses almost exclusively on the experimental side of RD. Nevertheless, equations 1.1 and 1.2 provide a simplified mathematical definition of

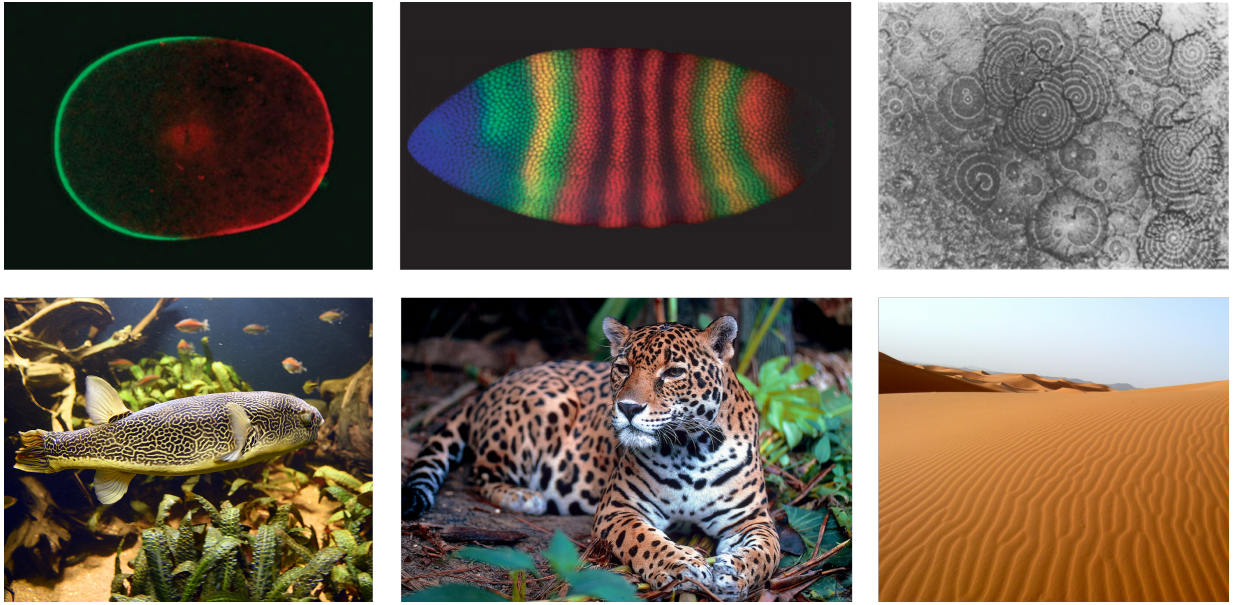


Figure 1.1: Examples of patterns found in nature. Top row: PAR proteins polarize the *C. elegans* egg cell; embryonal patterning of even-skipped (red) in *Drosophila melanogaster*; aggregation patterns formed by the slime mold *Dictyostelium discoideum*. Bottom row: Skin pattern of a pufferfish (*Tetraodon mbu*); spotted fur of a Jaguar (*Panthera onca*); sand ripples in a desert. Sources and licenses of images are detailed in the Image Credits.

such a system.

$$\frac{\partial a(\vec{x}, t)}{\partial t} = D_a \nabla a + f(a, b) \quad (1.1)$$

$$\frac{\partial b(\vec{x}, t)}{\partial t} = D_b \nabla b + f(a, b) \quad (1.2)$$

Here, the concentration changes of the two morphogens, a and b , at a certain position and time depend on the molecular diffusion of each morphogen as well as on a function f , which describes the reactions occurring in the system. Most systems identified to date are composed of more than two morphogens or morphogen states, and often not all components influencing the system have been identified. Furthermore, many times the exact rates of reaction and diffusion are unknown. The majority of mathematical models of RD therefore simplify the true dynamics and need to be utilized with proper care.

1.2 Model systems for reaction-diffusion and control schemes

Several model systems have been described and used to learn about the underlying dynamics and reactions, as well as the phenomenon of pattern formation itself. Two of the most

prominent systems to date are the Belousov-Zhabotinsky reaction (BZ reaction) and the Carbon monoxide oxidation on Pt(110) crystals (CO oxidation). In the latter case of CO oxidation, it was found that the platinum(110)-catalyzed reaction $2CO + O_2 \rightarrow 2CO_2$ displayed a variety of spatiotemporal concentration patterns when run under controlled, low pressure conditions [7]. At low CO partial pressure, growing elliptical CO fronts could be visualized on the surface by using photoemission electron microscopy (PEEM). By elevating the partial pressure of CO, spiral waves could be observed in the system (see Figure 1.2) [8]. To suppress spatiotemporal chaos and gain control over this pattern forming reaction, global delayed feedback via the partial pressure of CO was introduced [9]. Here, the total signal as obtained via PEEM was integrated and fed back via CO pressure with a variable delay. Control over the patterns could thereby be achieved, and new patterns formed. Interestingly, in a certain delay regime, a standing wave phenotype emerged.

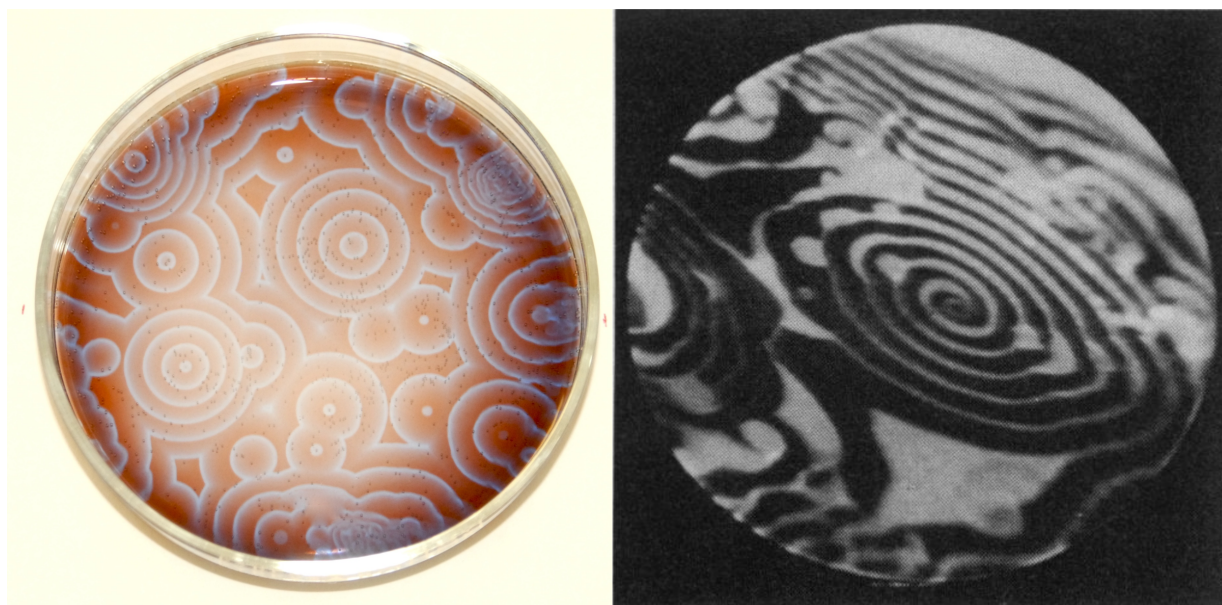


Figure 1.2: Examples of model RD systems. Left: Photograph of Belousov-Zhabotinsky reaction running in a petri dish. Right: Carbon monoxide oxidation on a Pt(110) crystal, observed by photoemission electron microscopy. Right image reprinted with permission from AAAS (Science): Ertl et al. (1991) [7]. For further license information please see the Image Credits.

The most frequently used model system for RD to date is the BZ reaction. The reaction itself is very complex and involves many intermediates. At its core, however, one autocatalytic reaction creates bromine, while another autocatalytic reaction consumes bromine to create bromate [10]. Most commonly, malonic acid or citric acid are oxidized by bromate, while cerium, manganese or complexes of iron are used as catalysts (and indicators in case of *Fe*). Bromine can be substituted with iodine, for example in the chlorite-iodide-malonic acid reaction (CIMA reaction). The BZ reaction and derivatives show synchronized bulk oscillations of the oxidation state when prepared in stirred containers. When distributed as a thin liquid film in petri dishes, or when confined to thin gels or porous membranes [11],

they form spatiotemporal patterns. Here, both dynamic patterns like spirals, travelling waves and bubbles, as well as stationary patterns like labyrinths, spots and inverse spots have been reported [11]. In an effort to control pattern formation, multiple light-sensitive reactions have been developed [12, 13]. Similar control schemes as for the CO oxidation could therefore be realized in the BZ reaction. An added benefit of using light to influence pattern formation is that more complex, local control schemes can be implemented [13, 14]. But even using only global feedback, a big spectrum of resonant system behaviors could be observed in the BZ reaction (Figure 1.3). Intriguingly, the system retained a memory of up to three distinct patterns when regularly photoactivated, as shown in the $f_p/f_0 = 2 : 1$ and $f_p/f_0 = 3 : 1$ cases in Figure 1.3.

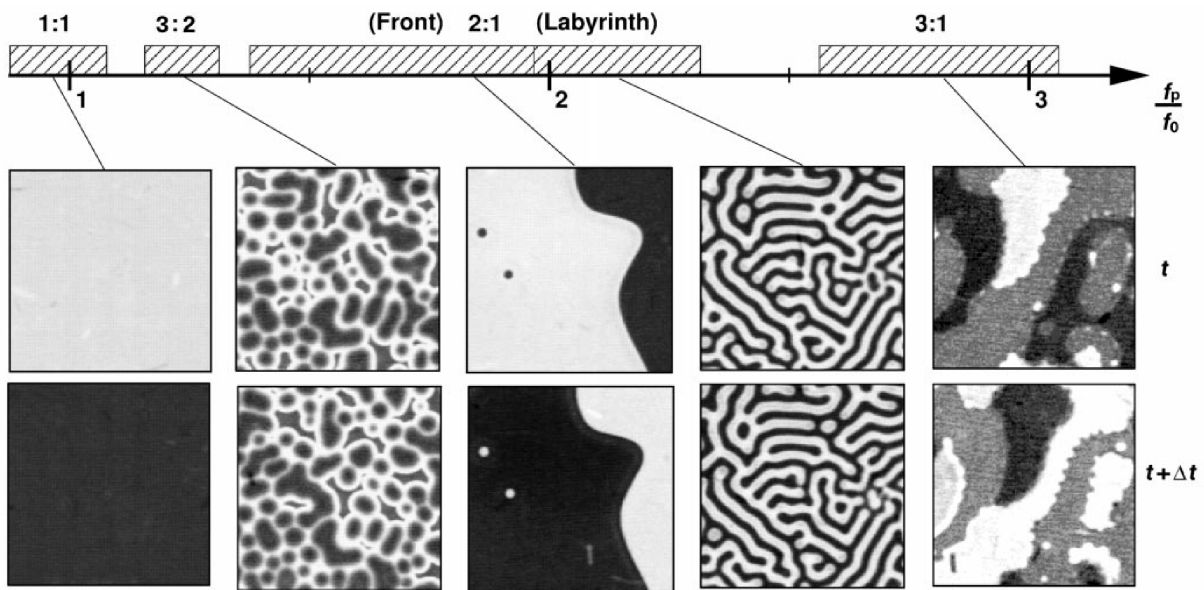


Figure 1.3: Periodic optical forcing of a light-sensitive Belousov-Zhabotinsky reaction. Bifurcation diagram showing different frequency-locked regimes observed as a function of f_p/f_0 where f_p is the perturbation frequency and f_0 is the natural frequency of the system. Patterns are shown in pairs, one above the other, at times separated by $\Delta t = 1/f_p$, except for the 1:1 resonance where $\Delta t = 1/2f_p$. Striped boxes on the horizontal axis mark perturbation frequency ranges with the same frequency-locking ratio. Reprinted with permission from Nature: Petrov et al., Nature 1997 [12]

Both CO oxidation and BZ reaction have been related to biological pattern formation, since the underlying principle of RD is common to all of these processes. It is important to have model systems recapitulating the phenomena observed in a biological environment. Here, working under biologically relevant conditions may tell us more about the systems that play a role in animal development, cell division or skin patterning. However, neither the high-temperature, low-pressure conditions used in CO oxidation, nor the countless chemicals used in BZ reaction are biocompatible in any way. Furthermore, biological pattern formation happens on different matrices, such as in tissues or on cell membranes, which may have tremendous impact on diffusion and reactions. Also for synthetic biologists,

it would be very desirable to have a biocompatible, modifiable RD system, which can be repurposed for their specific application. For an overview about biological systems used for RD research, please refer to section 2.5.

1.3 The Min system of *Escherichia coli*

The Min system of *Escherichia coli* (*E. coli*) is a very versatile biological RD system and the main subject of this thesis.

1.3.1 The Min system *in vivo*

The Min system is important in ensuring symmetrical division of *E. coli* cells. The *min* operon as well as the three Min proteins were named after the “minicells“ phenotype that occurs when the Min system is disturbed or deleted [15]. Division of *E. coli* is initiated by the formation of a protoring of the protein filamentous temperature sensitive Z (FtsZ) at the prospective division site. FtsZ, anchored to the membrane by FtsA and ZipA, then recruits further factors of the cell division machinery, such as FtsN, FtsW, FtsBLQ and many more [16, 17, 18]. The assembled “divisome“ consists of the Z-ring, associated intracellular stabilizers, proteins that cross the plasma membrane, and cell wall synthases that build and remodel septal peptidoglycan. Septation and division is associated with FtsZ-treadmilling as well as peptidoglycan synthesis, but currently it remains unclear whether FtsZ contributes any of the force required for division [19]. Positioning the division machinery in the cell middle is crucial to obtain two viable daughter cells. Therefore *E. coli* utilizes two systems that together ensure proper site selection (see Figure 1.4). Firstly, there is a system termed nucleoid occlusion. To make sure that cells do not attempt to divide at a position where the bacterial chromosomal DNA is located, the protein SlmA binds to genomic DNA and inhibits formation of FtsZ protorings above the chromosome by direct interaction with FtsZ [20]. Since the nucleoid is distributed into the prospective daughter cells after DNA replication, this system alone restricts cell division to the three division zones close to either pole or at midcell.

Secondly, the Min system further restricts division to a small zone in the cell middle. The Min system of *E. coli* shows rapid pole to pole oscillations driven by a RD-mechanism. It consists of three proteins, MinC, MinD and MinE. MinC binds to MinD and is an inhibitor of FtsZ-polymerization, and thus conveys the biological function to the Min oscillations [21]. However, it merely passively follows the oscillations caused by the interactions of MinD, MinE and the cell membrane. Since it is not required for pattern formation it is not in the focus of our interest.

MinD

MinD is an ATPase of the deviant Walker A class, distinguished by carrying the amino acid sequence $X - K - G - G - X - X - K - [T/S]$ in its P-loop, a sequence that

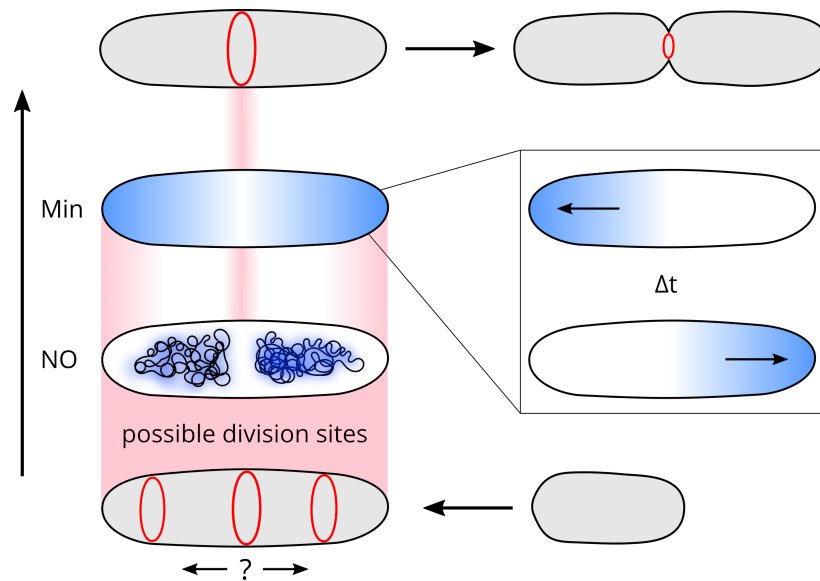


Figure 1.4: Schematic representation of division site selection in *E. coli*. Clockwise, starting bottom right: Without nucleoid occlusion (NO) and the Min system, the cell cannot find the cell middle to achieve symmetrical division. NO restricts division to either midcell or to the cell poles, leading to symmetrical divisions as well as polar divisions. The Min system oscillates from pole to pole and thereby restricts FtsZ to a narrow zone at midcell.

directly contacts the bound nucleotide [22]. The proteins of this family are special in that the binding of nucleotide triphosphate is commonly linked to an interaction of the ATPase with itself or other proteins. This is also true for MinD, which dimerizes upon ATP binding [22]. This step enables the protein to bind to the membrane, since it carries a C-terminal amphipathic helix that confers weak membrane-binding activity [23]. The monomer-dimer transition is thus also a membrane switch and the central switch in the Min cycle. ATP-hydrolysis by MinD is a very slow process. MinE however, the second protein involved in Min oscillations, can bind to a membrane-bound MinD-dimer and enhance its hydrolysis activity significantly. MinE can therefore induce release of MinD from the membrane. Figure 1.5 shows a crystal structure of a MinD dimer with nucleotide and a bound MinE dimer [24].

MinE

MinE is a small protein of only 88 amino acids, or about 10 kDa. Despite this small size, MinE carries many different functions. MinE's primary function, the activation of MinD's ATPase, is located in a segment near the N-terminus of the protein (AA 13-31) [25, 26]. This sequence (NTANIAKERLQIIVAERRR) folds into an α -helical segment when the protein is interacting with MinD, but is differently structured in free MinE [24]. MinE(13-31) alone is capable of interacting with MinD [25, 27], but both MinE(13-31) and MinE(1-31) have been reported to be unable to form patterns with MinD [28].

Perhaps the most striking property of MinE is the conformational change it can undergo

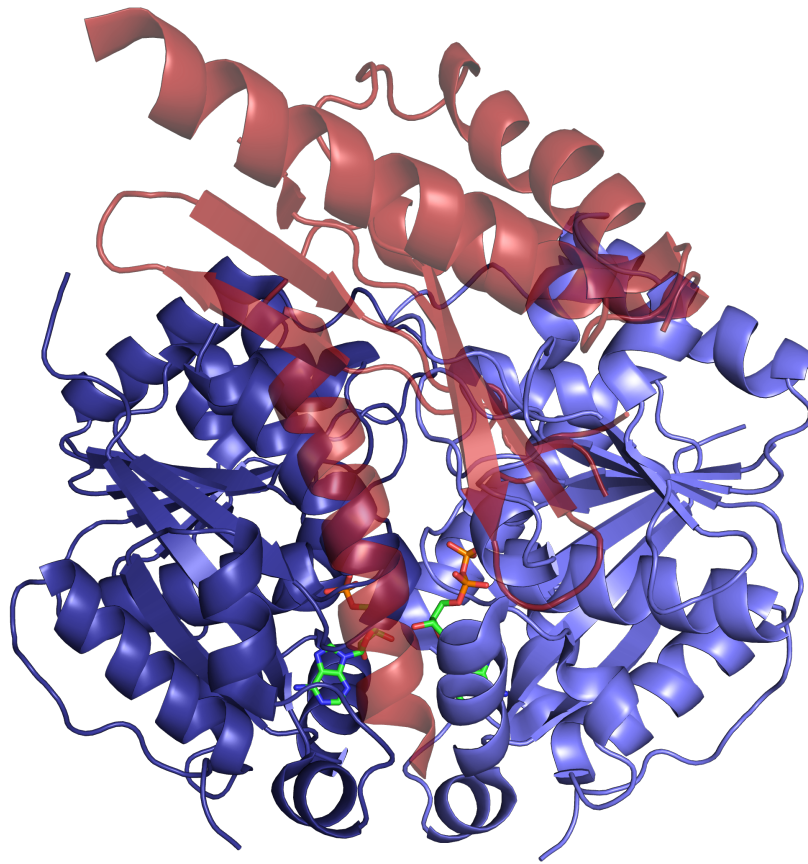


Figure 1.5: Crystal structure of a MinD dimer, bound to two ADP and to a MinE dimer. The MinD monomers are colored in different shades of blue, while MinE is transparent red in the foreground. Note that the membrane targeting sequences of MinD and the interacting MinE were not crystallized, but would be located below the structures at the chosen perspective. Source: PDB 3R9J [24]

between a so called latent state (6β) and an active state (4β) (Figure 1.6) [24]. Recent results have shown that the conformational rearrangement is initiated when a MinE dimer encounters an ATP-bound MinD dimer [29]. To make the interacting residues accessible for MinD-sensing, the MTS is transiently released from the 6β -conformation while in solution [30]. Both subunits of the MinE dimer seem to rearrange their conformation, yet without forming a monomeric intermediate [31]. It was long unclear, why MinE rearranges so drastically instead of remaining in an active form, since mutants that force MinE into the active conformation still support pattern formation [32]. However, new insights reveal that by utilizing the MinE-switch, the concentration range in which the system can sustain patterns is vastly extended, and thus this measure confers additional robustness to the Min system [33]. Interestingly, the 6β conformation, where the MTS are both sequestered and only transiently released, allows MinE to diffuse freely in the cytoplasm, without regularly binding to the membrane. In contrast, the 4β conformation has the MTS released and has therefore been implicated in a further property that defines MinE, namely the rapid

rebinding of active MinE to the membrane and nearby ATP-MinD dimers [31]. Lastly, and as mentioned above, MinE is a constitutive dimer, a property encoded diffusely in the “topological specificity domain“ [34], meaning MinE(31-88). Disentangling and isolating some of the functions of MinE by analyzing defined mutations like I24N (locks MinE in 4 β), L3E and L4E (weakens MTS and many more mutants was initiated by Simon Kretschmer, whose work also provided the basis for parts of this thesis.

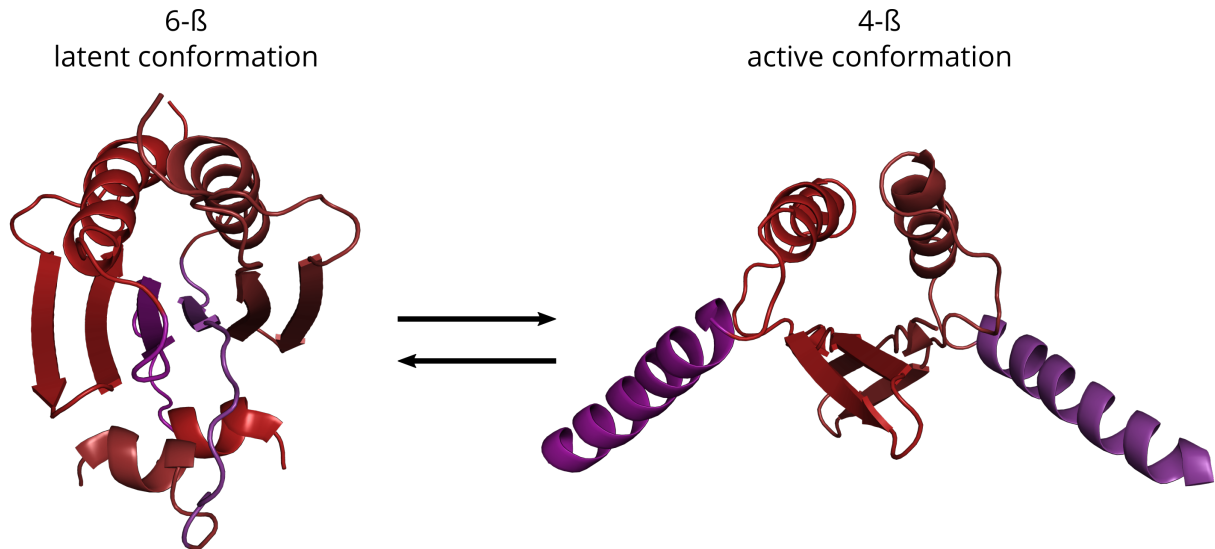


Figure 1.6: Conformational changes of MinE visualized with the help of crystal structures in the latent (6 β -sheets) conformation (left) and in the active (4 β -sheets) conformation (right). The two monomers are indicated in slightly brighter or darker red, respectively. Magenta depicts the region in the latent conformation that becomes alpha helical in the active conformation and contacts MinD. Sources: PDB 2KXO (latent) [35] PDB 3R9J (active) [24]

Min oscillation mechanism

This section will combine the information collected in the previous chapter about MinD and MinE to lay out the mechanism of oscillation. In an individual *E. coli* cell, MinD and MinE are always present at roughly 2000 copies each [36]. Since ATP is provided by the cell’s metabolism, MinD will bind ATP, dimerize and bind the plasma membrane, which contains about 30% negatively charged lipids. Membrane bound MinD induces positive feedback, whereby it recruits further MinD to the same region via a so-far undescribed interaction. MinD will therefore form a local zone of MinD on the plasma membrane. MinE will be recruited by the membrane-bound MinD. While in the initial phase, MinD self-recruitment prevails, over time MinE becomes enriched in the zone and MinE-induced ATP hydrolysis and subsequent MinD detachment becomes dominant. The MinD zone therefore dissolves and the proteins return to the cytoplasm. MinD now redistributes to another region on the plasma membrane, where MinE density is low enough to allow formation of a new MinD zone. This starts the next oscillation cycle, as MinE will eventually become cytoplasmic

and bind to the newly formed zone. In the geometry of an *E. coli* cell and with the protein numbers present, the Min system always identifies and oscillates along the long axis of the cell, thereby defining the cell middle as described above. Please note that in the literature, the MinE bound to a MinD zone and accumulating near midcell is often referred to as the “E-ring“, even though lateral contacts between MinE dimers have not been shown and the ring shape of the MinE zone is merely a function of the rod-shaped cell morphology [37].

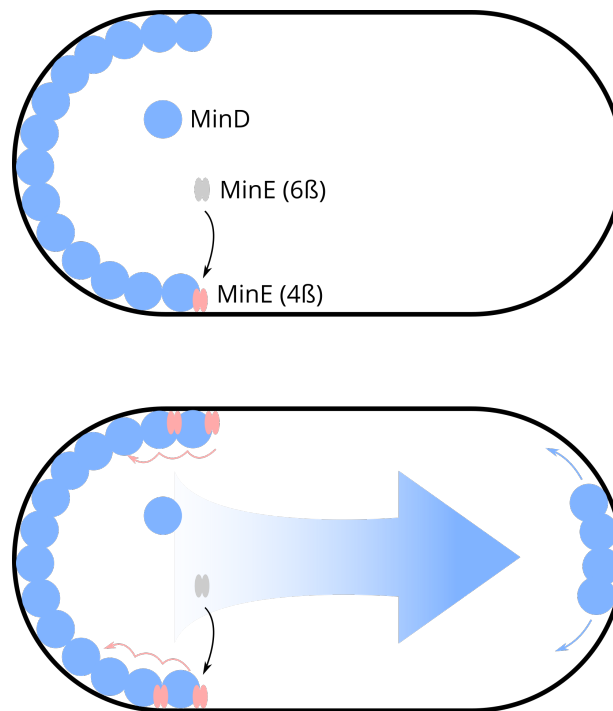


Figure 1.7: Simplified schematic of Min oscillations *in vivo*. (top) MinD accumulates in a polar zone via positive feedback. (bottom) MinE switches from the latent to the active conformation upon encountering ATP-bound MinD to over time populate the polar MinD zone. MinD detachment via MinE becomes dominant over MinD positive feedback and the polar zone is rapidly dissolved. Cytosolic MinD exchanges ADP for ATP, dimerizes again and rebinds the membrane where the MinE occupancy is low enough - at the opposite pole.

1.3.2 Bottom-up reconstitution of the Min system

In vitro assays for the Min system have been established early on, such as ATPase assays to test activity of wild-type proteins in comparison with MinD- or MinE-mutants or to confirm protein integrity [38]. However, only a decade ago the idea arose that much may be learned from the Min system by reconstituting the oscillation *in vitro*, and observing it via microscopy [39]. This bottom-up, simple reconstitution of MinD and MinE with ATP on an supported lipid bilayer (SLB) showed that the Min proteins self-organize into travelling waves and spirals in an open geometry with a large bulk, as illustrated in Figure 1.8. MinE was shown to accumulate over the course of a travelling wave and reach its

maximum membrane concentration at the end of a MinD-zone, consistent with the behavior *in vivo*. In contrast, it remains puzzling why the wavelength *in vitro* is approximately ten times larger than *in vivo* [39]. In addition to the open geometry, the Min system was also reconstituted in a flow-cell by the Mizuuchi-lab, which lead to several, in part controversial, observations [40]. To be able to better compare the geometries, Figure 1.8 shows representations of the two setups. While travelling waves and spirals were the only consistent pattern observed in the well setup, additional, partly ill-defined patterns were reported for the flow-cell by the authors, such as “amoebae“, “bursts“, “mushrooms“ and “snakes“ [40, 41, 28]. Of these, the burst patterns seem the most interesting, since they arise where MinD availability is the limiting factor, and have been compared to *in vivo* polar zones that transiently form [29].

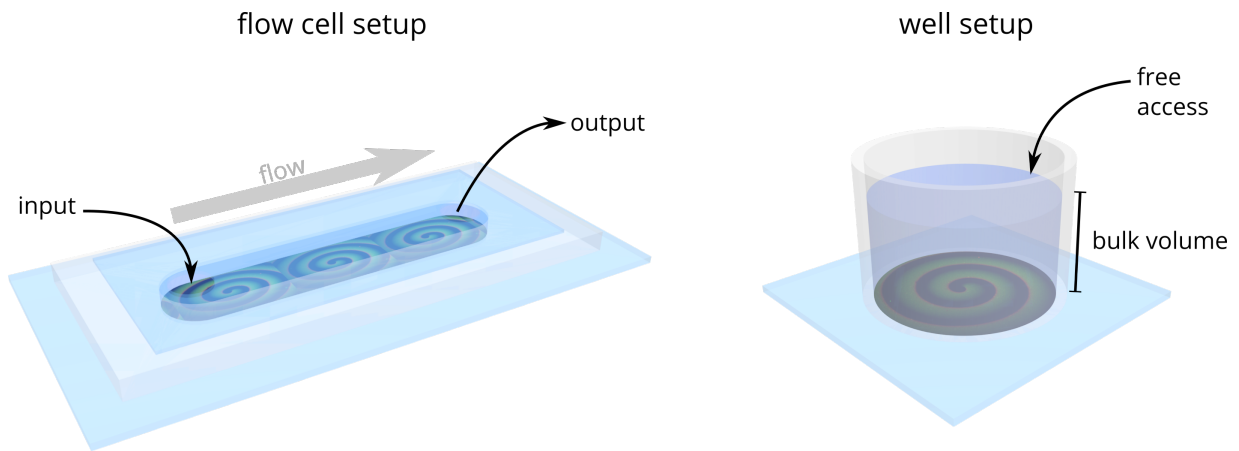


Figure 1.8: Schematic comparison of a flow cell setup for *in vitro* reconstitution of the Min system with a well setup. While in a flow cell, buffers can be exchanged quickly via the inlet and outlet, direct access with pipets, for example for control during SLB-formation, is only possible in the well setup. Another important distinction is the difference in bulk volume, which is much larger in a well setup.

In a series of single-molecule, Foerster Resonance Energy Transfer (FRET) and Fluorescence Recovery After Photobleaching (FRAP) experiments using the well setup, it was shown that MinE accumulates towards the rear of a Min concentration wave by rapid re-binding of MinE-dimers [31]. Therefore, an updated model for wave propagation (Figure 1.9) was proposed by the authors and has since been accepted in the field [42]. While initially, both rapid rebinding and direct MinE-membrane interaction were thought to be important for conferring robustness to the system and enlarging the $[\text{MinE}]/[\text{MinD}]$ ratio in which patterns can form, recent results show that MinE’s switch alone enables this [33].

1.3.3 Controlling self-organization in the Min system

As for controlling self-organization by the Min system, multiple approaches have been pursued in the past. One approach relies on patterning the support on which the SLB is formed, thereby limiting the Min protein’s binding to arbitrarily shaped SLB patches.

The patterning was achieved by depositing gold layers on a glass support and photolithographically removing it in certain regions by ion etching [43]. The results showed that the Min system reacts to the patterned membrane in different ways: If a checkerboard pattern with a wavelength much above the Min system's was used, alignment of the resulting Min patterns was hardly influenced by the SLB pattern. Rather, individual patches were isolated and no coherent pattern spanning multiple patches emerged. When the SLB pattern was on the same order as the Min pattern, the Min pattern became highly irregular and therefore was clearly influenced by the patterned support. Small gold patches with large spacing well beyond the characteristic wavelength of the Min system did not seem to influence Min pattern formation at all. Interestingly, on isolated patches with elongated geometries and widths similar to the intrinsic Min wavelength, the waves always oriented themselves along the longer axis of the patch. Thus, Min waves can be guided by patterning the membrane on which the reaction happens. In an effort to more closely mimick the *in vivo* geometry in Min reconstitution, an assay was developed where the membrane is structured in three dimensions by forming it on a microstructured polydimethylsiloxane (PDMS) support [44, 45]. PDMS is a soft polymer that can be molded by curing it on a pre-structured silicon wafer. A membrane formed on the PDMS closely follows the shape of the underlying support. Thereby, micrometer-sized rod-shaped microcompartments could be formed. Preparing the Min reaction as in the described well setup and then lowering the buffer to the rim of the microcompartments allowed the isolation of the reaction within. This *in vitro* reconstitution of Min proteins shows regular oscillations reminiscent of *in vivo* Min oscillations in these compartments, although the wavelength is still about ten times as large [44]. The study also showed that MinD and MinE alone can select the longer axes in elongated compartments and provide spatial cues, for example for FtsZ. However, as with most measures of confinement, the final concentration of proteins in each microchamber can vary and is hard to estimate [46].

Going even further to mimick *in vivo* geometries, Min proteins have been reconstituted in flow-cells of varying length, width and shape, providing a presumably fully membrane-clad compartment [46]. In rectangular chambers of side lengths varying between 10 μm and 80 μm and at different aspect ratios, the behavior of Min proteins was recorded. Interestingly, most of the so-created phase diagram was occupied by travelling wave patterns and rotational patterns. Only a small region within the phase diagram displayed oscillations. A potential pitfall of any strategy involving a flow-cell is that protein concentrations are unknown and likely vary between chambers of different sizes. This is due to the fact that Min proteins are loaded and will bind to the tubings and channels they run in, as well as to the membrane as soon as they encounter it. This has been used by other researchers to create a variety of patterns from channel inlet to outlet [28]. The authors of this study on fully confined microfluidic chambers therefore employed a fluorescence calibration with GFP to estimate the final concentrations. They calculated average concentrations of 4.5 μM MinD and 6 μM MinE which is significantly higher than the concentrations found *in vivo*. Additionally, taking into consideration the publication "Stationary patterns in a two-protein reaction-diffusion system" enclosed in this thesis, we need to reconsider the relevance of the data gathered in this study. An N-terminal purification tag was later shown to alter

Min protein behavior *in vitro* and *in vivo*, with the possibility of big shifts in the phase diagram obtained by the authors [47]. By varying the buffer conditions, mainly changing the salt concentration in the reaction buffer, it has been shown that the wavelength and integrity of Min patterns can be altered [41]. Furthermore, in the same study it was shown that Min patterns do not rely on native *E. coli* lipids to be able to perform their reaction, but rather only require negatively charged headgroups, such as PG, PS or cardiolipin. Also by changing the percentage of negatively charged headgroups in the membrane, the Min patterns could be altered in wavelength. Even at 0% negatively charged lipids, the Min proteins still form a pattern, but the protein density on the membrane is very low.

Another interesting approach to control Min protein patterns was explored *in vivo* by ‘sculpting’ live *E. coli* cells into different shapes and following an sfGFP-tagged MinD via microscopy [48]. By inhibiting both cell division and shape maintenance via MreB by antagonistic drugs, the authors could grow *E. coli* cells in triangular, square or rectangular PDMS-chambers, and the cells filled the given shape without disrupting Min protein integrity. Interestingly, also here Min proteins were found to sustain rotational, longitudinal, diagonal, stripe and transversal oscillation modes. The authors conclude that Min proteins capture the symmetry and scale of the cell boundary and are highly adaptable.

All of these efforts to control the Min system show a highly adaptable RD-system that can produce many different outcomes depending on the concentrations, support, buffer and geometry. Yet surprisingly, none of the studies to date attempted to control Min protein patterns *in situ* or look at what modes apart from oscillatory ones might be available in the Min system.

1.4 Objective of this thesis

To which degree can we control biological self-organization? Which further possibilities does the Min system offer in terms of pattern diversity and network architecture? So far, the possibilities provided by the *in vitro* reconstitution of the Min system have predominantly been used for investigations of the original Min function. Measuring protein residence times [31], shaping supports to look at geometries and axis selection [43] and reaction confinement to recapitulate pole-to-pole oscillations [44, 49, 46] are such examples. Another angle has been to utilize mutants to understand why the Min system, especially MinE, carries so many different functions, which of them are essential for self-organization, and how they contribute to robustness of the system [33, 32].

While these are all relevant and important studies, the Min system offers another, so far untapped, opportunity: Being the only biological RD-system to date that needs so few components which are so easily purified and reconstituted *in vitro*, the Min system should be turned into the staple model system for biological RD. This thesis therefore had distinct objectives to improve the versatility and utility of the Min system for pattern formation. 1) To find a way to control Min protein patterns *in situ* using light, similar to the two established model systems, the Belousov-Zhabotinsky reaction and the Carbon monoxide oxidation on Pt(110) crystals. 2) To explore whether the Min system is capable of repro-

ducibly forming non-oscillatory patterns, as predicted for a general case by Alan Turing [5] and as many natural systems, e.g. in skin patterning, do. 3) To reduce the complexity in the Min system to its absolute minimum by substituting MinE with a minimal peptide and rebuilding pattern formation from there. All of these objectives were investigated using an *in vitro* reconstitution of the Min system in a precisely controllable well setup [39], the detailed protocols for which are now also more easily available to the scientific community [50].

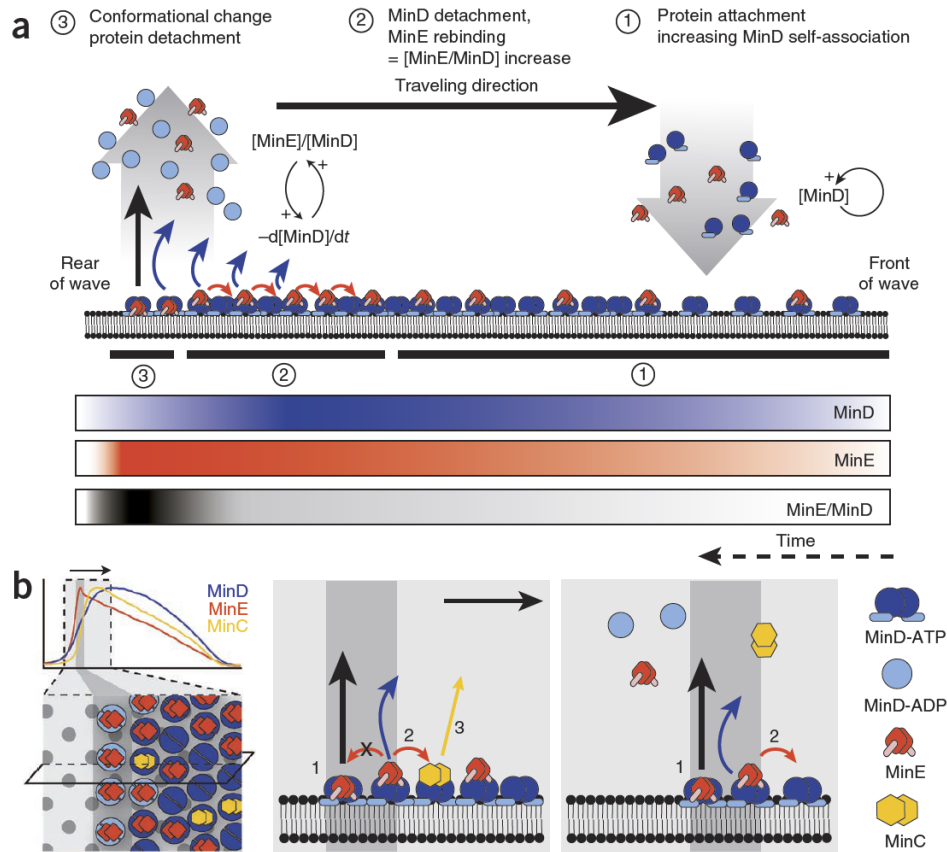


Figure 1.9: Model of Min-protein wave propagation. (a) Starting from the front of the protein wave (or at the beginning of an oscillation cycle, right), MinD-ATP starts to bind to the membrane. With increasing density, the MinD dimers bind longer to the membrane and diffuse more slowly. MinE dimers bind to membrane-bound MinD, but the concentration of MinE is at first too low to result in membrane detachment becoming dominant. At a sufficiently high $[\text{MinE}]/[\text{MinD}]$ ratio, protein detachment starts to dominate. Because of rapid MinE rebinding to MinD, the $[\text{MinE}]/[\text{MinD}]$ ratio can continuously increase toward the rear of the wave. This behavior guarantees that eventually all membrane-bound MinD dimers are in complex with MinE. At a $[\text{MinE}]/[\text{MinD}]$ ratio of about 1, interaction of MinE with the membrane induces a conformational change, which results in the displacement of all MinC (not shown here). Finally, all proteins rapidly leave the membrane. (b) Illustration of the order of events at the rear of the protein wave. Shown are top (left) and side (middle and right) views of Min proteins bound to the membrane. As seen in the side view, before detachment from the membrane, either MinE forms a complex with MinD, which is present in an altered conformation involving membrane binding by MinE (1), or MinE rebinds to a neighboring membrane-bound MinD, if available (2). Because the density of membrane-bound MinD is higher toward the front of the wave, rebinding MinE is biased in this direction, giving rise to the local saturation of MinD with MinE. After detachment of MinC from MinD (3), MinE can occupy the overlapping binding site on MinD. Reprinted with permission from Nature structural and molecular biology [31]

Publications

Optical Control of a Biological Reaction-Diffusion System

In this manuscript, the development and application of a peptide-based photoswitch for the *in vitro* Min system is detailed. Direct photomanipulation of this system adds great utility and uncovers novel resonance phenomena.

Reprinted with permission from P. Glock, J. Broichhagen, S. Kretschmer, P. Blumhardt, J. Mücksch, D. Trauner, and P. Schille, “Optical Control of a Biological Reaction-Diffusion System,” *Angewandte Chemie International Edition*, vol. 57, pp. 2362–2366, feb 2018. Copyright (2018) John Wiley and Sons.

Source online: <https://doi.org/10.1002/anie.201712002>

Synthetic Biology

International Edition: DOI: 10.1002/anie.201712002
German Edition: DOI: 10.1002/ange.201712002

Optical Control of a Biological Reaction–Diffusion System

Philipp Glock, Johannes Broichhagen, Simon Kretschmer, Philipp Blumhardt, Jonas Mücksch, Dirk Trauner, and Petra Schwille*

Abstract: Patterns formed by reaction and diffusion are the foundation for many phenomena in biology. However, the experimental study of reaction–diffusion (R–D) systems has so far been dominated by chemical oscillators, for which many tools are available. In this work, we developed a photoswitch for the Min system of *Escherichia coli*, a versatile biological *in vitro* R–D system consisting of the antagonistic proteins MinD and MinE. A MinE-derived peptide of 19 amino acids was covalently modified with a photoisomerizable crosslinker based on azobenzene to externally control peptide-mediated depletion of MinD from the membrane. In addition to providing an on–off switch for pattern formation, we achieve frequency-locked resonance with a precise 2D spatial memory, thus allowing new insights into Min protein action on the membrane. Taken together, we provide a tool to study phenomena in pattern formation using biological agents.

Spatiotemporal patterns and oscillations formed by reaction–diffusion (R–D) type mechanisms are found throughout nature. They are essential for the regulation of diverse life processes, from ensuring correct division of many bacterial cells^[1] to the development of higher organisms.^[2,3] However, the inherent nonlinearity underlying such processes makes them hard to predict theoretically, and in particular the existence of many unknowns hampers the development of comprehensive mathematical models. Currently, the best understood experimental R–D type systems are the Belousov–Zhabotinsky (BZ) reaction and the oxidation of carbon monoxide on a single crystal surface (110) of platinum.^[4,5] The BZ reaction comprises a highly complex chemical reaction scheme with many reactants and intermediates. Furthermore,

the reaction is quickly depleted of bromate and malonic acid, which halts its oscillatory behavior unless reagents are continuously replenished. Carbon monoxide oxidation can only be observed using a photoemission electron microscope with precise pressure and temperature control. Here, R–D behavior is only observed at temperatures above 450 K, and gas partial pressures must stay within a narrow range to sustain the oscillatory reaction. Research on both the BZ reaction and carbon monoxide oxidation has greatly benefited from the development of means to externally influence the reaction *in situ*, which has uncovered new avenues of research, as well as novel spatiotemporal patterns.^[6–8] Notably, the BZ Reaction has been applied to testing Turing's predictions on morphogenesis by nonlinear dynamics.^[9]

Another, still not fully characterized, reaction–diffusion system, which is intrinsically biological and therefore much closer to many of the important occurrences of R–D mechanisms in living systems, is the MinDE system of *Escherichia coli*. MinD is an ATPase that cycles between a membrane-bound dimeric state (ATP) and a monomeric state in solution (ADP; Figure 1 A). MinE antagonizes MinD membrane attachment by elevating its intrinsically low ATPase activity.^[10] While there have been many studies related to the supposedly primary function of the Min system, namely positioning the division septum in several bacterial species as well as plant organelles,^[11] its potential as a fundamental biological *in vitro* R–D model system has not been widely recognized. In contrast to the other available model systems, the two pattern-forming constituents of the Min system can be biochemically engineered in many ways.^[12] The reaction can be sustained for many hours, and both MinD and MinE can be directly fluorescently labelled and followed individually without significantly disturbing or complicating the reaction network. The Min reaction runs at room temperature and can be observed through widely available laser scanning or total internal reflection fluorescence (TIRF) microscopes.

Because of the great relevance of the Min proteins as an archetypical biological pattern-forming system, we set out to develop new tools to influence and control their dynamics *in situ*. An ideal way to achieve external control is by optical manipulation. We herein describe the development of a photoswitch for the Min system based on a short alpha-helical peptide taken from MinE. This is, to our knowledge, the first time a biological reaction–diffusion system has been optically controlled in a direct and reversible manner.

Our photoswitch is capable of locally removing MinD from the membrane in dynamic *in vitro* self-organization assays. To this end, we modified a short peptide derived from MinE (amino acids ($\alpha\alpha$) 13–31) to contain two cysteines with amino acid spacings of ($i/i + 7$) or ($i/i + 11$). A small-molecule

[*] P. Glock, S. Kretschmer, P. Blumhardt, J. Mücksch, Prof. Dr. P. Schwille
Cellular and Molecular Biophysics
Max Planck Institute of Biochemistry
Am Klopferspitz 18, 82152 Martinsried (Germany)
E-mail: schwille@biochem.mpg.de

Dr. J. Broichhagen, Prof. Dr. D. Trauner
Department of Chemistry, Ludwig Maximilians University of Munich
Butenandtstr. 5–13, 81377 Munich (Germany)

Dr. J. Broichhagen
Current address: Department of Chemical Biology
Max Planck Institute for Medical Research
Jahnstr. 29, 69120 Heidelberg (Germany)
Prof. Dr. D. Trauner
Current address: Department of Chemistry
Silver Center for Arts and Science, New York University
100 Washington Square East, New York, NY 10003 (USA)

Supporting information and the ORCID identification number(s) for the author(s) of this article can be found under:
<https://doi.org/10.1002/anie.201712002>.

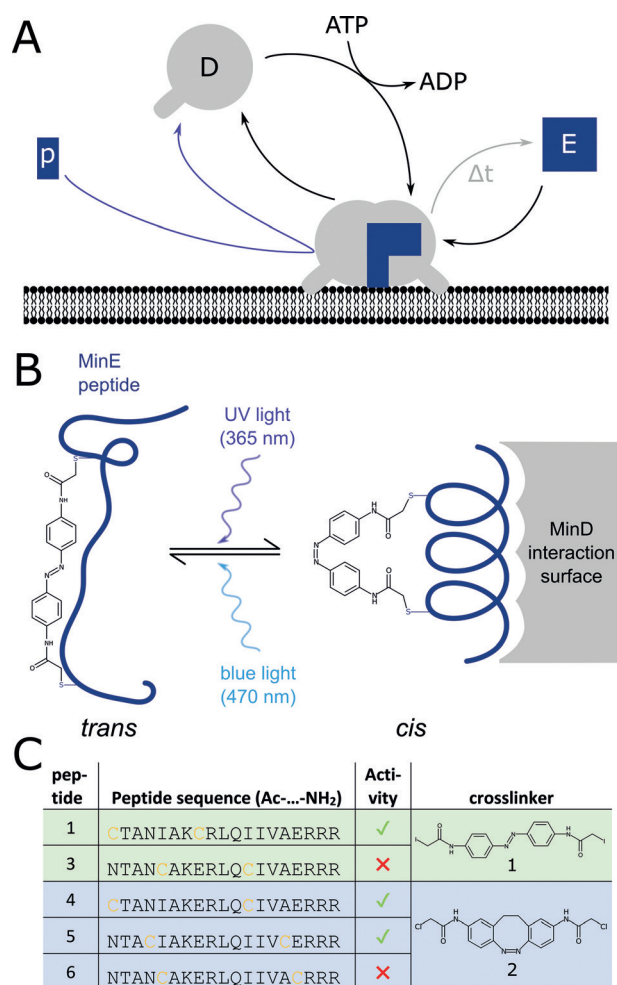


Figure 1. Peptide photoswitch design. A) A simplified schematic of MinDE protein dynamics, as well as extrinsic activation by a photo-activated peptide (purple arrow) B) A small molecule based on an azobenzene core was covalently linked to two cysteines within the peptide. The UV-light-induced *trans*-to-*cis* isomerization of the azobenzene moiety reversibly influences peptide structure. C) Register shift of MinE residues that were exchanged for cysteines and the resulting peptide activity in *in vitro* Min self-organization assays. Shaded colors indicate spacings for cross-linking (green $i/j + 7$; blue $i/j + 11$), with the respective small molecule crosslinkers shown to the right.

bridge that incorporates the photoisomerizable azobenzene moiety was covalently crosslinked to both of the cysteines through alpha-halogeno acetamide chemistry. Photoisomerization of the crosslinker is thereby expected to induce a conformational change in such a way that alpha-helicity of the peptide is broken in the dark and blue-light-activated state (*trans*), while it is promoted when the peptide is illuminated with UV light (*cis*).^[13,14] Based on the crystal structure (PDB ID: 3R9I),^[15] we expected the alpha-helical state to interact with MinD, activate its ATPase activity, and thereby initiate MinD detachment from the membrane. Two different azobenzene crosslinkers were incorporated (Figure 1B; light green and light blue backgrounds), with slightly different spectral characteristics and a different $\alpha\alpha$ spacing required for the switch (Figure S1 in the Supporting Information).

Cysteines were incorporated into the peptide at positions that we expected to be redundant for structural or functional MinE peptide integrity, while also keeping the crosslinker away from the interaction site. However, two of the designed peptides, both containing the I17C mutation, failed to show activity in *in vitro* self-organization assays (data not shown). This suggests that I17 is important for proper MinE function, contrary to what was reported for the respective residue in *Neisseria gonorrhoeae* MinE.^[17] While peptides 4 and 5, which have the *cis*-stable crosslinker, are functional (Video S4 in the Supporting Information, here activated with an LED), activation by the microscope scanning laser does not allow simultaneous imaging and activation, and thus was impractical for this study. Therefore, peptide 1 was used for this study throughout, with the added benefit of lower interference from the imaging lasers.

The photoswitch was tested in conditions under which MinD and MinE form dynamic wave patterns. An *in vitro* Min assay was started, wave propagation was observed, and then peptide 1 was added. We presume that the activated photoswitch has a higher affinity for MinD than wild-type MinE, and can thus displace MinD completely at a relatively lower concentration. Indeed, activating the UV-responsive peptide 1 in a running *in vitro* Min reaction led to an almost complete local dissociation of MinD from the membrane (Figure 2A and Video S1). This state was transient and was succeeded by renewed occurrence of travelling waves unless recurring pulses of UV light kept the photoswitch active (Video S2). This relaxation behavior is mostly due to thermal relaxation of the azobenzene, as well as light from the imaging (see discussion in the Supporting Information). In contrast to the waves observed before switching, which were ordered and parallel travelling waves (see kymograph in Figure 2B), the re-established waves consisted of small, randomly oriented wavelets (Video S1). This state resembled that seen at the *de novo* onset of *in vitro* Min self-organization.^[18] The orientation and movements appeared chaotic, yet single points on the observed membrane quickly returned to regular oscillations, as observed by MinD fluorescence (Figure 2C). Over time, adjacent membrane areas again aligned their emanating oscillations to planar wave fronts (Figure 2B).

Since non-specific photoeffects have been previously reported for the Min system,^[19] we subjected a control assay without the peptide photoswitch to the same illumination scheme as our highest intensity experiments (see Video 3 for a side-by-side comparison). Apart from a slight thinning of the wave bodies, no effects were observed.

Light-activated versions of the Belousov–Zhabotinsky reaction demonstrate frequency-locked resonant patterns, that is, entrainment upon periodic global switching, thereby uncovering new patterns and system behaviors.^[7] Even though the BZ reaction is purely chemical and does not occur in nature, we hypothesized that similar phenomena would be observed when forcing an *in vitro* Min reaction. To periodically apply defined pulses of UV or blue light in a predetermined and reproducible manner, we developed a custom Python program to control illumination via the LED unit (code available, see Experimental Section). Indeed, spatial and temporal entrainment could be induced by

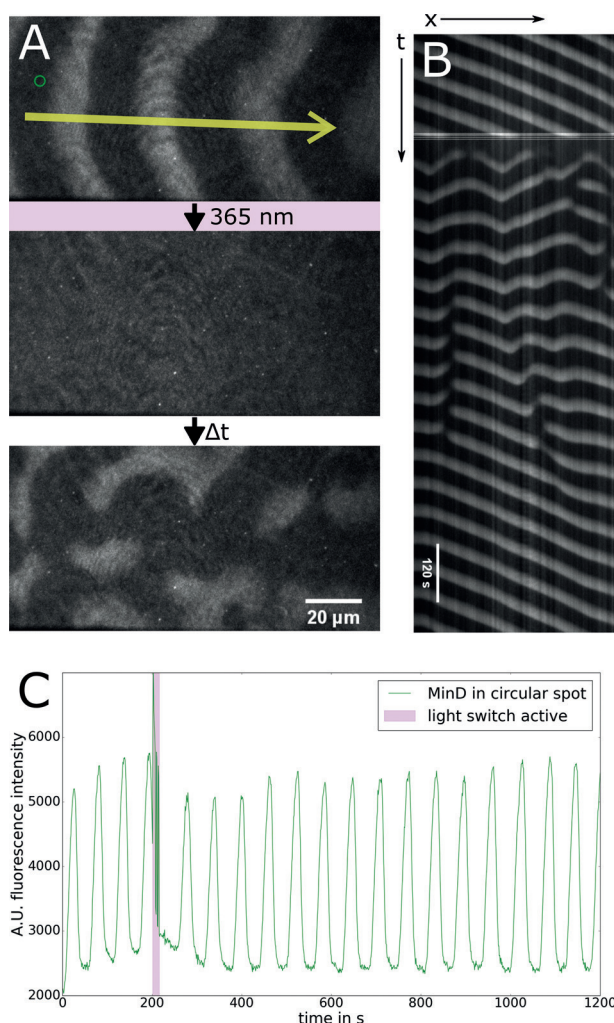


Figure 2. A) Min protein pattern formation can be externally controlled with a UV-switchable MinE peptide. In vitro Min assays were supplemented with peptide 1 (0.5 μM MinD (50% mRuby3^[16]-MinD), 1 μM MinE, 2.25 μM peptide 1), and the effects on Min patterns upon UV illumination were visualized by TIRF microscopy. Representative fluorescence images, from top to bottom: before photoactivation, immediately thereafter (1 s), and 120 seconds later. B) Kymograph along a line selection [marked yellow in (A)]. C) Fluorescence intensity in a small circular region [diameter 3.56 μm, marked with green circle in (A)] plotted over time shows quick return of Min dynamics to regular oscillations after switching.

periodically activating our photoswitch peptide (Figure 3). Each switching cycle consisted of a short “on” pulse (UV light) and an “off” pulse (blue light) evenly spaced over the respective entraining period. Detailed descriptions of the entrainment schemes used can be found in the Supporting Information. The entrainment frequency f_p was chosen to be approximately twice the frequency of the running waves f_0 . Shortly after initiating the periodic optical activation, the reaction reorganized into a new spatiotemporal pattern that differed in wavelength from the original travelling waves (Video S5) and displayed two alternating states of MinD coverage. The first state generated was virtually the negative image (in terms of MinD fluorescence) of the second state. MinD membrane coverage alternated at each $f_0/2$. Intriguingly,

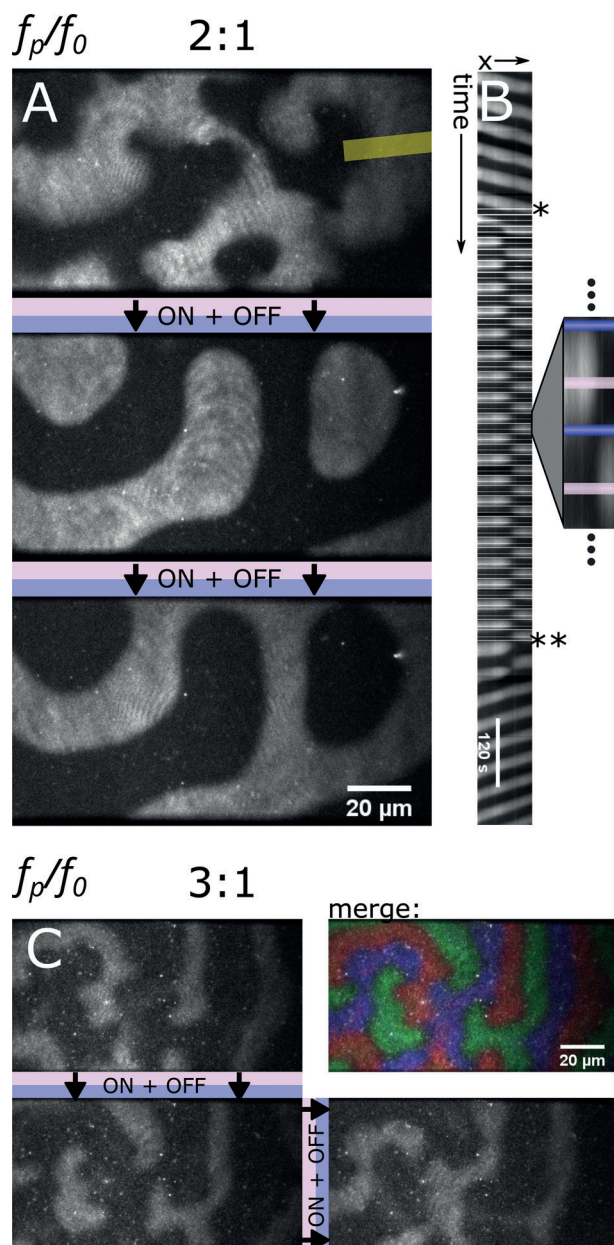


Figure 3. Resonance, and thus entrainment, is elicited from running in vitro Min assays by periodically activating a photoswitch peptide (1 μM MinD (30% mRuby3-MinD), 3 μM MinE, 2.6 μM peptide photo-switch). A) 2:1 (entraining frequency to natural frequency) entrainment displays two alternating patterns, shown in panels 2 and 3. B) Kymograph of a line selection [marked yellow in (A)] shows the standing-wave-like phenotype during resonance (*/*: beginning/end of periodic optical forcing). C) 3:1 entrainment (0.6 μM MinD (30% mRuby3-MinD), 1 μM MinE, 2.25 μM peptide 1) displays three alternating patterns.

ingly, after the optical entrainment was halted, the alternating states persisted for a few cycles before transitioning back to a travelling wave pattern, thus demonstrating that the induced pattern critically depends on external driving. The resonant response can be maintained for more than 20 cycles, with little change in the spatiotemporal pattern after the first few iterations (Figure 3B and Video S5). This in turn means that

the system is able to maintain a memory of the same resonant pattern for more than 13 minutes while it is in the $f_p/f_0 = 2$ regime. The type of pattern that was generated by the optical driving shows similarities to the previously reported standing waves,^[20] but studies in BZ reactions have identified similar patterns as oscillatory clusters, since they lack a characteristic wavelength.^[21] Indeed, the initial transition from running waves to the resonance pattern involved compaction of MinD covered areas, meaning that those membrane areas develop smooth, rounded edges and deviate from the original wavelength to achieve that. While investigating a light controlled BZ formulation, Petrov and colleagues not only created resonant patterns like the above at $f_p/f_0 = 2$, but also showed several other resonance regimes at f_p/f_0 of 3, 3/2 and 1.^[7] In our system, we also found resonance at 3/1, which consists of three interconverting and mutually exclusive MinD surface distributions (Figure 3C and Video S6). However, assays forced into a 3/1 resonance displayed a tendency to lock into the $f_p/f_0 = 2$ regime after a number of cycles or became asynchronous and showed changing patterns over time. The $f_p/f_0 = 1$ resonance, which we would expect to be an oscillation of the entire field of view at once, from MinD covered to unbound, could not be achieved. This may well be due to the fact that the Min reaction takes place on a membrane surface, as opposed to the in-solution BZ reaction. Taken together, periodic optical entrainment of an in vitro Min assay uncovered new spatiotemporal patterns and phenomena.

Our group and others have previously demonstrated that persistent binding of MinE to either the membrane or membrane-bound MinD is required to form regular and functional spatiotemporal patterns.^[20,22] Our photoswitch now enabled us to uncouple MinE membrane interaction from rapid rebinding of MinE to neighboring MinD dimers by evaluating the hysteresis observed during entrainment. Specifically, we tested whether, during induced 2/1 resonance, MinE would stay membrane-bound after MinD is detached by the activated peptide. Indeed, when MinD was detached with our photoswitch, MinE did not immediately follow, but instead continued to reside on membrane areas previously shared with MinD (Figure 4 and Video S7). During this time, MinD continued to attach to areas outside of this MinE carpet. Once a high density of MinD was reached in those areas, MinE bound to the newly created MinD patches. Intriguingly, MinE stayed bound for several seconds after the majority of MinD had left a membrane patch (Figure 4B). Similar MinE dynamics, although less pronounced in their delay, have been reported for “burst” patterns.^[20] Future experiments could address whether this persistence is solely based on MinE membrane attachment via its very short membrane targeting sequence,^[15] or to what degree dimerization or multimerization of the protein help to stabilize it on the membrane. Additionally, the amount of bound MinE did not gradually accumulate over the course of a wave, as reported for travelling waves.^[22] Rather, it accumulated very quickly towards its maximum density on a pre-formed MinD cluster (Figure 4B). In summary, our direct observation of MinE persistence on the membrane complements previous studies on the matter and gives a strong indication for the lag

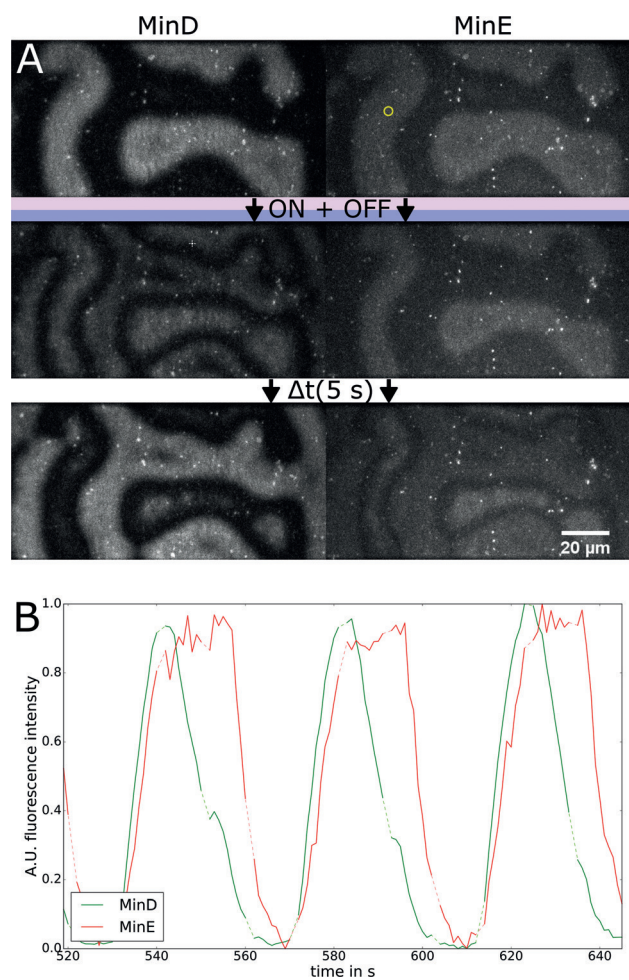


Figure 4. Direct visualization of MinE persistent binding through optical entrainment. An in vitro Min assay is optically driven into the $f_p/f_0 = 2$ resonance regime (1 μM MinD, 2 μM MinE, 2.6 μM peptide 1). Panels of MinD and MinE fluorescence in the same field of view were recorded almost simultaneously (50 ms delay). A clear delay of MinE unbinding is shown upon MinD release by photoactivated peptide 1. B) Time-resolved fluorescence measurements for both proteins in a small circular selection [yellow in (A)] reveal MinE persistent binding during resonance (green MinD; red MinE; dotted lines indicate values excluded due to photoswitch illumination).

time of MinE membrane detachment as the origin of hysteresis during induced resonance.

To conclude, we have demonstrated that a reaction–diffusion-based pattern-forming protein system can be controlled by light, to the point that spatiotemporal entrainment by an external driving frequency becomes feasible. Due to the comparatively simple network architecture, technical accessibility, facile manipulation of proteins through mutagenesis, and ease of modifying conditions in our in vitro system, we anticipate exciting future applications for both research in nonlinear dynamics and ultimately the study and manipulation of cellular morphogenesis based on reaction–diffusion. Although its transfer to the living cell may still face several technical challenges, our assay conferring optical control appears to be a valuable tool in bottom-up synthetic biology. While the current photoswitch design is sufficient to control

pattern formation, there is a lot of potential for optimization of both the peptide primary structure and the crosslinker solubility. Optimization of the peptides to achieve cell permeability, or genetically encoding them, might accomplish the control of Min dynamics in living cells such as *Escherichia coli*.^[23] Future technical improvement of the optical setup will, for example, allow inscription of custom spatial patterns into the system by utilizing spatial light modulators. In this way, the assay could be used for storing predefined spatial information over many minutes in a biologically accessible system, or to create pre-defined benchmark settings for testing and improving mathematical models.

Experimental Section

Imaging: Images were acquired on a custom TIRF setup based on an inverted Zeiss AxioObserver.D1 microscope body. A Zeiss alpha Plan-Apochromat 63x/1.46 Oil Corr M27 objective was used in all cases. The sample was excited with 561 nm and 640 nm lasers, depending on the fluorophores present. Data were collected on an Andor iXon 897 Ultra camera using the Andor Solis software.

Photoswitching: A pE-2 LED unit (purchased from CoolLED) with 365 nm and 470 nm LEDs installed was connected to the microscope's back port using the manufacturer's adapter. The unit was controlled with a custom software implemented in Python 3 (code and documentation available via GitHub: https://github.com/philglock/CoolLED_control) via USB (virtual com port).

See the Supporting Information for all additional materials and methods.

Acknowledgements

P.G. is supported by GRK 2062—Molecular Principles of Synthetic Biology and would like to thank Peter Schultz, Beatrice Ramm, Leon Harrington, Stefan Pettera, and Henri Franquelim. J.M., P.B. and P.G. acknowledge support from the International Max Planck Research School for Molecular Life Sciences. J.B. would like to acknowledge SFB TRR 152 and David H. Woodmansee for providing precursors. D.T. acknowledges support from SFB TRR 152 and an ERC Advanced Grant. P.S. would like to acknowledge MaxSynBio.

Conflict of interest

The authors declare no conflict of interest.

Keywords: chemical oscillators · optical control · photoswitches · pattern formation · synthetic biology

How to cite: *Angew. Chem. Int. Ed.* **2018**, *57*, 2362–2366
Angew. Chem. **2018**, *130*, 2386–2390

- [1] P. A. de Boer, R. E. Crossley, L. I. Rothfield, *Cell* **1989**, *56*, 641–649.
- [2] P. Müller, K. W. Rogers, B. M. Jordan, J. S. Lee, D. Robson, S. Ramanathan, A. F. Schier, *Science* **2012**, *336*, 721–724.
- [3] A. M. Turing, *Philos. Trans. R. Soc. London Ser. B* **1952**, *237*, 37–72.
- [4] A. T. Winfree, *Science* **1972**, *175*, 634–636.
- [5] G. Ertl, *Science* **1991**, *254*, 1750–1755.
- [6] O. Steinbock, V. Zykov, S. C. Muller, *Nature* **1993**, *366*, 322–324.
- [7] V. Petrov, Q. Ouyang, H. L. Swinney, *Nature* **1997**, *388*, 655–657.
- [8] M. Kim, M. Bertram, M. Pollmann, A. Von Oertzen, A. S. Mikhailov, H. H. Rotermund, G. Ertl, *Science* **2001**, *292*, 1357–1360.
- [9] N. Tompkins, N. Li, C. Girabawe, M. Heymann, G. B. Ermentrout, I. R. Epstein, S. Fraden, *Proc. Natl. Acad. Sci. USA* **2014**, *111*, 4397–4402.
- [10] Z. Hu, J. Lutkenhaus, *Mol. Cell* **2001**, *7*, 1337–1343.
- [11] A review on control of cell division by the Min system: Y. Shih, M. Zheng, *Environ. Microbiol.* **2013**, *15*, 3229–3239.
- [12] S. Kretschmer, K. Zieske, P. Schwillie, *PLoS One* **2017**, 1–16.
- [13] J. R. Kumita, O. S. Smart, G. A. Woolley, *Proc. Natl. Acad. Sci. USA* **2000**, *97*, 3803–3808.
- [14] S. Samanta, C. Qin, A. J. Lough, G. A. Woolley, *Angew. Chem. Int. Ed.* **2012**, *51*, 6452–6455; *Angew. Chem.* **2012**, *124*, 6558–6561.
- [15] K. T. Park, W. Wu, K. P. Battaile, S. Lovell, T. Holyoak, J. Lutkenhaus, *Cell* **2011**, *146*, 396–407.
- [16] B. T. Bajar, E. S. Wang, A. J. Lam, B. B. Kim, C. L. Jacobs, E. S. Howe, M. W. Davidson, M. Z. Lin, J. Chu, *Sci. Rep.* **2016**, *6*, 20889.
- [17] H. Ghasriani, T. Ducat, C. T. Hart, F. Hafizi, N. Chang, A. Al-Baldawi, S. H. Ayed, P. Lundström, J.-A. R. Dillon, N. K. Goto, *Proc. Natl. Acad. Sci. USA* **2010**, *107*, 18416–18421.
- [18] M. Loose, E. Fischer-Friedrich, J. Ries, K. Kruse, P. Schwillie, *Science* **2008**, *320*, 789–792.
- [19] V. Ivanov, K. Mizuuchi, *Proc. Natl. Acad. Sci. USA* **2010**, *107*, 8071–8078.
- [20] A. G. Vecchiarelli, M. Li, M. Mizuuchi, L. C. Hwang, Y. Seol, K. C. Neuman, K. Mizuuchi, *Proc. Natl. Acad. Sci. USA* **2016**, 201600644.
- [21] V. Vanag, L. Yang, M. Dolnik, A. Zhabotinsky, I. Epstein, *Nature* **2000**, *406*, 389–391.
- [22] M. Loose, E. Fischer-Friedrich, C. Herold, K. Kruse, P. Schwillie, *Nat. Struct. Mol. Biol.* **2011**, *18*, 577–583.
- [23] C. Hoppmann, V. K. Lacey, G. V. Louie, J. Wei, J. P. Noel, L. Wang, *Angew. Chem. Int. Ed.* **2014**, *53*, 3932–3936; *Angew. Chem.* **2014**, *126*, 4013–4017.

Manuscript received: November 22, 2017

Revised manuscript received: December 19, 2017

Accepted manuscript online: December 21, 2017

Version of record online: January 26, 2018

Supporting Information

Optical Control of a Biological Reaction–Diffusion System

*Philipp Glock, Johannes Broichhagen, Simon Kretschmer, Philipp Blumhardt, Jonas Mücksch, Dirk Trauner, and Petra Schwille**

anie_201712002_sm_miscellaneous_information.pdf

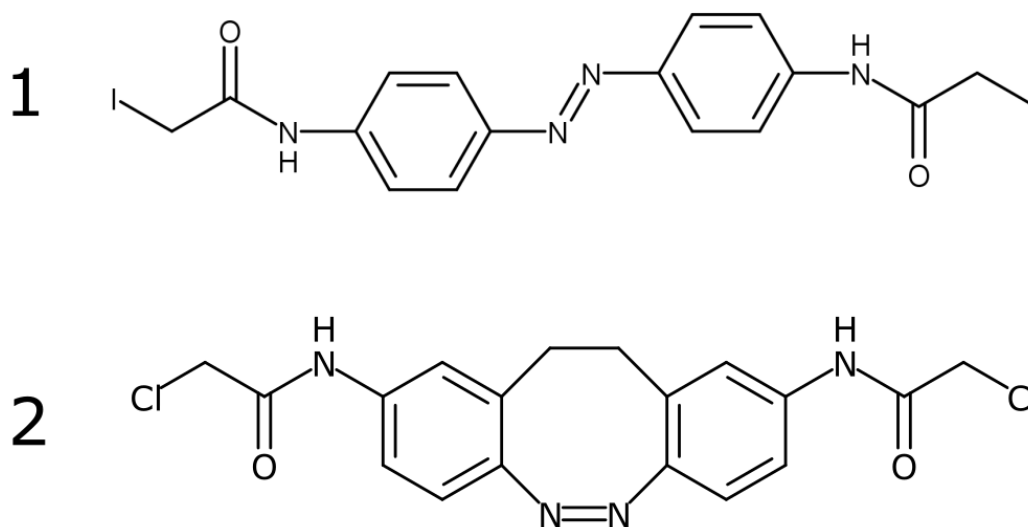


Figure S1: Structures of the two azobenzene-incorporating crosslinkers
 (1) Iodoacetamide crosslinker used for peptides 1 and 3 (2) cis-stable chloroacetamide crosslinker used for peptides 4 to 6

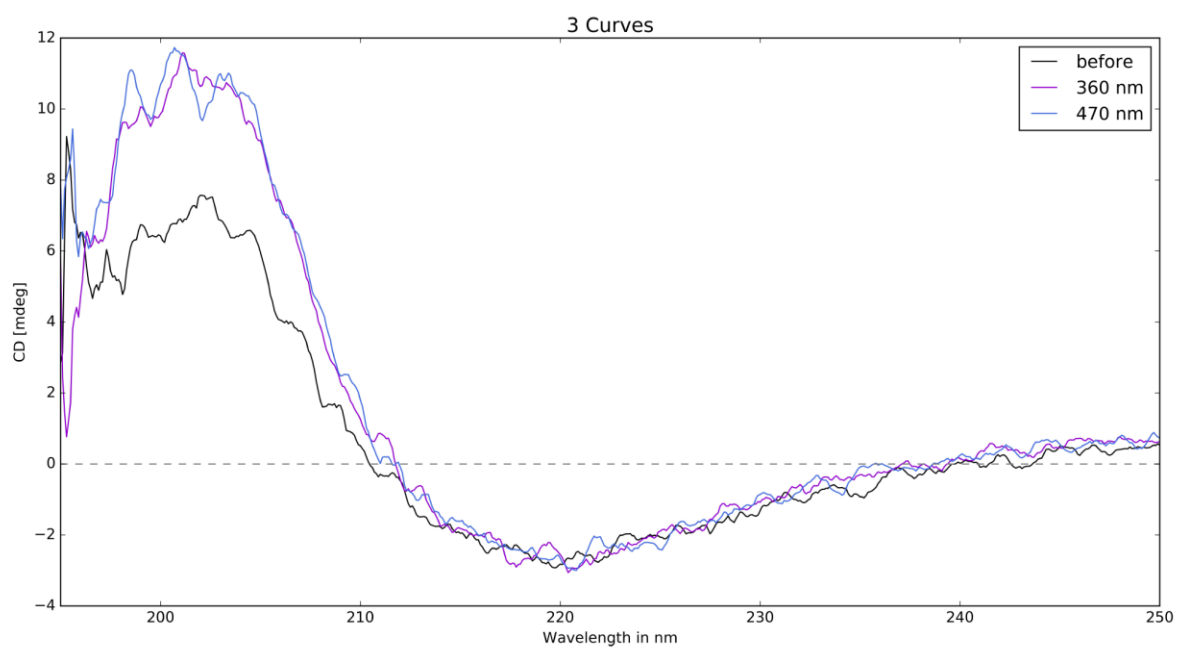


Figure S2: CD spectra of peptide 1 (crosslinked) show no change in helicity upon UV light illumination

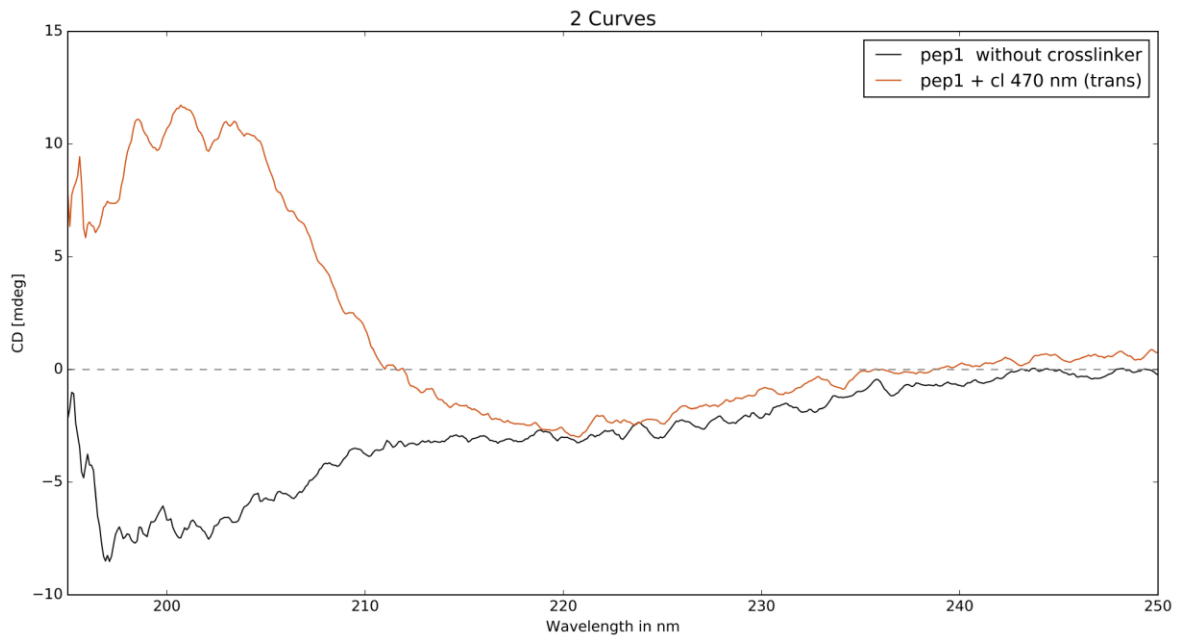


Figure S3: CD spectra of peptide 1 with and without crosslinker show structural changes

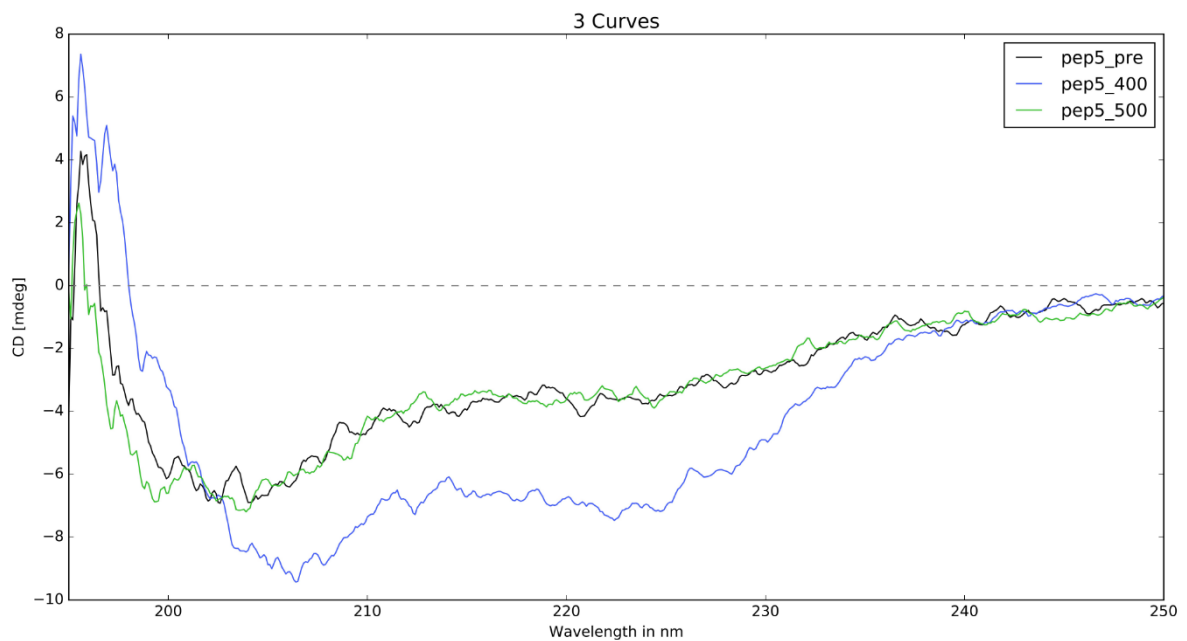


Figure S4: CD spectra of peptide 5 (crosslinked) before and after blue light illumination show change in helicity

Supplementary Discussion

Circular dichroism of peptides:

To verify our strategy also in terms of peptide structure, we performed circular dichroism (CD) on our crosslinked peptides. Peptide 5 clearly showed the expected increase in alpha-helicity upon illumination with 400 nm light, as evidenced by increased negative bands at 208 nm and 222 nm. This change was reversible by illuminating with 500 nm. Interestingly, peptide 1 did not show any major changes of its structure upon illumination with 365 nm light. No alpha-helicity can be seen in

the spectrum in either state. With the exact same spacing and crosslinker, Kumita and colleagues showed photocontrol of helicity in a model peptide ^[1]. We therefore speculate that the primary structure of our peptide shows too little preference for folding into an alpha helix on its own. And indeed, the part of MinE that we chose is a beta-sheet and not alpha-helical when properly folded into the MinE protein ^[2]. Also, the peptide alone without crosslinker shows little alpha-helicity in solution (Figure S3). Upon release of the sequence from MinE, which happens when MinD is sensed, it likely folds while inserting itself into the interaction pocket and becomes alpha-helical ^[3]. Our peptide 1 for the (*i*/*i*+7) spacing probably forms the active alpha-helix only when bound to MinD. The crosslinked azobenzene still restricts the peptide conformation in this MinD-interacting state, but it does not impact the primary structure in solution. The different behavior of peptide 5 can be of two-fold origin. One option is that the difference in residues that were substituted for cysteines in this peptide already favor a higher degree of alpha-helicity. The other option is that, since the crosslinker spans four more residues, the alpha-helical conformation becomes thermodynamically more favorable also in solution. Finally, the strategy we used here does not switch 100 percent of the azobenzenes present, so any changes in measured CD will be contributed only by the population of molecules that changed conformation.

Since both peptides (1 and 5) show similar activity in our *in vitro* self-organization assays we do not see these counterintuitive CD spectra as a major flaw.

Illumination intensity, field and peptide diffusion estimations:

We estimate the switching region to be equivalent with the exit pupil of the objective (diameter 397 μm). The applied powers were measured to be 790 μW (365 nm) and 444 μW (470 nm). To judge whether the recovery originates from spontaneous back-isomerization or diffusion of MinE peptide, we estimate a characteristic diffusion time of the MinE switch by a simple scaling approach ($\Delta t \sim \Delta x^2/D$). The diffusion coefficient of MinE (2.4 kDa) was estimated to be $D=195 \mu\text{m}^2/\text{s}$, based on the diffusion coefficient of GFP (24 kDa, $D=95 \mu\text{m}^2/\text{s}$ ^[4]). Consequently, the characteristic time of MinE peptide to diffuse from the edge of the switching regime to the center of the field of view or vice versa is around 200 s and thereby much longer than the reversion to running waves takes. The fast recurrence of waves is therefore almost exclusively due to thermal reversion of the peptide and light-induced back-isomerization.

Supplementary Videos

Supplementary video 1: Min protein pattern formation can be externally controlled with a UV-switchable MinE peptide.

MinDE protein pattern formation can be reset by using our photoactivatable peptide. MinD (0.5 μM , spiked with 50% mRuby3-MinD) and MinE (1 μM) self-organize on a supported lipid bilayer (DOPC:DOPG 2:1) in presence of 2.25 μM of photoswitchable peptide 1. For 200 seconds, undisturbed pattern formation is shown, then several short pulses of 365 nm light are given (6s on, 2s off, 2s on, 2s off, 2s on).

Supplementary video 2: MinDE protein pattern formation can be continuously inhibited by regularly activating the photoswitch.

MinD (0.8 μM , spiked with 50% mRuby3-MinD) and MinE (1 μM) self-organize on a supported lipid bilayer (DOPC:DOPG 2:1) in presence of 2.25 μM of photoswitchable peptide 1. For 300 seconds,

undisturbed pattern formation is shown. Then, a short pulse of 365 nm light is given every 20 seconds to keep the photoswitch active and thereby continuously deplete MinD from the membrane. From 680 seconds on, the assay is undisturbed and new patterns start to arise.

Supplementary video 3: Unspecific photo-effects do not lead to resonance phenomena in MinDE self-organization assays.

Two MinDE self-organization assays are treated identically, with one of them containing 2.25 μM of photoswitch peptide 1 (lower half). MinD (1 μM , spiked with 30% mRuby3-MinD) and MinE (2 μM) self-organize on an mSLB surface. After 300 seconds, an identical illumination scheme was started on both assays, consisting of a short 365 nm pulse, followed by a wait time that makes up a total time of 10 seconds before a short blue light pulse, again amounting to a total time of 10 seconds with waiting period. This switching regime is kept up until 640 seconds from the start of the assay. From that time point onwards, the self-organization is left undisturbed.

Supplementary video 4: Peptide 4 can be locally photoactivated by using a scanning laser. MinDE self-organization (0.6 μM MinD (30% mRuby3-MinD), 1 μM MinE, contains 1.5 μM photoswitch peptide 4) is observed on a confocal laser scanning microscope. A circular region is activated multiple times by scanning it with a 405 nm laser and the resulting changes in the pattern are observed. No times given due to delays associated with activating regions of interest.

Supplementary video 5: Resonance, and thus entrainment, is elicited from running in vitro Min assays by periodically activating a photoswitch peptide. MinDE self-organization (1 μM MinD (30% mRuby3-MinD), 3 μM MinE, contains 2.6 μM photoswitch peptide 1) is observed using TIRF microscopy. After 300 seconds of undisturbed (except for the imaging light) wave propagation, an illumination scheme is started. 2 seconds of 365 nm illumination (at 10% LED power) are followed by 8 seconds of no activation, followed by 2 seconds of 470 nm activation, again followed by 8 seconds without activation. This scheme is carried out for a total of 41 repetitions.

Supplementary video 6: Resonance, and thus entrainment, is elicited from running in vitro Min assays by periodically activating a photoswitch peptide. MinDE self-organization (0.6 μM MinD (30% mRuby3-MinD), 1 μM MinE, contains 2.25 μM photoswitch peptide 1) is observed using TIRF microscopy. After 300 seconds of undisturbed (except for the imaging light) wave propagation, an illumination scheme is started. The sample is illuminated with 1.5 seconds of 365 nm, followed by 4.5 seconds of no activation, then 2 seconds of 470 nm followed by 4 seconds without activation. The illumination scheme is carried out for 28 cycles.

Supplementary video 7: Direct visualization of MinE persistent binding through optical entrainment. MinDE self-organization (1 μM MinD (30% mRuby3-MinD), 2 μM MinE (30% Alexa647-MinE), contains 2.6 μM photoswitch peptide 1) is observed using TIRF microscopy. After 300 seconds of undisturbed (except for the imaging light) wave propagation, an illumination scheme is started. 2 seconds of 365 nm illumination are followed by 8 seconds of no activation, followed by 2 seconds of 470 nm activation, again followed by 8 seconds without activation. This scheme is carried out for a total of 17 repetitions.

Experimental Section

Protein preparation and labeling: His-MinD and His-MinE were purified as previously described ^[5]. mRuby3-MinD ^[6] was cloned from a sequence optimized, custom ordered mRuby3 DNA fragment that was inserted in place of EGFP on pET28a-EGFP-MinD ^[7]. While the brightness of mRuby3 clearly surpasses mCherry, we would not recommend using mRuby3 for in vivo experiments or purification of unstable proteins, since the maturation of the fluorophore takes multiple days at 4° C. For more efficient cysteine-labelling, three amino acids (KCK) were inserted at the N-terminus of His-MinE, directly following the His-tag, via site-directed mutagenesis. Purification of both constructs was done as described previously ^[5]. KCK-MinE was labeled with Alexa Fluor 647 C₅ maleimide (purchased from Thermo Fisher Scientific) according to the manufacturer's instructions and labelling efficiency was measured spectrometrically to be 60%.

Peptide preparation: Peptides were synthesized by our in-house Biochemistry Core Facility using Fmoc-chemistry and purified by RP-HPLC. Peptide-crosslinker reactions were performed as described by Samanta et al. ^[8]. Reacted peptides were again purified via RP-HPLC and their identity was verified via LC-MS.

Azobenzene crosslinker synthesis: (*E*)-*N,N'*-(Diazene-1,2-diylbis(4,1-phenylene))bis(2-iodoacetamide) was synthesized as previously described ^[1]. (*Z*)-*N,N'*-(11,12-Dihydrodibenzo[*c,g*][1,2]diazocine-2,9-diyl)bis(2-chloroacetamide) was synthesized as previously described ^[8].

Supported Lipid bilayers: Supported lipid bilayers were formed by fusion of small unilamellar vesicles on glass coverslips (Menzel 24x24, #1.5). Coverslips were first cleaned using piranha solution (3:1 sulfuric acid 98% and 50% H₂O₂). "mSLB" Lipids (67% DOPC, 33% DOPG, purchased from Avanti) ^[9] dissolved in chloroform were dried under an N₂ stream and subsequently placed under vacuum for at least one hour. The dried lipid film was hydrated in reaction buffer (150 mM KCl, 25 mM Tris-HCl pH 7.5, 5 mM MgCl₂) at a concentration of 4 mg/ml. The solution was subjected to freeze-thaw cycles until clear and extruded 35 times through a membrane with 50 nm pore size (Avanti mini extruder). Lipid aliquots were used either directly or stored at -20 °C and sonicated before use. To form SLBs, lipids were further diluted to 0.5 mg/ml and added on top of the clean glass support. Lipid vesicle fusion was carried out for 3 minutes, with a further dilution step of 1:3 after 1 minute. Membranes were washed with 2 ml reaction buffer to remove residual vesicles.

In vitro Min assays: Min proteins were added into a final volume of 200 µl reaction buffer on top of a supported lipid membrane. All assays contained 2.5 mM of ATP as energy source. Photoswitch peptide, taken from small aliquots of a 400 µM stock solution in water, was added last after confirming normal self-organization behavior microscopically.

Literature

- [1] J. R. Kumita, O. S. Smart, G. A. Woolley, *Proc. Natl. Acad. Sci.* **2000**, *97*, 3803–3808.
- [2] K. T. Park, W. Wu, K. P. Battaile, S. Lovell, T. Holyoak, J. Lutkenhaus, *Cell* **2011**, *146*, 396–407.
- [3] K.-T. Park, M. T. Villar, A. Artigues, J. Lutkenhaus, *Proc. Natl. Acad. Sci.* **2017**, *114*, 201707385.
- [4] Z. Petrášek, P. Schwille, *Biophys. J.* **2008**, *94*, 1437–1448.
- [5] M. Loose, E. Fischer-Friedrich, J. Ries, K. Kruse, P. Schwille, *Science* **2008**, *320*, 789–792.

- [6] B. T. Bajar, E. S. Wang, A. J. Lam, B. B. Kim, C. L. Jacobs, E. S. Howe, M. W. Davidson, M. Z. Lin, J. Chu, *Sci. Rep.* **2016**, *6*, 20889.
- [7] K. Zieske, J. Schweizer, P. Schwille, *FEBS Lett.* **2014**, *588*, 2545–2549.
- [8] S. Samanta, C. Qin, A. J. Lough, G. A. Woolley, *Angew. Chemie - Int. Ed.* **2012**, *51*, 6452–6455.
- [9] A. G. Vecchiarelli, M. Li, M. Mizuuchi, K. Mizuuchi, *Mol. Microbiol.* **2014**, *93*, 453–463.

***In Vitro* Reconstitution of Self-Organizing Protein Patterns on Supported Lipid Bilayers**

This manuscript is a detailed methods paper on the *in vitro* reconstitution of Min protein patterns. It accompanies a video to be found here:

<https://www.jove.com/video/58139/in-vitro-reconstitution-self-organizing-protein-patterns-on-supported>.

Published under CC BY-NC-ND 3.0

Full citation: B. Ramm, P. Glock, and P. Schwille, “In Vitro Reconstitution of Self-Organizing Protein Patterns on Supported Lipid Bilayers,” *Journal of Visualized Experiments*, p. e58139, jul 2018

Source online: <https://dx.doi.org/10.3791/2F58139>

Author Contributions to *In Vitro* Reconstitution of Self-Organizing Protein Patterns on Supported Lipid Bilayers

P.G. and B.R. conducted *in vitro* experiments on SLBs, as well as protein purifications and biochemical assays. P.G. prepared figures 1, 3 and 6, whereas B.R. prepared figures 2, 4 and 5. Both authors wrote the manuscript. All authors discussed the results and revised the manuscript. Therefore, the contribution of P.G. and B.R. is estimated to be shared equally. This manuscript provides mainly methods to the present thesis, and is therefore considered minor in terms of scientific novelty.

Signatures:

Philipp Glock

Beatrice Ramm

Prof. Petra Schwille

Video Article

In Vitro Reconstitution of Self-Organizing Protein Patterns on Supported Lipid Bilayers

Beatrice Ramm^{*1}, Philipp Glock^{*1}, Petra Schwille¹¹Department of Cellular and Molecular Biophysics, Max Planck Institute of Biochemistry^{*}These authors contributed equallyCorrespondence to: Petra Schwille at schwille@biochem.mpg.deURL: <https://www.jove.com/video/58139>DOI: [doi:10.3791/58139](https://doi.org/10.3791/58139)

Keywords: Biochemistry, Issue 137, In vitro reconstitution, MinD, MinE, supported lipid bilayer, pattern formation, microstructures, self-organization

Date Published: 7/28/2018

Citation: Ramm, B., Glock, P., Schwille, P. *In Vitro* Reconstitution of Self-Organizing Protein Patterns on Supported Lipid Bilayers. *J. Vis. Exp.* (137), e58139, doi:10.3791/58139 (2018).

Abstract

Many aspects of the fundamental spatiotemporal organization of cells are governed by reaction-diffusion type systems. *In vitro* reconstitution of such systems allows for detailed studies of their underlying mechanisms which would not be feasible *in vivo*. Here, we provide a protocol for the *in vitro* reconstitution of the MinCDE system of *Escherichia coli*, which positions the cell division septum in the cell middle. The assay is designed to supply only the components necessary for self-organization, namely a membrane, the two proteins MinD and MinE and energy in the form of ATP. We therefore fabricate an open reaction chamber on a coverslip, on which a supported lipid bilayer is formed. The open design of the chamber allows for optimal preparation of the lipid bilayer and controlled manipulation of the bulk content. The two proteins, MinD and MinE, as well as ATP, are then added into the bulk volume above the membrane. Imaging is possible by many optical microscopies, as the design supports confocal, wide-field and TIRF microscopy alike. In a variation of the protocol, the lipid bilayer is formed on a patterned support, on cell-shaped PDMS microstructures, instead of glass. Lowering the bulk solution to the rim of these compartments encloses the reaction in a smaller compartment and provides boundaries that allow mimicking of *in vivo* oscillatory behavior. Taken together, we describe protocols to reconstitute the MinCDE system both with and without spatial confinement, allowing researchers to precisely control all aspects influencing pattern formation, such as concentration ranges and addition of other factors or proteins, and to systematically increase system complexity in a relatively simple experimental setup.

Video Link

The video component of this article can be found at <https://www.jove.com/video/58139/>

Introduction

Spatiotemporal patterns are essential in nature, regulating complex tasks both on the multicellular and cellular level, from morphogenesis to regulated cell division^{1,2}. Reaction-diffusion systems play an important role in establishing these patterns, but are still not well understood. A prime example of a reaction-diffusion system and the best characterized biological system so far is the *Escherichia coli* MinCDE system^{3,4,5,6,7}. The MinCDE system oscillates from cell pole to cell pole in *E. coli* to determine the middle of the cell as the future division site. This system is based on the ATPase MinD, the ATPase activating protein MinE, and the membrane as a spatial reaction matrix⁸. MinC is not part of the pattern formation mechanism, but is the actual functional agent: an inhibitor of the main divisome protein FtsZ^{5,6}. MinC binds to MinD and therefore follows the oscillations, resulting in a time-averaged protein concentration gradient that is maximal at the cell poles and minimal at the cell middle, only allowing FtsZ to polymerize at midcell^{9,10}. The MinCDE system is part of the larger family of Walker A ATPases that are key to the spatiotemporal organization in bacteria², for positioning and transporting protein complexes¹¹ and plasmids¹² and for regulating cell division¹³ and chromosome segregation¹⁴. Hence, the MinCDE reaction-diffusion system not only represents an archetypal reaction-diffusion system, but has also attracted attention because of its relevance for the spatiotemporal organization in bacteria.

Detailed functional studies of the MinCDE system *in vivo* are complicated, as manipulation of proteins and gene deletion typically result in cell division defects. Furthermore, changing the membrane composition or the properties of the cytosol *in vivo* is very challenging^{15,16}. Changes to the system and influencing factors are hard to interpret in the complex environment of the cell, even more so if it is disturbed in such an essential function as cell division. We and others have therefore turned to an *in vitro* reconstitution approach, reducing the system to its core components: MinD, MinE, ATP as an energy source, and the supported lipid bilayer as a reaction matrix^{6,17,18}. This bottom-up approach allows to probe the mechanism of self-organization in detail without the complexity of a living cell. The proteins form traveling surface waves⁶ and other kinds of patterns^{17,19} under these conditions, albeit with a wavelength that is usually about a magnitude larger than *in vivo*. The use of an open chamber facilitates precise control over all aspects influencing pattern formation: protein concentrations⁶, protein properties²⁰, membrane composition¹⁰, buffer composition, and ATP concentration⁹, as well as addition of other factors such as crowding agents²¹ and other divisome proteins²². In comparison, the *in vitro* reconstitution of the MinCDE system in a flow-cell^{18,19,23} can be used to probe the influence of flow^{17,23}, protein limiting conditions¹⁹, membrane composition¹⁹ and full 3D confinement¹⁸ on protein patterns, but renders an exact control of protein/component concentration and sequential component addition much more complicated.

Using this open chamber, we also patterned the support of the planar lipid bilayers by which one can probe how geometrical boundaries influence pattern formation²¹, a phenomenon that has recently also been investigated *in vivo* using bacteria molded into microstructures⁷. We also employed this assay to investigate how defined mutations in MinE affect pattern formation of the system²⁰. Furthermore, the same basic assay format has been employed to investigate how pattern formation can be controlled by light, introducing an azobenzene-crosslinked MinE peptide into the assay, and imaging with TIRF microscopy²⁴.

We found that, in order to replicate the MinDE pattern formation observed *in vivo* in an *in vitro* system, confinement was key. Using rod-shaped microcompartments, with dimensions adjusted to the larger wavelength of MinDE *in vitro* (10 x 30 μm), clad with a supported lipid bilayer allowed the reconstitution of MinDE pole-to-pole oscillations and protein gradient formation^{10,25}. In this assay, the supported lipid bilayers are deposited on a patterned PDMS substrate that contains several hundred replicas of rod-shaped microcompartments that remain open on the top. By this, the reaction can be set up in an open chamber, and subsequently the buffer is lowered to the rim of the microcompartments, thereby confining the reaction to a small volume. Even though these compartments have an air-buffer interface on one side and hence do not represent a full 3D confinement by membrane, the protein dynamics mimicked *in vivo* oscillations^{10,25}. Compared to full 3D confinement, which shows very similar results¹⁸, the open microstructures assay is relatively simple and easy to handle and can also be performed by laboratories that are not equipped with specialized microfluidics equipment and clean-room facilities.

Here, we present an experimental protocol for reconstituting MinCDE pattern formation on supported lipid bilayers *in vitro* using an open chamber that allows for control of all components and easy access by optical microscopy and, with minor modifications, is also adaptable for surface-probe techniques²⁶. Next to planar supported lipid bilayers, we also show how protein confinement can be obtained using simple patterned supported lipid bilayers on rod-shaped PDMS microstructures. These assays, although optimized for the MinCDE system, can also be transferred to other protein systems that interact in a similar way with the membrane, such as FtsZ²⁷ or a minimal actin cortex²⁸.

Protocol

1. Protein Production

1. Protein expression

1. Transform *E. coli* BL21 (DE3) pLysS with the respective plasmid for expression of MinD⁶, EGFP-MinD²⁹, mRuby3-MinD²⁴, MinE⁶ or MinC³⁰. For plasmid maps, please see supplementary information.
2. Inoculate an overnight culture in LB medium with a single colony using the respective antibiotics (e.g., 100 $\mu\text{g}/\text{mL}$ Ampicillin or 50 $\mu\text{g}/\text{mL}$ Kanamycin) and incubate at 37 °C for 14-16 h while shaking.
3. Inoculate 500 mL of TB medium containing the respective antibiotic with the overnight culture (1:200 dilution) and incubate culture at 37 °C while shaking at 180 rpm.
4. Induce protein expression by adding 0.5 mM IPTG when the culture reaches an optical density at 600 nm of 0.5-0.7. In case of EGFP-MinD or mRuby3-MinD, shift cells to an incubator with 16 °C and grow cells for 14-16 h, and in case of MinC, MinD or MinE, grow cells for 3-4 h at 37 °C after induction.
Note: Induction of MinC, MinD or MinE expression is toxic for the cells, as overexpression results in cell division defects; hence, it is important that incubation time at 37 °C is kept below 4 h. If more protein is needed, increase the amount of culture, but not incubation time.
5. After respective incubation time harvest cells by centrifugation at 4000 x g for 10 min and store the cell pellet at -80 °C until further use.

2. Protein purification

Note: Proteins can be purified either using prepacked Ni-NTA columns on an automated protein purification system or using Ni-NTA beads for gravity-flow bench purification.

1. For purification with prepacked Ni-NTA columns on automated protein purification systems use buffer A1 (50 mM sodium phosphate pH 8.0, 500 mM NaCl, 10 mM imidazole), buffer B1 (50 mM sodium phosphate pH 8.0, 500 mM NaCl, 20 mM imidazole), and buffer C1 (50 mM sodium phosphate pH 8.0, 500 mM NaCl, 250 mM imidazole). For gravity-flow bench purification using Ni-NTA beads use buffer A2 (50 mM Tris-HCl pH 8.0, 300 mM NaCl, 10 mM imidazole), buffer B2 (50 mM Tris-HCl pH 8.0, 300 mM NaCl, 20 mM imidazole), and buffer C2 (50 mM Tris-HCl pH 8.0, 300 mM NaCl, 250 mM imidazole). Supplement all buffers with 10 mM β -mercaptoethanol or 0.4 mM TCEP (tris(2-carboxyethyl)phosphine) as reducing agent right before use.
2. Resuspend cells in 20-30 mL of buffer A1 or A2 supplemented with EDTA-free protease inhibitor, 100 $\mu\text{g}/\text{mL}$ lysozyme, ~250 U/mL DNase and 0.2 mM Mg^{2+} -ADP (Mg^{2+} -ADP in case of MinD or EGFP-MinD purification only, from a 100 mM ADP stock in 100 mM MgCl_2 with pH adjusted to 7.5).
3. Lyse cells using a tip sonicator (30% amplitude, 2.5 min, 30 s pulse, 30 s off) while keeping the vial containing the cells in an ice bath.
4. Remove cell debris by centrifuging the cell lysate for 45 min at 25,000 x g and 4 °C.
5. Incubate the supernatant on Ni-NTA column or Ni-NTA beads.
 1. For prepacked Ni-NTA columns, load the sample onto the column using the sample pump of an automated protein purification system.
 2. For bench-top purification, incubate the sample with Ni-NTA beads in a 50 mL reaction tube on a rotating shaker at 4 °C for 1 h. For the subsequent steps, transfer the Ni-NTA beads into an empty column using a 25 mL pipette.
6. Wash with at least 5 column volumes of buffer A1 or A2.
7. Wash with at least 5 column volumes of buffer B1 or B2.
8. Elute protein with buffer C1 or C2.
9. Assess protein purity via SDS-PAGE.
10. Optional: Further purify protein by applying it to a gel filtration column equilibrated in storage buffer (50 mM HEPES/KOH pH 7.2, 150 mM KCl, 10% glycerol, 0.1 mM EDTA, 0.4 mM TCEP, (0.2 mM Mg^{2+} -ADP in case of MinD)).
Note: Gel filtration is recommended for MinD to remove aggregated protein fraction.

11. If no gel-filtration is employed, exchange Ni-NTA elution buffer to storage buffer (50 mM HEPES/KOH pH 7.2, 150 mM KCl, 10% glycerol, 0.1 mM EDTA, 0.4 mM TCEP, (0.2 mM Mg-ADP in case of MinD)) using a gravity flow desalting column (see **Table of Materials**).
 12. Shock-freeze proteins in aliquots in liquid nitrogen and store at -80 °C until further use.
 13. Measure protein stock concentration using Bradford Assay, and determine protein activity with an ATPase assay²⁰.
Note: Do not assess protein concentration using absorption at 280 nm. The presence of nucleotide during MinD purification and the lack of tryptophans in MinE distort A₂₈₀ concentration measurements. Use Bradford or BCA assays to measure protein concentrations instead.
3. Protein labeling
- Note: The fusion of a fluorescent protein to the small protein MinE induces major changes to its diffusive properties and function; hence, chemical labeling of the protein (cysteine at position 51) is preferred over fusion to fluorescent proteins.
1. Dissolve 0.125 mg of maleimide-dye conjugate in 5-10 µL of DMSO (dimethyl sulfoxide) and add under shaking to a 0.5 mL MinE aliquot in storage buffer at pH 7.2, prepared as detailed above.
 2. Incubate for 2 h to overnight at 4 °C or 2 h at RT under gentle shaking or stirring.
 3. Separate dye and protein using a gravity flow desalting column equilibrated with storage buffer (50 mM HEPES/KOH pH 7.2, 150 mM KCl, 10% glycerol, 0.1 mM EDTA, 0.4 mM TCEP).
 4. To further remove any unattached dye, dialyze the protein against an excess of storage buffer.
 5. Verify successful labelling by measuring the extinction at the maximum for the respective dye and calculate the estimated labeling efficiency. Please refer to the dye manufacturer's instructions for a detailed protocol on estimating the degree of labeling. Analyze with SDS-PAGE and determine total mass by mass spectrometry for further useful information about sample homogeneity and labeling success.

2. Small Unilamellar Vesicle (SUV) Preparation

1. Generation of multilamellar vesicles
 1. Calculate the amount of lipid(s) in chloroform for your desired mixture and final SUV volume. The concentration should be 4 mg/mL of lipids in Min buffer (25 mM Tris-HCl pH 7.5, 150 mM KCl, 5 mM MgCl₂). For a standard Min assay a mixture of 7:3 DOPC:DOPG (mol percent) is recommended. When using *E. coli* polar lipid extract, use SLB buffer (25 mM Tris-HCl pH 7.5, 150 mM KCl) for all preparation steps.
Note: It is not recommended for first time users to use *E. coli* polar lipid extract as the generation of homogenous SLBs with this mixture is much more challenging.
 2. Using a positive displacement pipette with glass tips, mix the lipids in chloroform in a 1.5 mL glass vial.
 1. Dry the lipids under a slight nitrogen stream while slowly turning the vial. Place the lipids under a stronger nitrogen stream for 10 to 20 minutes. Place the vial containing the dried lipid film in a vacuum desiccator and apply vacuum for at least 1 h.
 3. Rehydrate the lipids in Min buffer by vortexing at room temperature until the mixture is homogeneously opaque.
Note: For generation of small unilamellar vesicles from multilamellar vesicles, lipids can either be extruded as described in 2.2. or sonicated as described in 2.3. In general, extrusion yields a narrower size distribution which can help with formation of supported lipid bilayers.
2. SUV preparation by extrusion
 1. Break lipid aggregates and multilamellar structures and further solubilize lipids by freeze-thawing for 7 to 10 cycles.
 1. Prepare a beaker with water at 70 °C to 99 °C on a hot plate and a container with liquid nitrogen.
 2. Hold the vial in liquid nitrogen with large tweezers until the nitrogen stops boiling. Then transfer the vial to hot water until the solution is completely thawed. Repeat these steps until the lipid mixture appears clear to the eye, depending on the mixture.
 2. Assemble a lipid extruder and pre-rinse the system with Min buffer. Extrude the lipid mixture between 35 and 41 times through a membrane of 50 nm pore size. Make sure to end on an odd number of passes to avoid aggregates that never traversed the membrane.
3. SUV preparation by sonication
 1. To better dissolve lipids in the buffer, put the glass vial containing the solution in a heat block set to 37 °C and vortex every 20 minutes for 1 minute. Incubate in total for about 1 h.
 2. Immerse the bottom of the vial in a sonicator bath (in this work 1.91 L, 80 W) by attaching the vial onto a clamp stand at the required height.
 3. Set the water height in the sonicator bath so that the solution surrounding the vial is thoroughly agitated by the pulses and sonicate the lipid mixture for about 20 minutes. Check for successful sonication by assessing the clarity of lipids.
4. SUVs can be stored at 4 °C for up to a week or frozen at -20 °C in small aliquots (~20 µL) and stored for several weeks. Thaw vials or tubes at room temperature and sonicate again as described under 2.2.3 or 5.3 until the solution is clear before using SUVs for preparation of supported lipid bilayers (SLBs). Please note that the narrow size distribution of SUVs obtained by extrusion is lost after freezing and subsequent thawing and sonication.

3. Cleaning Glass Coverslips

Note: Cleaning and hydrophilization of glass coverslips is an important factor for homogenous and fluid supported lipid bilayers. Glass coverslips can be cleaned using a piranha solution, made from a ratio of 7:2 sulfuric acid to 50% hydrogen peroxide (3.1), or with an oxygen plasma in a plasma cleaner (3.2). Both methods yield similar results.

1. Piranha cleaning of coverslips
 1. Apply piranha solution
 1. Distribute glass coverslips on an inverted glass Petri dish or other inert surface. With a glass pipette, add 7 drops of concentrated sulfuric acid (98%) to the center of each coverslip.
CAUTION: Sulfuric acid is strongly acidic and corrosive. Work in a fume cupboard and with proper protective equipment only.
 2. Add two drops of 50% hydrogen peroxide to the middle of the acid drops.
CAUTION: Hydrogen peroxide is corrosive to the eyes and skin.
 3. Cover the reaction and incubate for at least 45 minutes.
Note: The maximum waiting time here is not critical for the outcome of the experiment and can be extended up to several days.
 2. Wash piranha cleaned coverslips.
 1. Pick up the coverslips individually using tweezers and rinse off acid with ultrapure water. Place the washed coverslips in non-stick holders or similar transportation device.
 2. Rinse each coverslip extensively with ultrapure water and dry the surface with pressurized gas (nitrogen, air only if oil-free). Mark the cleaned side of the coverslip with permanent marker.
2. Plasma cleaning of coverslips
 1. Rinse coverslips with excess ethanol and afterwards with excess ultrapure water. Dry coverslips with pressurized gas. Assemble chamber as described in 4.
 2. After chamber assembly as described in 4 take the coverslips with attached chamber and place in plasma cleaner with oxygen as process gas. Clean coverslips with plasma (in this work 30% power, 0.3 mbar oxygen pressure for 1 min was used). Do the cleaning right before SLB formation as described in 5, as the hydrophilizing effect of plasma cleaning wears off over time.
Note: Timing and power of plasma cleaning should be optimized using fluorescently labeled membranes, as too little or excessive plasma cleaning can both lead to immobile membranes or membranes with holes.

4. Chamber Assembly

1. With sharp scissors, cut off and discard the lid and the conical part of a 0.5 mL reaction tube. Apply UV-glue to the upper rim of the tube and distribute evenly by using a pipette tip.
2. Glue the tube upside down to the previously cleaned coverslip. In case of piranha cleaning make sure to glue it to the cleaned side of the glass. Cure the UV-glue by placing multiple chambers underneath a 360 nm lamp or LED for 5 to 15 minutes.

5. Supported Lipid Bilayer (SLB) Formation

1. Pre-heat heat block to 37 °C and incubate 2 mL reaction tubes with Min or SLB buffer, 1 tube per chamber.
2. Blow nitrogen into the assembled and cured chambers to remove any dust or other particles that may have settled during the UV curing and assembly. Plasma clean as described in 3.2 if you have not cleaned your coverslips with Piranha solution (3.1). Place chambers on heat block.
3. Dilute a 20 μ L aliquot of clear lipids (at 4 mg/mL) with 130 μ L of Min buffer or SLB buffer in case of *E. coli* polar lipid extract, yielding a working concentration of 0.53 mg/mL. In case lipids were frozen, sonicate first by holding the tube into a bath sonicator before adding buffer, then sonicate again with buffer.
4. Add 75 μ L of lipid mixture to each chamber and set a timer to 3 minutes (for DOPC/DOPG mixtures; longer incubation may be necessary for other lipid mixtures). In case of *E. coli* polar lipid extract, pipette CaCl_2 from a 100 mM stock into the chamber to a final concentration of 3 mM. During the incubation time, the vesicles burst on the hydrophilic glass surface and fuse to form a coherent SLB.
5. After 60 seconds, add 150 μ L of Min buffer to each chamber.
6. Washing the chambers: After another 120 seconds (3 minutes total) wash each chamber by adding 200 μ L of Min or SLB buffer, carefully pipetting up and down a few times, removing and adding another 200 μ L.
 1. After each chamber has been washed once, proceed to wash the first chamber thoroughly until the 2 mL of buffer are used up. Washing of SLBs needs some experience to perfect the extent of motions in the chamber and find the correct washing intensity.
Note: Never remove all liquid from the chamber to avoid drying of the SLB.
Note: On top of washing, membrane properties will vary depending on many additional factors: Type of lipids and their relative concentrations in lipid mixtures, preparation method for SUVs, surface treatment and prior cleaning of support.

6. Self-organization Assay

1. Adjust buffer volume in the chamber to 200 μ L Min buffer minus the amount of protein and ATP solution, then add MinD, labeled MinD, MinE, and, if desired, MinC. Gently mix components by pipetting. Example concentrations are 1 μ M MinD (doped with 30% EGFP-MinD), 1 μ M MinE (doped with 10% chemically labeled MinE) and 0.05 μ M MinC, but patterns form over a range of concentrations^{6,10,20,30}.
2. Add 2.5 mM ATP (from 100 mM ATP stock in 100 mM MgCl_2 , pH 7.5) to start the self-organization of MinDE.
Note: The order of the component addition (MinD, MinE and ATP) can be varied and will not influence the final pattern outcome⁴.
3. Observe MinDE self-organization on the fluorescence microscope (see **Table of Materials**). MinDE self-organization can also be observed using TIRF microscopy. For imaging eGFP-MinD, use a 488 nm Argon laser or comparable diode laser (e.g., 490 nm). For imaging mRuby3-MinD, it is best to employ a 561 nm diode laser.
Note: Avoid high levels of excitation for longer times as we and others¹⁷ have observed phototoxicity in the MinDE system, leading to irreversible protein polymerization on the membrane.

7. PDMS microstructures

Note: PDMS (polydimethylsiloxane) is a polymer that can be used for the production of microstructures and microfluidic devices. A patterned silicon wafer serves as a mold for casting the PDMS structures. The PDMS structures then serve as a support for SLB formation and assay setup.

1. Either produce silicon wafer with microcompartments yourself using photolithography (see Zieske and Schwille for a detailed protocol³¹ or Gruenberger *et al.* for a video protocol³²) or order your desired silicon wafer from a foundry. For the pattern of the wafer used herein please see supplementary information.
2. Production of PDMS microstructures from patterned silicon wafers.
 1. Use a plastic cup to weigh 10 g of PDMS base and 1 g of PDMS crosslinker. Either use a mixing device to mix and degas the PDMS mixture or manually mix the PDMS and then degas under vacuum.
 2. Use a pipette tip to drop a small amount of PDMS directly onto the structure on the silicon wafer.
Note: Be careful not to scratch the silicon wafer.
 3. Immediately place a #1 coverslip onto the PDMS drop and take the upper end of a clean pipette tip to gently press the coverslip onto the silicon wafer. The PDMS should be spreading thinly between the coverslip and the silicon wafer.
 4. Place the wafer with the coverslips into an oven and cure the PDMS for 3-4 hours or overnight at 75 °C. Remove the wafer from the oven and let it cool down to room temperature. With a razor blade, carefully remove the coverslip with the attached PDMS from SI wafer.
Note: To prevent the silicon wafer from getting dirty or damaged, always cover the microstructures with PDMS and a coverslip. However, PDMS ages, resulting in cracks in the microstructures, hence do not use PDMS structures that are older than two to three weeks.

8. Self-organization in PDMS Microstructures

1. Use coverslips with PDMS microstructures to attach a chamber as described under 4.
2. Clean and hydrophilize surface in an oxygen plasma cleaner as described under 3.2.2. Do not piranha clean PDMS substrates.
3. Setup a MinDE self-organization assay as described under 6.
4. After setting up the assay, check for regular MinDE pattern formation and properly formed microstructures on the fluorescence microscope.
5. When regular MinDE patterns have formed (10 - 30 min), gently pipette up and down twice to mix components and then remove the buffer step by step by pipetting. Remove the large bulk of buffer using a 100 μ L pipette and then carefully remove the rest using a 10 μ L pipette.
Note: This step might need some practice. If too much buffer is taken out or the process takes too long, the microstructures will be dried out; if too little is taken, the proteins will not be confined in the microstructures, but continue to form traveling surface waves.
6. Immediately close the chamber with a lid to avoid drying of the residual buffer in the microstructures.
7. To allow for longer imaging times, plug a moistened piece of sponge inside the chamber and then close with lid. Make sure the sponge does not contact the surface of the coverslip.
8. Before imaging of the microstructures check on the surface that the buffer was lowered enough, so that in the surface above the microstructures MinDE pattern formation has halted. Image MinDE oscillations in microstructures. Check that microstructures are not dried out or are drying out during imaging.
Note: Discard coverslips with microcompartments after each use, as cracks in the PDMS form.

9. Analysis of MinDE pattern formation

1. Quantify wave length, wave velocity and wave profiles of the MinDE self-organization on planar supported lipid bilayers. FIJI with the standard set of packaged plugins is sufficient for basic analysis³³.
2. Analyze pole-to-pole oscillations in microcompartments by obtaining kymographs and time-averaged protein concentration profiles. Basic kymographs can be obtained by re-slicing a time series along a line selection in FIJI.

Representative Results

Protein purification following our protocol should yield Min proteins of adequate purity. As a reference, **Figure 1** provides an SDS-PAGE image of MinD, fluorescently labelled MinD, MinE, and MinC. The individual steps of the procedure to perform a MinDE self-organization assay on non-patterned supported lipid bilayers are described in **Figure 2**. Using this protocol, regular MinDE traveling surface waves can be observed throughout the chamber (**Figure 3**). The wavelength can vary slightly within the chamber, but in general patterns look similar. The edges of the chamber should not be used for quantitative comparisons, as membranes that form on the UV glue seem to have different properties than on the glass surface (see **Figure 3C**). The traveling surface waves can be analyzed by plotting the intensity along the propagation direction (**Figure 3B**). While MinD fluorescence plateaus rather fast from the leading edge of the wave and then sharply decreases at the trailing edge, MinE fluorescence increases almost linearly from the start of the MinD wave and reaches its maximum after MinD at the trailing edge, where it falls off markedly⁶.

Next to protein quality, the quality of the supported lipid bilayers is most critical for a regular self-organization of MinCDE. On the one hand if the membrane is washed too excessively or the underlying surface has been cleaned and thus charged too strongly, holes can form in the membrane (**Figure 6A**, top). On the other hand if the membrane is not washed properly or the underlying surface is not cleaned/hydrophilized, vesicles will stick to the membrane or the membrane fluidity will be compromised (**Figure 6A**, bottom). Even though not as apparent as when observing the membrane directly via labeled lipids, these problems can also be detected from the MinD fluorescence signal, as patterns are not regular and the fluorescence in the maxima is not homogenous but contains "holes" or bright spots as shown in the middle panel of **Figure 6A**.

For the MinDE self-organization in rod-shaped PDMS microstructures the procedure is summarized in **Figure 4**. Several protocol steps do not need to be repeated, as proteins and lipids can be reused. Like on non-patterned substrates, the substrate is cleaned and hydrophilized (by plasma-cleaning), a supported lipid bilayer is formed on the PDMS and the self-organization assay is set up in a volume of 200 μ L. To check that a proper membrane has formed and MinDE self-organizes on the membrane, the chambers are imaged. When a proper membrane has been formed, MinDE forms regular traveling surface waves on the surface of the PDMS between the individual microstructures and also self-organizes at the bottom of the microstructures as the waves can freely move over the entire membrane-covered surface (**Figure 5A**). After buffer removal, the surface between the compartments should not show any propagating MinDE patterns (**Figure 5B**), as it should be entirely dry. If MinDE patterns are still moving, more buffer needs to be removed. The proteins are now confined in the rod-shaped microcompartments by the membrane-clad PDMS and by air on the upper interface (**Figure 5C**), in which they will self-organize. Under these conditions the two proteins can perform pole-to-pole oscillations as shown in **Figure 5D**. As a fraction of MinD and MinE is always membrane-bound, also during buffer removal, the concentrations after buffer removal are not comparable to input concentrations. Due to this effect the concentrations also vary between individual microstructures on the same coverslip as they depend on the position of the patterns before buffer removal. Silicon wafer production or PDMS molding from the silicon wafer can result in incomplete microstructures that cannot be used for analysis (**Figure 6B**). Furthermore, due to the buffer removal microstructures might dry out during the process, and hence, should be excluded from further analysis (**Figure 6B**). As a result only a fraction of the microstructures in one chamber shows the desired pole-to-pole oscillations. To analyze protein dynamics in the microstructures, a kymograph can be obtained by drawing a selection over the entire structure (**Figure 5E**). When MinCDE oscillate from pole-to-pole, MinC and MinD will show a time-averaged concentration gradient with maximum concentration at the compartment poles and minimal concentration in the middle of the compartment (**Figure 5F**).

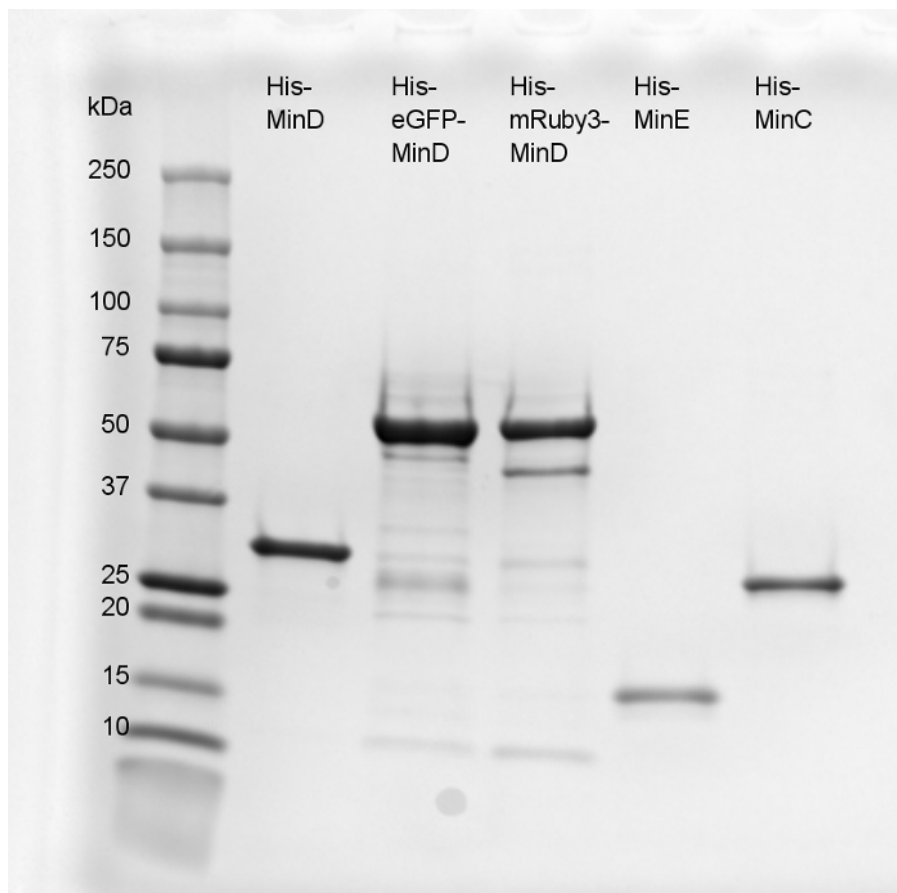


Figure 1: SDS-PAGE showing the final products of protein purifications. His-MinD (33.3 kDa), His-eGFP-MinD (60.1 kDa), His-mRuby3-MinD (59.9 kDa), His-MinE (13.9 kDa) and His-MinC (28.3 kDa) are shown in order. [Please click here to view a larger version of this figure.](#)

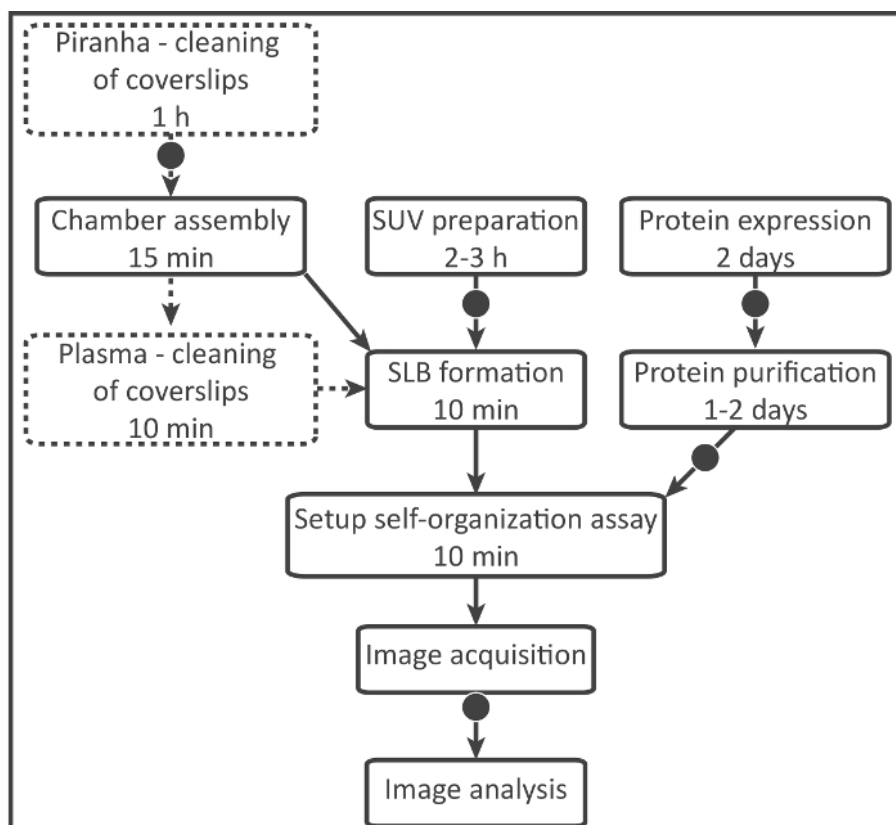


Figure 2: Process flow diagram showing the individual steps and timing of the protocol for a self-organization on non-patterned supported lipid bilayers (Steps 1-6). Dashed boxes indicate that one of these two options can be used for cleaning. Arrows marked by circles indicate where the protocol can be paused and resumed later. [Please click here to view a larger version of this figure.](#)

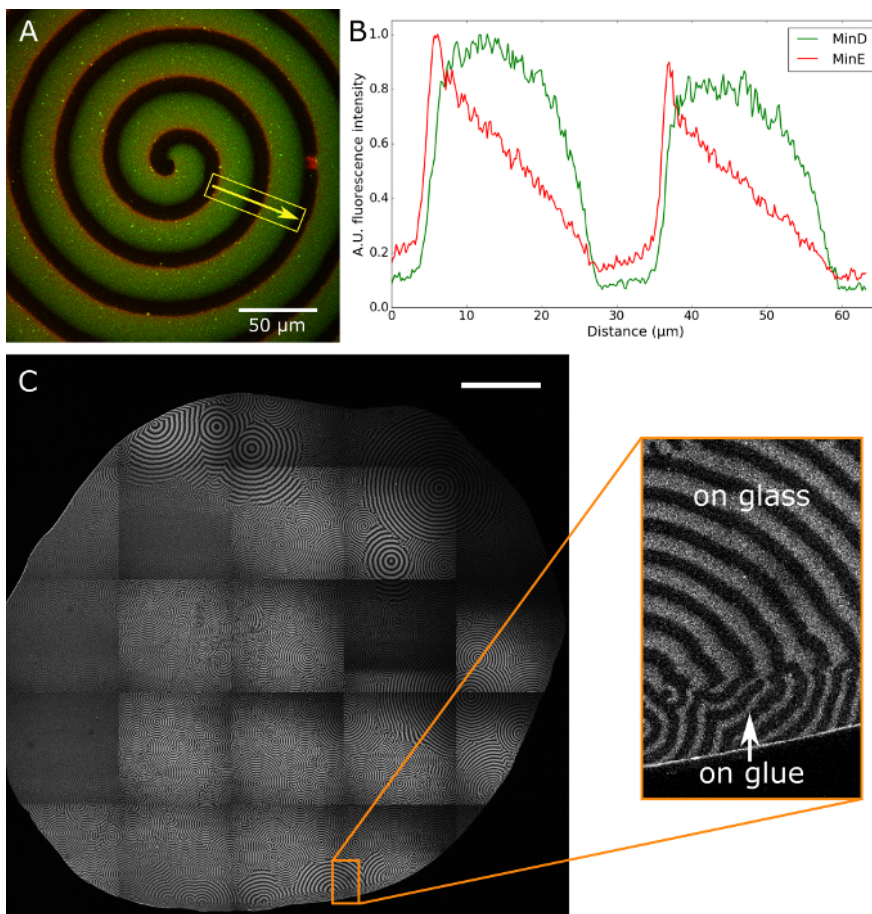


Figure 3: Imaging of MinDE assay by confocal microscopy. A) Regular Min spiral, from which wave propagation speed, intensity plot and speed measurements can be obtained. Concentrations used: 0.6 μM MinD (30% eGFP-MinD), 1.8 μM His-MinE (30% His-MinE-Alexa647) **B)** Example normalized intensity plot for the region marked in A. **C)** Overview of entire assay chamber (scale bar: 1 mm, same protein concentrations as above). Spirals turning either direction as well as target patterns can be observed. The magnified region shows how wave patterns differ on the UV-gel. [Please click here to view a larger version of this figure.](#)

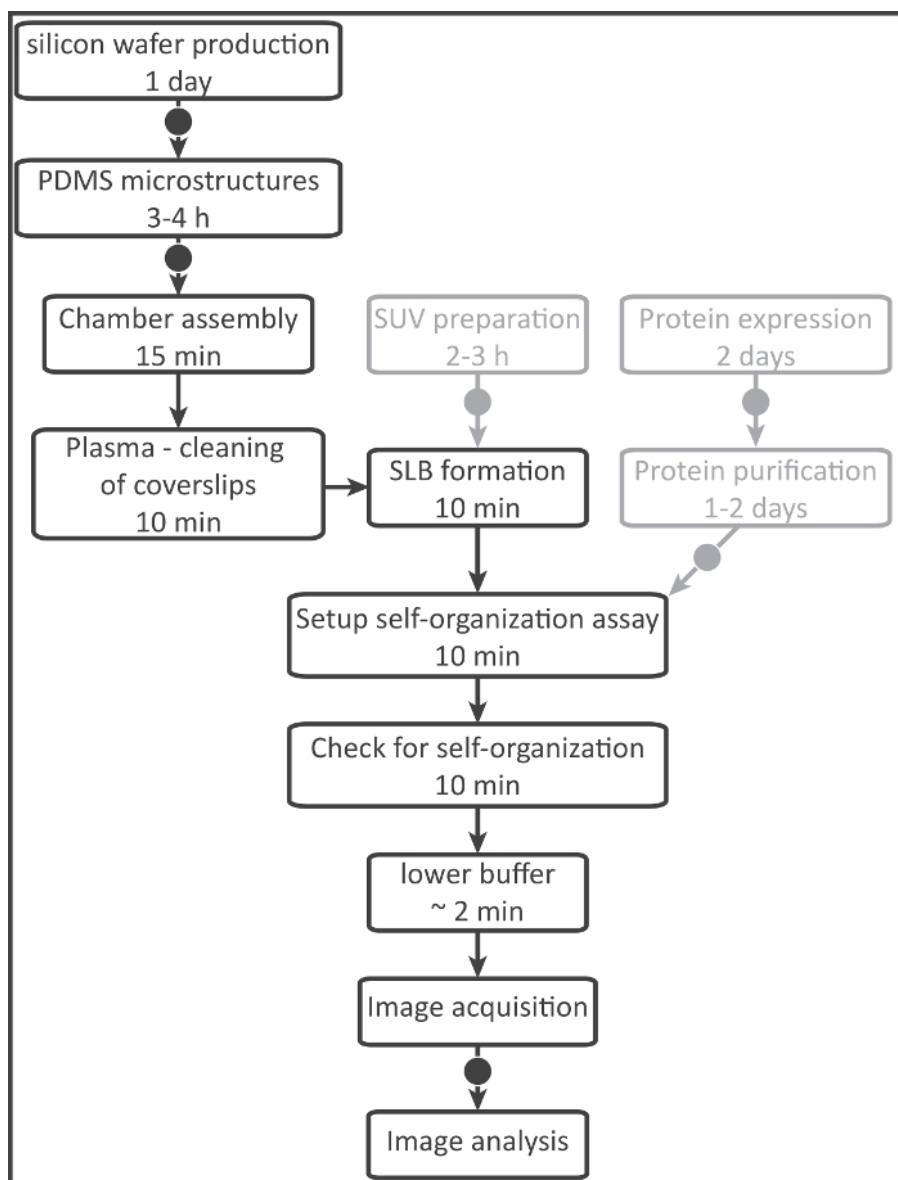


Figure 4: Process flow diagram showing the individual steps and timing of the protocol for self-organization in rod-shaped microstructures (Steps 1-5, 7, 8). Grey boxes indicate steps where products can be reused from the protocol on non-patterned supported lipid bilayers. Arrows marked by circles indicate where the protocol can be paused and resumed later. [Please click here to view a larger version of this figure.](#)

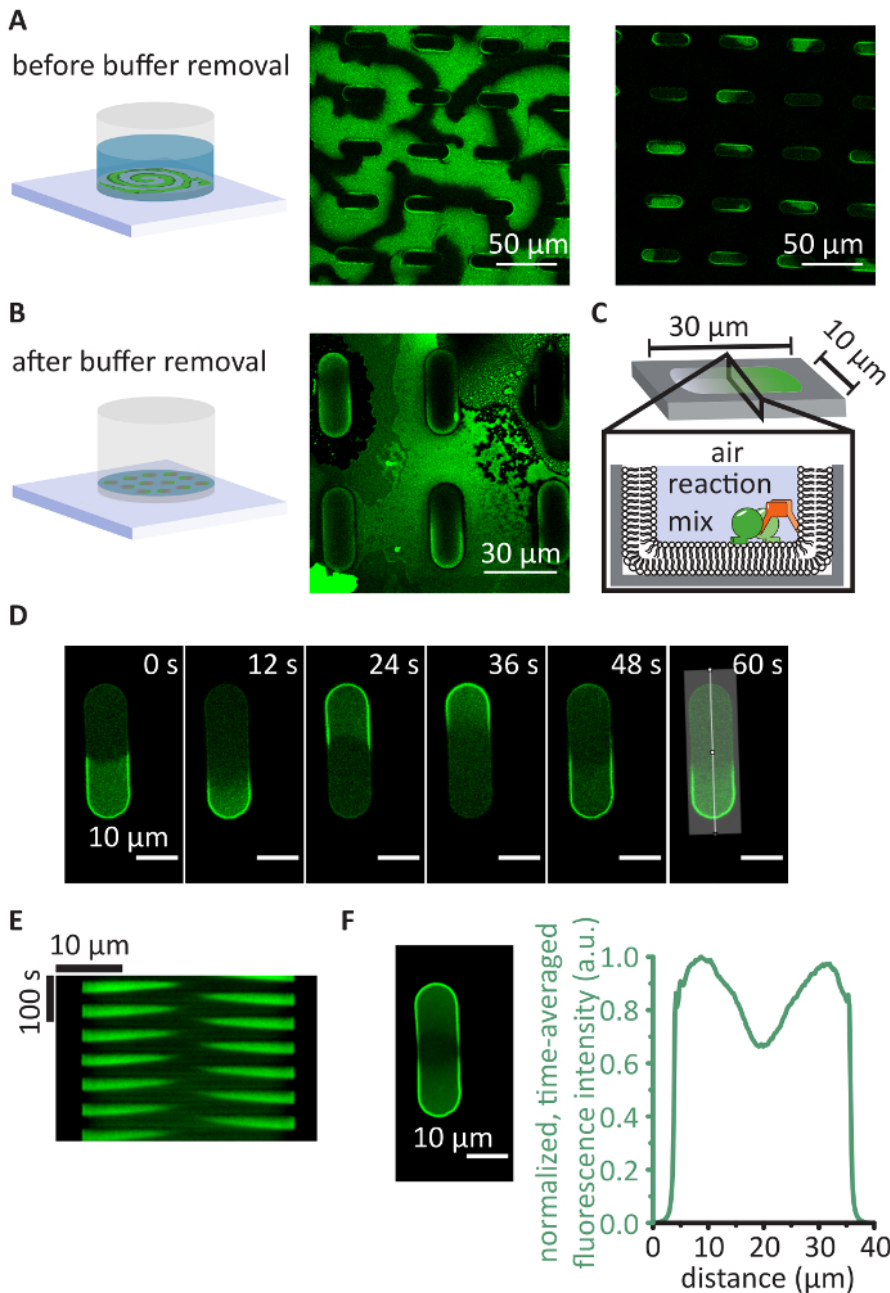


Figure 5: Representative results for MinDE pattern formation in rod-shaped PDMS microcompartments. **A)** MinDE self-organize on the surface of the PDMS forming traveling surface waves (1 μM MinD (30% EGFP-MinD), 2 μM MinE and 2.5 mM ATP). **B)** After the buffer is lowered to the height of the microstructures, the protein self-organization stops on the planar surface between the microcompartments. **C)** Schematic of one rod-shaped microcompartment. **D)** Representative images of MinDE pole-to-pole oscillations after buffer removal. **E)** Kymograph of the oscillations along the highlighted line shown in D). **F)** Image and profile of the average fluorescence intensity of the time-series shown in D) clearly showing the protein gradient that is maximal at microcompartment poles and minimal at compartment middle. [Please click here to view a larger version of this figure.](#)

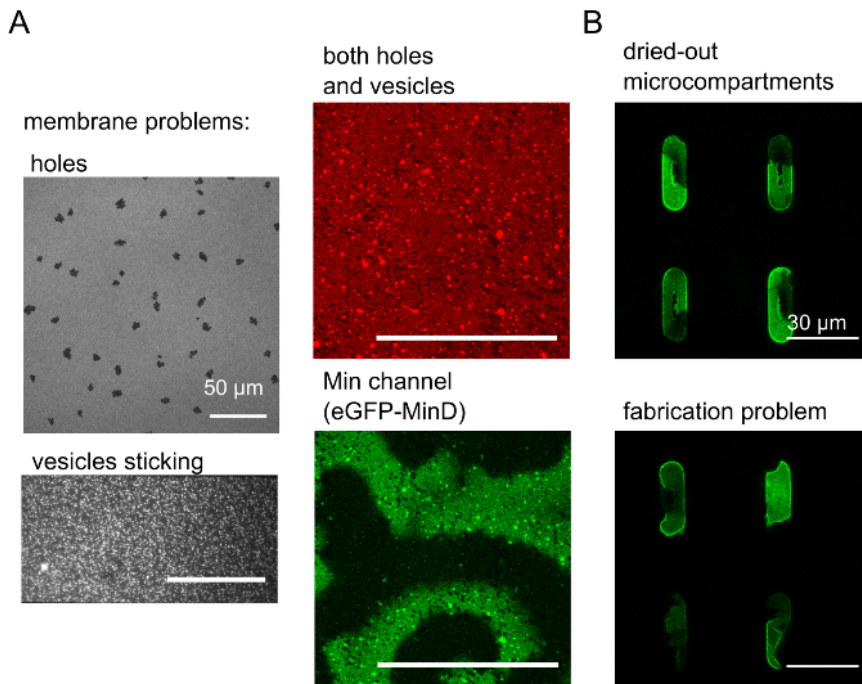


Figure 6: Examples of negative experimental outcomes. A) Over-washed membranes accumulate holes, while suboptimal vesicle preparations and lipid compositions lead to sticking vesicles. The two center panels show a combination of both problems and how they become visible when observing Min oscillations. Membranes were labelled with 0.05% Atto655-DOPE. (scale bars: 50 μm) **B)** Top panel: Dried out microcompartments can be caused by too much buffer removal or when the buffer evaporates over time. Bottom panel: Incomplete compartments can be formed during wafer production or PDMS molding. (scale bars: 30 μm) [Please click here to view a larger version of this figure.](#)

Supplementary File 1: Plasmid map for His-MinD. [Please click here to download this file.](#)

Supplementary File 2: Plasmid map for His-EGFP-MinD. [Please click here to download this file.](#)

Supplementary File 3: Plasmid map for His-mRuby3-MinD. [Please click here to download this file.](#)

Supplementary File 4: Plasmid map for His-MinE. [Please click here to download this file.](#)

Supplementary File 5: Plasmid map for His-MinC. [Please click here to download this file.](#)

Supplementary File 6: CAD file for silicon wafer of rod-shaped microcompartments. [Please click here to download this file.](#)

Discussion

We have described a protocol for the *in vitro* reconstitution of MinCDE self-organization on planar supported lipid bilayers and in lipid bilayer covered 3D structures, using the example of rod-shaped PDMS microstructures. In order to obtain valuable data from these assays, the most important factors to control are protein and membrane quality.

To ensure protein quality, protein mass should be confirmed using SDS-PAGE and mass spectrometry. Furthermore, it should be verified that proteins are soluble and not aggregated, by using analytical gel filtration or dynamic light scattering. Gel filtration can be used to remove any aggregated fraction of proteins. Careful pH adjustment and quality of added nucleotides is critical, as the addition of non-adjusted or partially degraded nucleotide to protein stocks or self-organizing assays is sufficient to eliminate protein activity, therefore abolishing self-organization.

Next to protein quality, membrane quality is most critical, and improper membrane formation is most often the cause for defective self-organization and the origin of artefactual surface structures.

When performing the protocol for the first time, it is helpful to label the supported lipid bilayers by including labeled lipids such as Atto-655-DOPE or Dil at low molar percentages (0.05%). Thereby the properties and quality of the membrane can be judged directly. Using FRAP, the fluidity of the membrane can be assessed. Furthermore, one can directly assess the quality of washing of the SLB, as there will either be too many vesicles, no fluid membrane, or no membrane at all, if it has been washed off. The open chamber approach allows to rigorously wash the membrane, and hence also to remove vesicles that are sticking on the surface of the SLB. The most crucial factors for obtaining fluid and homogenous supported lipid bilayers are the cleaning and hydrophilicity of the support surface and the correct size and homogeneity of the SUVs. It can be helpful to check SUV size and size distribution using dynamic light scattering. For narrow size distributions, we recommend

extruding the vesicles rather than sonicating them. Other methods of cleaning coverslips, *e.g.*, treatments with strong bases, basic detergents, or using coverslips directly after rinsing with water, may yield good results, depending on the application and lipid mixture.

The first half of the protocol presented here, *in vitro* reconstitution on planar supported lipid bilayers in open chambers, has the advantage of rendering the surface accessible for optical microscopies, such as TIRF microscopy³⁰, FRAP analysis⁶, single-particle tracking³⁴, as well as surface probe techniques such as atomic force microscopy²⁶. The large homogeneous area allows for better statistics at defined concentrations. Furthermore the open chamber approach allows to precisely control protein concentration and a rapid and simple addition of further components, hence permitting to titrate protein concentration in a single chamber²⁰. The assay can also be expanded by addition of other bacterial divisome components such as FtsZ^{22,35}, ZipA²² or the chimeric protein FtsZ-YFP-MTS^{10,35}.

Other groups have taken a similar approach to reconstituting the Min system *in vitro*, but use a flow-cell instead of an open chamber^{17,18,19}. Flow-cells have certain advantages, in particular when a fully enclosed 3D environment is needed¹⁸, the influence of flow^{17,19,23} or membrane composition²³ on MinCDE patterns is investigated, or if protein patterns are to be observed under protein limiting conditions¹⁹. Nonetheless, local control of molecular concentrations is more difficult. Protein components, especially MinD, strongly bind to the membrane they first encounter^{18,19}. In our experience, the proteins frequently exhibit non-specific binding to tubing, inlets, syringes and other microfluidic parts. Hence, local protein concentrations differ from input concentrations¹⁸ and also vary over the length of the flow-cell, resulting in a variety of different protein patterns on the membrane between inlet and outlet, as observed by others¹⁹.

The second half of the protocol presented here, the *in vitro* reconstitution in rod-shaped microstructures re-using the open chamber approach on a patterned support covered by lipid bilayers allows for a simple mimic of *in vivo* protein behavior even though precise control over protein concentrations is lost due to buffer removal. Note that because the wavelength of MinDE is about one order of magnitude larger *in vitro* than *in vivo* the rod-shaped microcompartments are also about one order of magnitude larger (10 x 30 μ m) than a rod-shaped *E. coli* cell.

Overall, this protocol allows for the precise control of all conditions including protein concentration, buffer composition and membrane properties. The use of 3D structured supports enables the reaction to be studied under spatial confinement, mimicking *in vivo* behavior without the need for complex microfluidics equipment.

Disclosures

The authors have nothing to disclose.

Acknowledgements

We thank Michael Heymann and Frank Siedler for production of silicon wafers, Core Facility MPI-B for assistance in protein purification and Simon Kretschmer and Leon Harrington for comments on the manuscript.

References

- Soh, S., Byrska, M., Kandere-Grzybowska, K., Grzybowski, B.A. Reaction-diffusion systems in intracellular molecular transport and control. *Angew Chemie Int Ed.* **49** (25), 4170-4198 (2010).
- Lutkenhaus, J. The ParA/MinD family puts things in their place. *Trends Microbiol.* **20** (9), 411-418 (2012).
- Shih, Y.-L., Zheng, M. Spatial control of the cell division site by the Min system in *Escherichia coli*. *Environ Microbiol.* **15** (12), 3229-3239 (2013).
- Halatek, J., Frey, E. Highly canalized MinD transfer and MinE sequestration explain the origin of robust MinCDE-protein dynamics. *Cell Rep.* **1** (6), 741-752 (2012).
- Raskin, D.M., De Boer, P.A.J. MinDE-dependent pole-to-pole oscillation of division inhibitor MinC in *Escherichia coli*. *J Bacteriol.* **181** (20), 6419-6424 (1999).
- Loose, M., Fischer-Friedrich, E., Ries, J., Kruse, K., Schwille, P. Spatial regulators for bacterial cell division self-organize into surface waves *in vitro*. *Science.* **320** (5877), 789-792 (2008).
- Wu, F., van Schie, B.G.C., Keymer, J.E., Dekker, C. Symmetry and scale orient Min protein patterns in shaped bacterial sculptures. *Nat Nanotechnol.* **10** (June), 719-726 (2015).
- Hu, Z., Lutkenhaus, J. Topological regulation of cell division in *E. coli*: Spatiotemporal oscillation of MinD requires stimulation of its ATPase by MinE and phospholipid. *Mol Cell.* **7** (6), 1337-1343 (2001).
- Meinhardt, H., de Boer, P.A.J. Pattern formation in *Escherichia coli*: A model for the pole-to-pole oscillations of Min proteins and the localization of the division site. *Proc Natl Acad Sci U S A.* **98** (25), 14202-14207 (2001).
- Zieske, K., Schwille, P. Reconstitution of self-organizing protein gradients as spatial cues in cell-free systems. *Elife.* **3**, e03949 (2014).
- Roberts, M.A.J., Wadhams, G.H., Hadfield, K.A., Tickner, S., Armitage, J.P. ParA-like protein uses nonspecific chromosomal DNA binding to partition protein complexes. *Proc Natl Acad Sci U S A.* **109** (17), 6698-6703 (2012).
- Vecchiarelli, A.G., Mizuuchi, K., Funnell, B.E. Surfing biological surfaces: Exploiting the nucleoid for partition and transport in bacteria. *Mol Microbiol.* **86** (3), 513-523 (2012).
- Thanbichler, M., Shapiro, L. MipZ, a spatial regulator coordinating chromosome segregation with cell division in *Caulobacter*. *Cell.* **126** (1), 147-162 (2006).
- Lim, H.C., Surovtsev, I.V., Beltran, B.G., Huang, F., Bewersdorf, J., Jacobs-Wagner, C. Evidence for a DNA-relay mechanism in ParABS-mediated chromosome segregation. *Elife.* **3**, e02758 (2014).
- Mileykovskaya, E., Fishov, I., Fu, X., Corbin, B.D., Margolin, W., Dowhan, W. Effects of phospholipid composition on MinD-membrane interactions *in vitro* and *in vivo*. *J Biol Chem.* **278** (25), 22193-22198 (2003).
- Renner, L.D., Weibel, D.B. Cardiolipin microdomains localize to negatively curved regions of *Escherichia coli* membranes. *Proc Natl Acad Sci U S A.* **108** (15), 6264-6269 (2011).

17. Ivanov, V., Mizuuchi, K. Multiple modes of interconverting dynamic pattern formation by bacterial cell division proteins. *Proc Natl Acad Sci U S A*. **107** (18), 8071-8078 (2010).
18. Caspi, Y., Dekker, C. Mapping out Min protein patterns in fully confined fluidic chambers. *Elife*. **5**, e19271 (2016).
19. Vecchiarelli, A.G. *et al.* Membrane-bound MinDE complex acts as a toggle switch that drives Min oscillation coupled to cytoplasmic depletion of MinD. *Proc Natl Acad Sci U S A*. **113** (11), E1479-E1488 (2016).
20. Kretschmer, S., Zieske, K., Schwille, P. Large-scale modulation of reconstituted Min protein patterns and gradients by defined mutations in MinE's membrane targeting sequence. *PLoS One*. **12** (6), e0179582 (2017).
21. Schweizer, J., Loose, M., Bonny, M., Kruse, K., Monch, I., Schwille, P. Geometry sensing by self-organized protein patterns. *Proc Natl Acad Sci*. **109** (38), 15283-15288 (2012).
22. Martos, A., Raso, A., Jiménez, M., Petrášek, Z., Rivas, G., Schwille, P. FtsZ polymers tethered to the membrane by ZipA are susceptible to spatial regulation by min waves. *Biophys J*. **108** (9), 2371-2383 (2015).
23. Vecchiarelli, A.G., Li, M., Mizuuchi, M., Mizuuchi, K. Differential affinities of MinD and MinE to anionic phospholipid influence Min patterning dynamics *in vitro*. *Mol Microbiol*. **93** (3), 453-463 (2014).
24. Glock, P. *et al.* Optical control of a biological reaction-diffusion system. *Angew Chemie Int Ed*. **57** (9), 2362-2366 (2018).
25. Zieske, K., Schwille, P. Reconstitution of pole-to-pole oscillations of min proteins in microengineered polydimethylsiloxane compartments. *Angew Chemie Int Ed*. **52** (1), 459-462 (2013).
26. Miyagi, A., Ramm, B., Schwille, P., Scheuring, S. High-speed AFM reveals the inner workings of the MinDE protein oscillator. *Nano Lett*. **18** (1), 288-296 (2017).
27. Ramirez-Diaz, D.A. *et al.* Treadmilling analysis reveals new insights into dynamic FtsZ ring architecture. *PLoS Biol*. **16** (5), e2004845 (2018).
28. Vogel, S.K., Petrasek, Z., Heinemann, F., Schwille, P. Myosin motors fragment and compact membrane-bound actin filaments. *Elife*. **2**, e00116 (2013).
29. Zieske, K., Schweizer, J., Schwille, P. Surface topology assisted alignment of Min protein waves. *FEBS Lett*. **588** (15), 2545-2549 (2014).
30. Loose, M., Fischer-Friedrich, E., Herold, C., Kruse, K., Schwille, P. Min protein patterns emerge from rapid rebinding and membrane interaction of MinE. *Nat Struct Mol Biol*. **18** (5), 577-583 (2011).
31. Zieske, K., Schwille, P. Reconstituting geometry-modulated protein patterns in membrane compartments. *Methods Cell Biol*. **128**, 149-163 (2015).
32. Gruenberger, A., Probst, C., Heyer, A., Wiechert, W., Frunzke, J., Kohlheyer, D. Microfluidic picoliter bioreactor for microbial single-cell analysis: fabrication, system setup, and operation. *J Vis Exp*. (82), e50560 (2013).
33. Schindelin, J. *et al.* Fiji: An open-source platform for biological-image analysis. *Nat Methods*. **9** (7), 676-682 (2012).
34. Loose, M., Kruse, K., Schwille, P. Protein self-organization: Lessons from the min system. *Annu Rev Biophys*. **40**, 315-336 (2011).
35. Arumugam, S., Petrášek, Z., Schwille, P. MinCDE exploits the dynamic nature of FtsZ filaments for its spatial regulation. *Proc Natl Acad Sci U S A*. **111** (13), E1192-E1200 (2014).

Materials List for:

In Vitro Reconstitution of Self-Organizing Protein Patterns on Supported Lipid Bilayers

Beatrice Ramm^{*1}, Philipp Glock^{*1}, Petra Schwille¹

¹Department of Cellular and Molecular Biophysics, Max Planck Institute of Biochemistry

*These authors contributed equally

Correspondence to: Petra Schwille at schwille@biochem.mpg.de

URL: <https://www.jove.com/video/58139>

DOI: [doi:10.3791/58139](https://doi.org/10.3791/58139)

Materials

Name	Company	Catalog Number	Comments
Reagents			
DOPC	Avanti Polar Lipids	850375	
DOPG	Avanti Polar Lipids	840475	
E.coli polar lipid extract	Avanti Polar Lipids	100600	
Adenosine 5'-triphosphate disodium salt trihydrate	Roche		
Adenosine 5'-diphosphate monopotassium salt dihydrate	Sigma	A5285-1G	
Sodium chloride	VWR	27810.295	
Potassium chloride	Roth	6781.1	
Tris-base	Sigma Aldrich	T1503-1kg	
Hydrochloric acid	Roth	9277.1	
TCEP-HCl	Termo Fisher Scientific	20491	
Ethylene Diamine Tetraacetate	Merck Millipore	1.08418.1000	
Sulfuric Acid 98%	Applichem	173163.1611	
Hydrogen Peroxide 50%	Applichem	147064.1211	
HEPES	Biomol	05288.1	
dimethyl sulfoxide (DMSO)	Merck	102950	Uvasol
Glycerol 86%	Roth	4043.1	
TB medium			
Isopropyl β-D-1-thiogalactopyranoside (IPTG)	Roth	2316.x	
Atto-655-DOPE	Atto Tec	AD 655-161	
Ni-NTA agarose	Qiagen	30210	
PDMS base	Dow Corning Corporation		SYLGARD 184
PDMS crosslinker	Dow Corning Corporation		
Materials			
UV Glue	Norland Products	6801	#68 and #63 both work well
Coverslips #1.5 24x24 mm	Menzel Gläser		
Coverslips #1 24x24 mm	Menzel Gläser		used only for PDMS microstructures
0.5 ml reaction tube	Eppendorf	0030123301	
culture flask 2L	Corning	e.g. 734-1905	
His-Trap HP	GE Healthcare Life Sciences		

Gelfiltration column: HiLoad Superdex 75 PG or 200 PG	GE Healthcare Life Sciences		
Econo-Pac 10DG desalting column prepacked column	Biorad	7322010	
dialysis device: Slide-A-Lyzer Dialysis Cassettes, 3.5K MWCO, 0.1 - 0.5 mL or 0.5-3 mL	Termo Fisher Scientific	66333 or 66330	
razor blade			
Instruments			
ultrapure water: Milli-Q Type 1 Ultrapure Water Systems	Merck		
automated protein purification system: Äkta Pure	GE Healthcare Life Sciences		
bath sonicator	Branson		e.g. Model 1510
ARE-250 mixer	Thinky Corporation		
Plasma cleaner Zepto	Diener electronic		use oxygen as process gas
positive displacement pipettes	Brand		Transferpettor models with glass tips
LSM780 confocal laser scanning microscope	Zeiss		Fitted with Zeiss C-Apochromat 40X/1.20 water-immersion objective
Plasmids			
pET28a-His-MinD_MinE	Department of Cellular and Molecular Biophysics, MPI of Biochemistry, Prof. Schwille		plasmid encoding His-MinD and non-tagged MinE to improve yield
pET28a-His-MinE	Department of Cellular and Molecular Biophysics, MPI of Biochemistry, Prof. Schwille		plasmid encoding His-MinE
pET28a-His-EGFP-MinD	Department of Cellular and Molecular Biophysics, MPI of Biochemistry, Prof. Schwille		plasmid encoding His-EGFP-MinD
pET28a-His-mRuby3-MinD	Department of Cellular and Molecular Biophysics, MPI of Biochemistry, Prof. Schwille		plasmid encoding His-mRuby3-MinD
pET28a-His- MinC	Department of Cellular and Molecular Biophysics, MPI of Biochemistry, Prof. Schwille		plasmid encoding His-MinC

Stationary Patterns in a Two-Protein Reaction-Diffusion System

In this manuscript, the capability of the Min system to form a diverse set of stationary patterns is demonstrated. The possibility to obtain such patterns further enhances the utility of the Min system.

Reprinted with permission from P. Glock, B. Ramm, T. Heermann, S. Kretschmer, J. Schweizer, J. Mücksch, G. Alagöz, and P. Schille, “Stationary patterns in a two-protein reaction-diffusion system,” *ACS Synthetic Biology*, p. acssynbio.8b00415, 2018. Copyright (2019) American Chemical Society.

Source online: <https://doi.org/10.1021/acssynbio.8b00415>

Stationary Patterns in a Two-Protein Reaction-Diffusion System

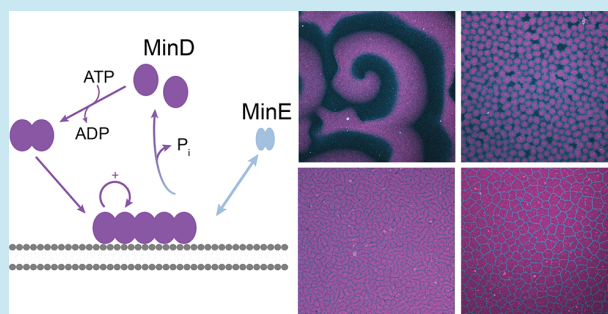
Philipp Glock,¹ Beatrice Ramm,¹ Tamara Heermann,¹ Simon Kretschmer, Jakob Schweizer, Jonas Mücksch,¹ Gökerberk Alagöz, and Petra Schwille*¹

Cellular and Molecular Biophysics, Max-Planck-Institut für Biochemie, Martinsried 82152, Germany

Supporting Information

ABSTRACT: Patterns formed by reaction-diffusion mechanisms are crucial for the development or sustenance of most organisms in nature. Patterns include dynamic waves, but are more often found as static distributions, such as animal skin patterns. Yet, a simplistic biological model system to reproduce and quantitatively investigate static reaction-diffusion patterns has been missing so far. Here, we demonstrate that the *Escherichia coli* Min system, known for its oscillatory behavior between the cell poles, is under certain conditions capable of transitioning to quasi-stationary protein distributions on membranes closely resembling Turing patterns. We systematically titrated both proteins, MinD and MinE, and found that removing all purification tags and linkers from the N-terminus of MinE was critical for static patterns to occur. At small bulk heights, dynamic patterns dominate, such as in rod-shaped microcompartments. We see implications of this work for studying pattern formation in general, but also for creating artificial gradients as downstream cues in synthetic biology applications.

KEYWORDS: pattern formation, self-organization, *in vitro* reconstitution, min proteins, reaction-diffusion system, stationary pattern



Pattern formation, the emergence of patterns in initially spatially homogeneous systems, is at the basis of biological systems. It often relies on reaction-diffusion mechanisms, as in the patterning of animal skin¹ and on multiple occasions in the development of animals.^{2,3} Hence, understanding reaction-diffusion mechanisms in detail is important in the context of cell and developmental biology, but it is mandatory for any fundamental approach toward the emergence of biological systems and for the bottom-up construction of artificial cells.

A prominent candidate for a simple model system to probe reaction-diffusion mechanisms is the Min system of *Escherichia coli*. The Min proteins perform pole-to-pole oscillations to determine the middle of the cell and future division site. This dynamic behavior results from reaction and diffusion of only two proteins—MinD and MinE—in the presence of and catalyzed by a lipid membrane. Due to its relevance for the intracellular organization of bacteria the system has been studied in depth *in vivo*.^{4–6} Its apparent simplicity also facilitated the development of multiple mathematical models^{7,8} as well as the reconstitution of the protein dynamics *in vitro*.⁹ The combined efforts resulted in a widely accepted hypothesis for the basic mechanism (Figure 1a): MinD is an ATPase that dimerizes in its ATP-bound state. This renders the membrane affinity of MinD with its weak membrane targeting sequence (MTS) sufficiently high to attach to the membrane, turning the MinD monomer–dimer transition into a membrane switch.¹⁰ The second protein, MinE, exhibits a latent cytosolic conformation and an active conformation in the presence of membrane-bound MinD, which in turn stimulates the ATPase

activity of MinD. MinE thus features its own, MinD-dependent switch. In the active conformation, a small MTS is formed that is hidden in the latent conformation. MinD shows a strong local positive feedback during membrane binding, recruiting further MinD, while MinE negatively regulates MinD membrane binding. Together, this network of interlinked switches promotes stable pattern formation in a large range of concentrations.¹¹

The *in vitro* reconstitution of this system has been used to investigate the dependence of the formed patterns on several parameters, such as membrane charge and buffer composition,¹² geometry,^{13–15} and the molecular features of Min proteins.^{11,16,17} In all of these investigations, Min proteins were mostly found to self-organize into traveling concentration waves on the surface.^{9,12} While smooth, directionally moving wavefronts can be primarily observed under steady state conditions on homogeneous membranes, additional dynamic patterns have been observed in a flow cell setup.^{16,18} However, despite a decade of reconstitution efforts, stationary patterns with finite wavelength or “Turing” patterns^{19,20} have not been reported for the Min system. As it is known that in reaction-diffusion systems, even relatively minor changes in system parameters can sometimes cause dramatic, qualitative changes in the observed patterns, it was our intention to explore

Received: October 2, 2018

Published: December 20, 2018

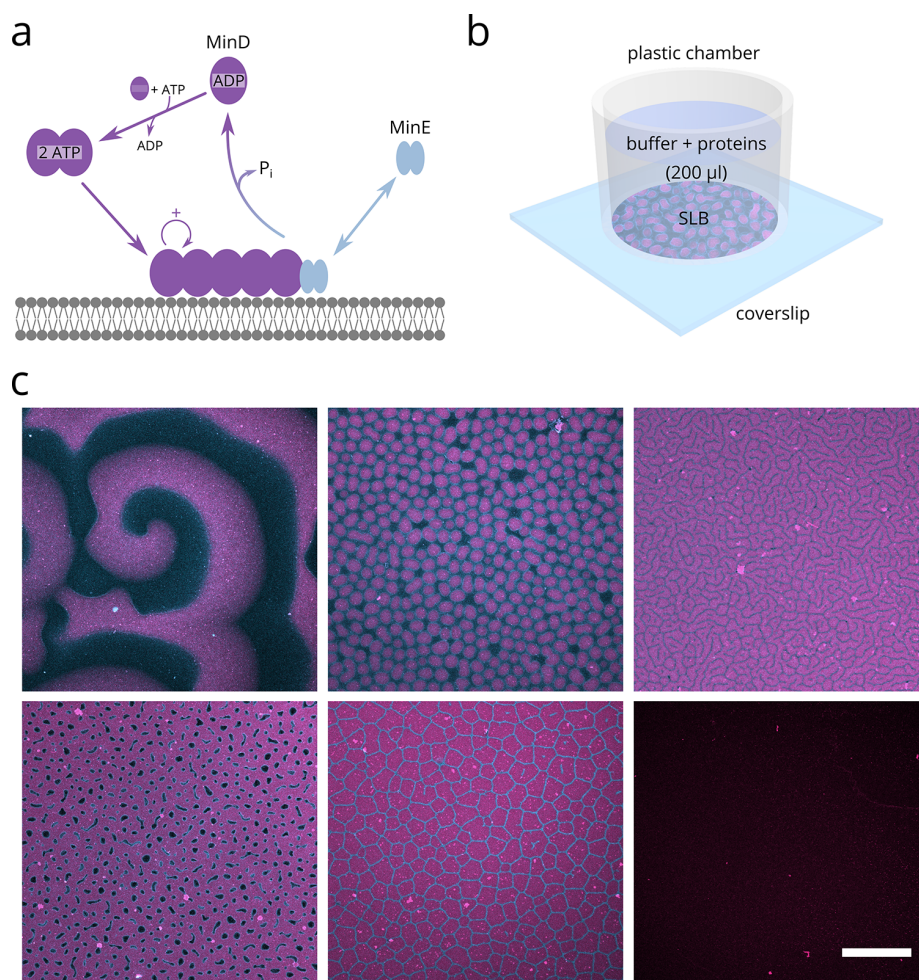


Figure 1. (a) Simplified schematic of Min protein self-organization. MinD (purple) is cytosolic in its ADP-bound state, but attaches to the membrane upon ATP-dependent dimerization. Membrane-bound MinD locally enhances self-recruitment, but also recruits MinE, which activates ATP-hydrolysis and thereby detaches MinD. (b) Experimental setup used: SLB is formed at the bottom of a round plastic chamber glued to a cleaned glass coverslip. Min proteins, ATP, and buffer solution together constitute the bulk volume of 200 μL . (c) Freeing the N-terminus of MinE leads to the formation of stationary patterns in reconstitution assays: Representative images for each pattern are shown. Top left: Traveling waves, observed at 0.5 μM MinD, 1.2 μM MinE-His. Top middle: Spots, here at 1.3 μM MinD, 4 μM MinE-His. Top right: Labyrinth (1.25 μM MinD, 2.5 μM MinE-His). Bottom left: Inverse spots (0.5 μM MinD, 0.125 μM MinE-His). Bottom middle: MinE-mesh (1.5 μM MinD, 3 μM MinE-His). Bottom right: no pattern (0.2 μM MinD, 1 μM MinE-His). (Scale bar: 50 μm , MinD: magenta, MinE-His: cyan; proteins were fluorescently labeled by doping MinD with 30% Alexa647-KCK-MinD and MinE-His with 30% Atto488-KCK-MinE-His, membrane prepared from 2:1 DOPC:DOPG).

whether such a transition from dynamic to static Min patterns could be evoked simply by titration.

Because most protein constructs used for *in vitro* applications carry additional modifications due to the need for purification, special attention was paid to the influence of such tags, particularly for MinE, which is the smaller protein. Previously, placement of the His-tag at the N- and C-terminus of MinE showed similar results with respect to pattern formation, although this was examined only at one specific experimental condition.⁹ We therefore revisited our standard MinE construct, which was cloned with an N-terminal His-tag and linker, and systematically investigated pattern formation while titrating the concentrations of MinD and MinE. Strikingly, moving this N-terminal attachment to the C-terminus, or cleaving it off to obtain the wild type protein had an astonishing effect on the observed dynamics in our *in vitro* assay, and opens up a big spectrum of intriguing patterns that

closely resemble Turing patterns.^{19,20} Thus, while the *in vitro* Min system was believed to be well understood, this new phenomenon of static patterns in such an easily accessible biological reaction-diffusion system offers many exciting perspectives for both experimentalists and theoreticians.

RESULTS AND DISCUSSION

Reconstituting MinD and MinE-His on a DOPC:DOPG (2:1) supported lipid bilayer in the presence of ATP resulted in a diverse set of patterns (Figure 1c). Traveling surface waves and spirals with the same characteristics as described for His-MinE could be obtained under some conditions. We classified the other, newly observed patterns as spots, labyrinths, inverse spots, and (MinE-) mesh, respectively. At low MinD concentrations, there are regimes where no patterns emerge and the membrane is mostly free of MinD and MinE (Figure 1c, last panel). Intriguingly, all patterns except the already

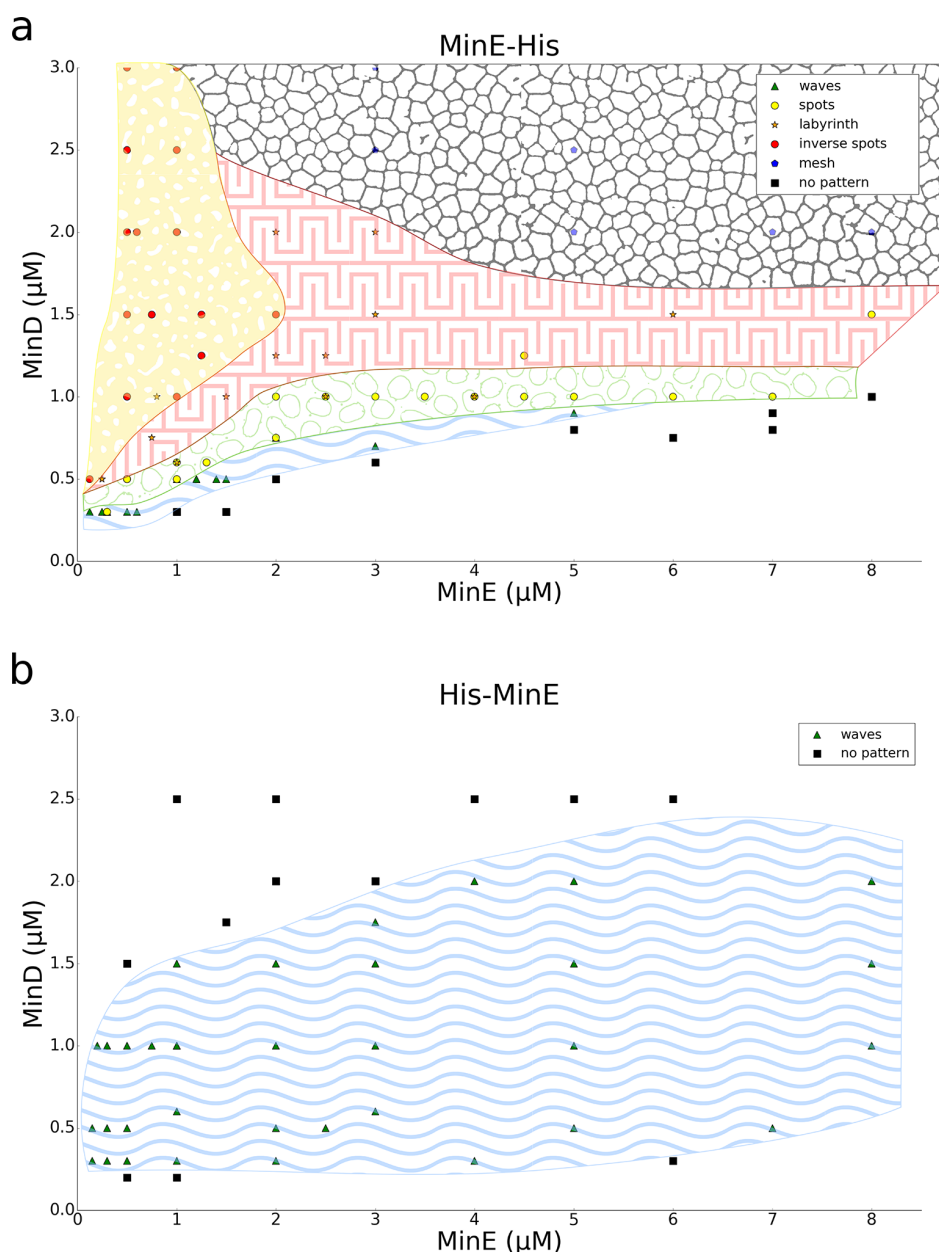


Figure 2. Pattern formation with MinE-His (a) differs considerably from patterns using the previously described His-MinE (b) construct. Varying amounts of MinD (doped with 30% Alexa647-KCK-MinD) and either MinE-His or His-MinE were reconstituted on 2:1 (DOPC:DOPG) SLBs. Pattern formation was assessed in well-mixed chambers after 1h incubation with the proteins and 2.5 mM ATP. The overlaid graphics represent schematic drawings to ease perception of the overall difference between the constructs. Observed patterns are depicted by the symbols described in the legends (top right). Data points depict single observations in separately prepared assay chambers.

described traveling waves are static, and have a strong resemblance to Turing patterns.^{19,20} Importantly, we solely state a qualitative similarity, without drawing conclusions about the mechanism or underlying instability. Gradual small changes can be seen in the patterns (Movie S1), which recover rapidly when photobleached (Movie S2). This shows that, while the overall protein distribution in the large scale pattern is mostly static, there is constant reaction and diffusion occurring, where proteins remain mobile and frequently bind and unbind the membrane. Looking at MinD and MinE separately reveals a differential distribution in the static patterns, often with MinE occupying the rim of MinD zones,

reminiscent of the *in vivo* MinE-ring formation and patterns reported by the Mizuuchi lab.¹⁸ For a separate representation of the membrane distribution of the two proteins in Figure 1c, please refer to Figure S1.

To systematically map out the occurrence of the various patterns as a function of Min protein concentrations, we titrated MinD and MinE-His and summarized the results in a phase diagram (Figure 2a). The striking difference between the two MinE constructs becomes apparent when this plot is compared to a similar diagram compiled from our formerly used protein construct, His-MinE (Figure 2b). Whereas His-MinE, as previously described, self-organizes into traveling

surface waves in a broad range of concentrations on glass supported lipid bilayers, and does not systematically show additional patterns, MinE-His forms waves only in a narrow range of MinD and MinE concentrations. The newly described patterns occupy most of the area in the phase diagram. The schematic regions depicted on top of the plotted values are simplified representations, where the sharp boundaries between types of patterns are drawn to guide the eye and do not reflect the situation in our assays. Rather, two phenomena should be highlighted specifically: First, the assays show multistability, a phenomenon already reported for axis selection and the number of nodes in confined oscillating Min reactions.²¹ Thus, we commonly observe two adjacent patterns within the same chamber, either separated spatially within the chamber (Figure S3), or temporally with one pattern following minutes to hours after another. This time-dependent pattern switch can even happen multiple times within the same, well-mixed assay. Second, while there are strong differences between the individual pattern types (spots, labyrinth, inverse spots, mesh), the transitions between the static patterns show gradual changes, and intermediate patterns are often observed (see also Figure S4). The phase diagram will shift by varying parameters such as membrane composition, buffer ingredients, or support of the lipid bilayer. However, the overall shape of the pattern space is expected to stay the same. We did some experiments using *E. coli* polar lipid extract to form the membrane, since this mixture has been used in the original publication. Similar to our results with the DOPC:DOPG (2:1) mixture, traveling waves forming with MinE-His occurred at lower MinD/MinE compared to the conditions giving rise to stationary patterns (two conditions found in Figure S5).

To exclude the possibility that static patterns are caused by the C-terminal His-tag, we also generated MinE as it is found in the cell, by expressing it as a His-SUMO-MinE fusion and cleaving it to retrieve the native protein *via* a selective SUMO protease. The wild type protein produces the same spectrum of patterns as MinE-His, confirming that His-MinE shows a markedly reduced diversity of obtainable patterns relative to wild type MinE and MinE-His (Figure 3). It is important to note that the scale of the patterns varies slightly between assays, even when using the same protein concentrations.

Given the stark difference in pattern diversity between the two MinE constructs, we wondered what kind of dynamic behavior the two proteins show *in vivo* compared to wildtype MinE. We expressed MinD tagged with superfolder GFP, and either His-MinE, MinE-His, or MinE wt under control of a lac promoter on a low-copy plasmid in $\Delta minDE$ cells. Analysis of the time-lapse data acquired with these constructs shows that all three constructs support MinD pole-to-pole oscillations *in vivo*. However, the oscillation periods observed with His-MinE were significantly longer and their spread vastly bigger than measured with wild type MinE or MinE-His (Figure 3b, see also Movie S3). On average, cells were also more elongated with His-MinE compared to MinE wt, hinting at a cell division phenotype as a consequence of the altered Min system.

Since the His-tag and linker in His-MinE are directly attached to the MTS, we suspected that a difference in membrane binding might be responsible for the reported changes. Therefore, we performed measurements of MinE binding to a membrane on a quartz crystal microbalance with dissipation monitoring (QCM-D). The data obtained indicate very similar membrane binding by both His-MinE and MinE-

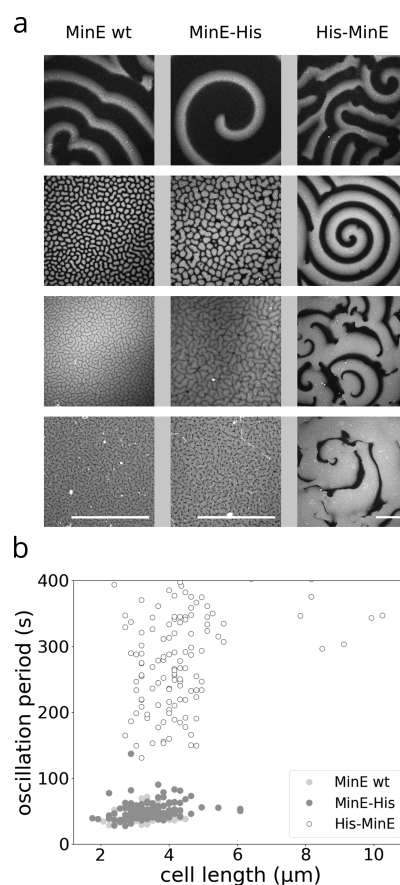


Figure 3. MinE-His and MinE-wt exhibit the same pattern diversity, whereas His-MinE is characterized by impaired pattern diversity *in vitro* and slower pole-to-pole oscillation *in vivo*. (a) Comparison of different MinD and MinE concentrations for all three MinE constructs. Top: 0.5 μM MinD, 1.3 μM MinE. Second row: 1 μM MinD, 3 μM MinE. Third row: 1.5 μM MinD, 1 μM MinE. Bottom row: 1.5 μM MinD, 0.5 μM MinE. (Scale bars: 50 μm . All images except left and middle panel in the last row were recorded at the same scale. MinD doped with 30% Alexa647-KCK-MinD in each case.) (b) *In vivo* oscillation periods at room temperature relative to cell length induced by the different MinE constructs and superfolder GFP-MinD when expressed in $\Delta(\text{minDE})$ background under IPTG induction. Number of cells measured: MinE wt ($n = 104$), MinE-His ($n = 143$), and His-MinE ($n = 189$). The full plot containing all outliers can be found as Figure S11, and single plots of MinE-His and MinE-wt in Figures S12 and S13.

His as well as untagged MinE (Figure 4a). We therefore conclude that the changes in pattern diversity *in vitro* and oscillation period *in vivo* are not due to differential membrane binding of the MinE constructs.

To test whether the linker placement affects the rate of ATP hydrolysis by stimulated MinD, we performed ATPase measurements. And indeed, an NADH-coupled measurement of the ATPase rates revealed that the two MinE constructs lead to a different stimulation of MinD ATPase activity. While the ATPase rate in the presence of His-MinE was measured at roughly 46 nmol ATP per minute and mg (MinD), it was only about two-thirds as high (28.8 nmol ATP per minute and mg (MinD)) in the presence of MinE-His and MinE wt. This shows that, in comparison to MinE wt, His-MinE is not impaired but hyper-active, which might be the cause for it to

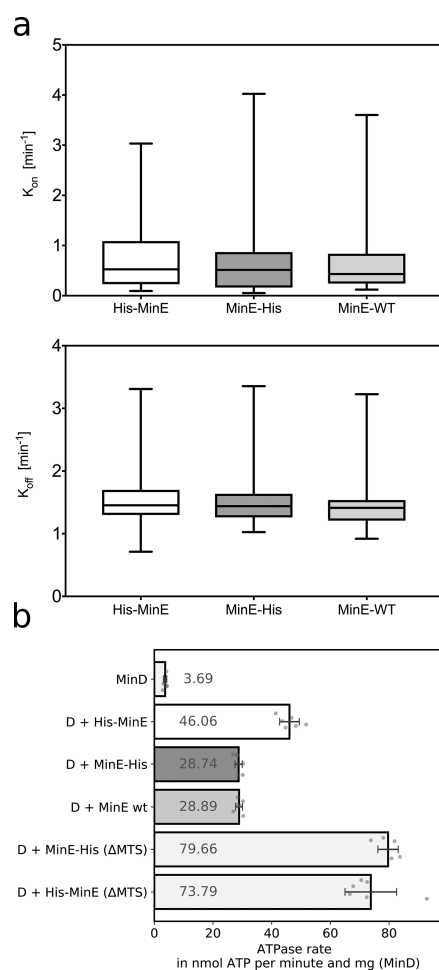


Figure 4. All MinE constructs with MTS bind the membrane with similar affinity, but MinE wt and MinE-His show reduced MinD ATPase stimulation compared to His-MinE. (a) QCM-D measurements of His-MinE, MinE wt, and MinE-His binding to membranes show no apparent difference in membrane binding and unbinding between the constructs. (b) ATPase rates of MinD plus different MinE constructs was measured in an NADH-coupled assay. Data are combined from two independent assays of triplicates for each condition. Error bars represent standard deviation; data points are overlaid.

support dynamic rather than stationary patterns (Figure 4b). Furthermore, we tested versions of MinE without the MTS, with the His-tag on either end of MinE, and found no significant difference between ATPase rate stimulation by those constructs at the tested concentrations. This further supports the notion that the His-tag does not impede MinE membrane binding.

Recent studies have generated new insights into the conformational dynamics of MinE by employing CD spectroscopy and hydrogen–deuterium exchange coupled to mass spectrometry.^{22,23} The authors suggest that there is no equilibrium between MinE's 6β -stranded and 4β -stranded version. Instead, within the 6β -stranded form, MinE transiently releases its MTS along with a loop segment connecting the MTS to the β -sheet. In this state, the switch from the 6β -stranded latent state to the 4β -stranded reactive state is subsequently triggered if MinE encounters, or “senses”,⁶ a membrane-bound MinD dimer. In a recent publication, MinE's

conformational switch was looked at from a dual theory-experiment perspective.¹¹ By using the MinE(I24N) mutant which is permanently locked in the 4β -conformation, the impact of MinE conformational switching on Min protein pattern formation was investigated. If addition of the N-terminal tag and linker would severely impact switching, similarly compromised pattern formation as with I24N would be expected for His-MinE. Instead, we observed a different phenotype where traveling waves are the only observed mode. We speculate that the higher ATPase rate and different phase diagram of MinE-His in comparison with His-MinE could be attributed to a slower return of the His-linker-MinE from the (reactive) 4β to the (latent) 6β -conformation. This would render MinE hyperactive and lead to a higher ATP turnover.

As a further confirmation that the difference between the MinE constructs is not due to membrane binding, MTS-deficient (missing amino acids 2–12) versions of His-MinE and MinE-His show slightly different self-organization characteristics in our *in vitro* assay, while the ATPase rate of both constructs remains the same. In particular, while both the Δ MTS MinE-His and Δ MTS His-MinE constructs displayed a reduced wavelength compared to the WT under wave conditions, we also noticed a difference in the patterns' spatial scale between the N- and C-terminally tagged Δ MTS constructs at the tested concentrations (Figure S5).

Having noticed all those discrepancies between the differentially tagged versions of MinE (see also Figure S6), we wondered whether important features of *in vitro* Min patterns established with His-MinE could also be observed with MinE-His and, conversely, if experiments with MinE-His could provide additional insights. Therefore, we thoroughly revisited several key, past experiments.

First of all, the overall shape of the MinD- and MinE-densities along a traveling wave profile remain unchanged by the new construct (Figure S7), consistent with results obtained by the Mizuuchi lab,¹² who use MinE-His for their experiments. MinE accumulates over the course of a wave and reaches maximal density where MinD density is already decaying. Rapid rebinding of MinE in the traveling wave has so far only been shown with the N-terminally tagged MinE, and should possibly be confirmed with C-terminally tagged MinE by future experiments.^{16,24} However, as highlighted by our phase diagrams (Figure 2), both His-MinE and MinE-His form Min patterns in a similar, broad range of MinE concentrations.¹¹

The reconstitution of Min proteins in PDMS microstructures was the first assay to mimic the rod shape of bacterial cells with simultaneous reaction confinement. While the oscillations differ from *in vivo* oscillations in scale, due to a larger wavelength and reaction volume, they nevertheless reproduce key aspects of *in vivo* behavior.²⁵ Briefly, an SLB is formed on a micropatterned PDMS support. MinD, MinE, and ATP are added into the large bulk volume, and self-organization is first observed everywhere on the membrane without lowering the buffer level. Once regular waves are running on top of the wells, the buffer is lowered, so that individual microcavities become isolated and the proteins and ATP confined within. His-MinE oscillates under these conditions with a very similar time-averaged protein concentration profile as observed *in vivo*. Performing the same assay with MinE-His also resulted in oscillating microcompartments when choosing MinD and MinE concentrations that lead to traveling waves in the bulk assay (Figure

5a). Intriguingly, MinE-His also supports pole-to-pole oscillations and other dynamic patterns when the buffer is

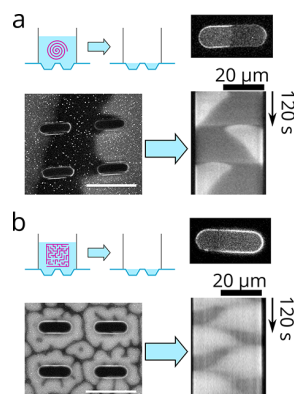


Figure 5. Reaction confinement leads to dynamic oscillations both under wave (a) and static conditions (b). Microchamber assays were performed, and pattern formation was observed before lowering the buffer. Irrespective of the observed pattern before buffer-removal, oscillations were observed in isolated microcompartments. (Concentrations: top $0.75 \mu\text{M}$ MinD, $2 \mu\text{M}$ MinE-His, bottom: $1.3 \mu\text{M}$ MinD, $4 \mu\text{M}$ MinE-His, 20% Alexa647-KCK-MinD in each, scale bars in overview images: $50 \mu\text{m}$).

lowered at conditions that initially form static patterns, such as labyrinths or spots (Figure 5b). Thus, there is only a minor difference in behavior between His-MinE and MinE-His under conditions where the bulk volume is limited. This is further supported by measurements in a flow cell, where almost exclusively dynamic patterns with MinE-His are observed, presumably due to the much lower bulk volume.^{12,16,18}

In a recent study, we showed that the MinDE system can act as a generic cue to position other membrane-bound or membrane-associated factors.²⁶ Probing the same effect with MinE-His confirmed the results obtained with His-MinE: The Min system can position model peripheral and lipid-anchored membrane proteins (Figure 6, Movies S5 and S6). The extent of regulation is similar where MinD and MinE-His form traveling waves (Figure S8). Additionally, the newly observed static patterns strongly exclude other proteins from areas where the membrane-bound MinD levels are high. Importantly, since the distributions of MinD and MinE are distinct in these static patterns, we can now clearly state that membrane-bound MinD alone is responsible for the observed positioning effect. The static patterns can therefore be used as a novel cue to position other membrane-associated proteins *in vitro*.

On top of this, the static patterns themselves offer intriguing possibilities for all kinds of *in vitro* investigations. Since the main difference in diffusion of the Min components depends on membrane-binding upon dimerization, the absolute size and bulk diffusion of either component are not crucially important. For example, fluorescent proteins have been added to both MinD and MinE *in vivo* without disturbing Min oscillations.^{4,27} Thus, attaching for instance functional secondary proteins to a fraction of MinDs is not likely to impact pattern formation to a relevant degree. This is further evidenced by many of our previous experiments where 20 to 30% of MinDs were tagged with the fluorescent proteins eGFP or mRuby3.^{11,17,28} One could therefore imagine assays where the Min system merely positions factors in a self-organized manner, which is especially compelling in a case where spots

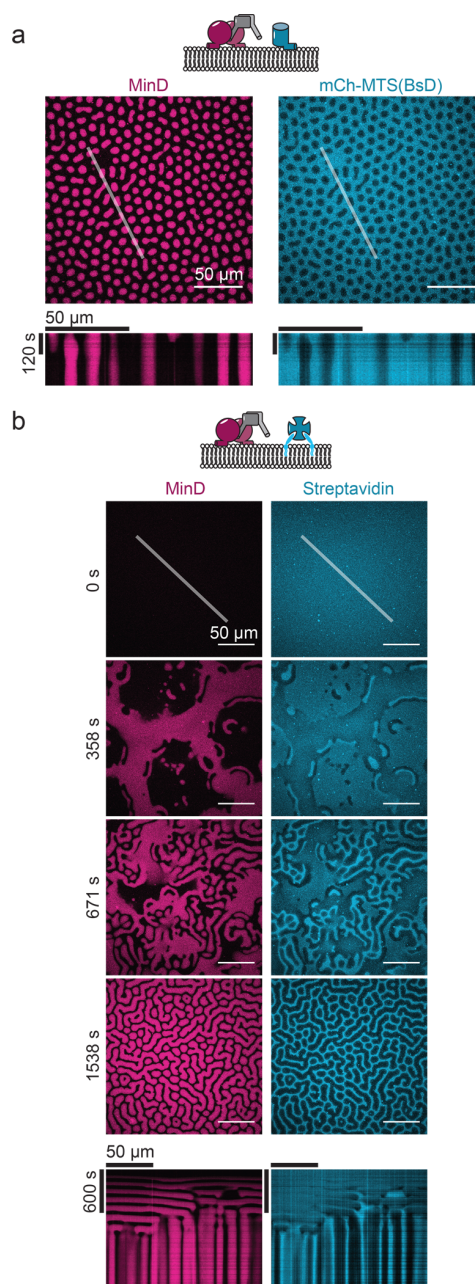


Figure 6. MinD and MinE-His are able to spatiotemporally regulate model peripheral and lipid-anchored proteins. (a) MinDE spot patterns formed with MinE-His exclude the model peripheral membrane protein mCh-MTS(BsD) ($0.75 \mu\text{M}$ MinD (30% eGFP-MinD). $2 \mu\text{M}$ MinE-His, $1 \mu\text{M}$ mCh-MTS(BsD)). Kymographs of the respective line selection. (b) MinDE static patterns formed in the presence of MinE-His are spatiotemporally regulating lipid-anchored streptavidin, forming a static inverse streptavidin pattern. Time-series of the establishment of MinDE labyrinth pattern and inverse streptavidin pattern ($1 \mu\text{M}$ MinD (30% eGFP-MinD); $2 \mu\text{M}$ MinE-His, Alexa647-Streptavidin, 69 mol % DOPC/30 mol % DOPG/1 mol % Biotinyl-CAP-PE). Kymograph along the line selection shown at time = 0 s.

are rendered sparse by adding more MinE-His (Figure S9). These new stationary patterns could be used for example to anchor polymerizing or depolymerizing factors for cytoskeletal proteins like actin or tubulin onto model membranes to create

new active systems. Another interesting experiment would be to tether any component essential for protein production to the MinD foci and thereby locally produce proteins *via* cell-free protein production.

Early experiments on mica as a support showed static patterns with His-MinE under certain conditions. These were not further investigated, however.⁹ It is puzzling also to us that the spectrum of intriguing patterns observed with MinE-His has not been reported before, but we have to assume that researchers using similar (large available bulk volume) setups previously tested MinE-His only under conditions of (effectively) low MinD concentration, where it forms traveling waves as observed with His-MinE. In the original paper's supplement, MinE-His is mentioned in that exact context, and no difference to His-MinE was found.⁹ Similarly, Vecchiarelli *et al.* find that MinE-His forms traveling waves in their flow-cell setup, likely because the bulk height or the total protein amounts are more limited.¹² This once again highlights how easily discoveries are overlooked and how important it is to test reconstituted systems under multiple conditions. This is particularly important in the case of self-organizing reaction-diffusion networks that are inherently sensitive to changes in parameter values due to the underlying nonlinearity of the molecular interactions. Overall, as also indicated by Figure 3, we are confident that under traveling wave conditions, MinE-His, His-MinE, and MinE-wt show similar characteristics, which validates our past results for the dynamic Min system.

The reported static patterns are unlikely to play a major role for the Min system in live *E. coli*. However, there are many Gram-positive bacteria, such as *B. subtilis*, that contain a static Min system^{29,30} that in the light of our results might also form their patterns through a highly dynamic reaction-diffusion mechanism tuned to yield a quasi-static protein distribution. Additionally, static Min patterns show multiple aspects of relevance:

First, their existence is proof of the big versatility of biological reaction-diffusion systems. On the basis of relatively simple physical principles and very few components, they can regulate complex tasks efficiently, while forming entirely different patterns in another context. This, in turn, highlights how important not just the concentration of a protein can become, but also the total available bulk volume, and thus particle number within an enclosure. Positive feedback in MinD recruitment amplifies this effect.

Second, the emergence of static patterns significantly enlarges the functionality toolbox provided by the Min system, making it more attractive for research on reaction-diffusion mechanisms and to use it for designing spatiotemporal cues in bottom-up synthetic biology. Requiring only two proteins, ATP and a membrane makes the system easily accessible, and naturally limits the complexity of mathematical models. Experimentalists interested in pattern formation have so far mostly turned to chemical reactions, like the Belousov-Zhabotinsky or the chloride-iodide-malonic-acid (CIMA) reaction. Both involve too many components and intermediates to hope for comprehensive modeling or simulating full complexity. In contrast the Min system is truly biological and therefore biocompatible, the proteins can be engineered in countless ways, and the reaction runs stably for many hours, even days without buffer exchanges. Intentional disturbances (example in Movie S4) can be introduced *via* a recently published photoswitch.²⁸ With this in mind, we have recently increased our efforts to make this versatile system available to

other researchers by sharing all plasmids and detailed protocols.³¹

METHODS

Plasmid Design and Cloning. pET28a-MinE-His, pET28a-MinE-His(Δ MTS), pET28a-MinE-KCK-His and pET28a-His-KCK-MinD were generated *via* homologous recombination in *E. coli*. For more details on the cloning procedure, including primers and all *in vivo* plasmids, please refer to the Supporting Information. A plasmid map for pET28a-His-MinE has recently been published.³¹

Proteins were expressed and purified as published previously.³¹ Expression of His-SUMO-MinE was done similarly, but protein in elution buffer (50 mM Tris-HCl pH 8, 300 mM NaCl, 250 mM imidazole, 10% glycerol, 10 mM 2-mercaptoethanol, EDTA-free protease inhibitor) was dialyzed against final storage buffer (50 mM HEPES pH 7.25, 150 mM KCl, 10% glycerol, 0.1 mM EDTA) while adding 1:100 parts of SUMO protease (His6-SenP2). Protease and cleaved tag were removed by adding excess Ni-NTA Agarose beads, incubating for 1–2 h on a rotating shaker at 4 °C and taking the supernatant.

Protein Concentration Measurements. Protein concentrations were all determined *via* a linearized, improved Bradford assay, as described here.³² Measurements were done in 96-well plates, and triplicates of each measured concentration were taken. A minimum of two different dilutions of the same protein stock were measured. Concentration determination of multiple proteins was done in the same assay where critical for comparison (all the MinE proteins used for ATPase rate comparison in Figure 4b).

Labeling and Determination of Degree of Labeling. Labeling of Min proteins was performed according to the dye manufacturer's instructions. A ratio of 3:1 dye to protein was found sufficient to achieve the desired labeling efficiency. A PD-10 buffer exchange column was used to remove most of the unbound dye, followed by overnight dialysis against excess storage buffer.

Cleaning of Coverslips. Twenty-four \times 24 mm #1.5 coverslips (obtained from Menzel) were piranha cleaned by adding 7 drops of sulfuric acid plus two drops of 50% hydrogen peroxide to the center of each coverslip. The reaction was incubated on the coverslips for at least 45 min before thoroughly rinsing with ultrapure water. For experiments showing the positioning of membrane proteins by MinDE the coverslips were plasma-cleaned with oxygen as a process gas instead of piranha-cleaning.

Assay Chamber Assembly. The bottom half and lid of 0.5 mL reaction tubes were cut off with sharp scissors. UV-glue (Norland optical adhesive #68) was applied with a pipet tip to the upper rim of the tube. The tube was then glued upside down onto the clean coverslip and cured under a UV lamp (365 nm) for 10 min.

Lipid Preparation. DOPC and DOPG as well as *E. coli* polar lipid extract (EPL) were obtained from Avanti and dissolved in chloroform at 25 mg/mL. Lipids were mixed in a 1.5 mL glass vial and the lipid film was dried on the lower rim of the glass under a slight nitrogen stream. The lipid film was further dried by applying vacuum for at least 1 h. Dried lipid films were rehydrated in Min buffer (150 mM KCl, 25 mM Tris-HCl pH 7.5, 5 mM MgCl₂) at 4 mg/mL by vortexing, then further processed by freeze-thawing for 8–10 cycles in liquid nitrogen/90 °C hot water. The obtained unilamellar

vesicles were extruded through a membrane with 50 nm pore size for 37 passes. EPL vesicles were prepared as described previously.¹⁷ Vesicles were then used, stored in the fridge for up to 2 weeks or frozen in liquid nitrogen, in which case they were briefly sonicated before use.

SLB Formation. Vesicles were diluted by adding 130 μL of Min buffer to a 20 μL aliquot of clear lipids at 4 mg/mL. 75 μL of this mixture were added to a chamber situated on a heat block at 37 °C. After 1 min, 150 μL of Min buffer was added. After 2 min (total time: 3 min), chambers were washed by adding 200 μL of prewarmed Min buffer, mixing a few times and removing 200 μL into liquid waste. This procedure was repeated until 2 mL of buffer per chamber had been used up. Washed SLB chambers were transferred from 37 °C to room temperature. For experiments shown in Figure S5, cover slides were piranha cleaned as above, and SLBs then prepared as described.¹⁷

PDMS Microstructures. PDMS microstructures were prepared as previously described.¹⁵ For a more detailed protocol including a wafer blueprint please refer to a more recent publication.³¹

Microscopy. Images were acquired on a commercial Zeiss LSM 780 microscope with Zeiss 40 \times W NA 1.2 Plan-Apochromat objective and 10 \times objectives. All live-cell images were taken on a custom-built TIRFM (total internal reflection fluorescence microscopy) setup as described.²⁸

Image Manipulations (FIJI). Microscopic images used in the figures and videos presented in the main text and Supporting Information were adjusted for brightness and contrast, and if necessary for presentation merged from two separately or concurrently recorded channels (e.g., MinD and MinE in Figure 1, MinD and membrane binders in Figure 6).

Spatiotemporal Regulation of Peripheral and Lipid-Anchored Proteins by MinDE. Experiments were performed as described.²⁶ In short, SLBs were formed with 70%/30% DOPC/DOPG and in case of streptavidin with 1% Biotinyl-CAP-PE. For experiments with peripheral membrane proteins MinD and MinE-His with 1 μM mCh-MTS(BsD) were incubated on SLBs for 1 h before image acquisition. For lipid-anchored streptavidin, streptavidin was bound to Biotinyl-CAP-PE SLBs, and excess streptavidin was removed by washing with buffer. The self-organization of MinDE was started by addition of ATP and a time-series was acquired.

Acquisition and analysis of QCMD data are described in the Supporting Methods.

ATPase Assay, NADH Coupled. ATPase rate was measured in an NADH-coupled assay, whereby the decrease in NADH concentration is monitored, and ATP concentration stays constant. To achieve this, phosphoenolpyruvate (PEP) (2 mM) and NADH (0.5 mM) were added to the proteins (all at 2 μM) in Min buffer (25 mM Tris-HCl pH 7.5, 150 mM KCl, 5 mM MgCl_2). Vesicles at 50 nm diameter (via extrusion) were added at a final concentration of 0.2 mg/mL. Additionally, 4.5 μL per well of a commercial enzyme mix containing pyruvate kinase (600–1000 U/mL) and lactate dehydrogenase (1000–1400 U/mL) were added to facilitate the reaction of ADP with PEP to pyruvate and ATP, and the reduction of pyruvate using NADH to L-lactate and NAD^+ . A 96-well plate format at 150 μL assay volume was used to measure all conditions concurrently and in triplicates. Decrease in absorption at 340 nm was measured to calculate the ATPase activity. NADH decomposition due to reasons other than ATPase activity was measured each time in control wells and

subtracted from the apparent ATPase rates. Only the linear parts of the measured values were used to obtain the ATPase rate. Note: ATPase rates reported here should only be interpreted as a relative comparison between MinE constructs. There is a large batch-to-batch variation in MinD's ATPase activity.

Bacterial Transformation and Agar Pads for Microscopy, Imaging. Live-cell imaging was performed with strain HL1 ($\Delta\text{minDE zcf117::Tn10 recA::cat}$).³³ HL1 was transformed with the plasmids pMLB_sfGFP_MinDMinE, pMLB_sfGFP-MinD N-His-linker MinE and pMLB_sfGFP-MinD MinE. Cells were inoculated from glycerol stocks and grown overnight in LB medium supplemented with ampicillin and tetracycline for 14–16 h at 37 °C and 270 rpm. Subsequently cells were diluted 1:200 in 20 mL fresh M9 medium (1 \times Gibco M9 minimal Salts (Thermo Fisher Scientific, Waltham, USA), 0.2% casamino acids (Amresco, Solon, Ohio), 0.4% glycerol, 2 mM MgSO_4 , 0.1 mM CaCl_2) supplemented with ampicillin and grown at 37 °C. When the cells reached an OD600 of \sim 0.1, MinD and MinE expression was induced by addition of 50 μM IPTG. Cell were grown for another 2–3 h until they reached an OD600 of \sim 0.3. They were then diluted in fresh M9 medium to an OD600 of 0.1 and 1 μL of the cell suspension was spotted on agar pads and dried for at least 20 min at room temperature, before the agar pads were flipped onto a glass-bottom dish (ibidi), that was lidded for imaging. Imaging settings and time intervals were optimized for each strain to acquire the maximum amount of oscillations with least bleaching.

Twenty-two by 22 mm coverslips were cleaned with 99% ethanol and ddH_2O . For preparation of agarose pads M9 media with 1.5% (w/v) UltraPure Low Melting Point Agarose (Life Technologies, Carlsbad, CA) was heated in the microwave and then allowed to cool before addition of the appropriate antibiotics and 50 μM IPTG. 800 μL of the liquid agarose mixture was pipetted onto a 22 by 22 mm coverslip positioned on a dime. Another coverslip was immediately placed on top yielding an evenly thick agarose coverslip sandwich. Pads were covered and left to solidify at room temperature for about 60 min. The top coverslip was removed and the pad was cut into 16 evenly sized, squared pads with a razor blade.

Analysis of bacterial oscillations using MicrobeTracker³⁴ and MATLAB is described in the Supporting Information.

■ ASSOCIATED CONTENT

📄 Supporting Information

The Supporting Information is available free of charge on the ACS Publications website at DOI: 10.1021/acssynbio.8b00415.

Figures S1–S13; Tables S1 and S2; Supporting Methods (PDF)

Movie S1 (AVI)

Movie S2 (AVI)

Movie S3 (AVI)

Movie S4 (AVI)

Movie S5 (AVI)

Movie S6 (AVI)

■ AUTHOR INFORMATION

Corresponding Author

*E-mail: schwille@biochem.mpg.de.

ORCID 

Philipp Glock: 0000-0002-0238-2634

Beatrice Ramm: 0000-0002-7402-1942

Tamara Heermann: 0000-0003-1607-0727

Jonas Mücksch: 0000-0002-1469-6956

Petra Schwille: 0000-0002-6106-4847

Author Contributions

P.G. and P.S. conceived the study, P.G. wrote the initial draft, P.G. performed self-organization assays generating data for phase diagrams and microscopy images and performed ATPase assays, B.R. and P.G. performed experiments regarding spatiotemporal regulation and reaction confinement in rod-shaped microcompartments, B.R. performed experiments concerning regulation of other membrane-bound proteins by Min reaction, S.K. performed self-organization assays on *E. coli* polar lipids, G.A. and B.R. performed *in vivo* experiments, T.H. performed QCM-D experiments and J.M. and T.H. analyzed QCM-D data, J.S. analyzed *in vivo* data, and P.G., B.R., T.H., S.K., and P.S. discussed and interpreted the results. All authors revised the manuscript.

Notes

The authors declare no competing financial interest.

ACKNOWLEDGMENTS

We would like to thank Core Facility MPIB for help with protein purifications, Katharina Nakel for assistance with cloning, Philipp Blumhardt for assistance with live-cell imaging, Anthony Vecchiarelli for sharing plasmid maps, and Piet de Boer for providing strain HL1 and plasmid pDR122. P.G. acknowledges support from the DFG-funded GRK2062 “Molecular principles of synthetic biology”. P.G. and J.M. are part of IMPRS-LS. We acknowledge further financial support from the DFG via the Graduate School of Quantitative Biosciences Munich (QBM) (S.K. and B.R.) and the project A09 of the SFB1032 “Nanoagents for the spatiotemporal control of molecular and cellular reactions” (S.K., T.H., and P.S.).

REFERENCES

- (1) Kondo, S., Iwashita, M., and Yamaguchi, M. (2009) How Animals Get Their Skin Patterns: Fish Pigment Pattern as a Live Turing Wave. *Int. J. Dev. Biol.* 53 (5–6), 851–856.
- (2) Economou, A. D., Ohazama, A., Porntaveetus, T., Sharpe, P. T., Kondo, S., Basson, M. A., Gritli-Linde, A., Cobourne, M. T., and Green, J. B. A. (2012) Periodic Stripe Formation by a Turing Mechanism Operating at Growth Zones in the Mammalian Palate. *Nat. Genet.* 44 (3), 348–351.
- (3) Sheth, R., Marcon, L., Bastida, M. F., Junco, M., Quintana, L., Dahn, R., Kmita, M., Sharpe, J., and Ros, M. A. (2012) Hox Genes Regulate Digit Patterning by Controlling the Wavelength of a Turing-Type Mechanism. *Science* 338 (6113), 1476–1480.
- (4) Raskin, D. M., and de Boer, P. a. (1999) Rapid Pole-to-Pole Oscillation of a Protein Required for Directing Division to the Middle of *Escherichia Coli*. *Proc. Natl. Acad. Sci. U. S. A.* 96 (9), 4971–4976.
- (5) Szeto, T. H., Rowland, S. L., Habrukowich, C. L., and King, G. F. (2003) The MinD Membrane Targeting Sequence Is a Transplantable Lipid-Binding Helix. *J. Biol. Chem.* 278 (41), 40050–40056.
- (6) Park, K. T., Wu, W., Battaile, K. P., Lovell, S., Holyoak, T., and Lutkenhaus, J. (2011) The Min Oscillator Uses MinD-Dependent Conformational Changes in MinE to Spatially Regulate Cytokinesis. *Cell* 146 (3), 396–407.
- (7) Halatek, J., and Frey, E. (2012) Highly Canalized MinD Transfer and MinE Sequestration Explain the Origin of Robust MinCDE-Protein Dynamics. *Cell Rep.* 1 (6), 741–752.
- (8) Halatek, J., and Frey, E. (2018) Rethinking Pattern Formation in Reaction–diffusion Systems. *Nat. Phys.* 14 (5), 507–514.
- (9) Loose, M., Fischer-Friedrich, E., Ries, J., Kruse, K., and Schwille, P. (2008) Spatial Regulators for Bacterial Cell Division Self-Organize into Surface Waves *In Vitro*. *Science* 320 (5877), 789–792.
- (10) Lackner, L. L., Raskin, D. M., and De Boer, P. a. J. (2003) ATP-Dependent Interactions between *Escherichia Coli* Min Proteins and the Phospholipid Membrane *In Vitro*. *J. Bacteriol.* 185 (3), 735–749.
- (11) Denk, J., Kretschmer, S., Halatek, J., Hartl, C., Schwille, P., and Frey, E. (2018) MinE Conformational Switching Confers Robustness on Self-Organized Min Protein Patterns. *Proc. Natl. Acad. Sci. U. S. A.* 115 (18), 4553–4558.
- (12) Vecchiarelli, A. G., Li, M., Mizuuchi, M., and Mizuuchi, K. (2014) Differential Affinities of MinD and MinE to Anionic Phospholipid Influence Min Patterning Dynamics *In Vitro*. *Mol. Microbiol.* 93 (3), 453–463.
- (13) Schweizer, J., Loose, M., Bonny, M., Kruse, K., Monch, I., and Schwille, P. (2012) Geometry Sensing by Self-Organized Protein Patterns. *Proc. Natl. Acad. Sci. U. S. A.* 109 (38), 15283–15288.
- (14) Caspi, Y., and Dekker, C. (2016) Mapping out Min Protein Patterns in Fully Confined Fluidic Chambers. *eLife* 5, 1–27.
- (15) Zieske, K., and Schwille, P. (2013) Reconstitution of Pole-to-Pole Oscillations of Min Proteins in Microengineered Polydimethylsiloxane Compartments. *Angew. Chem., Int. Ed.* 52 (1), 459–462.
- (16) Vecchiarelli, A. G., Li, M., Mizuuchi, M., Hwang, L. C., Seol, Y., Neuman, K. C., and Mizuuchi, K. (2016) Membrane-Bound MinDE Complex Acts as a Toggle Switch That Drives Min Oscillation Coupled to Cytoplasmic Depletion of MinD. *Proc. Natl. Acad. Sci. U. S. A.* 113 (11), E1479–E1488.
- (17) Kretschmer, S., Zieske, K., and Schwille, P. (2017) Large-Scale Modulation of Reconstituted Min Protein Patterns and Gradients by Defined Mutations in MinE’s Membrane Targeting Sequence. *PLoS One* 12, 1–16.
- (18) Ivanov, V., and Mizuuchi, K. (2010) Multiple Modes of Interconverting Dynamic Pattern Formation by Bacterial Cell Division Proteins. *Proc. Natl. Acad. Sci. U. S. A.* 107 (18), 8071–8078.
- (19) Turing, A. M. (1952) The Chemical Basis of Morphogenesis. *Philos. Trans. R. Soc. B Biol. Sci.* 237 (641), 37–72.
- (20) Kondo, S., and Miura, T. (2010) Reaction-Diffusion Model as a Framework for Understanding Biological Pattern Formation. *Science* 329 (5999), 1616–1620.
- (21) Wu, F., Halatek, J., Reiter, M., Kingma, E., Frey, E., and Dekker, C. (2016) Multistability and Dynamic Transitions of Intracellular Min Protein Patterns. *Mol. Syst. Biol.* 12 (6), 873.
- (22) Ayed, S. H., Cloutier, A. D., McLeod, L. J., Foo, A. C. Y., Damry, A. M., and Goto, N. K. (2017) Dissecting the Role of Conformational Change and Membrane Binding by the Bacterial Cell Division Regulator MinE in the Stimulation of MinD ATPase Activity. *J. Biol. Chem.* 292 (50), 20732–20743.
- (23) Park, K.-T., Villar, M. T., Artigues, A., and Lutkenhaus, J. (2017) MinE Conformational Dynamics Regulate Membrane Binding, MinD Interaction, and Min Oscillation. *Proc. Natl. Acad. Sci. U. S. A.* 114 (29), 7497–7504.
- (24) Loose, M., Fischer-Friedrich, E., Herold, C., Kruse, K., and Schwille, P. (2011) Min Protein Patterns Emerge from Rapid Rebinding and Membrane Interaction of MinE. *Nat. Struct. Mol. Biol.* 18 (5), 577–583.
- (25) Zieske, K., and Schwille, P. (2014) Reconstitution of Self-Organizing Protein Gradients as Spatial Cues in Cell-Free Systems. *eLife* 3, 1–19.
- (26) Ramm, B., Glock, P., Mücksch, J., Blumhardt, P., García-Soriano, D. A., Heymann, M., and Schwille, P. (2018) The MinDE System Is a Generic Spatial Cue for Membrane Protein Distribution *In Vitro*. *Nat. Commun.* 9 (1), 3942.
- (27) Raskin, D. M., and de Boer, P. a. (1997) The MinE Ring: An FtsZ-Independent Cell Structure Required for Selection of the Correct Division Site in *E. Coli*. *Cell* 91 (5), 685–694.
- (28) Glock, P., Broichhagen, J., Kretschmer, S., Blumhardt, P., Mücksch, J., Trauner, D., and Schwille, P. (2018) Optical Control of a

Biological Reaction-Diffusion System. *Angew. Chem., Int. Ed.* 57 (9), 2362–2366.

(29) Edwards, D. H., and Errington, J. (1997) The Bacillus Subtilis DivIVA Protein Targets to the Division Septum and Controls the Site Specificity of Cell Division. *Mol. Microbiol.* 24 (5), 905–915.

(30) Bramkamp, M., Emmins, R., Weston, L., Donovan, C., Daniel, R. A., and Errington, J. (2008) A Novel Component of the Division-Site Selection System of Bacillus Subtilis and a New Mode of Action for the Division Inhibitor MinCD. *Mol. Microbiol.* 70 (6), 1556–1569.

(31) Ramm, B., Glock, P., and Schwille, P. (2018) In Vitro Reconstitution of Self-Organizing Protein Patterns on Supported Lipid Bilayers. *J. Visualized Exp.* No. 137, e58139.

(32) Ernst, O., and Zor, T. (2010) Linearization of the Bradford Protein Assay. *J. Visualized Exp.* No. 38, 1–6.

(33) Hale, C. A., Meinhardt, H., and de Boer, P. A. (2001) Dynamic Localization Cycle of the Cell Division Regulator MinE in Escherichia Coli. *EMBO J.* 20 (7), 1563–1572.

(34) Sliusarenko, O., Heinritz, J., Emonet, T., and Jacobs-Wagner, C. (2011) High-Throughput, Subpixel Precision Analysis of Bacterial Morphogenesis and Intracellular Spatio-Temporal Dynamics. *Mol. Microbiol.* 80 (3), 612–627.

Supplementary Information for

Stationary patterns in a two-protein reaction-diffusion system

Philipp Glock, Beatrice Ramm, Tamara Heermann, Simon Kretschmer, Jakob Schweizer, Jonas Mücksch, Gökberk Alagöz,
Petra Schwille

Petra Schwille

E-mail: schwille@biochem.mpg.de

This PDF file includes:

Supplementary Methods and Materials

Figs. S1 to S13

Tables S1 to S2

Captions for Movies S1 to S6

References for SI

Supporting Information Text
Supplementary Figures.

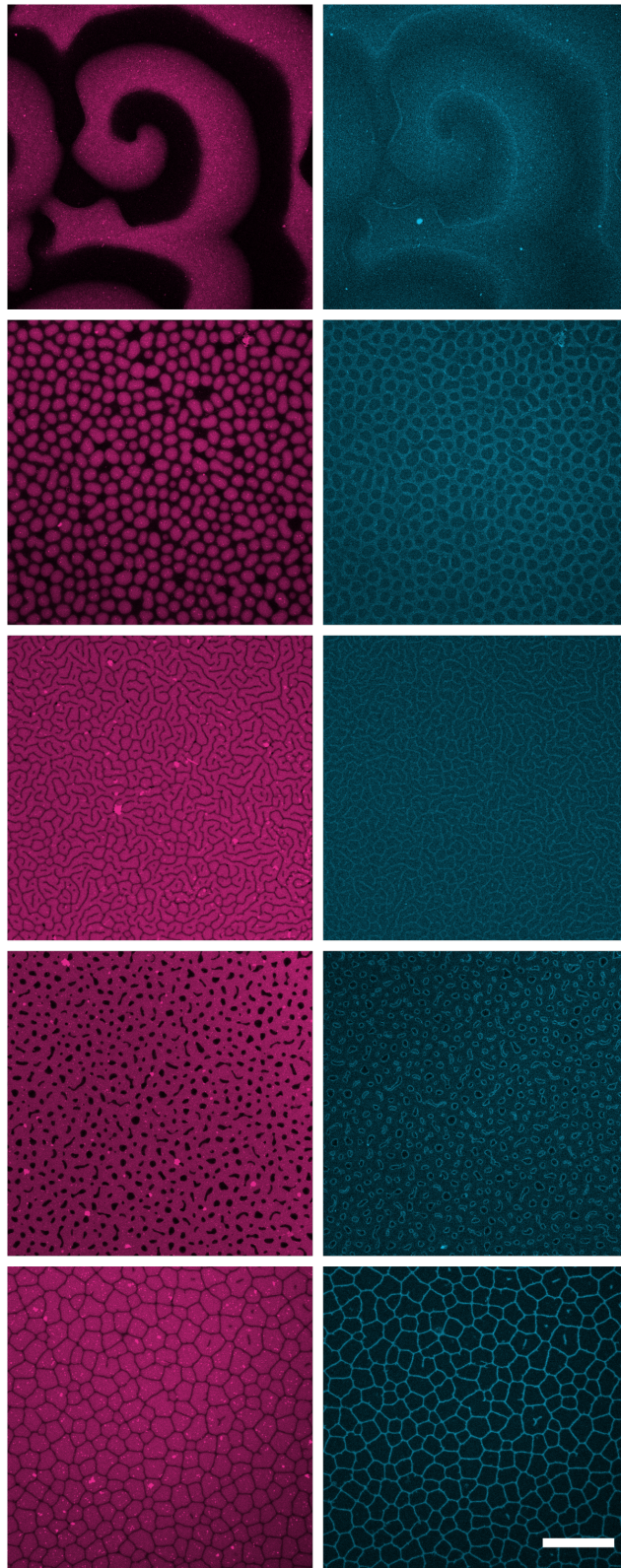


Fig. S1. MinD and MinE-His show differential distributions on the membrane From top to bottom, each MinD distribution is presented next to the corresponding fluorescence recorded for MinE-His. Travelling waves, observed at 0.5 μM MinD, 1.2 μM MinE-His. Spots, here at 1.3 μM MinD, 4 μM MinE-His. Labyrinth (1.25 μM MinD, 2.5 μM MinE-His). Inverse spots (0.5 μM MinD, 0.125 μM MinE-His). MinE-mesh (1.5 μM MinD, 3 μM MinE-His). (Scale bar: 50 μm , MinD: magenta, MinE-His: cyan, proteins were fluorescently labelled by doping MinD with 30 percent Alexa647-KCK-MinD and MinE-His with 30 percent Atto488-KCK-MinE-His)

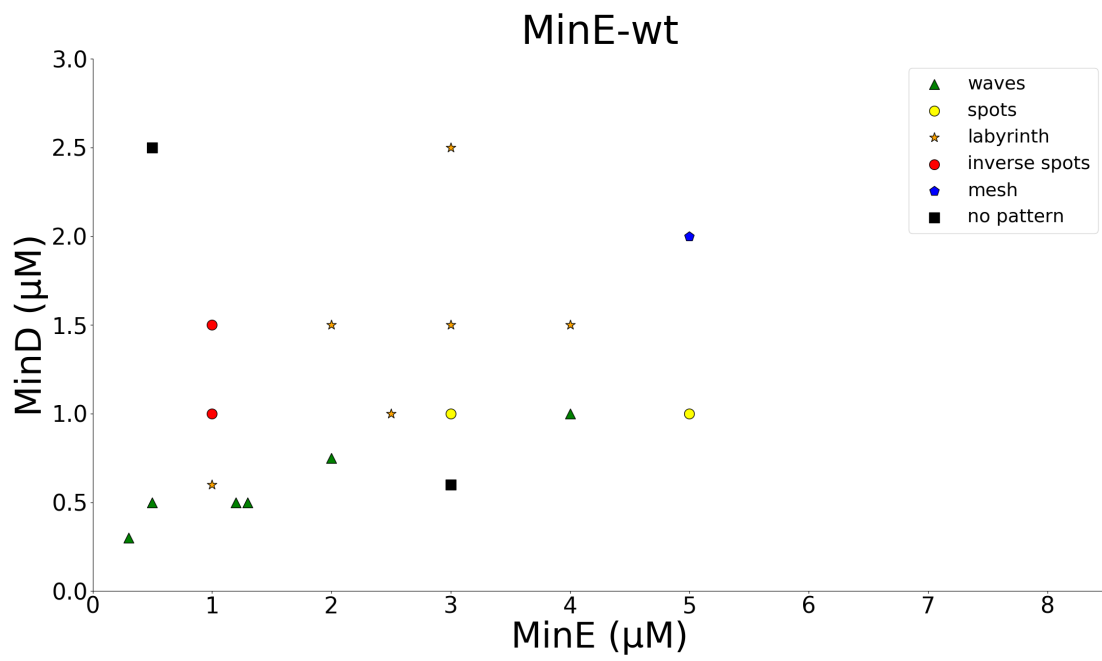


Fig. S2. Phase diagram for MinE-wt. Data points depict single observations.

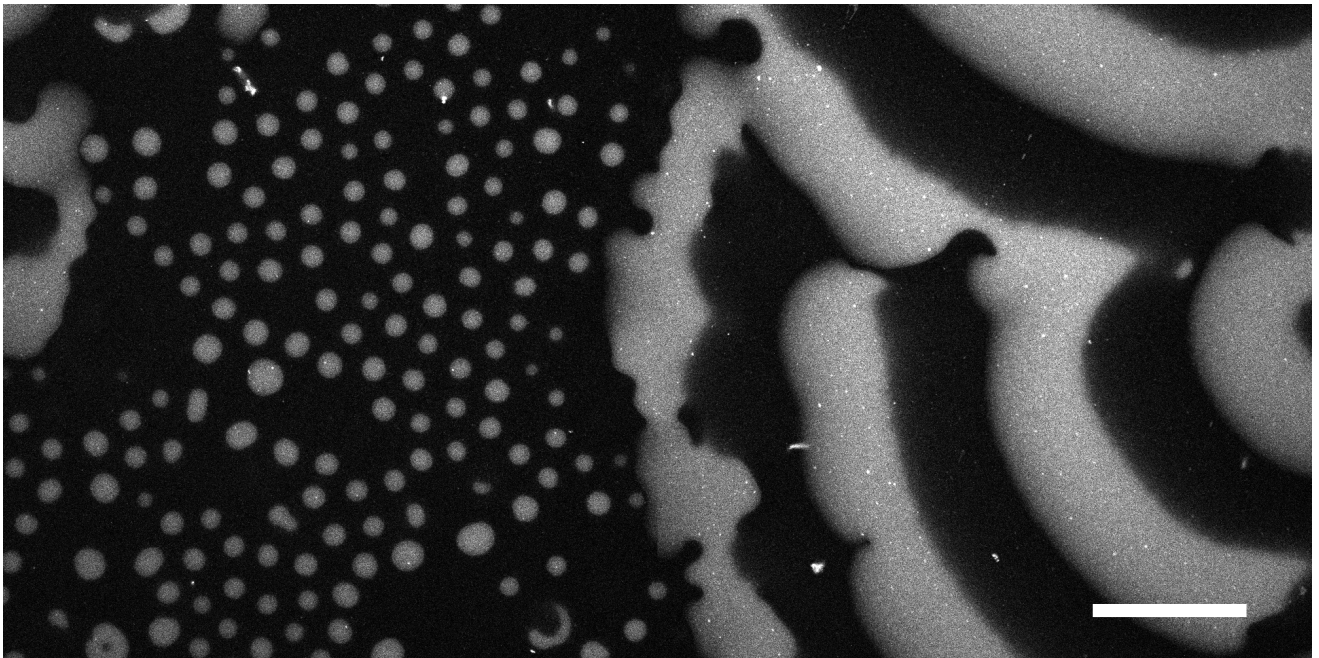


Fig. S3. Spots and waves coexist within the same experiment Two adjacent field of views, stitched together from a bigger tilescan, are shown. 1 μM MinD (doped with 30% Alexa647-KCK-MinD), 4 μM MinE-His, scalebar 50 μm

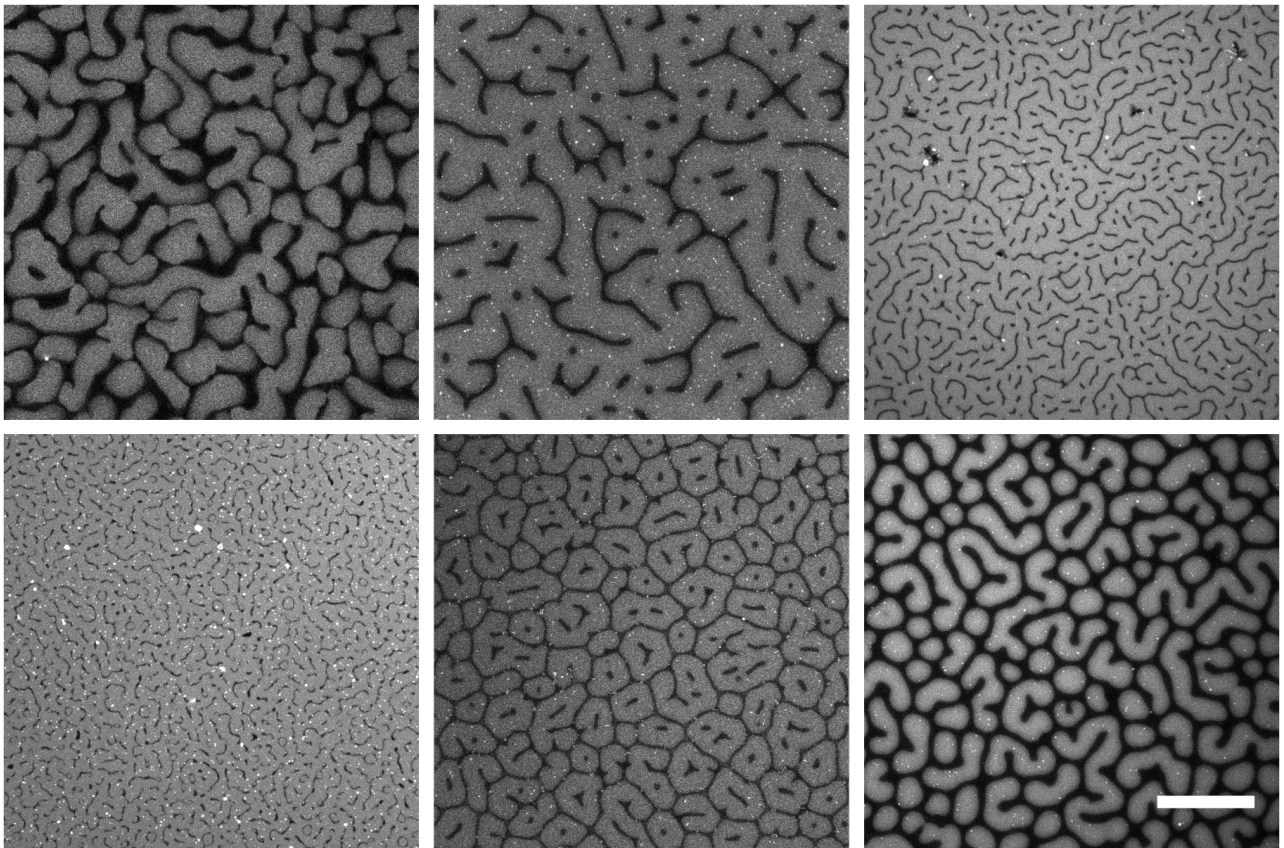


Fig. S4. : Intermediate patterns between the named patterns in Figure 1 are often observed. top left: 0.5 μM MinD, 0.5 μM MinE-His. top middle: 0.5 μM MinD, 0.5 μM MinE-His. top right: 1 μM MinD, 1 μM MinE-His. bottom left: 1 μM MinD, 1 μM MinE-His. bottom middle: 1 μM MinD, 2 μM MinE-His. bottom right: 1 μM MinD, 2.5 μM MinE-His. (scalebar: 50 μm , same scale for all images. MinD doped with 30% Alexa647-KCK-MinD)

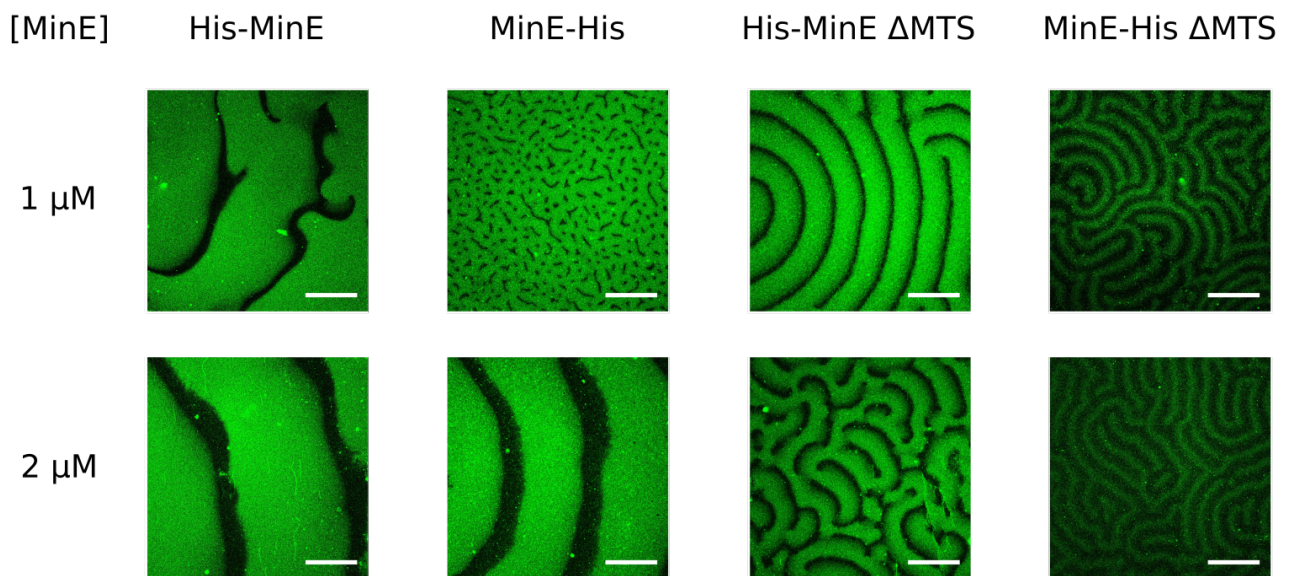


Fig. S5. MinE-His forms static patterns also on *E. coli* polar lipid extract (second panel). Deleting the entire membrane targeting sequence reveals additional differences between His-MinE and MinE-His. Microscopy images of self-organization assays containing 1 μ M MinD, doped with 20% eGFP-MinD and 1 μ M or 2 μ M of the indicated MinE proteins. (scalebars: 50 μ m)

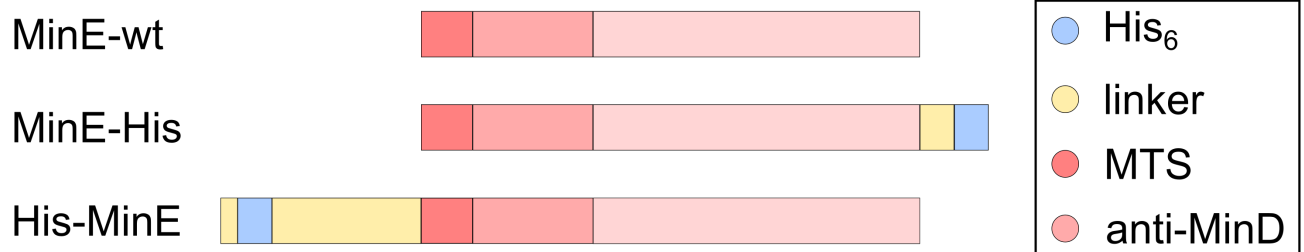


Fig. S6. His-MinE carries a disproportionately large linker at the N-terminus. Schematic representation of the MinE proteins used in this publication. The length of each section corresponds to the number of amino acids present in the protein primary structure. Total length of MinE-wt is 87 AA, MinE-His 99 AA, His-MinE 123 AA.

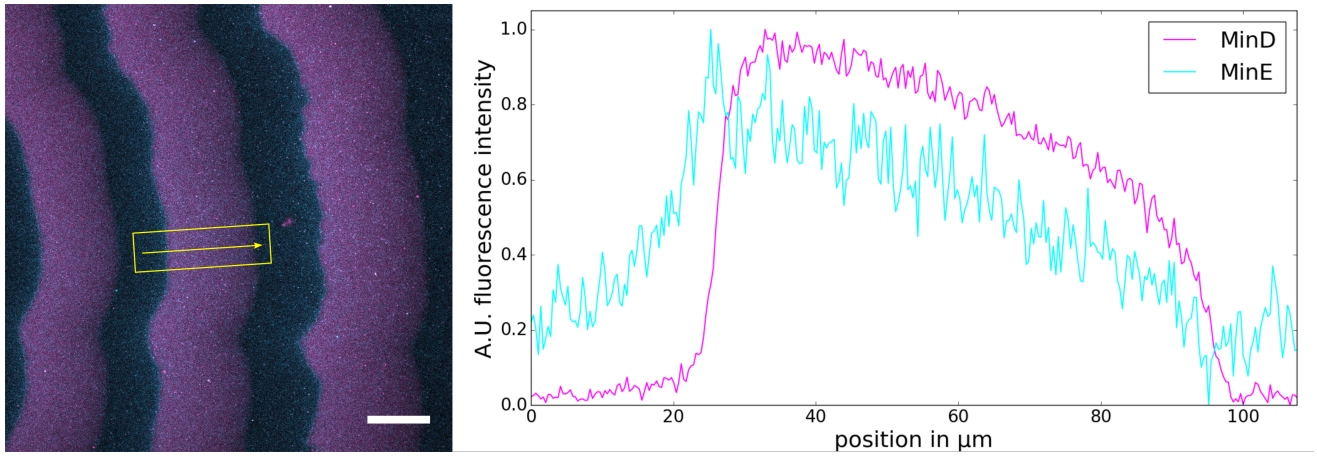


Fig. S7. Wave profiles of travelling Min waves with MinE-His look similar to wave profiles with His-MinE. Plotted on the right is the fluorescence intensity normalized to the maximal value of the selection marked on the left. MinE-His, like previously shown for His-MinE, accumulates over the course of a travelling wave and reaches its maximum after MinD intensity drops. (scalebar: 50 μm)

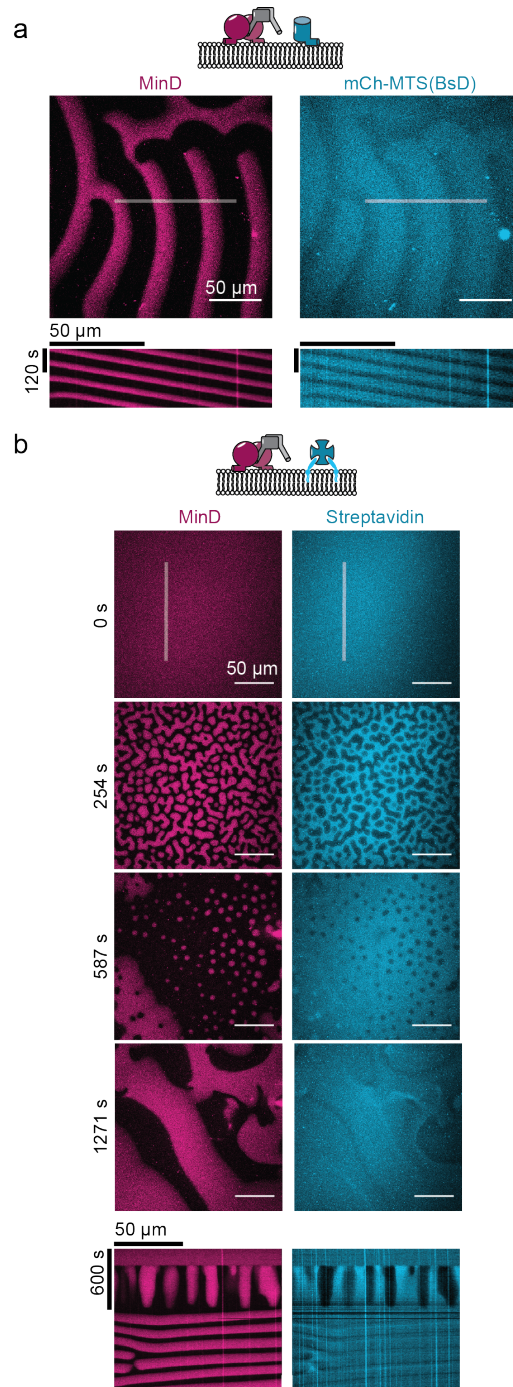


Fig. S8. MinD and MinE-His waves are able to spatiotemporally regulate model peripheral and lipid-anchored proteins. a) MinDE waves formed with MinE-His exclude the model peripheral membrane protein mCh-MTS(BsD) (0.5 μM MinD (30% EGFP-MinD), 1 μM MinE-His, 1 μM mCh-MTS(BsD)). Kymographs of the respective line selection. b) MinDE waves formed in the presence of MinE-His spatiotemporally regulate lipid-anchored streptavidin. Time-series of the establishment of MinDE waves and inverse streptavidin patterns (0.75 μM MinD (30% EGFP-MinD), 2 μM MinE-His, Alexa647-Streptavidin, 69 mol% DOPC/ 30 mol % DOPG/1 mol % Biotinyl-CAP-PE). Kymograph along the line selection shown at time = 0 s.

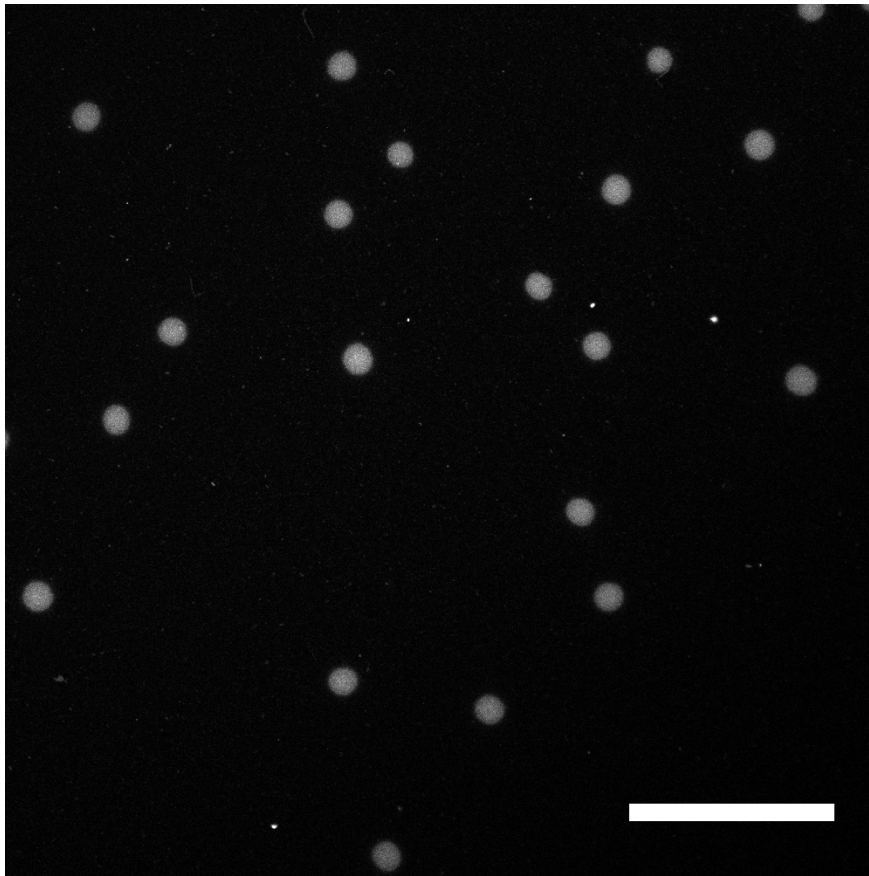


Fig. S9. Reaction-diffusion pattern formed by MinD and MinE-His at high MinE concentration (1 μM MinD, doped with 30% Alexa647-KCK-MinD, 7 μM MinE-His). This sparse spots pattern could become useful in positioning proteins or molecules of interest for in vitro experiments, creating distinct foci. (scalebar: 50 μm)

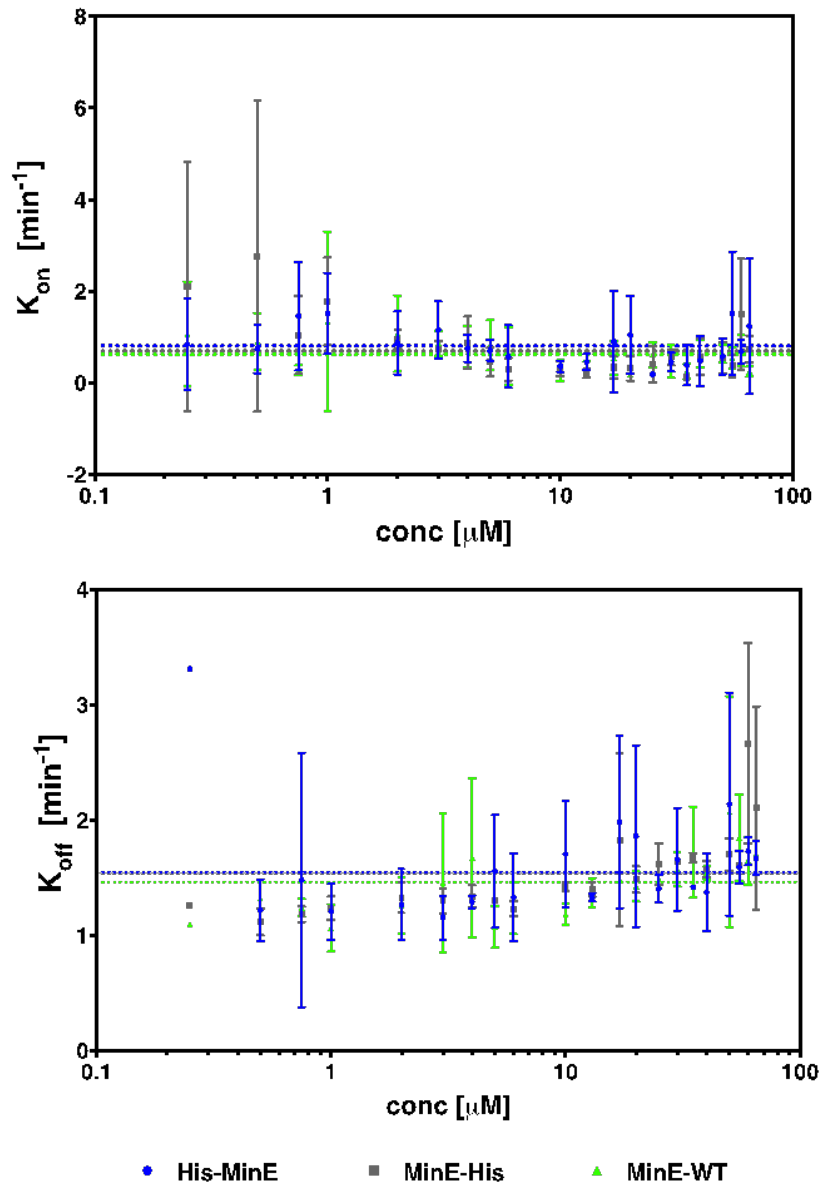


Fig. S10. Scatter plot depicting mean ($n=3$) K_{off} and K_{on} values \pm SD as determined in our QCM-D experiments, in relation to the concentration of His-MinE (blue circles), MinE-His (grey squares) or MinE WT (green triangle). The mean value of K_{off} and K_{on} over the whole concentration range, is depicted as dotted line in the representative color of every construct.

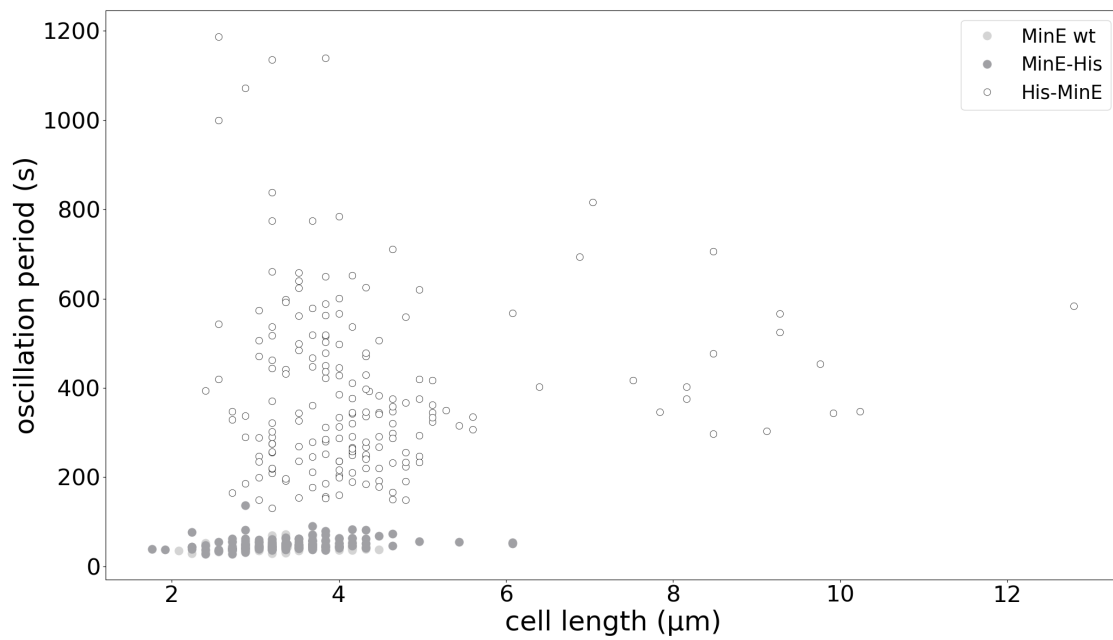


Fig. S11. *In vivo* oscillation periods at room temperature relative to cell length induced by the different MinEs and superfolder GFP-MinD when expressed in $\Delta(\text{minDE})$ background under IPTG induction. The complete plot containing number of cells: MinE wt (n=104), MinE-His (n=143) and His-MinE (n=189) is shown with all outliers.

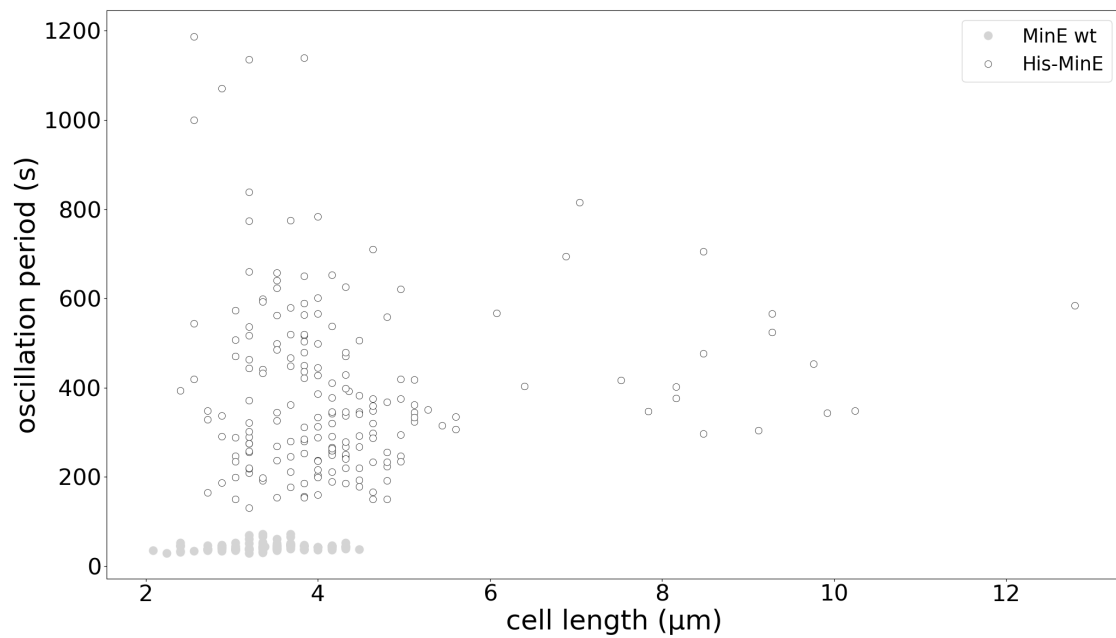


Fig. S12. *In vivo* oscillation periods at room temperature relative to cell length induced by the different MinEs and superfolder GFP-MinD when expressed in delta(minDE) background under IPTG induction. Only MinE wt (n=104) and His-MinE (n=189) are shown with all their outliers, while MinE-His has been separately plotted in Supplementary Figure 13.

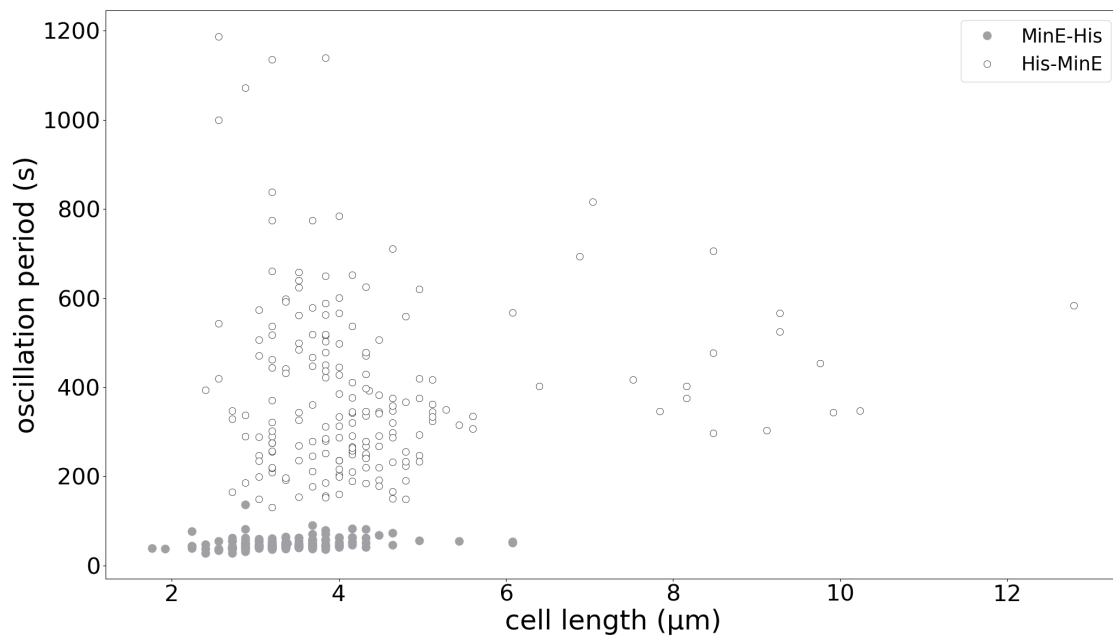


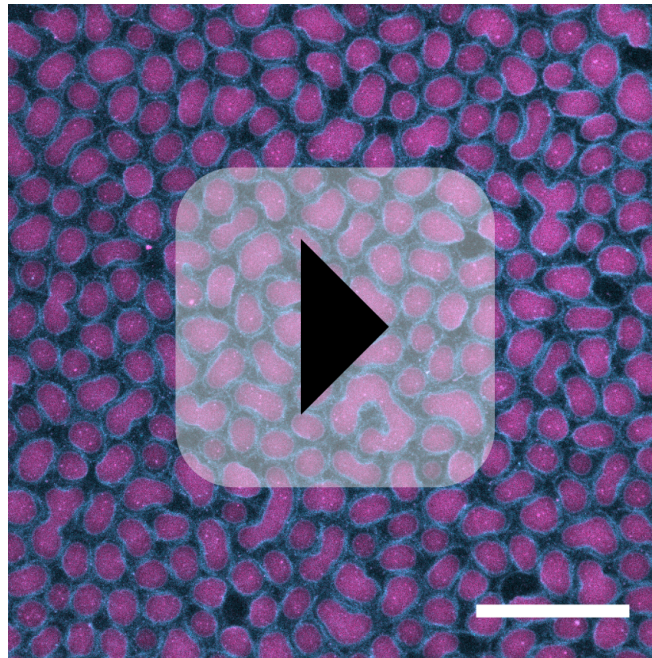
Fig. S13. *In vivo* oscillation periods at room temperature relative to cell length induced by the different MinEs and superfolder GFP-MinD when expressed in delta(minDE) background under IPTG induction. Only MinE-His (n=143) and His-MinE (n=189) are shown with all their outliers, while MinE-wt has been separately plotted in Supplementary Figure 12.

Table S1. Determined second signature (S2) values for the evaluation of the QCM-D system performance during analysis of MinE-His, His-MinE and MinE WT membrane binding affinity. S2 values are indicated and the percentage deviation from the reference values for harmonics 3, 5, 7, 9, 11 and 13 (2.45, 2.5, 2.49, 2.45, 2.46 and 2.47, respectively) is stated (1).

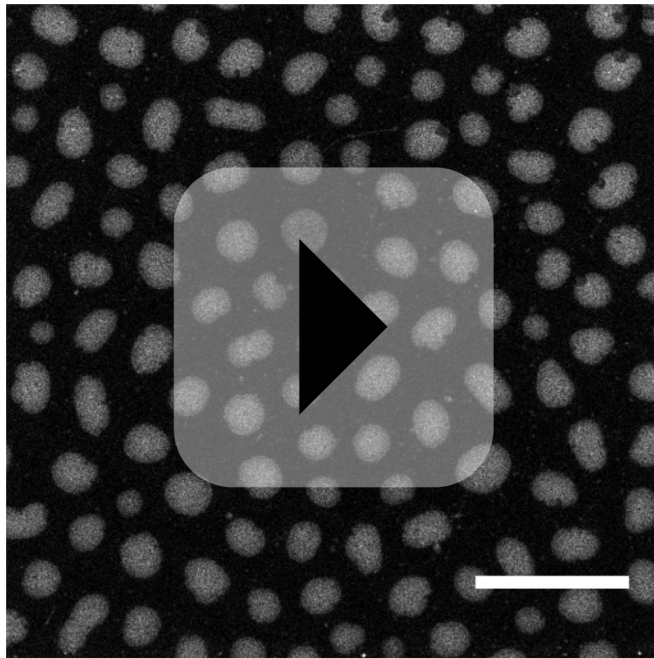
	overtone	replicate 1		replicate 2		replicate 3	
		S2	deviation [%]	S2	deviation [%]	S2	deviation [%]
MinE-His	1	2,13	-	1,9	-	2,18	-
	3	2,39	2,45	2,45	0	2,39	2,45
	5	2,38	4,8	2,47	1,2	2,37	5,2
	7	2,38	4,42	2,46	1,2	2,45	1,61
	9	2,38	2,86	2,43	0,82	2,4	2,04
	11	1,8	26,83	2,44	0,81	2,41	2,03
His-MinE	13	3,19	29,15	2,44	1,21	2,39	3,24
	1	2,08	-	2,23	-	2,09	-
	3	2,43	0,82	2,44	0,41	2,46	-0,41
	5	2,44	2,4	2,4	4	2,41	3,6
	7	2,5	0,4	2,43	2,41	2,47	0,8
	9	2,51	2,45	2,41	1,63	2,45	0
MinE WT	11	2,64	7,32	2,44	0,81	26,04	958,54
	13	2,73	10,53	2,42	2,02	2,4	2,83
	1	2,18	-	2,11	-	2,13	-
	3	2,46	0,41	2,4	2,04	2,48	1,22
	5	2,45	2	2,4	4	2,44	2,4
	7	2,48	0,4	2,46	1,2	2,5	0,4
MinE WT	9	2,45	0	2,43	0,82	2,47	0,82
	11	2,47	0,41	2,44	0,81	2,47	0,41
	13	2,45	0,81	2,44	1,21	2,46	0,4

Supplementary Table 1.

Supplementary Videos.



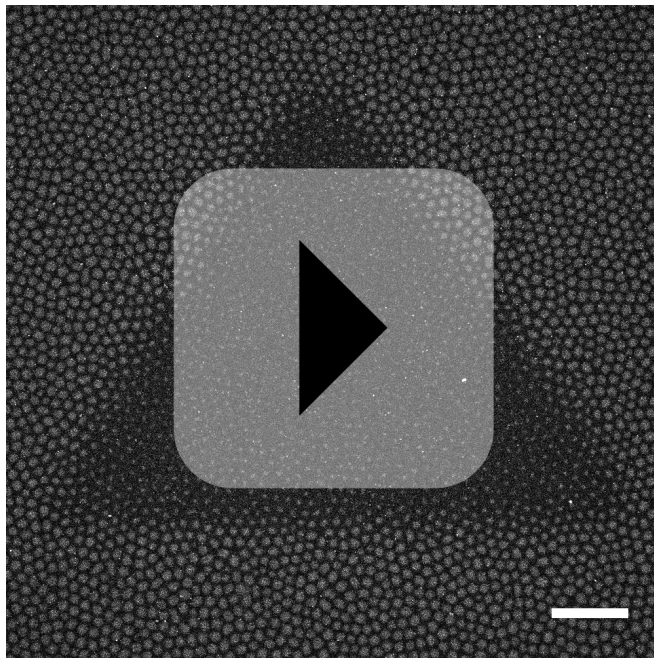
Supplementary Movie 1. Gradual small changes happen in the otherwise static patterns. The video has been sped up 333x relative to real time to make it easier to visualize changes. (MinD, doped with 30% Alexa647-KCK-MinD, magenta; MinE, doped with 30% MinE-KCK-His Atto488, cyan, scalebar:50 μm)



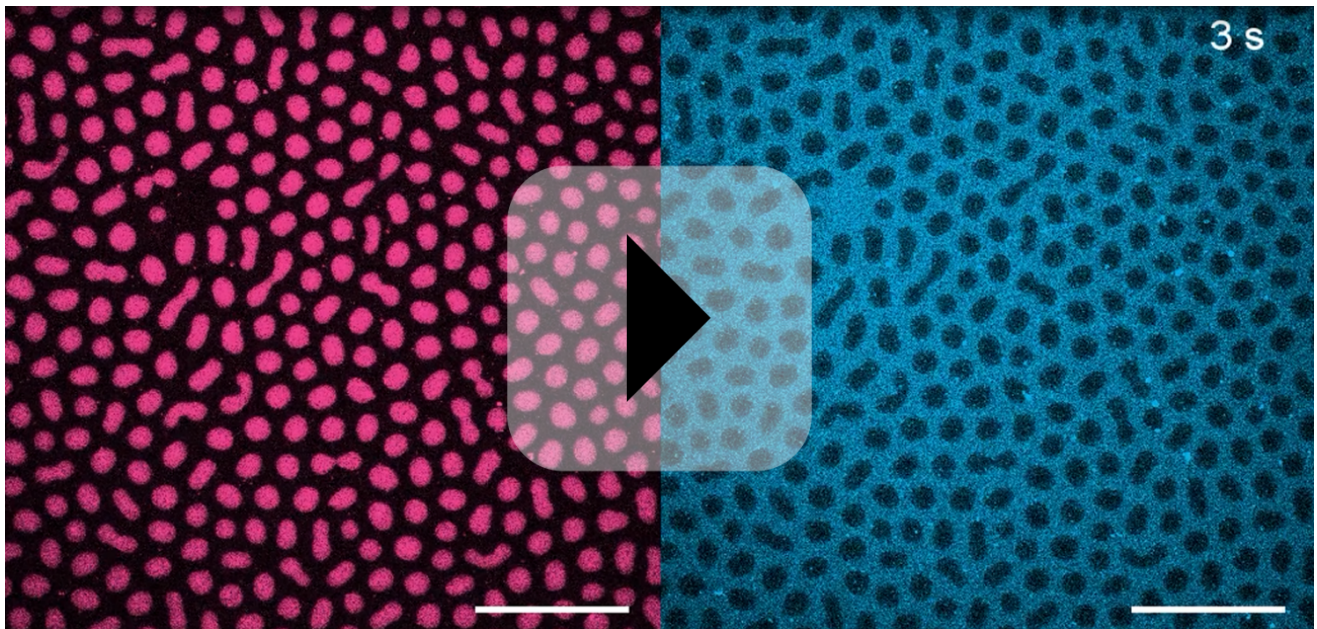
Supplementary Movie 2. Static patterns recover rapidly upon photobleaching. Data was recorded at 1.21 seconds per image, and is replayed at 15 fps. (0.6 μM MinD, doped with 30% mRuby3-MinD, 1 μM MinE-His, scalebar:50 μm)



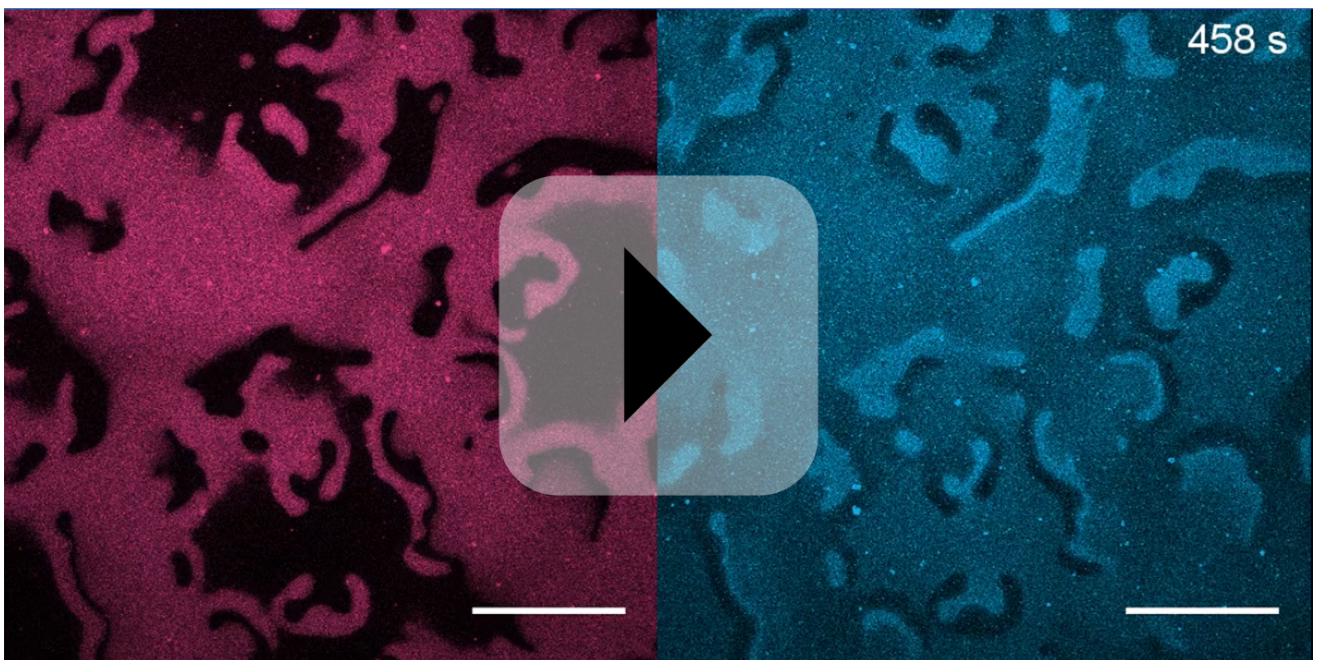
Supplementary Movie 3. His-MinE oscillates slower in vivo than MinE wild type and MinE-His Three timelapse recordings of cells expressing superfolder GFP and either MinE-wt, MinE-His or His-MinE are played next to each other at the same relative speed. (scalebar: 20 μ m)



Supplementary Movie 4. Static patterns formed with MinE-His can be externally modified by using the Min photoswitch peptide. Here, a triangular region was photoactivated with the 405 nm scanning laser of a laser scanning microscope. (0.6 μM MinD (30% Alexa647-KCK-MinD), 0.75 μM MinE-His, 2 μM photoswitch peptide (cis-stable azobenzene version), scalebar:100 μm).



Supplementary Movie 5. MinDE spot patterns formed with MinE-His exclude the model peripheral membrane protein mCh-MTS(BsD) (0.75 μM MinD (30% EGFP-MinD), 2 μM MinE-His, 1 μM mCh-MTS(BsD))



Supplementary Movie 6. MinDE static patterns formed in the presence of MinE-His are spatiotemporally regulating lipid-anchored streptavidin, forming a static inverse streptavidin pattern. (1 μ M MinD (30% EGFP-MinD). 2 μ M MinE-His, Alexa647-Streptavidin, 69 mol % DOPC/ 30 mol % DOPG/1 mol % Biotinyl-CAP-PE).

Supplementary Methods.

Details on cloning procedures. Homologous recombination in *E. coli* was prepared by thawing an aliquot of chemically competent TOP10 cells on ice. Between 50 ng and 200 ng (for big and small fragments) of fragments containing complementary nucleotide overhangs between 15 and 22 nt (combined) were added to the cells and incubated for another 10 minutes on ice. Heat shock was performed for 40 seconds at 42 °C and cells were immediately returned to ice. 200 µl of SOC medium was added and bacterial outgrowth was performed by shaking at 37 °C, 300 rpm for 1 h on a thermoshaker. Dilutions (1:1 for difficult recombinations, 1:10, 1:100) of the suspension were then plated on LB agar plates containing the respective antibiotics (for pET28a and pET28M Kanamycin at 50 µg/mL, pMLB Carbenicillin/Ampicillin at 100 µg/mL). In all cases, DpnI digests were used after PCR reactions to cut and disable the original plasmid based on its methylated status. Bacterial colonies harboring recombined plasmid were verified via Sanger sequencing.

Plasmids

pET28a-MinE-His was generated via homologous recombination of two fragments in TOP10 cells. The vector plus His-tag was amplified from pET28a-BsMTS-mCherry-His (primers PG7 and PG89). MinE plus linker was amplified from pET28a-MinE using primers PG90 and PG92.

pET28a-deltaMTS-MinE-His was generated via homologous recombination of two fragments PCR-amplified from pET28a-MinE-His. One fragment was amplified using primers PG43 and pG109. The second fragment was amplified with primers PG44 and PG89.

pET28a-MinE-KCK-His was recombined from pET28a-MinE-His using two PCR products. One half of the vector was amplified using primers PG114 and PG43. The other half was amplified with primers PG115 and PG44. Fragments were then recombined in TOP10.

pET28a-His-KCK-linker-MinE was made by amplifying pET28a-MinE using primers KN292 and KN293. The open vector was then re-ligated with blunt ends, yielding the final plasmid.

pET28a-His-KCK-MinD-MinE was made in a similar fashion by amplifying from pET28a-MinD-MinE using primers KN252 and KN253. Blunt re-ligation yielded the final plasmid.

pET28M-N-SUMO1-MinE was created via homologous recombination in TOP10 cells from two fragments. The vector fragment was amplified from pET28M-SUMO1-GFP (EMBL: https://www.embl.de/pepcore/pepcore_services/cloning/sumo/) using primers THE2 and THE3. The insert was amplified from pET28a-MinE using primers THE1 and THE4.

Plasmids for in vivo imaging of MinDE pole-to-pole oscillations are based on plasmid pDR122 (Raskin and de Boer, 1999). pVRb18_up1700 encoding sfGFP was a gift from Christopher Voigt (Addgene plasmid # 49712). pMLB_sfGFP_MinDMinE encodes an N-terminal fusion of sfGFP to MinD with a short linker (Glu-Phe) and a wildtype MinE sequence. pMLB_sfGFP_MinD N-His-linker MinE encodes for the same sfGFP-MinD fusion and a MinE that contains the same N-terminal His-linker as on pET28a_His-MinE. pMLB_sfGFP-MinD MinE encodes for the same sfGFP-MinD fusion and a MinE that contains the same C-terminal His-linker as on pET28a_MinE-His. pMLB_sfGFP_MinDMinE was generated by seamless assembly of three PCR fragments: vector backbone from template pDR122 (BR30, BR31), sfGFP from template pVRb18_up1700 (BR53, BR33) and the MinD and MinE coding region from plasmid pET28a_MinD_MinE (BR54, BR55). pMLB_sfGFP_MinD_N-His-linker-MinE was generated via homologous recombination of two fragments in TOP10 cells. The fragment containing the vector and sfGFP-MinD as well as part of MinE was amplified from pMLB_sfGFP_MinDMinE using primers KN392 and KN393. The N-terminal part of MinE as well as His-tag and linker were amplified from pET28a-MinE (primers KN391_MinE_Linkers_FW and BR55_MinE_rev). pMLB_sfGFP_MinD_MinE-His was generated from pMLB_sfGFP_MinDMinE via PCR with overhangs and re-ligation in TOP10 cells. Primers KN390_MinE-chis_FW and KN389_MinE-chis_RV were used for the amplification.

QCMD and analysis. Silicon Dioxide (SiO₂) covered quartz crystal sensors (Biolin Scientific, Gothenburg, Sweden) were pre-treated with piranha-solution (H₂SO₄:H₂O₂, 3:1; 1h), rinsed with ultrapure water and thoroughly dried under a stream of nitrogen. Sensors were mounted in the flow modules of the QSense Analyzer (Biolin Scientific, Gothenburg, Sweden) and resonance frequencies were obtained for both air and buffer (QSoft Version 2.5.36; Biolin Scientific, Gothenburg, Sweden). To qualitatively review the systems performance, second signature, S₂, values were calculated as indicated in Cho et al. (Supplementary Table 1) (Cho et al., 2010). After baseline stabilization, supported lipid bilayer formation (SLB) was induced through 1 mg/mL SUVs (DOPC:DOPC, 70:30 mol %) in Min Buffer with 5 mM CaCl₂ (flow rate: 0.15 mL/min). Succeeding lipid deposition, flow rate was reduced to 0.1 mL/min and protein construct dilutions ranging between 0.25 µM and 65 µM (in Min Buffer) were adsorbed and desorbed under constant flow. All measurements were conducted at 24 °C. If not indicated otherwise, all presented and analyzed data sets correspond to the frequency changes of the 9th overtone. Raw data export was performed using QTools 3 Version 3.1.25.604 (Biolin Scientific, Gothenburg, Sweden). Further data analysis was executed using a customized MATLAB R2018a (The MathWorks, Inc., Natick, USA) script to fit one-exponential kinetic models to the adsorption and the desorption phase of each individual binding event. Data visualization was performed using GraphPad Prism 7.0d (GraphPad Software, La Jolla, USA).

The MinDE system is a generic spatial cue for membrane protein distribution in vitro

This article describes how the Min system can spatially regulate other membrane-bound factors, providing new opportunities to utilize the system for synthetic biology. This phenomenon may also be a general mechanism of spatiotemporal regulation *in vivo*.

Published under CC BY 4.0

Full citation: B. Ramm, P. Glock, J. Mücke, P. Blumhardt, D. A. García-Soriano, M. Heymann, and P. Schille, “The MinDE system is a generic spatial cue for membrane protein distribution in vitro,” *Nature communications*, vol. 9, p. 3942, sep 2018







Source online: <https://doi.org/10.1038/s41467-018-06310-1>

ARTICLE

DOI: 10.1038/s41467-018-06310-1

OPEN

The MinDE system is a generic spatial cue for membrane protein distribution in vitro

Beatrice Ramm ¹, Philipp Glock ¹, Jonas Mücksch ¹, Philipp Blumhardt ¹, Daniela A. García-Soriano ¹, Michael Heymann ¹ & Petra Schwille¹

The *E. coli* MinCDE system has become a paradigmatic reaction-diffusion system in biology. The membrane-bound ATPase MinD and ATPase-activating protein MinE oscillate between the cell poles followed by MinC, thus positioning the main division protein FtsZ at midcell. Here we report that these energy-consuming MinDE oscillations may play a role beyond constraining MinC/FtsZ localization. Using an in vitro reconstitution assay, we show that MinDE self-organization can spatially regulate a variety of functionally completely unrelated membrane proteins into patterns and gradients. By concentration waves sweeping over the membrane, they induce a direct net transport of tightly membrane-attached molecules. That the MinDE system can spatiotemporally control a much larger set of proteins than previously known, may constitute a MinC-independent pathway to division site selection and chromosome segregation. Moreover, the here described phenomenon of active transport through a traveling diffusion barrier may point to a general mechanism of spatiotemporal regulation in cells.

¹Max Planck Institute of Biochemistry, Am Klopferspitz 18, 82152 Martinsried, Germany. Correspondence and requests for materials should be addressed to P.S. (email: schwille@biochem.mpg.de)

Free energy-driven spatiotemporal organization is key to transforming a pool of molecules into a functional cell capable of exercising complex tasks characteristic of life, such as metabolism and self-replication.

The establishment of spatiotemporal cellular patterns and structures in higher organisms is predominantly mediated through active mechanisms that involve cytoskeletal filaments and motor proteins. Bacteria with their small size and lack of organelle substructures, however, largely rely on reaction–diffusion to orchestrate molecular transport and positioning^{1,2}. In particular the MinD/ParA ATPase family is essential for plasmid and chromosome segregation³, the positioning of FtsZ^{4,5} and other protein complexes⁶. The most prominent representative of this protein family is the *Escherichia coli* MinCDE system, which has become a model reaction–diffusion system in biology, extensively studied in vivo^{7,8}, in vitro^{9–11}, and in silico^{9,12,13}. The MinCDE proteins oscillate from pole-to-pole within the rod-shaped bacterial cell, positioning FtsZ, the scaffold protein for cell division, at midcell^{7,14,15}. The ATPase MinD dimerizes upon ATP binding, which enhances its affinity via a C-terminal membrane-targeting sequence (MTS) for the spatial reaction matrix, the membrane¹⁶. Membrane-bound MinD recruits MinE, which in turn stimulates the ATPase activity of MinD causing MinDE membrane detachment¹⁷. MinC is not needed for pattern formation, but merely follows the MinDE oscillations^{9,14,18}. Thereby, a steady-state concentration gradient of MinC is established with a concentration minimum at midcell¹². Since MinC inhibits FtsZ polymerization, its spatiotemporal patterning restricts FtsZ ring formation to midcell^{19–21}.

The oscillatory mechanism for positioning FtsZ by the MinCDE system in *E. coli* is not conserved across prokaryotes. For instance, *Bacillus subtilis* uses a static, polarly localized MinCD system²². So why does *E. coli* employ such an eccentric and energy-consuming mechanism? And could the MinDE oscillations have additional roles apart from positioning MinC^{23–25}? Several studies reported that MinCDE deletion leads to chromosome segregation defects that cannot be explained by impaired division only^{26–28}. In fact, *E. coli* lacks any ParABS system that other bacteria employ for active chromosome segregation, and how exactly *E. coli* segregates its chromosomes is highly debated^{24,29,30}. MinD is the closest homolog to ParA in *E. coli* and thus has been suggested to act as driving force for chromosome segregation by direct DNA binding²⁴. Another hint for additional roles of the MinCDE system came from the analysis of the *E. coli* inner membrane proteome in Δ minCDE and wildtype strains that showed that the abundance of peripheral membrane proteins is regulated by MinCDE²⁵. Interestingly, these studies mostly implicate MinDE oscillations, but not MinC, as contributing factors.

Despite these cues, further experimental proof for the extent as well as the underlying mechanism of how MinDE mediate these processes is still lacking. Since MinCDE deletions or manipulations in vivo immediately affect cell division, an unbiased, differentiated functional analysis is nearly impossible. We have therefore turned to an in vitro approach reconstituting MinDE oscillations on supported lipid bilayers (SLBs)⁹, where the proteins form traveling surface waves, and in rod-shaped microcompartments¹⁰, where the proteins perform pole-to-pole oscillations mimicking their behavior in vivo. Reducing the system to its core components, MinDE, ATP and the membrane, we directly address MinDE function without the side-effects of component deletion or modification obtained in vivo.

Here, by reconstituting MinDE oscillations in vitro, we demonstrate that their ability of redistributing membrane-attached proteins into steady-state gradients is not limited to direct interaction partners of MinDE. Rather, ATP-driven MinDE

self-organization may constitute a dynamic diffusion barrier, causing directed transport of functionally completely unrelated lipid-anchored proteins. Our results imply a much more fundamental role of MinDE in division site selection and chromosome segregation in *E. coli* than simply establishing a MinC gradient and provide the framework for positioning of molecules in artificial cells. Furthermore, our study poses the question whether related reaction–diffusion systems, such as ParABS systems¹, Cdc42³¹ and PAR³² proteins, are also capable of regulating a large set of proteins by similar nonspecific interactions. This may point to a so far unknown generic mechanism of coupling large-scale molecular rearrangements and gradient formation to ATP consumption.

Results

MinDE regulate a model peripheral membrane protein. To test the hypothesis that MinDE oscillations are involved in spatiotemporal positioning of chromosomes and membrane proteins, we used our well-established in vitro reconstitution assay on large planar SLBs, where MinDE form traveling surface waves⁹. We first evaluated the simplest scenario: regulation of monomeric, peripheral membrane proteins by MinDE. We designed a model peripheral membrane protein, mCh-MTS(BsD), consisting of the monomeric, fluorescent protein mCherry³³ and a C-terminal amphipathic helix, the MTS from *B. subtilis* MinD. This MTS is well-characterized and localizes other fluorescent proteins to the inner membrane in *E. coli*, but is unlikely to specifically interact with MinDE^{16,34}. When we added this protein to negatively charged SLBs, we observed homogenous membrane coverage (Fig. 1a). Intriguingly, mCh-MTS(BsD) also formed traveling surface waves when co-reconstituted with MinDE. These waves were perfectly anticorrelated with the traveling MinDE waves (Fig. 1a, b, Supplementary Movie 1). When the fluorescence intensity of mCh-MTS(BsD) on the membrane is compared in the presence and in the absence of MinDE, intensities are lower in the presence of the MinDE waves (Fig. 1c). To quantify this effect, we analyzed the mean fluorescence intensity of mCh-MTS(BsD) images for three regions: the full image, and the pixels located in the minima and maxima of the MinDE wave (Fig. 1d, Methods section). Indeed, MinDE waves reduced the overall membrane density of mCh-MTS(BsD), and in particular in the wave maxima (Fig. 1e). Importantly, this spatial regulation of mCh-MTS(BsD) is unlikely to be caused by specific interactions with MinDE (unlike the spatiotemporal regulation of FtsZ filaments by MinDE waves that include MinC^{20,35}) and can thus be considered generic.

Regulation of peripheral membrane proteins is robust. To demonstrate that the spatiotemporal regulation of peripheral membrane proteins by MinDE is generic, we designed a set of mCherry model membrane proteins (mCh-MTS) with amphipathic helices from different proteins endogenous in *E. coli*: MreB, FtsA and FtsY (MTS(1×MreB)-mCh, MTS(2×MreB)-mCh³⁶, mCh-MTS(FtsA)³⁷, MTS(FtsY)-mCh³⁸) (Fig. 2a). All mCh-MTS constructs bound to the membrane (Supplementary Fig. 1a, b) and were susceptible to spatial regulation by the MinDE wave, resulting in an anticorrelated mCherry wave on the membrane (Fig. 2b, Supplementary Movie 2). In contrast, the control containing His-mCh, unable to bind to the membrane (Supplementary Fig. 1a, b), showed no spatiotemporal regulation. MTS(1×MreB)-mCh also weakly bound to the membrane and was regulated by MinDE, although in the past no membrane binding of a similar construct could be detected in vivo³⁶. To exclude photoinduced artefacts we imaged MTS(2×MreB)-mCh

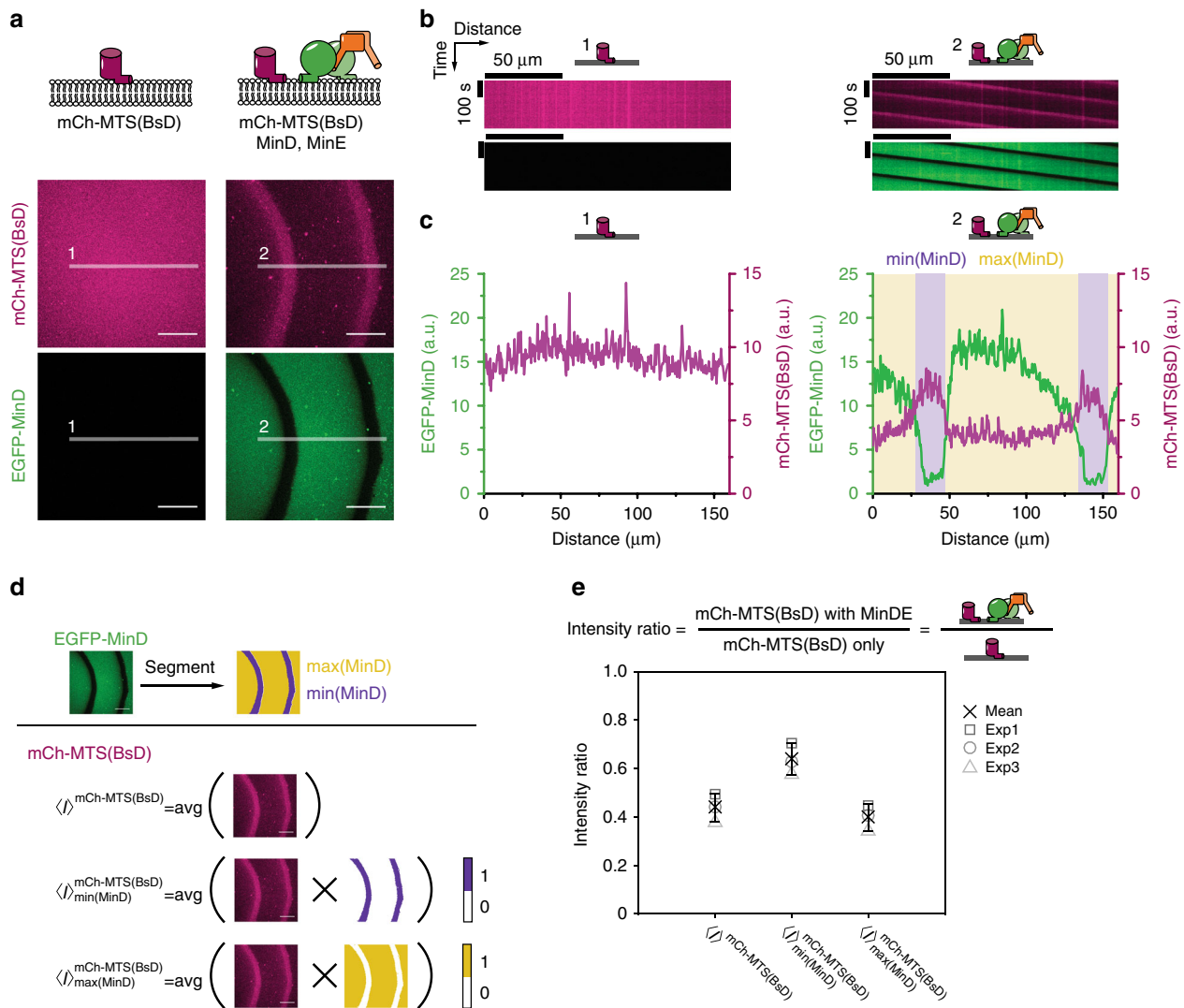


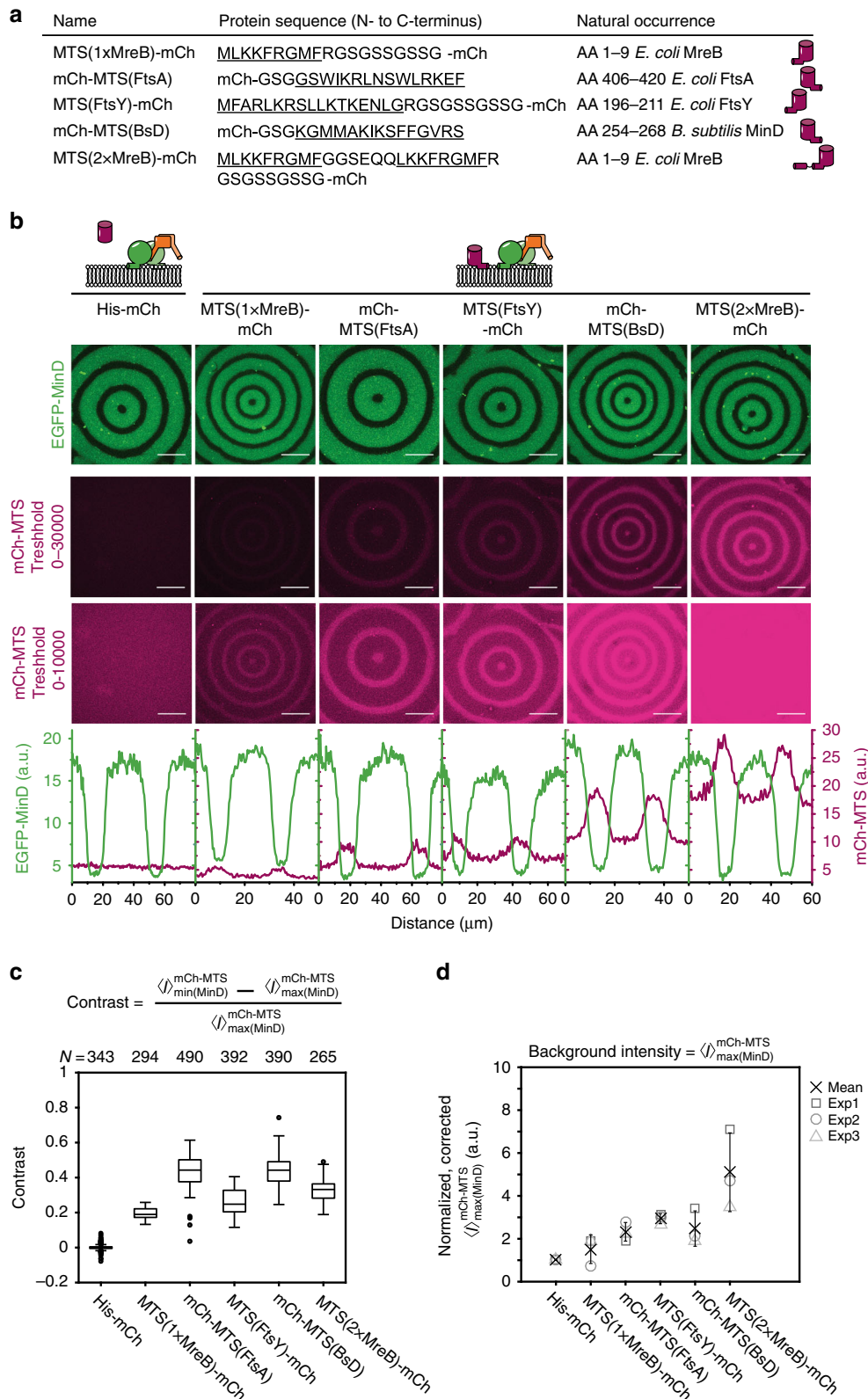
Fig. 1 MinDE can spatiotemporally regulate a model peripheral membrane protein. **a** mCh-MTS(BsD), mCherry fusion to the C-terminal amphipathic helix of *B. subtilis* MinD, homogeneously covers SLBs in the absence of MinDE (1 μM mCh-MTS(BsD)). In the presence of MinDE and ATP mCh-MTS(BsD) forms traveling surface waves that are anticorrelated to the MinDE wave (1 μM mCh-MTS(BsD), 1 μM MinD (30% EGFP-MinD), 1 μM MinE). Scale bars: 50 μm. **b** Kymographs of the line selections shown in **a**. Scale bars: 50 μm and 100 s. **c** Intensity profiles of the line selections shown in **a**. mCh-MTS(BsD) fluorescence (magenta) on the SLBs in the presence of MinDE is reduced and shows clear maxima in the minima of the MinDE waves (min(MinD)) and clear minima in the MinDE wave maxima (max(MinD)). **d** Schematic of the analysis process. EGFP-MinD images are segmented to generate two binary masks that are subsequently multiplied with mCh-MTS(BsD) images to obtain average intensities for the full image and in the minimum and maximum of the MinDE wave. **e** Intensity ratio of the average fluorescence of mCh-MTS(BsD) in the presence over in the absence of MinDE. Intensity ratios are shown for the average intensity of the full image ($I^{mCh-MTS(BsD)}$), in the MinDE minimum ($I^{mCh-MTS(BsD)}_{min(MinD)}$) and in the MinDE maximum ($I^{mCh-MTS(BsD)}_{max(MinD)}$). Each data point (exp 1-3) is generated from at least one time series consisting of 75 images in one sample chamber. Cross and error bars depict the mean values and standard deviations from three independent experiments

with non-labeled MinDE and observed the same traveling surface waves for MTS(2×MreB)-mCh (Supplementary Fig. 2a).

The membrane affinity and the extent of spatial regulation differed quite drastically between mCh-MTS constructs (Fig. 2b). To quantify this effect, we analyzed the mCherry and EGFP-MinD fluorescence intensity for the whole image, as well as in the minima and maxima of the MinDE wave (Supplementary Fig. 3) as described (Fig. 1d). We furthermore determined the contrast of the resulting mCh-MTS waves, defined as the average signal in the mCherry maximum above the background ($I^{mCh-MTS}_{min(MinD)} - I^{mCh-MTS}_{max(MinD)}$) divided by the background intensity ($I^{mCh-MTS}_{max(MinD)}$) (Fig. 2c). We assume that the background intensity $I^{mCh-MTS}_{max(MinD)}$ is a measure for the overall binding strength

of the mCh-MTS binders (Fig. 2d). $I^{mCh-MTS}_{max(MinD)}$ increases from (MTS(1×MreB)-mCh) to (MTS(2×MreB)-mCh), predicted to have the weakest and strongest membrane affinity, respectively (Fig. 2d). Interestingly, the contrast did not directly depend on the binding strength, but the constructs with the highest contrast, mCh-MTS(FtsA) and mCh-MTS(BsD), displayed intermediate background intensity. These two constructs contain a C-terminal MTS like MinD, whereas all other constructs contain an N-terminal MTS. The two termini of mCherry might differ in their flexibility, changing the properties of the mCh-MTS constructs.

Contrary to MinDE pattern formation regulating mCh-MTS constructs on the membrane, MinDE patterns themselves were



not affected by mCh-MTS constructs: average MinD intensities on the membrane (Supplementary Fig. 3d-f) and wavelength and velocity of MinDE waves were similar in the presence of all mCh-MTS constructs and the control His-mCh (Supplementary Fig. 4). Spatiotemporal positioning of the strongest mCh-MTS, MTS(2xMreB)-mCh, is robust, as it occurred for all tested

MinD/MinE ratios (10–0.1) (Supplementary Fig. 5a, b), for all mCh-MTS/MinDE ratios, as high as 30 and as low as 0.1 (Supplementary Fig. 6), and also at the lowest equimolar MinDE concentration that still supported self-organization in our assay (MinDE = 0.4 μM) (Supplementary Fig. 5c-e), albeit with varying strength.

Fig. 2 MinDE regulate a variety of peripheral membrane proteins to different extents. **a** Overview of the model peripheral membrane proteins employed. All amphipathic helices were fused to mCherry at their endogenous terminus. **b** Representative images of the MinDE wave (upper panel) and the anticorrelated mCh-MTS wave with two different brightness settings (middle and lower panels) on the membrane (1 μM mCh-MTS, 1 μM MinD (30% EGFP-MinD), 1 μM MinE). All images in one row were acquired and displayed using the same instrumental settings. Fluorescence intensity line plots of the corresponding images (EGFP-MinD fluorescence in green, mCh-MTS fluorescence in magenta) show the difference in the extent of the spatial regulation (lowest panel). **c** mCh-MTS constructs with a C-terminal amphipathic helix exhibit highest contrast. Box plot of the contrast of mCh-MTS constructs, lines are median, box limits are quartiles 1 and 3, whiskers are 1.5 \times interquartile range (IQR) and points are outliers. **d** mCh-MTS intensity in the MinDE maximum ($I_{\text{max(MinD)}}^{\text{mCh-MTS}}$) normalized to His-mCh and corrected for the fluorescent protein fraction. Each data point (square, sphere, triangle) corresponds to one independent experiment (exp 1–3) and was generated from at least one tile scan (7 by 7) in one sample chamber (number of images $N_{\text{His-mCh}} = 343$, $N_{\text{MTS(1}\times\text{MreB)-mCh}} = 294$, $N_{\text{mCh-MTS(FtsA)}} = 490$, $N_{\text{MTS(FtsY)-mCh}} = 392$, $N_{\text{mCh-MTS(BsD)}} = 390$, $N_{\text{MTS(2}\times\text{MreB)-mCh}} = 265$). Cross and error bars represent the mean value and standard deviation of the three independent experiments. Scale bars: 50 μm

Next, we designed two constructs harboring two copies of the *E. coli* MinD MTS, mCh-MTS(2 \times MinD) and mCh-Jun-MTS(1 \times MinD), which both strongly bound to the membrane (Supplementary Fig. 1a, c). Intriguingly, they were also efficiently regulated by MinDE (Supplementary Fig. 7, Supplementary Movie 3). These two proteins should have a similar membrane affinity as the alleged MinD species on the membrane, a MinD dimer. This suggests that MinDE membrane binding involves higher-order recruitment or oligomerization. Membrane binding of mCh-MTS (1 \times MinD), containing a single copy of the *E. coli* MinD MTS, could not be detected in agreement with previous reports¹⁶ (Supplementary Fig. 1a, c). Thus regulation by MinDE was also negligible (Supplementary Fig. 7).

Taken together, we show that MinDE spatiotemporally regulates model peripheral membrane proteins over a wide range of concentrations through a nonspecific mechanism independent of the specific amphipathic helix employed. This regulation can be rationalized by a competition for membrane binding sites between MinDE and mCh-MTS constructs.

MinDE is a spatial sorter for lipid-anchored proteins. Next, we asked whether MinDE dynamics could also regulate proteins that, unlike mCh-MTS constructs, are unable to dissociate from the membrane, similar to transmembrane proteins in vivo. Full transmembrane proteins are static on SLBs, because they are in contact with the support³⁵. Thus, to mimic a diffusible transmembrane protein in our assays, we used Alexa647-labeled streptavidin coupled to biotinylated lipids in the SLB (Fig. 3b). The tetrameric streptavidin binds two to three biotinylated lipids simultaneously rendering the dissociation of streptavidin negligible on the timescale of the MinDE waves, while the lipid-anchoring ensures diffusive mobility in the membrane³⁹. The resulting streptavidin membrane density was about $6.6 \times 10^3/\mu\text{m}^2$ and, assuming a streptavidin footprint of 25 nm², covers about 17% of the total available membrane area (Supplementary Fig. 12)³⁹. Upon initiating MinDE self-organization by ATP addition, an anticorrelated, directional movement of streptavidin was observed (Fig. 3a, c, Supplementary Movie 4, Supplementary Fig. 8). The kymograph of streptavidin movement differed from those obtained with mCh-MTS constructs in that streptavidin amassed in MinDE minima (compare Figs. 3c and 1b). Even more strikingly, over time streptavidin accumulated in areas where MinDE waves were colliding, or at the edges of MinDE spirals, whereas centers of MinDE spirals were depleted in streptavidin after longer incubation (Fig. 3d, Supplementary Fig. 8). Fluorescence intensity line plots through these stable spirals revealed that streptavidin depletion is correlated with MinDE enrichment and vice versa (Fig. 3d). Regulation of streptavidin and gradient formation was also evident if non-labeled MinDE were used or when dyes were exchanged to mRuby3-MinD and Alexa488-streptavidin (Supplementary Fig. 2b, c). Hence, MinDE self-organization establishes directional mass transport into large-scale streptavidin gradients on the membrane, beyond streptavidin

merely following the MinDE pattern. To test whether this gradient formation is reversible and maintained by the MinDE self-organization, and not due to other effects such as streptavidin 2D crystal formation⁴⁰, we used sodium orthovanadate (Na_3VO_4), a generic, competitive phosphatase inhibitor. Addition of Na_3VO_4 to an assay with established MinDE spirals led to MinDE detachment from the membrane (Fig. 3e), followed by the equalization of small scale streptavidin patterns within seconds. The large-scale streptavidin gradients disappeared only after several hundreds of seconds, reestablishing a homogenous distribution (Fig. 3e, Supplementary Movie 5, Supplementary Fig. 8). Hence, MinDE self-organization spatiotemporally regulates membrane-bound streptavidin, establishing directional mass transport and maintaining large-scale concentration gradients. In summary, MinDE self-organization represents a molecular sorting system for membrane-anchored molecules.

MinDE regulate proteins when mimicking in vivo conditions.

Having found that MinDE regulates unrelated proteins in vitro, we asked whether this could be a relevant phenomenon in vivo. First, we confirmed that MinDE also spatiotemporally regulate both mCh-MTS(BsD) and lipid-anchored streptavidin on membranes made from *E. coli* polar lipid extract (Supplementary Fig. 9). Second, as MinC is an integral part of the MinCDE system in vivo, we showed that the regulation of mCh-MTS (BsD) and lipid-anchored streptavidin is independent of MinC addition (Supplementary Fig. 10). Third, we determined the membrane densities of MinD and MTS(2 \times MreB)-mCh for four different MinDE concentrations using Fluorescence Correlation Spectroscopy based image calibration (Supplementary Figs. 11, 12, Supplementary Methods). At standard conditions ($[\text{MinDE}] = 1 \mu\text{M}$), peak MinD-membrane densities were high ($1.3 \times 10^4/\mu\text{m}^2$) (Supplementary Fig. 13). However, when protein concentrations were lowered to the limit where self-organization still occurred ($[\text{MinDE}] = 0.4 \mu\text{M}$) (Supplementary Fig. 5c–e), peak MinD densities ($1.8 \times 10^3/\mu\text{m}^2$) were similar to MTS(2 \times MreB)-mCh membrane densities ($2.0\text{--}2.6 \times 10^3/\mu\text{m}^2$) and on the same order of magnitude as the estimated in vivo densities of about $1 \times 10^3/\mu\text{m}^2$ (Supplementary Fig. 13, Supplementary Note 1). Hence, our in vitro assay allows to observe spatiotemporal positioning of membrane proteins by MinDE without the interference of a complex cellular environment, while keeping central conditions comparable to the in vivo situation.

MinDE induce generic protein gradients in microcompartments.

We subsequently visualized MinDE pole-to-pole oscillations in rod-shaped microcompartments in the presence of the two model membrane proteins, mCh-MTS(BsD) and lipid-anchored streptavidin (Fig. 4a). In the past, we demonstrated that confinement of MinDE in microcompartments leads to

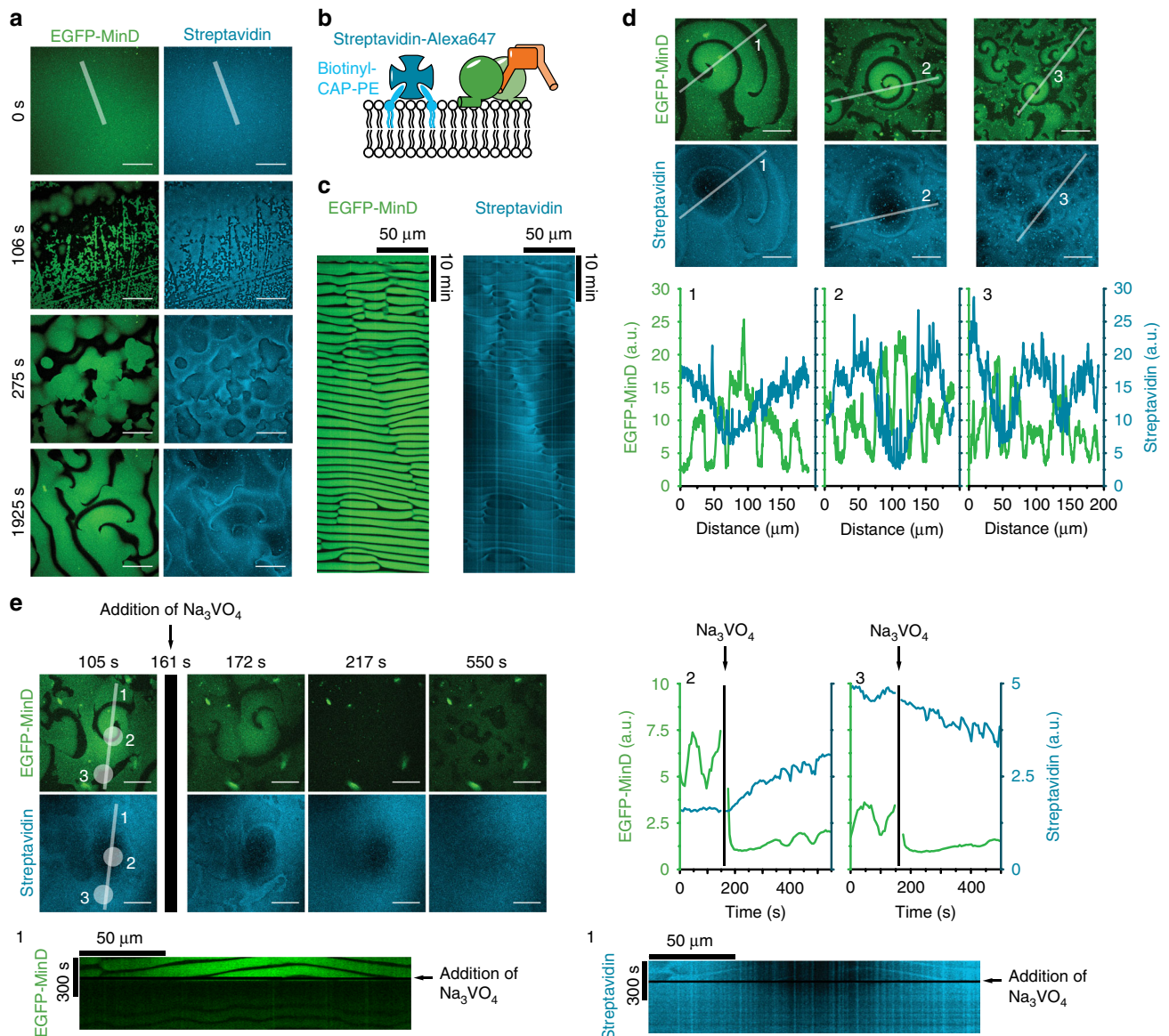


Fig. 3 MinDE spatiotemporally position a lipid-anchored protein resulting in large-scale concentration gradients. **a** MinDE self-organization spatiotemporally regulates lipid-anchored streptavidin. Representative time series of MinDE self-organization on a SLB with Biotinyl-CAP-PE-bound streptavidin (1 μM MinD, 1 μM MinE, streptavidin-Alexa647). ATP is added at $t = 0$ s to start self-organization. Scale bars: 50 μm . **b** Schematic of the experimental setup. Tetrameric streptavidin is anchored to the SLB by binding two to three Biotinyl-CAP-PE lipids and MinDE and ATP are added. **c** Kymograph of the line selections shown in **a**. Scale bars: 50 μm and 10 min. **d** MinDE self-organization leads to large-scale concentration gradients of streptavidin. Representative images of streptavidin distribution in MinDE spirals after >1 h of MinDE self-organization on SLBs. Fluorescence intensity line plots of EGFP-MinD and streptavidin distribution of selections shown in the respective images. Scale bars: 50 μm . **e** Large-scale streptavidin gradient formation by MinDE is reversible. Representative images and kymograph (1) of a running MinDE assay in the presence of anchored streptavidin. Addition of sodium orthovanadate (Na_3VO_4) leads to MinDE detachment which in turn leads to homogenization of streptavidin fluorescence on the membrane. Fluorescence intensity of streptavidin (cyan) and EGFP-MinD (green) is plotted over the duration of the time-lapse in the center (2) and at the rim of the MinDE spiral (3). Scale bars: 50 μm and 300 s. All experiments were performed independently three or more times under identical conditions

pole-to-pole oscillations similar to the observations *in vivo*¹⁰, albeit on a larger length scale. Indeed, MinDE spatially regulated streptavidin and mCh-MTS(BsD) in microcompartments (Fig. 4b, e, Supplementary Movie 6, 7). Similar to the behavior of the different protein waves on large SLBs, the difference in the resulting counter-oscillations in microcompartments was also evident. Whereas mCh-MTS(BsD) fluorescence was decreased in MinDE occupied areas, but was otherwise homogeneously distributed, the streptavidin fluorescence accumulated at the rear of

the MinDE wave (Fig. 4b, e). When MinDE oscillate from pole-to-pole *in vivo*, a time-averaged concentration gradient of MinD is established. MinC, antagonist of FtsZ assembly that passively follows MinD oscillations, shows the same time-averaged concentration gradient. We analyzed the time-averaged concentration gradient of MinD and, in agreement with our previous study¹⁰, in both cases the MinD concentration showed the characteristic profile with maxima at the compartment poles and minima at mid-compartment, featuring a pronounced dip

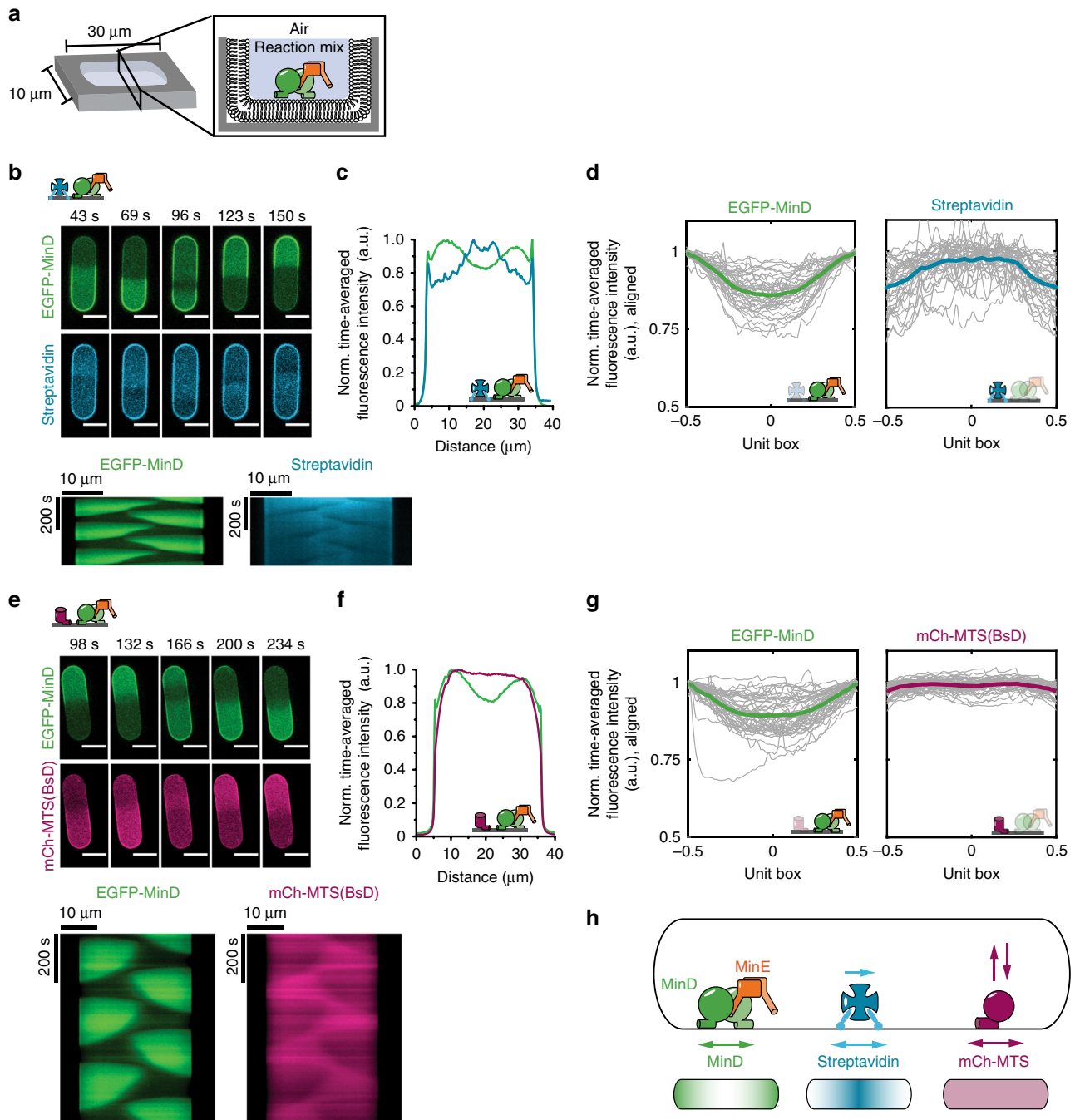


Fig. 4 MinDE induce oscillatory and time-averaged concentration gradients of model membrane proteins in microcompartments. **a** Experimental setup: PDMS-microcompartments are lined with an SLB and covered by air to confine the proteins. **b** Representative time-lapse images and kymographs of MinDE oscillations and streptavidin counter-oscillations in the compartments (1 μ M MinD, 2 μ M MinE, streptavidin-Alexa647). Brightness of the streptavidin channel was corrected for bleaching using histogram matching in Fiji. Scale bars: 10 μ m. **c** Time-averaged fluorescence intensity profiles of MinDE (green) and streptavidin (cyan) oscillation in **b** showing clear concentration gradients for both MinD and streptavidin. **d** Time-averaged fluorescence intensity profiles (gray lines) for EGFP-MinD and streptavidin aligned and projected to a unit box (see Supplementary Fig. 14 for details). Bold, colored lines represent the mean profiles, generated from three independent experiments with $N = 35$ microcompartments. **e** Representative time-lapse images and kymographs of MinDE oscillations and mCh-MTS(BsD) counter-oscillations in PDMS microcompartments (1 μ M MinD (30% EGFP-MinD), 2 μ M MinE, 0.5 μ M mCh-MTS(BsD)). Scale bars: 10 μ m. **f** Time-averaged fluorescence intensity profiles of MinDE (green) and mCh-MTS(BsD) (magenta) oscillations in **e** showing a clear protein gradient for MinD and homogenous protein distribution of mCh-MTS(BsD). **g** Time-averaged fluorescence intensity profiles (gray lines) for EGFP-MinD and mCh-MTS(BsD) aligned and projected to a unit box. Bold, colored lines represent the mean profiles, generated from three independent experiments with in total $N = 45$ microcompartments. **h** Schematic explaining how the MinDE system positions lipid-anchored streptavidin and mCh-MTS constructs in rod-shaped microcompartments. MinDE oscillations drive counter-oscillations of lipid-anchored streptavidin and mCh-MTS constructs, thereby establishing a time-averaged concentration gradient of lipid-anchored streptavidin with maximal concentration in the geometric center, but no concentration gradient of mCh-MTS

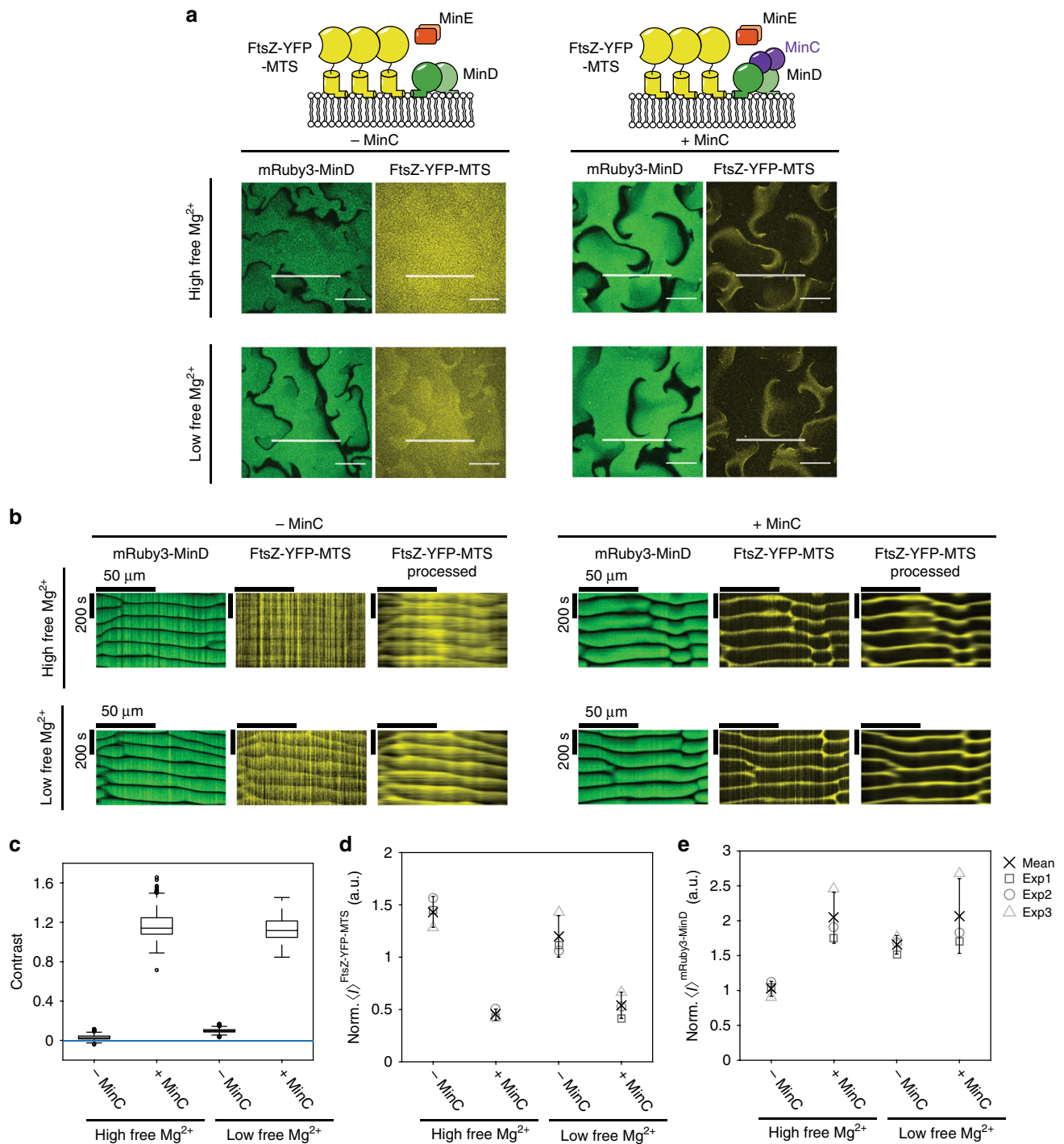


Fig. 5 MinC enhances spatiotemporal regulation of FtsZ-YFP-MTS by MinDE. **a** Representative images of MinDE self-organization in the presence of FtsZ-YFP-MTS with high and low free Mg^{2+} (-5 and -1 mM Mg^{2+}) and with and without MinC ($1 \mu M$ MinD (30 % EGFP-MinD), $1 \mu M$ MinE, $0.5 \mu M$ FtsZ-YFP-MTS, with and without $0.05 \mu M$ MinC) corresponding to the timepoint of 6.5 min. All images of the same spectral channel were acquired and displayed using the same instrumental settings. **b** Kymographs of the line selections shown in **a**. The kymograph for FtsZ-YFP-MTS is displayed for unprocessed images (middle panels) and preprocessed images (see Methods) (right panels). **c** MinC increases the regulation of FtsZ-YFP-MTS. Box plot of the contrast of FtsZ-YFP-MTS, lines are median, box limits are quartiles 1 and 3, whiskers are $1.5 \times$ IQR and points are outliers. Blue line marks no difference between the intensities in the minima and maxima of the MinDE wave (zero contrast). **d** Average FtsZ-YFP-MTS intensity of the full image normalized to a fluorescent standard. **e** Average mRuby3-MinD density of the full image normalized to a fluorescent standard. Each data point (square, sphere, triangle) (exp 1-3) was generated from one time series consisting of 150 frames. Cross and error bars represent the mean value and standard deviation of the three independent experiments

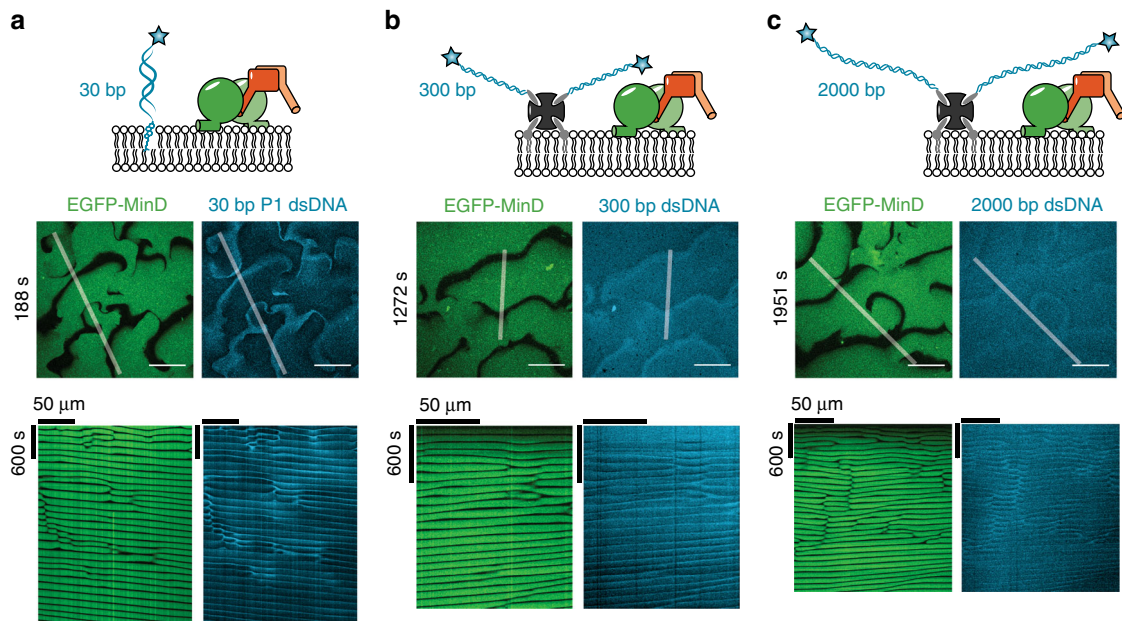


Fig. 6 MinDE spatiotemporally regulate membrane-anchored DNA. **a** MinDE self-organization can regulate short membrane-anchored DNA fragments. Representative images and kymograph of a time-series of MinDE self-organization in the presence of 30 bp P1 dsDNA bound to the membrane by a cholesterol anchor (1 μ M MinD (30% EGFP-MinD), 1 μ M MinE, 10 nM TEG-cholesterol-dsP1). **b** Representative images and kymograph of a time-series of MinDE self-organization spatiotemporally regulating 300 bp long dsDNA bound to lipid-anchored streptavidin (1 μ M MinD (30% EGFP-MinD), 1 μ M MinE, 300 bp lambda DNA, streptavidin). **c** Representative images and kymograph of a time-series of MinDE self-organization spatiotemporally regulating 2000 bp long dsDNA bound to lipid-anchored streptavidin. All experiments were performed independently two (**c**) or three (**a**, **b**) times under similar conditions. Scale bars: 50 μ m

(average profile depth of 0.61 ± 0.28 and 0.44 ± 0.24 , compare to Supplementary Fig. 14) (Fig. 4c, d, f, g). We further analyzed the time-averaged concentration profiles of the respective model membrane proteins. Streptavidin showed a clear time-averaged concentration profile with a negative profile depth of -0.42 ± 0.35 , indicating enrichment in the middle of the microcompartment (Fig. 4c, d, Supplementary Fig. 14). In contrast, the time-averaged concentration of mCh-MTS(BsD) was almost homogeneous along the long axis of the compartment (average profile depth of -0.06 ± 0.13) (Fig. 4f, g, Supplementary Fig. 14). Hence, MinDE spatially regulate model peripheral and membrane-anchored proteins in rod-shaped microcompartments and induce steady-state concentration gradients of membrane-anchored proteins with concentration maxima at mid-compartment (Fig. 4h).

We propose this to be of relevance in *E. coli*. So far, division site selection by the MinCDE system was considered to only depend on the inhibitory action of MinC on FtsZ. However, FtsZ does not bind to the membrane by itself, but via two distinct membrane anchors, ZipA and FtsA. ZipA, a single-pass transmembrane protein⁴¹, cannot be reconstituted on SLBs preserving its mobility³⁵. Hence, it is also not regulated by MinDE in vitro³⁵, but could potentially be enriched at midcell by MinDE in vivo. FtsA, in turn, is binding to the membrane via its C-terminal amphipathic helix³⁷, and would thus be expected to behave like its corresponding mCh-MTS construct mCh-MTS(FtsA) (Fig. 2b). However, while full-length FtsA was regulated by MinDE, the kymograph of the regulation was more similar to lipid-anchored streptavidin than to mCh-MTS (FtsA) (compare Supplementary Fig. 15, Supplementary Movie 8 to Figs. 1b and 3c). This suggests that FtsA rather behaves like a permanently membrane-attached protein than a monomeric peripheral membrane protein, which is in agreement with previous reports of FtsA oligomerization^{42–44}. Hence, we propose that FtsA is counter-oscillating to MinDE in vivo, and depending on the oligomerization state, would possibly be enriched at midcell.

MinC enhances MinDE-dependent regulation of FtsZ-YFP-MTS. The capability of MinDE to enrich permanently anchored proteins in the middle of rod-shaped compartments and to position the FtsZ anchor FtsA, opened the question for the additional role of MinC. In vivo MinC is strictly required for correct placement of the division site to prevent a minicell phenotype^{7,15} and inhibits FtsZ polymerization in vivo and in vitro^{19–21}. Nevertheless, slow FtsZ oscillations⁴⁵ and FtsZ treadmilling dynamics in vivo were slightly altered in Δ minCDE strain, but not in a Δ minC strain⁴⁶. To evaluate whether MinDE alone can influence FtsZ dynamics and what contribution MinC has in the positioning of FtsZ, we revisited previous experiments, i.e., the co-reconstitution of MinCDE with FtsZ-YFP-MTS. FtsZ-YFP-MTS is a chimeric protein, consisting of the fluorescent protein YFP, a truncated *E. coli* FtsZ (1–366) and the MinD MTS⁴⁷. This protein binds to the membrane without its adaptor proteins, FtsA and ZipA, greatly simplifying the system. Under high free Mg^{2+} conditions, FtsZ-YFP-MTS forms thick, treadmilling filament bundles^{10,20,48}, whereas under low free Mg^{2+} conditions⁴⁸, it forms dynamic chiral vortices similar to native FtsZ and FtsA⁴⁹. Hence, we co-reconstituted MinDE and FtsZ-YFP-MTS with high and low free Mg^{2+} concentration and in the presence or absence of MinC. The spatiotemporal regulation of thick FtsZ-YFP-MTS bundles formed at high free Mg^{2+} in solution (~ 5 mM Mg^{2+}) was hardly detectable if only MinDE were present in the assay, but very strong when MinC was supplied, in agreement with our previous reports^{10,20}. (Fig. 5a, b, Supplementary Movie 9). In the case of low free Mg^{2+} (~ 1 mM Mg^{2+}), FtsZ-YFP-MTS forms dynamic rings that were also visibly regulated by MinDE alone, but also here the regulation was drastically increased in the presence of MinC (Fig. 5a, b, Supplementary Movie 9). The contrast of the FtsZ-YFP-MTS regulation (Fig. 5c) increased with the amount of FtsZ-YFP-MTS on the membrane (Fig. 5d) and decreased with the amount of MinD on the membrane (Fig. 5e).

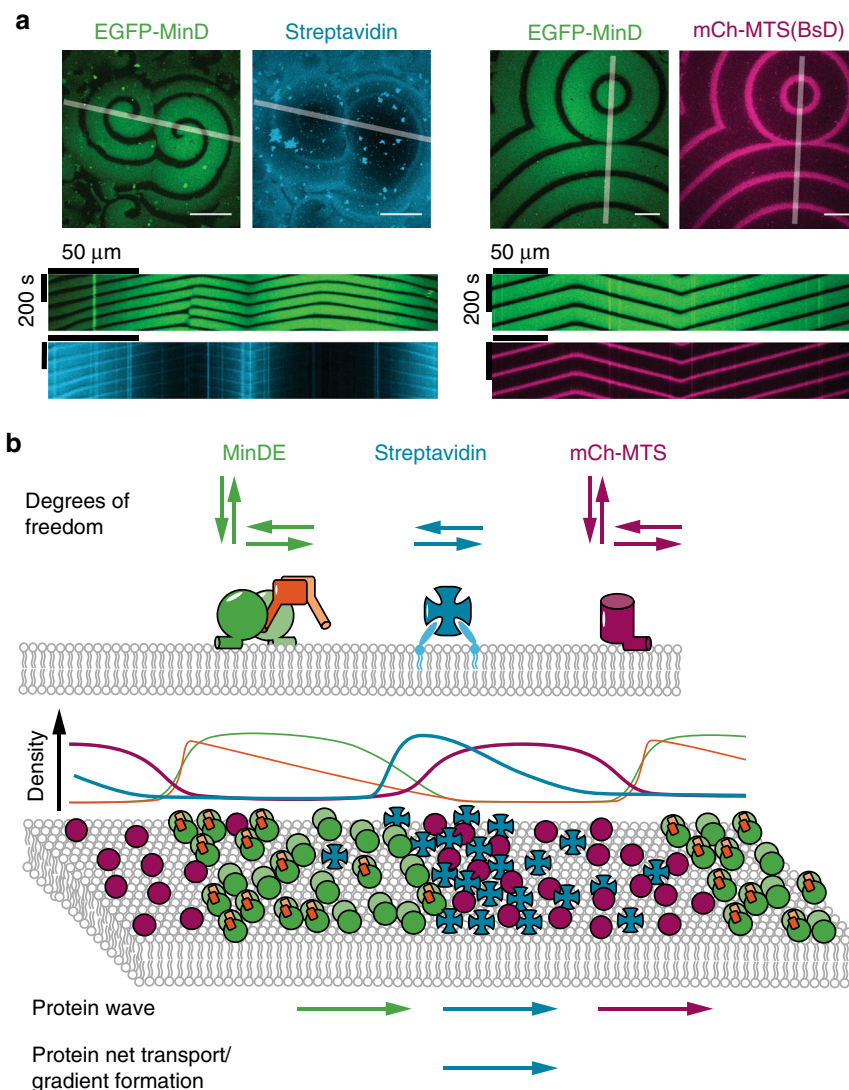


Fig. 7 MinDE-driven dynamics of model membrane proteins in vitro suggest that MinDE form a propagating diffusion barrier. **a** Representative images and kymographs of colliding MinDE waves in the presence of mCh-MTS(BsD) and lipid-anchored streptavidin bound to biotinylated lipids (1 μ M MinD (30% EGFP-MinD), 1 μ M MinE, 1 μ M mCh-MTS(BsD) or streptavidin-Alexa647). Scale bars: 50 μ m. **b** Schematic of the underlying protein behavior resulting in spatiotemporal regulation of model peripheral and membrane-anchored proteins. While mCh-MTS and MinDE can also attach and detach to and from the membrane, streptavidin can only diffuse laterally on the membrane. Schematic density profiles and protein localization on the membrane (magenta: mCh-MTS, green: MinD, orange: MinE, cyan: lipid-anchored streptavidin). The MinDE wave propagates directionally, even if individual proteins show a random movement on the membrane. Both model peripheral and membrane-anchored proteins show a wave propagation in the direction of the MinDE wave. mCh-MTS while more abundant in the MinDE minima covers the membrane homogeneously. In contrast the resulting secondary wave of streptavidin shows an inhomogeneous profile and results in a net transport of the membrane-anchored protein

This is consistent with previous results that at high Mg^{2+} concentration, FtsZ-YFP-MTS density on the membrane is higher and individual monomers have a longer residence time on the membrane compared to low free Mg^{2+} concentration⁴⁸, while MinC leads to depolymerization of FtsZ-YFP-MTS reducing its density on the membrane²⁰. Images acquired with higher magnification showed that neither the large FtsZ-YFP-MTS bundles nor the small dynamic vortices were laterally moved by MinDE, unlike lipid-anchored streptavidin (Supplementary Fig. 16, Supplementary Movie 10). Both, FtsZ-YFP-MTS filaments and dynamic rings, are also not diffusing laterally on the membrane, independent of the presence of MinDE^{20,48}. Hence, it can be concluded that for lateral transport of membrane-anchored proteins by MinDE, diffusive mobility is a prerequisite. Instead, FtsZ-YFP-MTS filaments and dynamic vortices varied in intensity in the MinDE minima and maxima suggesting that MinDE are

regulating the membrane binding of FtsZ-YFP-MTS. Interestingly, MinDE waves were patterned, showing a negative image of the FtsZ-YFP-MTS filaments and rings (Supplementary Fig. 16), indicating that MinDE can spatiotemporally regulate proteins, even while coupling over small membrane gaps⁵⁰ or in this case immobile obstacles.

In summary, we show that MinDE-dependent regulation of FtsZ-YFP-MTS increases with decreasing FtsZ-YFP-MTS density on the membrane and is drastically enhanced by MinC.

MinD regulates DNA-membrane tethers. Several studies report a defect in chromosome segregation when MinCDE are deleted in *E. coli*^{26–28}. Based on simulations that showed that chromosome segregation can be achieved by static or oscillatory gradients of chromosome-membrane tethers, MinD was suggested to drive chromosome segregation by direct, but transient DNA binding²⁴.

In light of our results, we hypothesized that any DNA-membrane tether could be spatially regulated by the MinDE system. Different chromosome-membrane contacts have been reported in *E. coli*, such as transertion^{30,51}, which itself has been suggested to aid chromosome segregation³⁰.

To model chromosome membrane tethering sites in the most simplistic fashion in our *in vitro* setup, we employed dsDNA with a fluorescence label and a TEG-cholesterol moiety for membrane binding on opposite ends. As the DNA sequence, we chose a 30-bp-long fragment from the P1 promoter of the *minB* operon in *E. coli*, shown to bind to MinD²⁴. When cholesteryl-tagged P1 fragments were included in a MinDE self-organization assay, the oligonucleotides formed traveling waves on the membrane that were anticorrelated to the MinDE waves and not correlated as would be expected for direct DNA binding by MinD (Fig. 6a, Supplementary Fig. 8, Supplementary Movie 11). The P1 fragments showed a phenomenologically similar behavior as the streptavidin-lipid conjugate, accumulating at sites where waves collide. This can be explained by the strong binding of TEG-cholesteryl oligonucleotides to membranes ($K_D = 16$ nM, $k_{\text{off}} = 6 \times 10^{-4}$ s⁻¹)⁵², rendering MinDE-induced dissociation unlikely. To rule out that the membrane-anchoring of the DNA mask binding to MinD, we performed control experiments with soluble P1 DNA fragments. We turned to TIRF microscopy (TIRFM) to be able to monitor even transient recruitment of DNA to the MinDE wave. Although the spatiotemporal positioning of membrane-anchored P1 fragment was clearly visible, we could not observe modulation of fluorescence intensity in the DNA channel with soluble P1 fragments under the same settings, nor with increased laser irradiation or DNA concentrations (Supplementary Fig. 17). Thus, we could not detect any recruitment or binding of DNA to MinDE waves. While these experiments cannot fully rule out that DNA binds to MinD, this interaction would be very weak.

If MinDE would indeed participate in chromosome segregation by regulating DNA-membrane tethers, the system needed to be capable of transporting larger cargo. Thus, we performed experiments with longer DNA molecules bound to streptavidin as a spacer. The 300 and 2000 bp long DNA strands were labeled with Cy5-fluorophore and biotin for immobilization on lipid-anchored streptavidin (mass: 185 kDa and 1.2 MDa, contour length: 100 and 640 nm). MinDE spatially organized the streptavidin-bound DNA in both cases (Fig. 6b, c, Supplementary Fig. 8, Supplementary Movie 12, 13). In summary, our results show that MinD is unlikely to bind DNA directly, but MinDE are able to regulate DNA-membrane tethers *in vitro*.

Discussion

Here we showed that the MinDE reaction–diffusion system can dictate the localization of membrane proteins in a spatiotemporal manner without specific molecular interactions *in vitro*. These proteins apparently establish a generic, nucleotide-dependent transport mode for membrane-bound diffusive molecules based on a moving diffusion barrier. This in turn implies a more fundamental role of MinDE in division site selection and chromosome segregation *in vivo* and may in the future be applied to position and transport molecules in artificial cells.

The spatiotemporal positioning by MinDE *in vitro* is independent of (1) the target's membrane anchoring (amphipathic helix, lipid anchor or cholesterol anchor), (2) the nature of the target (protein or DNA), (3) the oligomerization state of the target protein, and (4) the target's dwell-time on the membrane (transiently or permanently bound). We hence conclude that MinDE can act as a generic spatial cue for the distribution of functionally unrelated membrane-bound molecules *in vitro*.

While sensitive to aspects such as diffusive mobility and membrane dwell-time of the regulated components, the observed MinDE-mediated dynamics likely reflect a common underlying mechanism. Comparing the spatiotemporal regulation of the two model membrane proteins that represent the distinct cases, transiently bound mCh-MTS and permanently attached lipid-anchored streptavidin, a stark difference in the effect is evident (Fig. 7a, Supplementary Movie 14). MinDE cannot induce large-scale gradients of mCh-MTS, suggesting that MinDE locally affect the attachment and/or detachment of these proteins by competition for membrane binding sites (Fig. 7b), explaining the overall reduction of mCh-MTS density on the membrane in the presence of MinDE. In contrast, MinDE induce large-scale gradients of the lipid-anchored streptavidin that can only laterally diffuse on the membrane. Hence, the moving MinDE wave front must lead to a directionally biased diffusion of streptavidin on the membrane and thus induce a net protein transport (Fig. 7b). Oligomerized peripheral membrane proteins, such as FtsA, have increased membrane dwell-times and are thus similarly regulated as permanently anchored proteins. In all cases, lateral mobility is a prerequisite for being positioned by MinDE. Consequently, static FtsZ-YFP-MTS networks, which do not diffuse on the membrane, are not subject to a net transport by MinDE. However, a weak, MinDE-induced regulation of protein abundance can be observed.

Further, MinDE drove counter-oscillations of both mCh-MTS(BsD) and lipid-anchored streptavidin in rod-shaped microcompartments. However, only the regulation of streptavidin resulted in a steady-state concentration gradient, where the protein was enriched at midcell. Hence, gradient formation in microcompartments is related to the occurrence of large-scale gradients on planar SLBs.

Based on these observations, we propose that MinDE surface waves constitute a propagating diffusion barrier. Although individual MinDE proteins do not move in a directed fashion on the membrane, but simply attach and detach^{9,18}, the MinDE wave front as a whole translocates directionally. This sliding concentration wave forms a mobile diffusion obstacle that directionally biases the diffusion of tightly membrane-attached proteins and outcompetes other peripheral membrane proteins during attachment. The detailed biophysical features of this nonspecific molecular transport process will be subject of further investigations.

MinDE membrane binding is a highly cooperative process^{53–55}, which is commonly attributed to the monomer-dimer transition of MinD during ATP binding¹⁶. However, MinD, sometimes in conjunction with MinC, was shown to assemble into higher-order structures on the membrane, similar to a 2D filament network^{55–58}. Strikingly, MinDE also regulated mCh-MTS(2×MinD) and the dimerizing mCh-Jun-MTS(1×MinD) with similar membrane affinity as a MinD dimer (Supplementary Fig. 7), further corroborating the existence of higher-order recruitment or oligomerization during MinD-membrane binding.

Additionally, MinDE have been shown to modify membranes and to preferentially bind to anionic lipids (Supplementary Note 2)^{53,57}. It will thus be interesting to investigate to what extent MinDE surface waves alter the local membrane properties, like viscosity or lipid content, to control attachment and diffusion of other membrane proteins in a more direct way.

Irrespective of the mechanistic details, the mobile diffusion barrier generated by MinDE *in vitro* is reminiscent of the rather static actin cortex in eukaryotes and the circumferentially rotating actin homolog MreB in bacteria, known to organize lipid domains and regulate protein diffusion^{59–61}. We therefore propose that this mechanism is also relevant *in vivo*. The sole purpose of the MinDE oscillations was long assumed to be the positioning of the

FtsZ-inhibitor MinC, although it seemed counterintuitive that such an energy-consuming process would not be utilized more efficiently by the cell. Several studies provided hints that MinDE oscillations influence chromosome segregation and the distribution and abundance of membrane proteins in vivo (Supplementary Table 1)^{25–28,46,62,63}. However, a differentiated and unbiased analysis in vivo remains challenging because: (1) MinCDE manipulations cause cell division defects; (2) observation of membrane dynamics in bacteria is complicated due to their small size, unfavorable optical properties and insufficient labeling strategies. Circumventing these problems, our in vitro assay plays to the strength of a reduced-complexity approach, allowing us to probe the influence of MinDE dynamics on membrane-bound proteins without the interference of a complex cellular environment. This reduction in complexity entails that MinDE self-organization in vitro and in vivo differ with respect to MinDE membrane densities and wavelength. Nevertheless, we confirmed that MinDE-mediated positioning of membrane proteins also occurs when the in vitro assay is closely mimicking in vivo conditions (Supplementary Figs. 9, 10, 13).

Consequently, MinDE might also drive counter-oscillations of membrane proteins in *E. coli*. Considering the results obtained here, it is, however, unlikely that all inner membrane proteins would be regulated. Proteins that are not freely diffusing on the membrane, such as streptavidin crystals (Fig. 7a, Supplementary Movie 14) or thick FtsZ-YFP-MTS bundles (Supplementary Fig. 16), cannot be moved laterally by the MinDE system. Hence, any protein that is anchored to the cell wall or whose diffusion is confined, e.g., by interaction with MreB filaments⁵⁹, would be exempt. Furthermore, depending on the exact mechanism of regulation, transmembrane proteins with none or small cytosolic domains, or proteins that favor a certain lipid composition, e.g. anionic phospholipids, may not be regulated or subject to other, stronger spatial cues.

Proteins potentially organized by MinDE in vivo include monomeric peripheral membrane proteins, whose abundance would be decreased by MinDE (Supplementary Fig. 18). This MinDE-induced decrease has already been observed for several such proteins in vivo, among them FtsY whose corresponding mCh-MTS construct was also regulated in vitro (Fig. 2, Supplementary Table 1)²⁵.

Furthermore, we did not detect direct DNA binding of MinD in our assay, which was proposed to explain the chromosome segregation defects occurring in $\Delta minCDE$ strains (Supplementary Table 1)^{24,26–28}. Instead we suggest that MinDE, as the closest homolog of ParABS systems mediating chromosome segregation in other bacteria, influence the spatiotemporal organization of DNA-membrane tethers, which are manifold in *E. coli*^{30,51}.

Finally, regulation of mobile transmembrane proteins and strongly membrane-bound oligomeric proteins, would result in their enrichment at midcell. The two FtsZ anchors, ZipA and FtsA, represent such protein classes and hence would be pre-positioned at the future division site (Supplementary Fig. 18). Indeed, ZipA and MinCDE counter-oscillate in vivo, so far accredited to recruitment of ZipA to FtsZ, that is periodically depolymerized by MinC⁶⁴. Several other observations also point towards such a mechanism (Supplementary Table 1). The presence of MinC strongly enhances division site selection, as demonstrated by the strong increase in regulation of the chimeric FtsZ-YFP-MTS when MinC was supplied (Fig. 5). However, both processes may be intertwined: MinC depolymerizes FtsZ and hence might free its membrane anchors to be positioned by MinDE.

In summary, the MinDE-dependent regulation of membrane-bound molecules by a propagating diffusion barrier can be seen as

an archetypal physicochemical mechanism based on two proteins only. Our data suggest that this reaction–diffusion system is capable of spatially regulating a much larger set of proteins than previously known. Other factors such as MinC augment the system by providing protein specificity.

Without doubt, our in vitro results will motivate future in vivo studies to discern to what extent MinDE is regulating nonspecific spatiotemporal organization of membrane proteins. We speculate that also other reaction–diffusion systems, such as ParABS¹, Cdc42³¹, and PAR³² proteins may be capable of regulating various proteins on their respective matrix. Moreover, our work lays the foundation to apply this simplistic regulatory mechanism for positioning artificial division machineries and chromosomes in constructing a synthetic cell from the bottom up. The ability to control MinDE waves by geometric cues and light will potentially allow a precise and controlled spatiotemporal targeting of any membrane-bound molecule^{50,65}.

Methods

Plasmids. A list of all plasmids and primers used in this study and their construction can be found in the Supplementary Information (Supplementary Table 2 and 3, Supplementary Methods).

Protein purification. Purification of His-MinD, His-EGFP-MinD, His-mRuby3-MinD, His-MinC, and His-MinE was performed essentially as described earlier⁹. For a detailed protocol see Ramm and Glock et al⁶⁶. In brief, proteins were purified via Ni-NTA affinity purification. Protein was further purified using gel filtration chromatography in storage buffer (50 mM HEPES, pH 7.25, 150 mM KCl, 10% Glycerol, 0.1 mM EDTA). Proteins were quick-frozen and stored in aliquots at -80°C until further use.

Purification of FtsA was performed similar as described earlier⁴⁹. FtsA was expressed as His-SUMO-Gly5 fusion from plasmid pML60⁴⁹ in *E. coli* OverExpress™ C41(DE3) pLysS (Sigma-Aldrich, St. Louis, USA) in autoinduction medium (ZYM5052)⁶⁷. Cells were lysed in lysis buffer (50 mM Tris-HCl pH 8.0, 500 mM NaCl, 10 mM MgCl₂, 10 mM imidazole, 0.4 mM TCEP, 1 mM ADP and 10 mM CHAPS, EDTA-free complete plus protease inhibitor (Roche, Basel, Switzerland), 10 U/ml DNase 1, 100 $\mu\text{g}/\text{ml}$ lysozyme) by sonication with a tip sonicator (2.30 min, 30 s pulses, 30% amplitude). After centrifugation to clear cell debris (30 min, 25,000 $\times g$, 4 $^{\circ}\text{C}$) the lysate was incubated with Ni-NTA agarose (Qiagen, Hilden, Germany) for 30 min. The agarose beads were washed thrice with wash buffer (50 mM Tris-HCl pH 8.0, 500 mM KCl, 10 mM MgCl₂, 20 mM imidazole, 0.4 mM TCEP, 1 mM ADP), subsequently protein was eluted (50 mM Tris-HCl pH 8, 500 mM KCl, 10 mM MgCl₂, 200 mM imidazol, 1 mM CHAPS, 0.4 mM TCEP, 1 mM ADP). Buffer was exchanged to labeling buffer (50 mM HEPES/NaOH pH 7.5, 500 mM KCl, 10 mM MgCl₂, 10 mM CaCl₂, 10% glycerol, 0.4 mM TCEP, 1 mM ADP) using a Econo-Pac 10DG desalting column (Biorad, Hercules, USA). About 50 μM SUMO-Gly5-FtsA was incubated with 1 μM SenP2, 50 μM Sortase A (highly efficient mutant)⁶⁸, 0.3 mM Cy5-LPETGG in labeling buffer for 2–3 h. Cy5-LPETGG was produced by solid-phase peptide synthesis using Fmoc chemistry. Cy5-FtsA was separated from SenP2, Sortase, non-reacted peptide and non-cleaved protein by gel-filtration chromatography on a 16/600 Superdex 200 pg column (GE Healthcare, Pittsburgh, USA) equilibrated in storage buffer (50 mM HEPES/NaOH pH 7.5, 500 mM KCl, 10 mM MgCl₂, 10% glycerol, 0.4 mM TCEP, 1 mM ADP). Protein aliquots were quick-frozen and stored at -80°C .

All mCh-MTS constructs were expressed in *E. coli* BL21 (DE3) (Agilent Technologies, Santa Clara, USA) in TB medium. Medium was inoculated from an overnight culture and cells were grown to an OD₆₀₀ of 0.5–0.8 at 37 $^{\circ}\text{C}$. Subsequently cells were induced with 0.5 mM IPTG and shifted to 16 $^{\circ}\text{C}$ for protein expression. After 12–16 h, cells were harvested by centrifugation and cell pellets were stored at -20°C until further use. For purification, cell pellets were resuspended in lysis buffer (50 mM Tris-HCl pH 8.0, 300 mM NaCl, 10 mM Imidazole, 0.4 mM TCEP, EDTA-free complete plus protease inhibitor (Roche), 10 U/ml DNase 1, 100 $\mu\text{g}/\text{ml}$ lysozyme) and lysed by sonication with a tip sonicator (2.30 min, 30 s pulses, 30% amplitude). After centrifugation to clear cell debris (45 min, 25,000 $\times g$, 4 $^{\circ}\text{C}$), the lysate was incubated with Ni-NTA agarose (Qiagen, Hilden, Germany) for 1 h. Beads were washed with wash buffer thrice (50 mM Tris-HCl pH 8.0, 300 mM NaCl, 20 mM imidazole, 10% glycerol, 0.4 mM TCEP) and subsequently the protein was eluted with elution buffer (50 mM Tris-HCl pH 8.0, 300 mM NaCl, 250 mM imidazole, 10% glycerol, 0.4 mM TCEP). Purity was assessed with SDS-PAGE and buffer was exchanged to storage buffer (50 mM HEPES/NaOH pH 7.25, 150 mM KCl, 0.1 mM EDTA, 10% glycerol, 0.4 mM TCEP) using a Econo-Pac 10DG desalting column (Biorad, Hercules, USA). Aliquots were snap-frozen and stored until further use at -80°C .

FtsZ-YFP-mts protein was purified as previously described⁴⁸ according to a protocol from Osawa et al.⁴⁷ Briefly, the protein was expressed in *E. coli* BL21 (DE3) (Laboratory of German Rivas, CIB, CSIC, Madrid, Spain). Cells were grown

until OD₆₀₀ of 0.8 and then protein expression was induced by addition of 0.5 mM IPTG and cells were shifted to 20 °C. After growth for 14–16 h cells were harvested by centrifugation at 3200 rpm and 4 °C. Subsequently, FtsZ-YFP-MTS was precipitated from the supernatant through 30% ammonium sulfate and a 20 min incubation on ice while slowly shaking. After centrifugation (3200 rpm, 4 °C) and re-suspension of the pellet, the protein was purified by anion exchange chromatography using a 5 × 5 ml Hi-Trap Q-Sepharose column (GE Healthcare, Chicago, USA).

Purity and integrity of all proteins was assessed using SDS-PAGE and mass spectrometry. All protein concentrations were measured using Bradford assay and the fluorescent fraction of every protein was determined by absorption spectroscopy using a V-650 spectrophotometer (Jasco, Pfungstadt, Germany).

Preparation of supported lipid bilayers. Coverslips were rubbed and rinsed with EtOH and ddH₂O and a plastic ring was glued on top to generate a sample chamber. The slide was further cleaned in a plasma cleaner (model Zepto, Diener electronic, Ebhausen, Germany) for 1 min at 30% power and 0.3 mbar with oxygen as process gas. All lipids were purchased from Avanti Polar Lipids (Alabaster, AL, USA). Small unilamellar vesicles were prepared at a concentration of 4 mg/ml in buffer A (25 mM Tris-HCl pH 7.5, 150 mM KCl, 5 mM MgCl₂) for DOPC/DOPG mixtures or buffer B (25 mM Tris-HCl pH 7.5, 150 mM KCl) for *E. coli* polar lipid extract. Unless otherwise noted the lipid composition was 70 mol % DOPC and 30 mol % DOPG, previously shown to yield similar MinDE behavior as on *E. coli* polar lipid extract^{10,11}. Lipids dissolved in chloroform were dried under a nitrogen stream and vials were placed in a desiccator to remove residual chloroform for at least 30 min. Afterwards lipids were slowly rehydrated in Buffer A or B and SUVs were generated by sonication in a sonicator bath until the solution appeared clear. To generate supported lipid bilayers (SLB) SUVs were added to the reaction chamber at a concentration of 0.5 mg/ml in buffer A for DOPC/DOPG mixtures or buffer C (25 mM Tris-HCl pH 7.5, 150 mM KCl, 3 mM CaCl₂) for *E. coli* polar lipid extract. After 4 min incubation on a 37 °C warm heating block, the SLB was washed 10 times with a total of 2 ml buffer B to remove excess vesicles. Before self-organization assays, the buffer in the chamber was exchanged with reaction buffer (25 mM Tris-HCl pH 7.5, 150 mM KCl, 5 mM MgCl₂).

Self-organization assays. Self-organization assays were performed similar as described earlier^{9,66}. Self-organization assays were performed on preformed SLBs in 200 µl reaction buffer (25 mM Tris-HCl pH 7.5, 150 mM KCl, 5 mM MgCl₂) supplemented with 2.5 mM Mg-ATP (stock: 100 mM ATP in 100 mM MgCl₂, adjusted to pH 7.5) and at a constant room temperature of 23 °C. MinD and MinE were used at 1 µM protein concentration each unless otherwise noted. MinC if included was used at a final concentration of 0.05 µM. For labeling MinD was doped with 30 mol % of EGFP-MinD/mRuby3-MinD in each case. For experiments with mCh-MTS constructs, all proteins were added to the sample chamber first (order MinD, MinE, (MinC), mCh-MTS) and then the reaction was started by addition of Mg-ATP. Sample chambers were mixed by pipetting, lidded and incubated for 1 h before image acquisition. For z-stack acquisition to determine membrane binding of mCh-MTS constructs, mCh-MTS was incubated at 1 µM final concentration in the absence of MinDE on labeled, preformed SLBs (70 mol % DOPC, 30 mol % DOPG, 0.05 mol % ATTO655-PE) in reaction buffer for more than 1 h before image acquisition.

Experiments with FtsA were conducted at 0.4 µM final concentration in 200 µl reaction buffer 2 (pH 7.5, 12.5 mM Tris-HCl, 25 mM HEPES/KOH, 325 mM KCl, 5% glycerol, 7.5 mM MgCl₂). FtsA was added directly after MinDE and before ATP addition, samples were mixed, lidded and reaction was started with 2.5 mM ATP directly before image acquisition.

Self-organization assays in the presence of FtsZ-YFP-MTS were performed in 200 µl reaction buffer. Proteins were added to the chamber first (1 µM MinD (30% mRuby3-MinD), 1 µM MinE, with and without 0.05 µM MinC, 0.5 µM FtsZ-YFP-MTS). Samples were mixed and lidded and self-organization of MinDE and FtsZ-YFP-MTS was started by addition of 2.5 mM Mg-ATP and 0.4 or 4 mM GTP, for high and low free Mg²⁺ concentrations, respectively. Image acquisition was started after 10 min of incubation with ATP and GTP.

Streptavidin-bound membranes. All three streptavidin forms used (non-labeled, Alexa647-labeled or Alexa488-labeled) were purchased from ThermoFisher Scientific (Waltham, USA). For experiments involving streptavidin anchored to biotinylated lipids SLBs were prepared as described above with the lipid composition of 69 mol % DOPC/30 mol % DOPG/1 mol % Biotinyl-CAP-PE or *E. coli* polar lipid extract doped with 1 mol % of Biotinyl-CAP-PE. After formation of SLBs the buffer was exchanged to 200 µl reaction buffer and streptavidin was added at concentration of 1 µg/ml. Chambers were incubated for 30–60 min at room temperature. Subsequently unbound streptavidin was removed from the chambers by washing five times with a total volume of 1 ml reaction buffer. MinD and MinE were added at 1 µM each in a total of 200 µl reaction buffer and the reaction was started directly before imaging by addition of ATP to a final concentration of 2.5 mM.

Inducing MinDE detachment with sodium orthovanadate. Na₃VO₄ stock solution was prepared from powder (Merck, Darmstadt, Germany) at a concentration of 200 mM. The solution was adjusted to pH 10 and heated alternately until the solution remained clear and colorless. MinDE self-organization in the presence of streptavidin was set up as described above. Self-organization of MinDE in the presence of streptavidin was imaged using definite focus. After several images, the scan head of the microscope was lifted to add Na₃VO₄ to the reaction at a final concentration of 2.5 mM. The opening of the scan head during the addition of Na₃VO₄ resulted in black images.

PDMS microcompartment preparation. Positive resist master molds of about 8 µm thickness were produced on a 4 inch silicon wafer (University Wafer) using ma-P 1275 (Microresist technology GmbH, Berlin, Germany) and a chrome mask (Compugraphics Jena GmbH, Jena, Germany), according to the manufacturer's data sheet and developed in ma-D531 (Microresist technology GmbH)¹⁰. We then spin-coated 200 µl of 1:20 Cytop CTL-809M in CTSolv.100E (both from Asahi Glass Co. Ltd., Japan) onto the master to covalently anchor the coating, before being allowed to slowly cool down to room temperature by turning off the hot plate.

PDMS base and curing agent (Sylgard 184, Dow Corning Corporation, Michigan, USA) were mixed at a ratio of 10:1 in an ARE-250 mixer (Thinky Corporation, Tokyo, Japan). A drop of about 1–2 µl of PDMS was carefully placed on the master. Then a coverslide (thickness #1) was dropped on top and gently pressed down to squeeze the PDMS into a thin film. The wafer was then placed into an oven at 75 °C for at least one hour. Using a razor blade the coverslides with attached PDMS were removed from the Si wafer and a plastic sample chamber was glued onto the PDMS-covered slide. Directly before preparation of supported lipid bilayers the PDMS covered slide was placed into an oxygen plasma cleaner (Zepto, Diener electronic) and cleaned (1 min, 30% power, 0.3 mbar).

Self-organization assay in PDMS microcompartments. Self-organization assays in microcompartments were performed essentially as described earlier^{10,66}. The self-organization assay was set up in 200 µl reaction buffer with 2.5 mM ATP, 1 µM MinD and 2 or 3 µM MinE. 0.5 µM mCh-MTS(BsD) was used for experiments with peripheral membrane proteins. In the case of lipid-anchored streptavidin membranes were prepared as described in streptavidin-bound membranes. After regular MinDE wave patterns formed on the surface of the PDMS, the volume of the buffer was lowered to the rim of the compartments by carefully removing buffer with a pipette. Hence, protein concentration inside the microcompartments are likely to be higher than original concentrations and are not comparable even between microcompartments in the same reaction chamber. A piece of sponge moistened in reaction buffer was plugged inside the reaction chamber to avoid drying of microcompartments and the chamber was sealed with a lid.

Cholesterol-anchored and soluble P1 dsDNA fragments. The DNA oligonucleotides FW_P1_30bp_sol, RV_P1_30bp_Al647 and FW_P1_30bp_chol were purchased from Eurofins Genomics (Ebersberg, Germany) and Sigma-Aldrich (St. Louis, USA), respectively. For DNA duplex formation oligonucleotides were dissolved in ddH₂O at 100 µM. The complementary oligonucleotides were mixed in buffer (10 mM Tris-HCl pH 8.0, 1 mM EDTA, 50 mM NaCl) at a concentration of 10 µM each. They were annealed by slow cooling from 95 °C to room temperature in a heating block yielding 10 µM DNA duplexes. DNA duplex were added to self-organization assays at a final concentration of 10 or 100 nM, directly after MinDE addition. The sample was mixed by pipetting, lidded and incubated for more than 1 h before image acquisition.

DNA anchored to lipid-anchored streptavidin. The 300 and 2000 bp linear DNA fragments were generated by amplifying the first 300/2000 bp of lambda DNA (NEB, Ipswich, USA) by PCR using the forward primer BR215_Cy5_tetO_-lambda_fw and the reverse primers BR120_5'BiotinTEG_l300_rev and BR122_5'BiotinTEG_l2000rev (Sigma-Aldrich), respectively. The resulting PCR products were biotinylated and labeled with Cy5 on opposite ends. PCR products were purified and purity and labeling was assessed by gel electrophoresis. SLBs were generated as described under streptavidin-bound membranes using non-labeled streptavidin. After removal of surplus streptavidin from the reaction chamber, reaction buffer was added to a volume of about 50 µl and 6 pmol/2 pmol of the 300 bp/2000 bp long PCR product was added. DNA containing chambers were incubated for 2–3 h, then unbound DNA was removed by gently washing three times with a total of 600 µl reaction buffer. To start self-organization 1 µM MinD with 30% mol EGFP-MinD, 1 µM MinE, and 2.5 mM ATP in a total of 200 µl reaction buffer were added.

Microscopy. All images unless otherwise mentioned were taken on a Zeiss LSM780 confocal laser scanning microscope using a Zeiss C-Apochromat 40x/1.20 water-immersion objective (Carl Zeiss AG, Oberkochen, Germany). Longer time-series were acquired using the built in definite focus system. All two-color images were acquired with alternating illumination to avoid cross-talk. EGFP-MinD was excited

using the 488 nm Argon laser, mCh-MTS constructs using the 561 nm DPSS laser and streptavidin-Alexa647 or Cy5-DNA using the 633 nm He-Ne laser. Images were typically recorded with a pinhole size of 1 Airy unit, 512×512 pixel resolution, and a scan rate of $1.58 \mu\text{s}$ per pixel. Time-series for EGFP-MinD and mCh-MTS constructs were acquired with ~ 4 s intervals, EGFP-MinD and streptavidin-Alexa647 with ~ 5 s intervals.

Images in total internal reflection fluorescence (TIRF) microscopy were acquired on a custom-built TIRF microscope⁶⁹ using a NIKON SR Apo TIRF 100x/1.49 oil-immersion objective, constructed around a Nikon Ti-S microscope body (both Nikon GmbH, Düsseldorf, Germany). Two laser lines (490 nm (Cobolt Calypso, 50 mW nominal) and 640 nm (Cobolt 06-MLD, 140 mW nominal, both Cobolt AB, Solna, Sweden)) were controlled in power and timing (AOTF, Gooch&Housego TF-525-250, Illminster, UK) and spatially filtered (kineFLEX-P-3-S-405.640-0.7-FCS-P0, Qioptiq, Hamble, UK). The beam was further collimated, expanded (3 \times) and focused on the objective's back aperture by standard achromatic doublet lenses. The TIRF angle was controlled by precise parallel offset of the excitation beam (Q545, PI, Karlsruhe, Germany). For detection, two channels were separated by a dichroic mirror (Chroma T555lpxr-UF1), bandpass filtered (Chroma ET525/50m and ET670/30m, all Chroma Technology Cooperation, Bellow Falls, VT) and re-positioned on two halves of the EMCCD camera (Andor iXon Ultra 897). Images were recorded with Andor Solis (Ver. 4.28, both Andor Technologies, Belfast, UK).

Image analysis. All images were processed using Fiji⁷⁰ (version v1.51q) or Matlab (R2016a, The MathWorks, Natick, USA). Brightness or contrast adjustments of displayed images were applied homogeneously.

Analysis of mean fluorescence intensities. Dual color time-series or tile scans were imported into Fiji and split into two separate image stacks. The EGFP-MinD stack was used to segment the MinDE waves in the images. To this end we used a custom-written ImageJ macro where the image from the EGFP-MinD channel was filtered using a median filter with radius 3–6 pixels, subsequently a “Pseudo-flat field correction” (BioVoxel macro, Jan Brocher) with radius 75 pixels was applied to remove unequal illumination. The resulting image was thresholded using the Huang method or in the case of experiments with FtsZ-YFP-MTS or MinDE titration with the Li method, to generate the binary mask of the MinDE wave. This mask was also inverted to generate the complimentary mask.

The original non-modified images from the two spectral channels and the two complementary binary masks were imported into Matlab (R2016a, The MathWorks, Natick, USA) and analyzed using a custom-written Matlab code. The average fluorescence intensity in the mCherry/FtsZ-YFP-MTS ($I_{\text{mCh-MTS}}^{\text{mCh-MTS}} / I_{\text{FtsZ-YFP-MTS}}^{\text{FtsZ-YFP-MTS}}$) and EGFP-MinD/mRuby3-MinD ($I_{\text{EGFP-MinD}}^{\text{EGFP-MinD}} / I_{\text{mRuby3-MinD}}^{\text{mRuby3-MinD}}$) spectral channel was obtained by pooling the means of individual images from one independent experiment. To obtain the average fluorescence intensity in the MinDE minima ($I_{\text{min(MinD)}}^{\text{mCh-MTS}} / I_{\text{min(MinD)}}^{\text{EGFP-MinD}}$) and maxima ($I_{\text{max(MinD)}}^{\text{mCh-MTS}} / I_{\text{max(MinD)}}^{\text{EGFP-MinD}}$) the binary masks were multiplied with the original images of the respective spectral channels, all zero values were removed and the mean was taken. All means from one independent experiment and condition were pooled together. All fluorescence intensity values from one experimental set were normalized to the fluorescence intensity values obtained for His-mCherry for experiments with mCh-MTS and to a fluorescent standard for experiments with FtsZ-YFP-MTS. The contrast of the resulting protein waves was calculated for every individual image as the difference between the average intensity in the MinDE minima and MinDE maxima ($I_{\text{min(MinD)}}^{\text{protein}} - I_{\text{max(MinD)}}^{\text{protein}}$) divided by the average intensity in the MinDE maxima ($I_{\text{max(MinD)}}^{\text{protein}}$).

Image preprocessing of FtsZ-YFP-MTS kymographs. Image stacks were blurred (Gaussian blur) using Fiji. Afterwards every image was divided by its mean. This processed stack was used to produce kymographs shown in Fig. 5b.

Analysis of fluorescence profiles in microcompartments. Time-series from microcompartments were averaged in Fiji (version v1.51q) and the resulting average intensity was plotted over the full compartment and exported as csv file. Furthermore kymographs of every individual microcompartment were generated and used to assess MinDE oscillations. Microcompartments not showing MinDE oscillations were removed from further analysis.

To analyze the temporal averages of the spatial protein distributions in the microcompartments, we projected the fluorescence signal for each compartment on its elongated axis using Fiji. The obtained profiles (examples for EGFP-MinD (blue) and streptavidin (red) in Supplementary Fig. 14) were analyzed using a home-written MATLAB code (R2016a, The MathWorks). In a first step, the edge of the microcompartments was located along the MinD profile (blue line in Supplementary Fig. 14) based on the increase of EGFP signal and the concomitant change of the first spatial derivative. The initial profiles were clipped accordingly. Subsequently, the two local maxima of the MinD profile were located in a two step procedure: First, their location was roughly estimated based on a polynomial fit of fourth order. Second, a 40 pixel region of interest was selected around these estimated positions and the corresponding section of the profile was fitted with a

quadratic function to locate the maximum more precisely. The positions of the located maxima are defining the edges of a unit box, onto which the profiles of both spectral channels were projected. We were seeking an easy way to classify the profiles in this unit box and therefore decided to fit the profiles with a quadratic function $f(x) = ax^2 + b$ (black dashed lines in Supplementary Fig. 14a), where $2a$ represents the overall curvature and hence the steepness of the profile and b accounts for the offset. As we projected the profiles onto a unit box of length 1, the depth of the profile and the curvature are identical, except for a constant prefactor, and are thus interchangeable terms. Homogeneously distributed fluorescence corresponds to a curvature of $a \approx 0$. A spatial distribution with enrichment in the center of the compartment yields $a < 0$, whereas proteins that are on average less likely to be found in the center will be classified with a curvature $a > 0$. In this classification, the MinD profile has a curvature $a > 0$.

Data availability

Data supporting the findings of this manuscript are available from the corresponding author upon reasonable request. The custom-written code for the analysis of the time-averaged fluorescence profiles in microcompartments can be found on github (https://github.com/BeaRamm/intensity_profiles). All other code is available from the corresponding authors upon reasonable request.

Received: 2 February 2018 Accepted: 10 August 2018

Published online: 26 September 2018

References

- Lutkenhaus, J. The ParA/MinD family puts things in their place. *Trends Microbiol.* **20**, 411–418 (2012).
- Surovtsev, I. V. & Jacobs-Wagner, C. Subcellular organization: a critical feature of bacterial cell replication. *Cell* **172**, 1271–1293 (2018).
- Leonard, T. A., Butler, P. J. & Löwe, J. Bacterial chromosome segregation: structure and DNA binding of the Soj dimer—a conserved biological switch. *EMBO J.* **24**, 270–282 (2005).
- Thanbichler, M. & Shapiro, L. MipZ, a spatial regulator coordinating chromosome segregation with cell division in *caulobacter*. *Cell* **126**, 147–162 (2006).
- Schumacher, D. et al. The PomXYZ proteins self-organize on the bacterial nucleoid to stimulate cell division. *Dev. Cell* **41**, 299–314 (2017).
- Roberts, M. A. J., Wadhams, G. H., Hadfield, K. A., Tickner, S. & Armitage, J. P. ParA-like protein uses nonspecific chromosomal DNA binding to partition protein complexes. *Proc. Natl Acad. Sci. USA* **109**, 6698–6703 (2012).
- Raskin, D. M. & De Boer, P. A. J. MinDE-dependent pole-to-pole oscillation of division inhibitor MinC in *Escherichia coli*. *J. Bacteriol.* **181**, 6419–6424 (1999).
- Wu, F., van Schie, B. G. C., Keymer, J. E. & Dekker, C. Symmetry and scale orient Min protein patterns in shaped bacterial sculptures. *Nat. Nanotechnol.* **10**, 719–726 (2015).
- Loose, M., Fischer-Friedrich, E., Ries, J., Kruse, K. & Schwille, P. Spatial regulators for bacterial cell division self-organize into surface waves in vitro. *Science* **320**, 789–792 (2008).
- Zieske, K. & Schwille, P. Reconstitution of self-organizing protein gradients as spatial cues in cell-free systems. *eLife* **3**, e03949 (2014).
- Vecchiarelli, A. G., Li, M., Mizuuchi, M. & Mizuuchi, K. Differential affinities of MinD and MinE to anionic phospholipid influence Min patterning dynamics in vitro. *Mol. Microbiol.* **93**, 453–463 (2014).
- Meinhardt, H. & de Boer, P. A. J. Pattern formation in *Escherichia coli*: a model for the pole-to-pole oscillations of Min proteins and the localization of the division site. *Proc. Natl Acad. Sci. USA* **98**, 14202–14207 (2001).
- Halatek, J. & Frey, E. Rethinking pattern formation in reaction-diffusion systems. *Nat. Phys.* **14**, 507–514 (2018).
- Raskin, D. M. & de Boer, P. A. J. Rapid pole-to-pole oscillation of a protein required for directing division to the middle of *Escherichia coli*. *Proc. Natl Acad. Sci. USA* **96**, 4971–4976 (1999).
- de Boer, P. A. J., Crossley, R. E. & Rothfield, L. I. A division inhibitor and a topological specificity factor coded for by the minicell locus determine proper placement of the division septum in *E. coli*. *Cell* **56**, 641–649 (1989).
- Szeto, T. H., Rowland, S. L., Rothfield, L. I. & King, G. F. Membrane localization of MinD is mediated by a C-terminal motif that is conserved across eubacteria, archaea, and chloroplasts. *Proc. Natl Acad. Sci. USA* **99**, 15693–15698 (2002).
- Hu, Z. & Lutkenhaus, J. Topological regulation of cell division in *E. coli*: Spatiotemporal oscillation of MinD requires stimulation of its ATPase by MinE and phospholipid. *Mol. Cell* **7**, 1337–1343 (2001).
- Loose, M., Fischer-Friedrich, E., Herold, C., Kruse, K. & Schwille, P. Min protein patterns emerge from rapid rebinding and membrane interaction of MinE. *Nat. Struct. Mol. Biol.* **18**, 577–583 (2011).

19. Dajkovic, A., Lan, G., Sun, S. X., Wirtz, D. & Lutkenhaus, J. MinC spatially controls bacterial cytokinesis by antagonizing the scaffolding function of FtsZ. *Curr. Biol.* **18**, 235–244 (2008).
20. Arumugam, S., Petrašek, Z. & Schwille, P. MinCDE exploits the dynamic nature of FtsZ filaments for its spatial regulation. *Proc. Natl Acad. Sci. USA* **111**, E1192–E1200 (2014).
21. Hu, Z., Mukherjee, A., Pichoff, S. & Lutkenhaus, J. The MinC component of the division site selection system in *Escherichia coli* interacts with FtsZ to prevent polymerization. *Proc. Natl Acad. Sci. USA* **96**, 14819–14824 (1999).
22. Marston, A. L., Thomaidis, H. B., Edwards, D. H., Sharpe, M. E. & Errington, J. Polar localization of the MinD protein of *Bacillus subtilis* and its role in selection of the mid-cell division site. *Genes Dev.* **12**, 3419–3430 (1998).
23. Rowlett, V. W. & Margolin, W. The Min system and other nucleoid-independent regulators of Z ring positioning. *Front. Microbiol.* **6**, 478 (2015).
24. Di Ventura, B. et al. Chromosome segregation by the *Escherichia coli* Min system. *Mol. Syst. Biol.* **9**, 686 (2013).
25. Lee, H.-L. et al. Quantitative proteomics analysis reveals the Min system of *Escherichia coli* modulates reversible protein association with the inner membrane. *Mol. Cell. Proteom.* **15**, 1572–1583 (2016).
26. Mulder, E., El'Bouhali, M., Pas, E. & Woldringh, C. L. The *Escherichia coli* minB mutation resembles gyrB in defective nucleoid segregation and decreased negative supercoiling of plasmids. *Mol. Genet. Genom.* **221**, 87–93 (1990).
27. Åkerlund, T., Gullbrand, B. & Nordström, K. Effects of the Min system on nucleoid segregation in *Escherichia coli*. *Microbiology* **148**, 3213–3222 (2002).
28. Jia, S. et al. Effect of the Min system on timing of cell division in *Escherichia coli*. *PLoS ONE* **9**, e103863 (2014).
29. Jun, S. & Mulder, B. Entropy-driven spatial organization of highly confined polymers: lessons for the bacterial chromosome. *Proc. Natl Acad. Sci. USA* **103**, 12388–12393 (2006).
30. Woldringh, C. L. The role of co-transcriptional translation and protein translocation (transertion) in bacterial chromosome segregation. *Mol. Microbiol.* **45**, 17–29 (2002).
31. Johnson, J. M., Jin, M. & Lew, D. J. Symmetry breaking and the establishment of cell polarity in budding yeast. *Curr. Opin. Genet. Dev.* **21**, 740–746 (2011).
32. Hoege, C. & Hyman, A. A. Principles of PAR polarity in *Caenorhabditis elegans* embryos. *Nat. Rev. Mol. Cell Biol.* **14**, 315–322 (2013).
33. Shaner, N. C., Steinbach, P. A. & Tsien, R. Y. A guide to choosing fluorescent proteins. *Nat. Methods* **2**, 905–909 (2005).
34. Szeto, T. H., Rowland, S. L., Habrukowich, C. L. & King, G. F. The MinD membrane targeting sequence is a transplantable lipid-binding helix. *J. Biol. Chem.* **278**, 40050–40056 (2003).
35. Martos, A. et al. FtsZ polymers tethered to the membrane by ZipA are susceptible to spatial regulation by Min waves. *Biophys. J.* **108**, 2371–2383 (2015).
36. Salje, J., van den Ent, F., de Boer, P. & Löwe, J. Direct membrane binding by bacterial actin MreB. *Mol. Cell* **43**, 478–487 (2011).
37. Pichoff, S. & Lutkenhaus, J. Tethering the Z ring to the membrane through a conserved membrane targeting sequence in FtsA. *Mol. Microbiol.* **55**, 1722–1734 (2005).
38. Parlitz, R. et al. *Escherichia coli* signal recognition particle receptor FtsY contains an essential and autonomous membrane-binding amphipathic helix. *J. Biol. Chem.* **282**, 32176–32184 (2007).
39. Dubacheva, G. V. et al. Controlling multivalent binding through surface chemistry: model study on streptavidin. *J. Am. Chem. Soc.* **139**, 4157–4167 (2017).
40. Darst, S. A. et al. Two-dimensional crystals of streptavidin on biotinylated lipid layers and their interactions with biotinylated macromolecules. *Biophys. J.* **59**, 387–396 (1991).
41. Hale, C. A. & De Boer, P. A. J. Direct binding of FtsZ to ZipA, an essential component of the septal ring structure that mediates cell division in *E. coli*. *Cell* **88**, 175–185 (1997).
42. Lutkenhaus, J., Pichoff, S. & Du, S. Bacterial cytokinesis: From Z ring to divisome. *Cytoskeleton* **69**, 778–790 (2012).
43. Szwedziak, P., Wang, Q., Bharat, T. A. M., Tsim, M. & Löwe, J. Architecture of the ring formed by the tubulin homologue FtsZ in bacterial cell division. *eLife* **3**, e04601 (2014).
44. Krupka, M. et al. *Escherichia coli* FtsA forms lipid-bound minirings that antagonize lateral interactions between FtsZ protofilaments. *Nat. Commun.* **8**, 15957 (2017).
45. Thanedar, S. & Margolin, W. FtsZ exhibits rapid movement and oscillation waves in helix-like patterns in *Escherichia coli*. *Curr. Biol.* **14**, 1167–1173 (2004).
46. Yang, X. et al. GTPase activity-coupled treadmilling of the bacterial tubulin FtsZ organizes septal cell wall synthesis. *Science* **355**, 744–747 (2017).
47. Osawa, M., Anderson, D. E. & Erickson, H. P. Reconstitution of contractile FtsZ rings in liposomes. *Science* **320**, 792–794 (2008).
48. Ramirez-Diaz, D. A. et al. Treadmilling analysis reveals new insights into dynamic FtsZ ring architecture. *PLoS Biol.* **16**, e2004845 (2018).
49. Loose, M. & Mitchison, T. J. The bacterial cell division proteins FtsA and FtsZ self-organize into dynamic cytoskeletal patterns. *Nat. Cell Biol.* **16**, 38–46 (2014).
50. Schweizer, J. et al. Geometry sensing by self-organized protein patterns. *Proc. Natl Acad. Sci. USA* **109**, 15283–15288 (2012).
51. Libby, E. A., Roggiani, M. & Goulian, M. Membrane protein expression triggers chromosomal locus repositioning in bacteria. *Proc. Natl Acad. Sci. USA* **109**, 7445–7450 (2012).
52. Pfeiffer, I. & Höök, F. Bivalent cholesterol-based coupling of oligonucleotides to lipid membrane assemblies. *J. Am. Chem. Soc.* **126**, 10224–10225 (2004).
53. Mileykovskaya, E. et al. Effects of phospholipid composition on MinD-membrane interactions in vitro and in vivo. *J. Biol. Chem.* **278**, 22193–22198 (2003).
54. Lackner, L. L., Raskin, D. M. & De Boer, P. A. J. ATP-dependent interactions between *Escherichia coli* Min proteins and the phospholipid membrane in vitro. *J. Bacteriol.* **185**, 735–749 (2003).
55. Miyagi, A., Ramm, B., Schwille, P. & Scheuring, S. High-speed AFM reveals the inner workings of the MinDE protein oscillator. *Nano. Lett.* **18**, 288–296 (2017).
56. Suefuji, K., Valluzzi, R. & Raychaudhuri, D. Dynamic assembly of MinD into filament bundles modulated by ATP, phospholipids, and MinE. *Proc. Natl Acad. Sci. USA* **99**, 16776–16781 (2002).
57. Hu, Z., Gogol, E. P. & Lutkenhaus, J. Dynamic assembly of MinD on phospholipid vesicles regulated by ATP and MinE. *Proc. Natl Acad. Sci. USA* **99**, 6761–6766 (2002).
58. Ghosal, D., Trambaiolo, D., Amos, L. A. & Löwe, J. MinCD cell division proteins form alternating copolymeric cytomotive filaments. *Nat. Commun.* **5**, 5341 (2014).
59. Oswald, F., Varadarajan, A., Lill, H., Peterman, E. J. G. & Bollen, Y. J. M. MreB-dependent organization of the *E. coli* cytoplasmic membrane controls membrane protein diffusion. *Biophys. J.* **110**, 1139–1149 (2016).
60. Strahl, H., Bürmann, F. & Hamoen, L. W. The actin homologue MreB organizes the bacterial cell membrane. *Nat. Commun.* **5**, (2014).
61. Chichili, G. R. & Rodgers, W. Cytoskeleton-membrane interactions in membrane raft structure. *Cell. Mol. Life Sci.* **66**, 2319–2328 (2009).
62. Jamroškovič, J., Pavlendová, N., Muchová, K., Wilkinson, A. J. & Barák, I. An oscillating Min system in *Bacillus subtilis* influences asymmetrical septation during sporulation. *Microbiology* **158**, 1972–1981 (2012).
63. Li, G. & Young, K. D. Isolation and identification of new inner membrane-associated proteins that localize to cell poles in *Escherichia coli*. *Mol. Microbiol.* **84**, 276–295 (2012).
64. Bisicchia, P., Arumugam, S., Schwille, P. & Sherratt, D. MinC, MinD, and MinE drive counter-oscillation of early-cell-division proteins prior to *Escherichia coli* septum formation. *mBio* **4**, e00856–13 (2013).
65. Glock, P. et al. Optical control of a biological reaction-diffusion system. *Angew. Chemie Int. Ed.* **57**, 2362–2366 (2018).
66. Ramm, B., Glock, P. & Schwille, P. In vitro reconstitution of self-organizing protein patterns on supported lipid bilayers. *JoVE* e58139, <https://doi.org/10.3791/58139> (2018).
67. Studier, F. W. in *Structural Genomics: General Applications*, Vol 1091 (ed. Chen, Y. W.) 315–331 (Humana Press: Totowa, NJ <https://link.springer.com/book/10.1007%2F978-1-62703-691-7#about> (2014).
68. Freiburger, L. et al. Efficient segmental isotope labeling of multi-domain proteins using Sortase A. *J. Biomol. NMR* **63**, 1–8 (2015).
69. Mücksch, J. et al. Quantifying reversible surface binding via surface-integrated fluorescence correlation spectroscopy. *Nano. Lett.* **18**, 3185–3192 (2018).
70. Schindelin, J. et al. Fiji: an open-source platform for biological-image analysis. *Nat. Methods* **9**, 676–682 (2012).

Acknowledgements

We thank MPIB Core Facility for assistance in protein purification, Stephan Uebel for peptide synthesis, Katharina Nakel and Michaela Schaper for assistance with cloning, Lei Kai for plasmid pCoofy1-mCherry, Martin Loose for plasmid pML60, Frank Siedler for help with Si wafer fabrication, Jan Brocher from BioVoxel for help with generating the Fiji macro and Ana Raso for establishing the FtsA purification protocol. Further we thank Kristina Ganzinger, Henri Franquelim, and Simon Kretschmer for helpful discussions, and Kristina Ganzinger and Hiromune Eto for comments on the manuscript. B. R. and D.G. are supported by a DFG fellowship through the Graduate School of Quantitative Biosciences Munich (QBM). B.R. and P.S. acknowledge funding through the DFG Collaborative Research Centre “Spatiotemporal dynamics of bacterial cells” (TRR 174/2017). P.S. acknowledges the support of the research network MaxSynBio via a joint funding initiative of the German Federal Ministry of Education and Research (BMBF) and the Max Planck Society. J.M. is grateful for financial support from the excellence cluster Nanosystems Initiative Munich. J.M., P.B. and P.G. acknowledge support from the International Max Planck Research School for Molecular Life Sciences. P.G. acknowledges support from GRK 2062—Molecular Principles of Synthetic Biology. MH

acknowledges support from the Joachim Herz Foundation through an Add-on Fellowship. We acknowledge support from the Center for NanoScience Munich.

Author contributions

B.R. designed and performed experiments. B.R. and P.S. conceived the study and wrote the manuscript. B.R. and J.M. analyzed the data. P.B. performed TIRF experiments. P.G. designed and purified proteins. M.H. manufactured Si wafer for microcompartments. D. G. purified FtsZ-YFP-MTS. All authors discussed and interpreted results and revised the manuscript.

Additional information

Supplementary Information accompanies this paper at <https://doi.org/10.1038/s41467-018-06310-1>.

Competing interests: The authors declare no competing interests.

Reprints and permission information is available online at <http://npg.nature.com/reprintsandpermissions/>

Publisher's note: Springer Nature remains neutral with regard to jurisdictional claims in published maps and institutional affiliations.



Open Access This article is licensed under a Creative Commons Attribution 4.0 International License, which permits use, sharing, adaptation, distribution and reproduction in any medium or format, as long as you give appropriate credit to the original author(s) and the source, provide a link to the Creative Commons license, and indicate if changes were made. The images or other third party material in this article are included in the article's Creative Commons license, unless indicated otherwise in a credit line to the material. If material is not included in the article's Creative Commons license and your intended use is not permitted by statutory regulation or exceeds the permitted use, you will need to obtain permission directly from the copyright holder. To view a copy of this license, visit <http://creativecommons.org/licenses/by/4.0/>.

© The Author(s) 2018

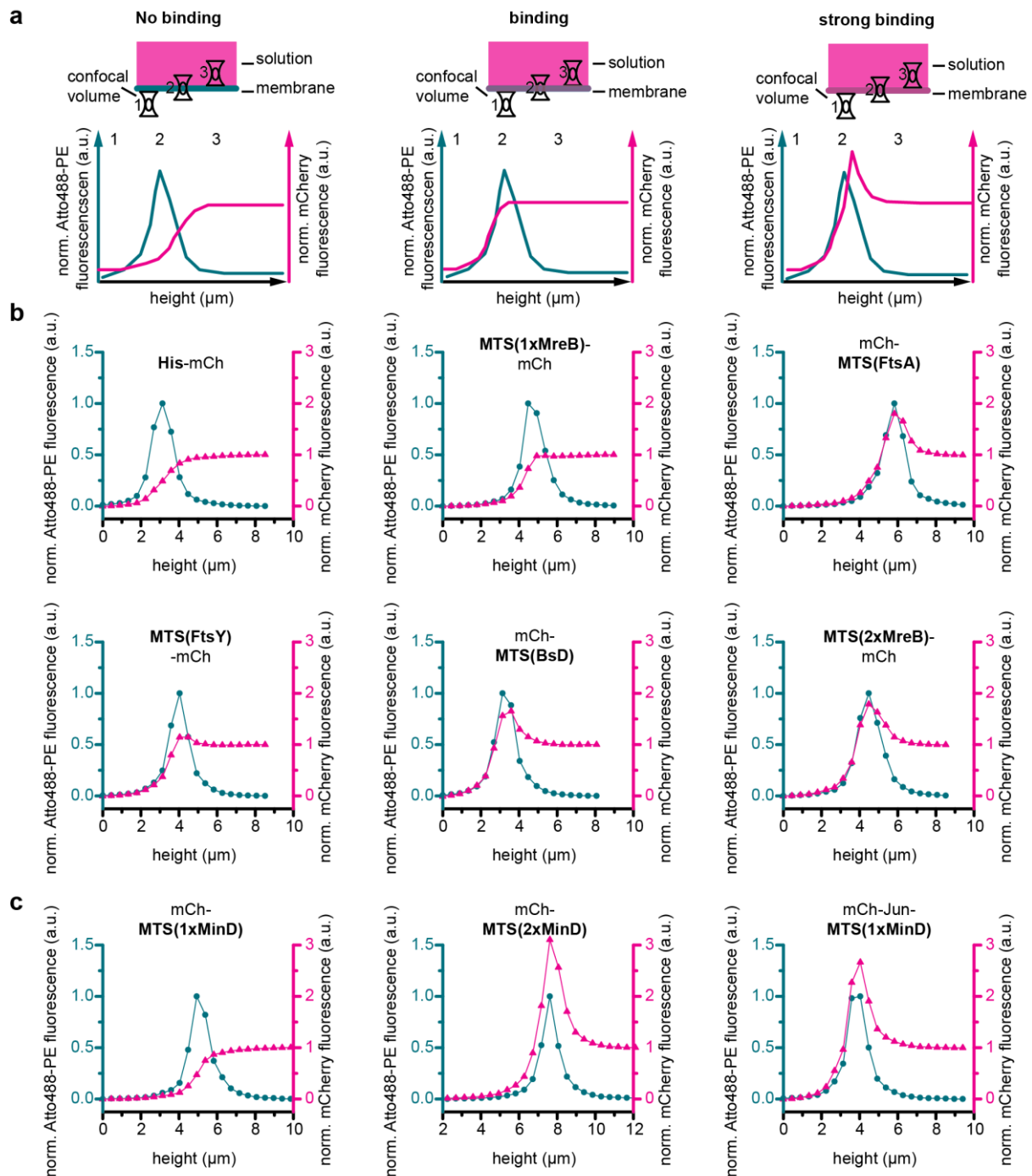
Supplementary Information

The MinDE system is a generic spatial cue for membrane protein distribution in vitro

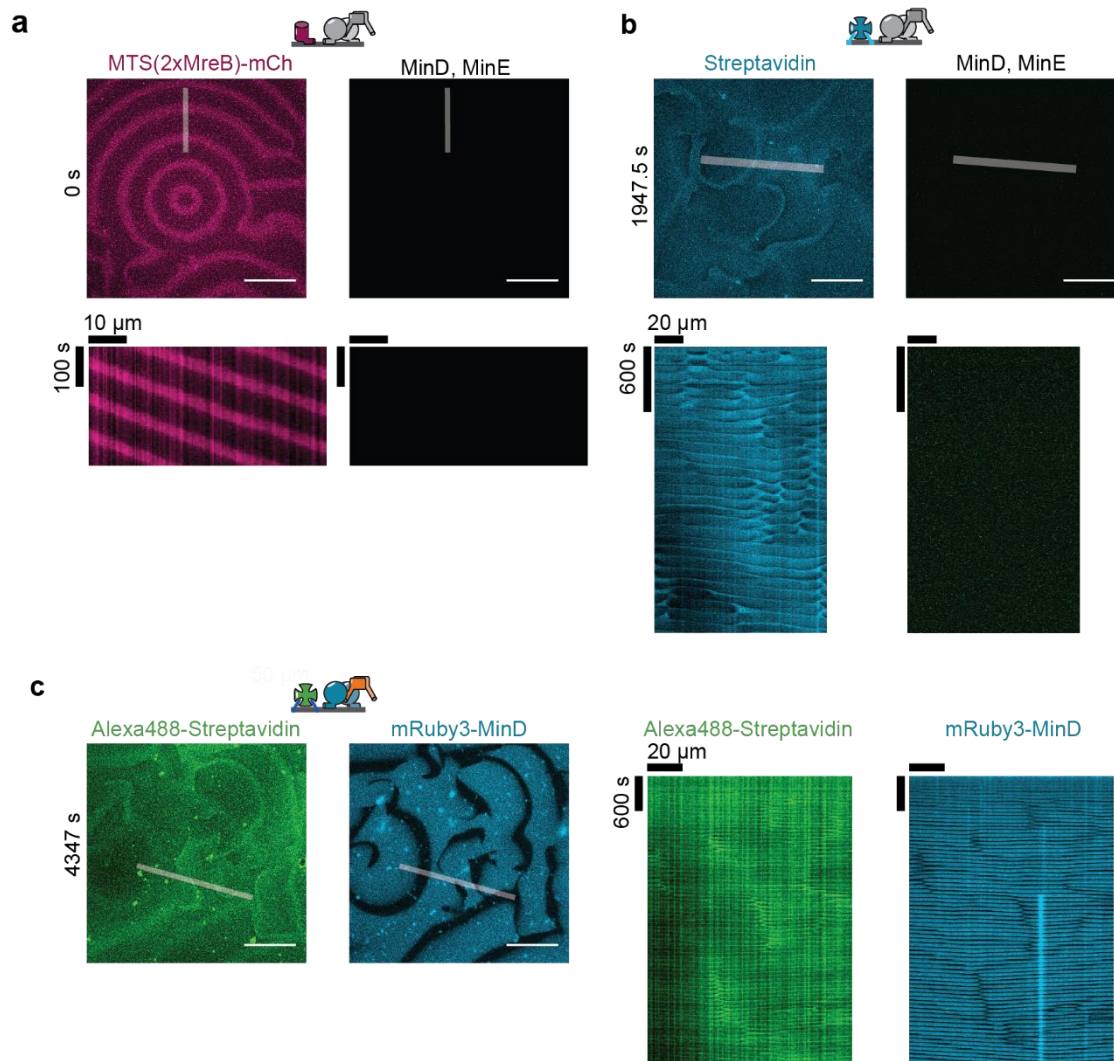
Beatrice Ramm¹, Philipp Glock¹, Jonas Mücksch¹, Philipp Blumhardt¹, Daniela A. García-Soriano¹, Michael Heymann¹, Petra Schwille^{1,*}

¹ Max Planck Institute of Biochemistry, Am Klopferspitz 18, D-82152 Martinsried, Germany.

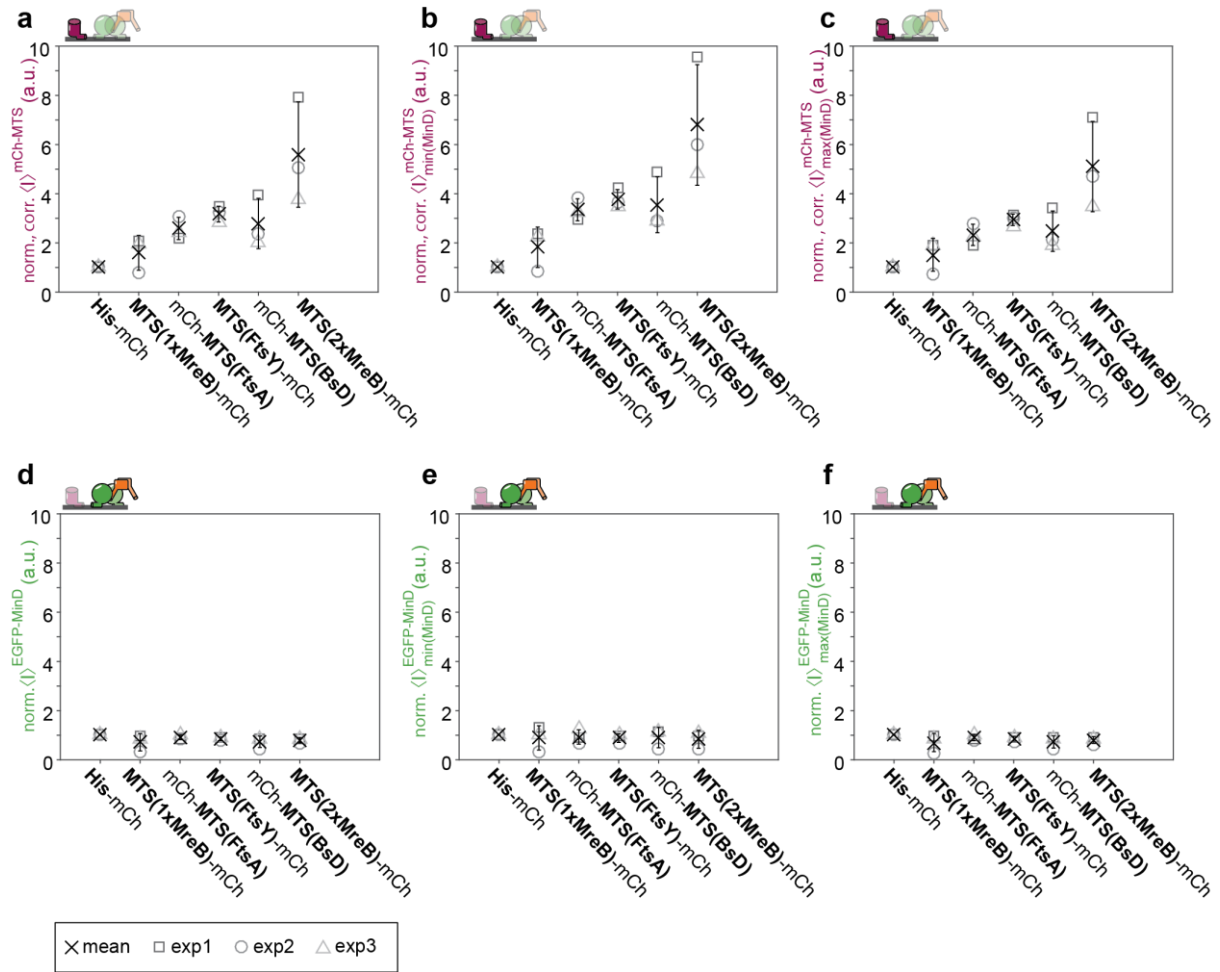
Correspondence and requests for materials should be addressed to P.S. (email: schwille@biochem.mpg.de)



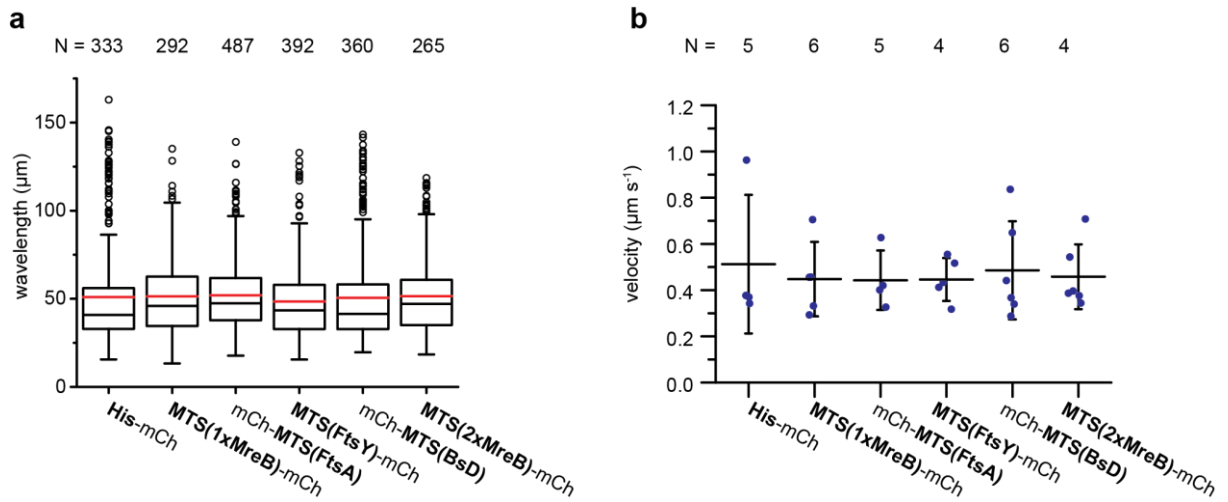
Supplementary Figure 1: Model peripheral membrane proteins, mCh-MTS constructs, bind to the membrane.
 a) Schematic explaining the experimental setup. Z-stacks of an assay chamber with a fluorescently labeled supported lipid bilayer (cyan) and the corresponding mCh-MTS constructs (magenta) are acquired (supported lipid bilayer (SLB): 70 mol % DOPC, 30 mol % DOPG, 0.05 mol % Atto655-PE, 1 μ M mCh-MTS). If no binding occurs, the fluorescence intensity signal of the mCh-MTS construct reaches its maximum spatially above the signal from the labeled SLB, when the confocal volume fully entered the solution. If weak binding occurs the maximum of the fluorescence intensity signal of the mCh-MTS coincides with the maximum of the SLB signal, as some of the protein is located on the membrane. If strong binding occurs and the mCh-MTS construct accumulates on the membrane, the signal of the mCh-MTS construct is higher on the membrane than in solution. b) Representative z-stacks of mCh-MTS constructs confirming binding of all mCh-MTS constructs except His-mCh. c) Representative z-stacks of mCh-MTS constructs harboring the *E. coli* MinD membrane targeting sequence (MTS). No binding can be detected for mCh-MTS(1xMinD), but strong binding for mCh-MTS(2xMinD) and mCh-Jun-MTS(1xMinD). mCh-MTS fluorescence (magenta triangles) is normalized to the first two values below the membrane and the last two values in solution. Atto-655-PE fluorescence (cyan spheres) is normalized to the minimal and maximal values.



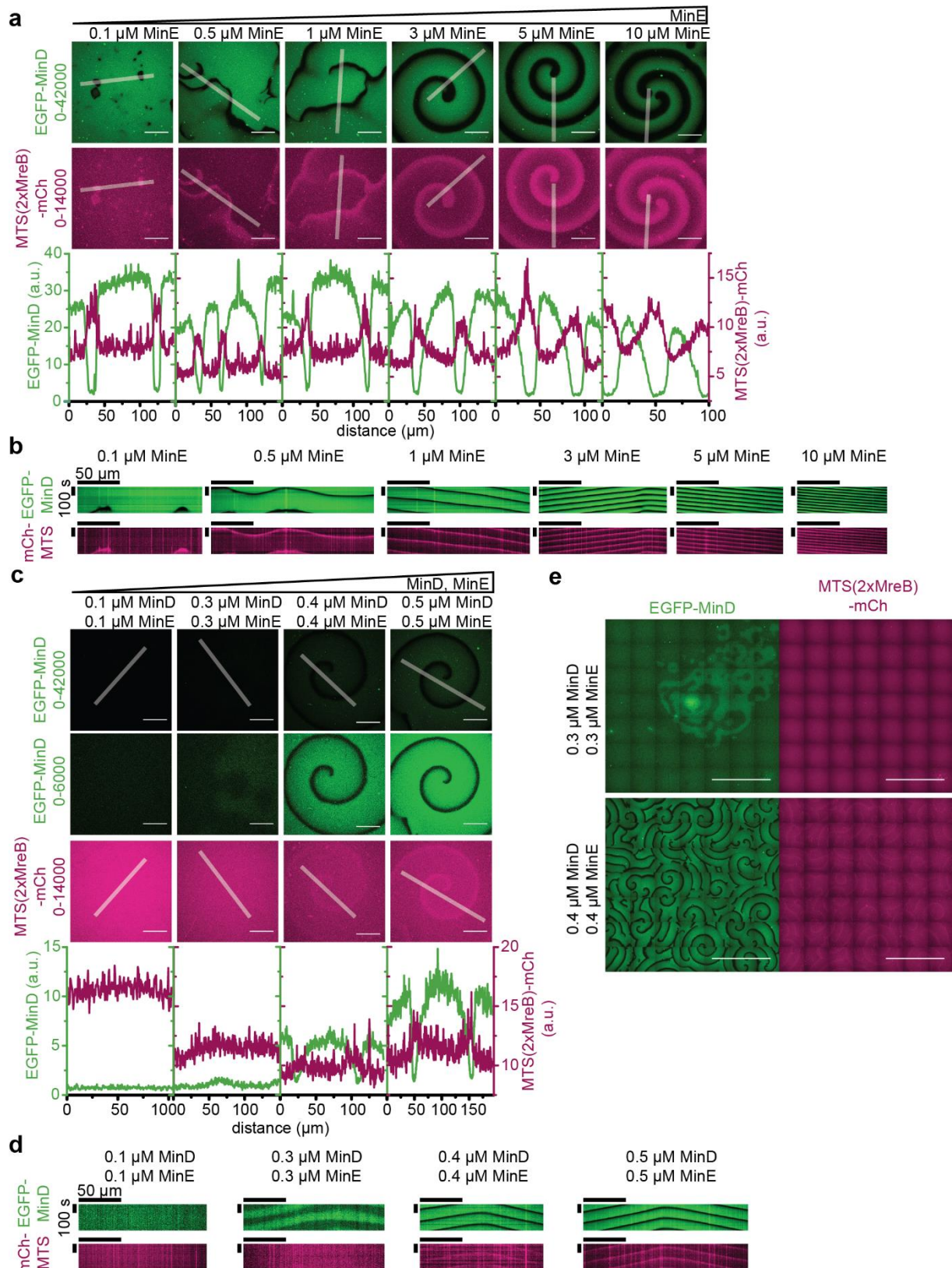
Supplementary Figure 2: Spatiotemporal regulation of MinDE is not a photoartifact. a) Positioning of MTS(2xMreB)-mCh by MinDE in the absence of labeled MinD/MinE (1 μ M MinD, 1 μ M MinE, 1 μ M MTS(2xMreB)-mCh, 2.5 mM ATP). b) Regulation of Alexa647-streptavidin anchored to biotinylated lipids by MinDE in the absence of labeled MinD/MinE (1 μ M MinD, 1 μ M MinE, Alexa647-streptavidin) c) Positioning of Alexa488-streptavidin by MinDE (1 μ M MinD (30 % mRuby3-MinD), 1 μ M MinE, Alexa488-streptavidin). Experiments were performed independently two (b and c) or three (a) times under identical or similar conditions.



Supplementary Figure 3: mCh-MTS constructs have different membrane affinities, but do not influence the membrane density of EGFP-MinD. a)-c) mCh-MTS intensity on the membrane, i.e. membrane affinity, increases from MTS(1xMreB)-mCh to MTS(2xMreB)-mCh. a) Average mCh-MTS intensity of the full image normalized to His-mCh and corrected for the fluorescent protein fraction ($\langle I \rangle^{mCh-MTS}$). b) Average mCh-MTS intensity in the MinDE wave minimum normalized to His-mCh and corrected for the fluorescent protein fraction ($\langle I \rangle_{\min(D)}^{mCh-MTS}$). c) Average mCh-MTS intensity in the MinDE wave maximum normalized to His-mCh and corrected for the fluorescent protein fraction ($\langle I \rangle_{\max(D)}^{mCh-MTS}$) (as shown in Fig. 2d). d)-f) EGFP-MinD intensity, i.e. density, on the membrane is not influenced by the addition of mCh-MTS constructs. d) Average EGFP-MinD intensity of the full image normalized to the fluorescence in the presence of His-mCh ($\langle I \rangle^{EGFP-MinD}$). e) Average EGFP-MinD intensity in the MinDE wave minimum normalized to the fluorescence in the presence of His-mCh ($\langle I \rangle_{\min(D)}^{EGFP-MinD}$). f) Average EGFP-MinD intensity in the MinDE wave maximum normalized to the fluorescence in the presence of His-mCh ($\langle I \rangle_{\max(D)}^{EGFP-MinD}$). Each data point (squares, spheres, triangles) (exp1-3) was generated from at least one tile scan (7 by 7) in one chamber. Cross and error bars represent the mean value and standard deviation of the three independent experiments with in total N images ($N_{His-mCh} = 343$, $N_{MTS(1xMreB)-mCh} = 294$, $N_{mCh-MTS(FtsA)} = 490$, $N_{mCh-MTS(BsD)} = 392$, $N_{mCh-MTS(BsD)} = 390$, $N_{MTS(2xMreB)-mCh} = 265$).

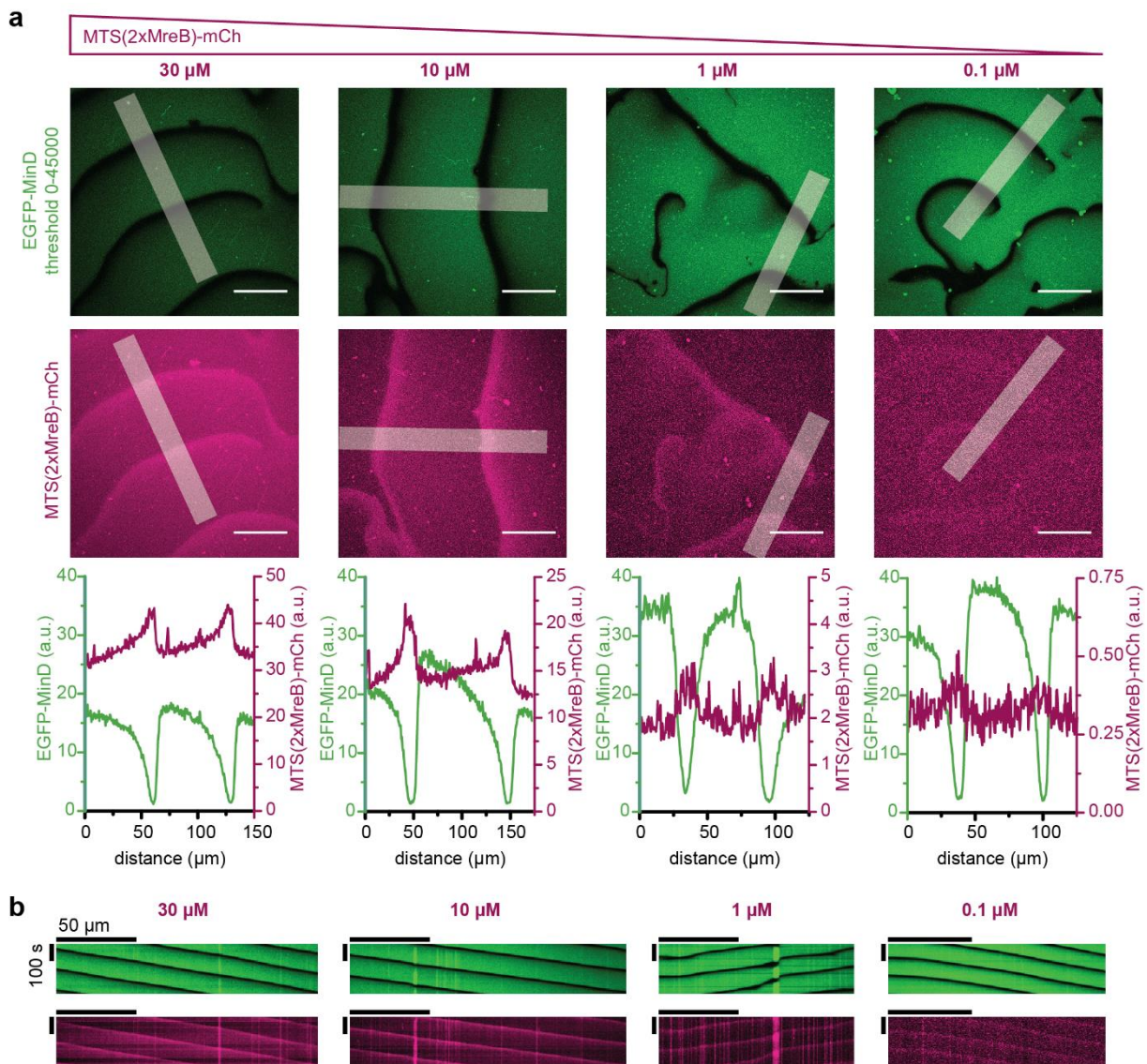


Supplementary Figure 4: The presence of model peripheral membrane proteins, mCh-MTS, does not change the wavelength or velocity of MinDE waves. a) Box plot of wavelength of the MinDE waves in the presence of the different mCh-MTS constructs. Box limits are quartiles 1 and 3 and whiskers are $1.5 \times \text{IQR}$, median is shown as a black line, mean is shown as a red line, points are outliers. (Data from three independent experiments shown in Figure 2b, with in total N measurements ($N_{\text{His-mCh}} = 333$, $N_{\text{MTS(1xMreB)-mCh}} = 292$, $N_{\text{mCh-MTS(FtsY)-mCh}} = 487$, $N_{\text{MTS(FtsY)-mCh}} = 392$, $N_{\text{mCh-MTS(BsD)}} = 360$, $N_{\text{MTS(2xMreB)-mCh}} = 265$). b) Velocity of MinDE waves in the presence of different mCh-MTS constructs. Line and error bars represent mean and standard deviation from three independent experiments shown in Figure 2 with measurements from N different time-series ($N_{\text{His-mCh}} = 5$, $N_{\text{MTS(1xMreB)-mCh}} = 6$, $N_{\text{mCh-MTS(FtsY)-mCh}} = 5$, $N_{\text{MTS(FtsY)-mCh}} = 4$, $N_{\text{mCh-MTS(BsD)}} = 6$, $N_{\text{MTS(2xMreB)-mCh}} = 4$).



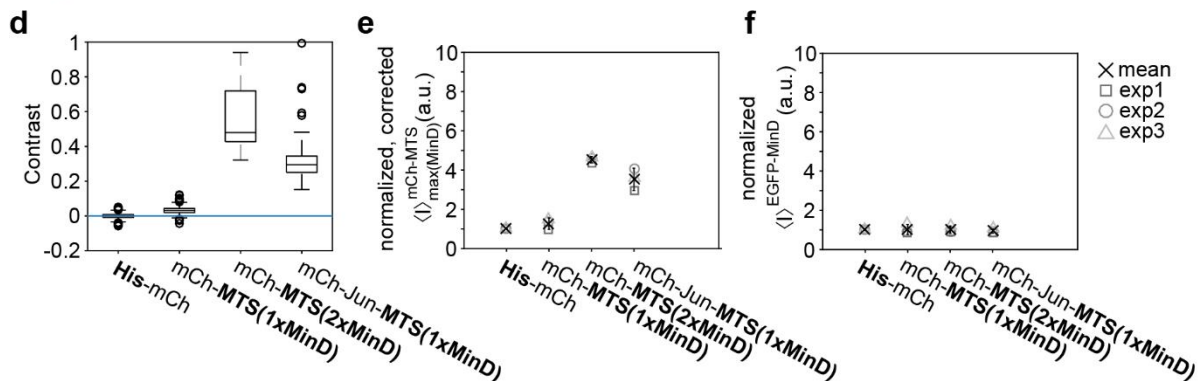
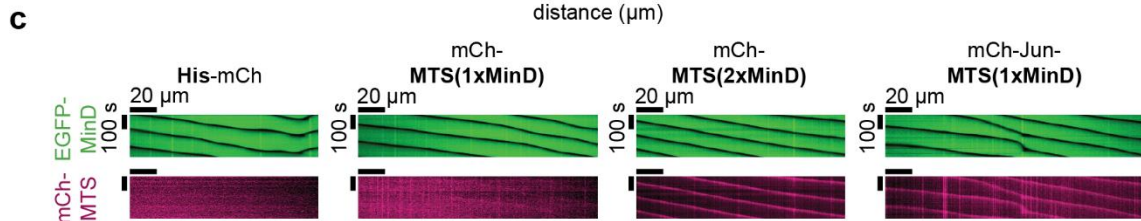
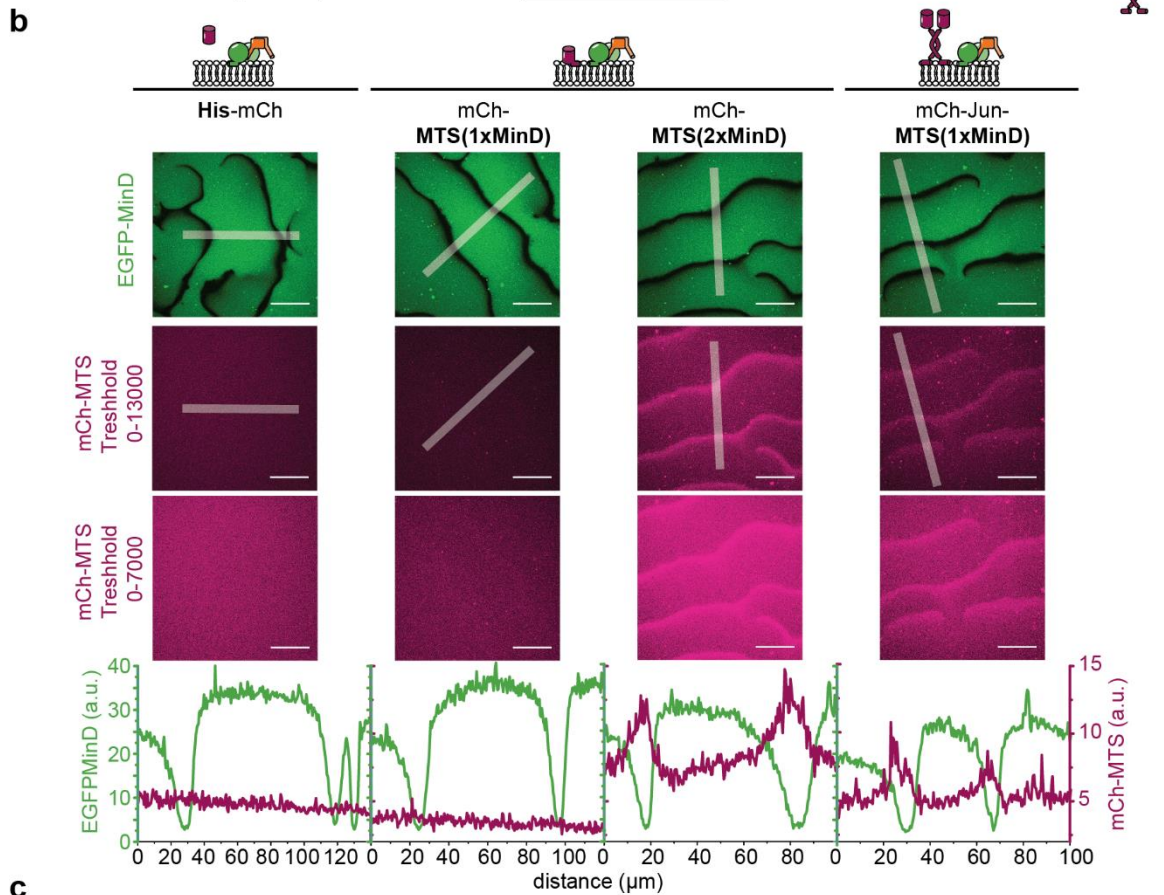
Supplementary Figure 5: MTS(2xMreB)-mCh is spatiotemporally regulated over a wide concentration range of MinD and MinE. a) MTS(2xMreB)-mCh is spatiotemporally regulated at different MinD/MinE ratios (1 μM MinD (30 % EGFP-MinD), 0.1 - 10 μM MinE, 1 μM MTS(2xMreB)-mCh). Representative images of MinDE self-organization (upper panel, green) in the presence of MTS(2xMreB)-mCh (middle panel, magenta). Fluorescence intensity line plots along the selection shown in the corresponding images (not necessarily full selection) (lowest panel). All images in one row were acquired and displayed using the same instrumental settings. Scale bars: 50 μm . b) Kymograph along the line selections shown in a). Scale bars: 100 s and 50 μm . c) MTS(2xMreB)-mCh is spatiotemporally regulated at all MinDE concentrations where MinDE are reliably self-organizing on the

membrane ($>0.4 \mu\text{M}$ MinD and MinE). Representative images of MinDE self-organization in two different brightness settings (two upper panels) in the presence of MTS(2xMreB)-mCh (lower panel). Fluorescence intensity line plots along the selection shown in the corresponding images (not necessarily full selection) (lowest panel). All images in one row were acquired and displayed using the same instrumental settings ($0.1 - 0.5 \mu\text{M}$ MinD (30 % EGFP-MinD), $0.1 - 0.5 \mu\text{M}$ MinE, $1 \mu\text{M}$ MTS(2xMreB)-mCh). Scale bars: $50 \mu\text{m}$. d) Kymograph along the line selections shown in c) Scale bars: 100 s and $50 \mu\text{m}$. e) MinDE only reliably self-organize at concentrations equal or higher than $0.4 \mu\text{M}$ MinDE. Representative tile scan of chambers containing $0.3 \mu\text{M}$ and $0.4 \mu\text{M}$ MinDE and $1 \mu\text{M}$ MTS(2xMreB)-mCh. At $0.3 \mu\text{M}$ MinDE patterns only form transiently in certain areas of the chamber, whereas at $0.4 \mu\text{M}$ MinDE patterns form reliably and also spatiotemporally regulate MTS(2xMreB)-mCh. Brightness/contrast settings are not comparable between images. Scale bars: $500 \mu\text{m}$. All experiments were performed independently two times under similar or identical conditions.



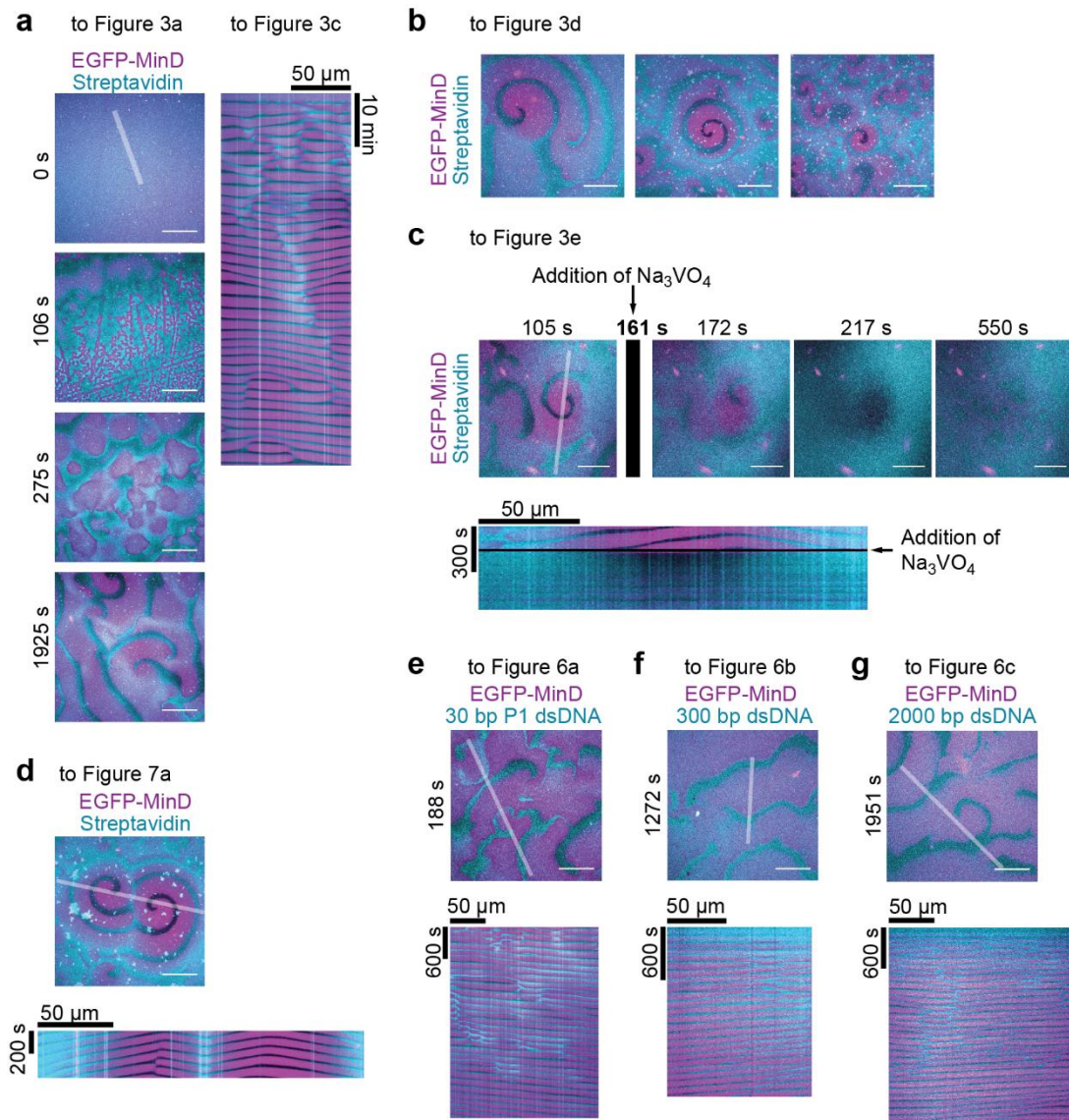
Supplementary Figure 6: MTS(2xMreB)-mCh is spatiotemporally regulated by MinDE over a wide MTS(2xMreB)-mCh/MinDE ratio. a) Representative images of the MinDE wave (upper panel, green) and the anticorrelated MTS(2xMreB)-mCh waves (lower panel, magenta) on the membrane ($30 \mu\text{M}$, $10 \mu\text{M}$, $1 \mu\text{M}$ or $0.1 \mu\text{M}$ MTS(2xMreB)-mCh, $1 \mu\text{M}$ MinD (30 % EGFP-MinD), $1 \mu\text{M}$ MinE). All images in one row were acquired using the same imaging settings, MTS(2xMreB)-mCh brightness/contrast settings were optimized for each image and are not comparable. Fluorescence intensity line plots along the selection shown in the corresponding images (not necessarily full selection) (lowest panel). Scale bars: $50 \mu\text{m}$. b) Kymograph along the line selections shown in a), but with line width 10 instead of the displayed line width 50. Scale bars: 100 s and $50 \mu\text{m}$. Experiments were performed independently three times under identical conditions.

a	Name	Protein sequence (N- to C-terminus)	Natural occurrence
	mCh-MTS(1xMinD)	mCh-GSG EEEEK GFLKRLFGG	
	mCh-MTS(2xMinD)	mCh-GSG EEEEK GFLKRLFGG GSG EEEEK GFLKRLFGG	AA 256-270
	mCh-Jun-MTS(1xMinD)	mCh-Jun-GGGGS EEEEK GFLKRLFGG	<i>E. coli</i> MinD

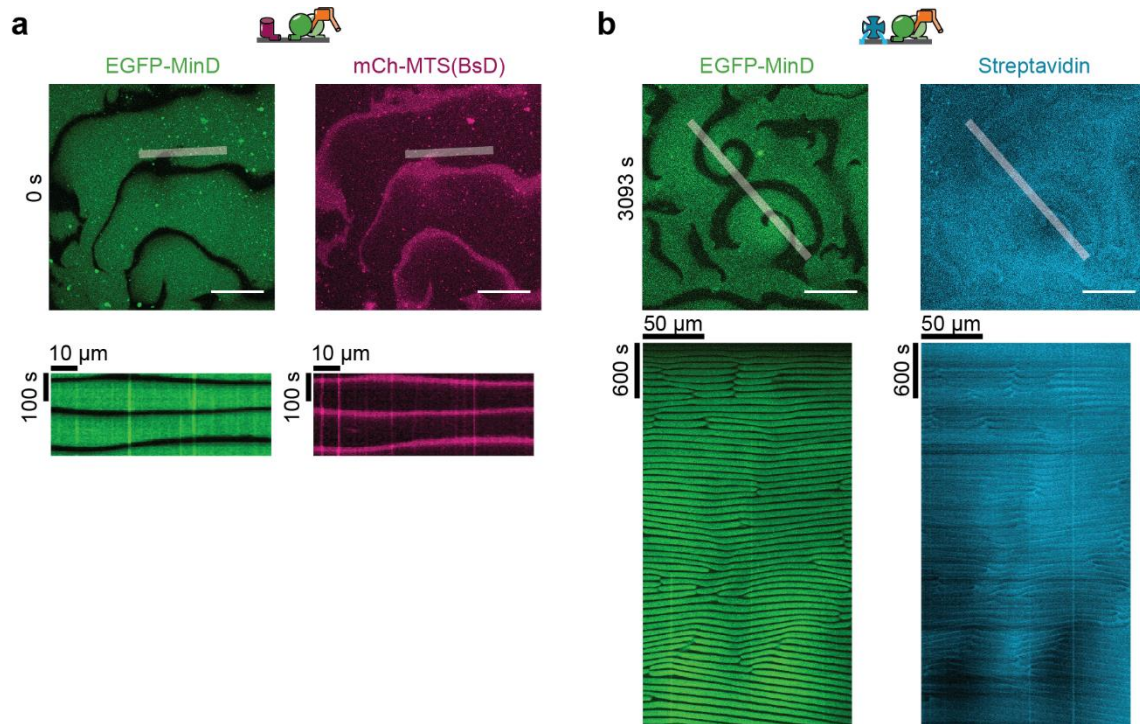


Supplementary Figure 7: Model membrane proteins containing two copies of the *E. coli* MinD amphipathic helix are spatiotemporally regulated by MinDE. a) Overview over the mCherry fusions to the *E. coli* MinD MTS. b) Representative images of the MinDE wave (upper panel, green) and the mCh-MTS constructs in two different brightness settings (middle and lower panels, magenta) on the membrane (1 μM mCh-MTS, 1 μM MinD (30 % EGFP-MinD), 1 μM MinE). All images in one row were acquired and displayed using the same instrumental settings. Fluorescence intensity line plots along the selection shown in the corresponding images (not necessarily full selection) show the difference in the extent of the spatial regulation (lowest panel). Scale bars: 50 μm . c) Kymograph along the line selections shown in b). Scale bars: 100 s and 20 μm . d) mCh-MTS constructs with two

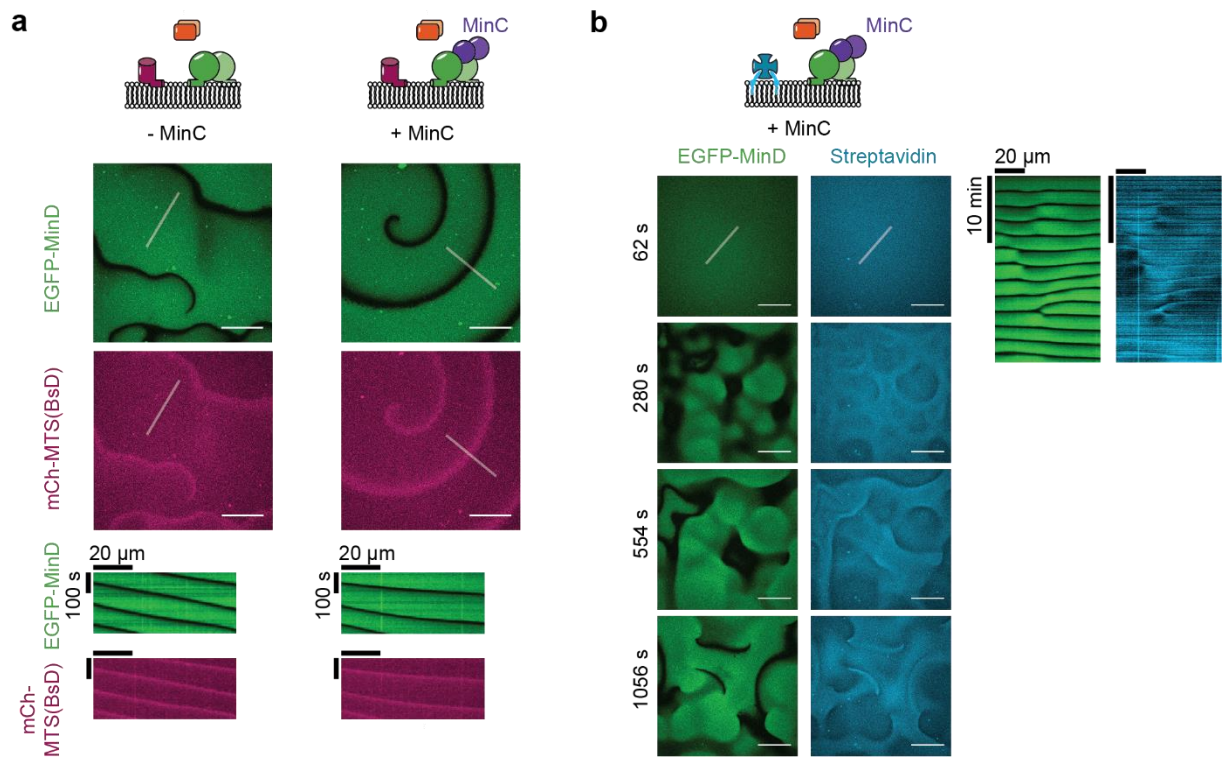
copies of the *E. coli* MinD MTS exhibit a high contrast. Box plot of the contrast of mCh-MTS constructs, lines are median, box limits are quartiles 1 and 3, whiskers are 1.5 x IQR and points are outliers, generated from three independent experiments with in total $N=294$ images per condition. Blue line marks no difference between the intensities in the minima and maxima of the MinDE wave (zero contrast). e) mCh-MTS intensity in the MinDE maximum ($\langle I \rangle_{\max(\text{MinD})}^{\text{mCh-MTS}}$) normalized to His-mCh and corrected for the fluorescent protein fraction. f) Average EGFP-MinD intensity of the full image normalized to the fluorescence in the presence of His-mCh ($\langle I \rangle^{\text{EGFP-MinD}}$). EGFP-MinD intensity, i.e. density, on the membrane is not influenced by the addition of mCh-MTS constructs. Each data point (squares, spheres, triangles) (exp1-3) was generated from 98 images in one sample chamber. Cross and error bars represent the mean value and standard deviation of the three independent experiments with in total $N=294$ images per condition.



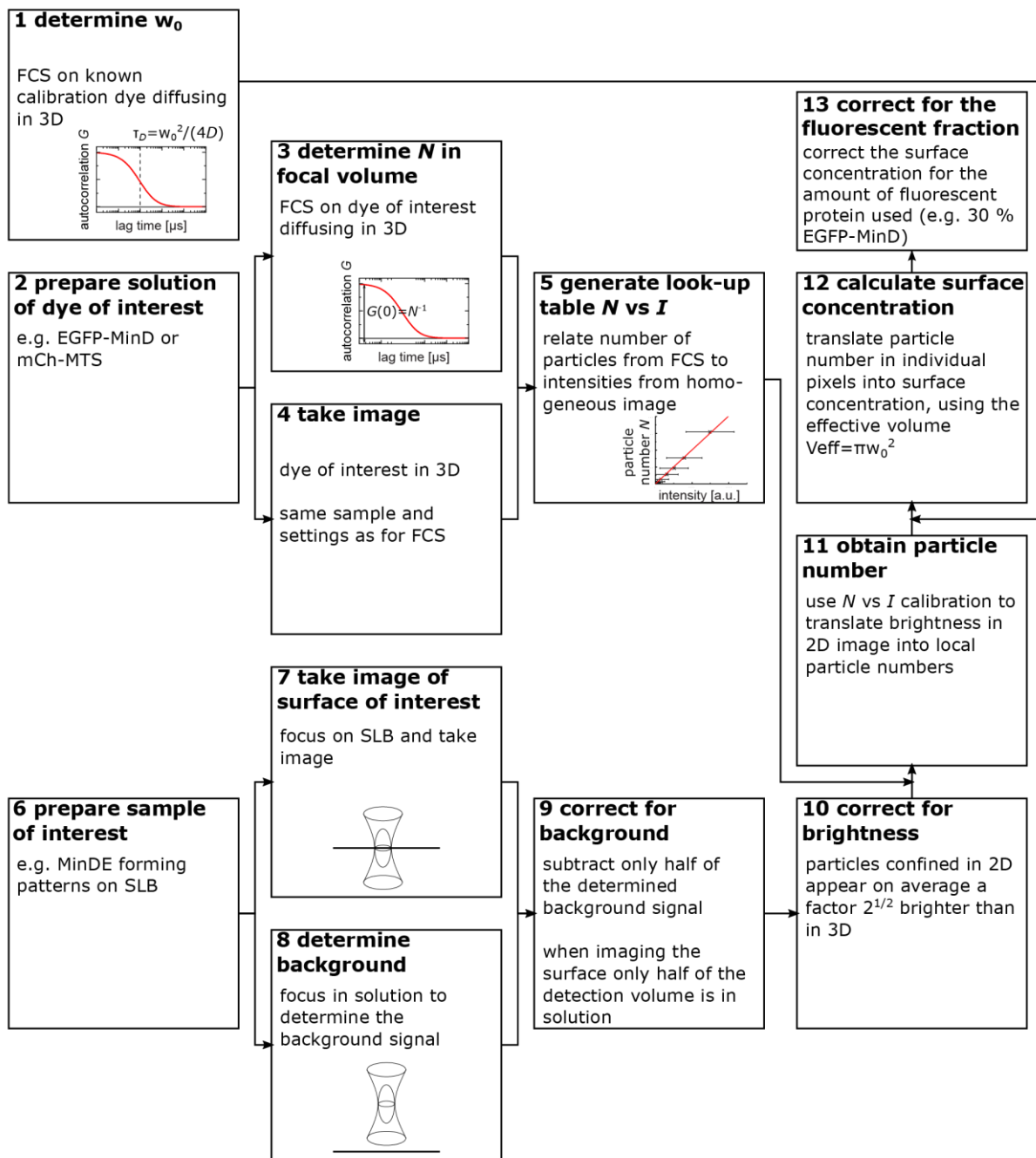
Supplementary Figure 8: Composite image of all separate channels shown in the main text involving streptavidin bound to biotinylated lipids. a) Composite image of MinDE self-organization (magenta) on a SLB with Biotinyl-CAP-PE-bound streptavidin (cyan) (1 μM MinD, 1 μM MinE, streptavidin-Alexa647) shown in Figure 3a. ATP is added at $t=0$ s to start self-organization. Scale bars: 50 μm . Kymograph along the line selection. b) MinDE self-organization leads to large scale concentration gradients of streptavidin. Representative composite images of streptavidin distribution in MinDE spirals after >1h of MinDE self-organization on SLBs as shown in Figure 3d. Scale bars 50 μm . c) Large scale streptavidin gradient formation by MinDE is reversible. Representative composite images and kymograph of a running MinDE assay in the presence of anchored streptavidin as shown in Figure 3e. Addition of sodium orthovanadate (Na_3VO_4) leads to MinDE detachment which in turn leads to homogenization of streptavidin fluorescence on the membrane. Scale bars: 50 μm . d) Streptavidin cannot dissociate in solution and is moved laterally on the membrane leading to accumulation on collision interfaces and depletion in spiral centers. Representative composite image of colliding MinDE waves in the presence of streptavidin bound to biotinylated lipids (1 μM MinD (30 % EGFP-MinD), 1 μM MinE, Alexa647-streptavidin) as shown in Figure 7a. Kymographs along the selection shown in the images. Scale bars: 50 μm . e) MinDE self-organization can regulate short membrane-anchored DNA fragments. Representative composite images and kymograph of a time-series of MinDE self-organization (magenta) in the presence of a 30 bp P1 dsDNA (cyan) bound to the membrane by a cholesterol anchor (1 μM MinD (30 % EGFP-MinD), 1 μM MinE, 10nM TEG-cholesterol-dsP1) shown in Figure 6a. Scale bars: 50 μm . f) Representative composite images and kymograph of a time-series of MinDE self-organization regulating 300 bp long dsDNA bound to lipid-anchored streptavidin (1 μM MinD (30 % EGFP-MinD), 1 μM MinE, 300 bp lambda DNA, streptavidin) shown in Figure 6b. Scale bars: 50 μm . g) Representative composite images and kymograph of a time-series of MinDE self-organization regulating 2000 bp long dsDNA bound to lipid-anchored streptavidin shown in Figure 6c. Scale bars: 50 μm .



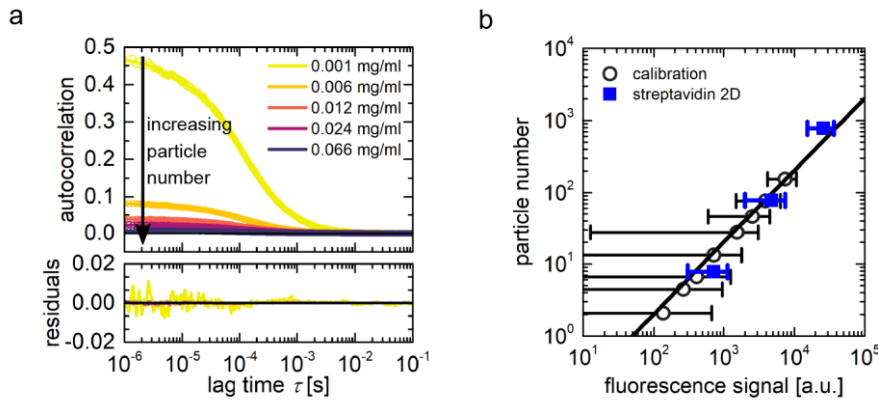
Supplementary Figure 9: MinDE position model membrane proteins on supported lipid bilayers made from *E. coli* polar lipid extract. a) Representative images and kymograph of the MinDE wave and the anticorrelated mCh-MTS(BsD) waves on SLBs made from *E. coli* polar lipid extract (1 μM MinD (30 % EGFP-MinD), 1 μM MinE, 1 μM mCh-MTS(BsD)). b) Representative images and kymograph of MinDE regulating Alexa647-streptavidin on SLBs made from *E. coli* polar lipid extract doped with 1 % Biotinyl-CAP-PE (1 μM MinD (30 % EGFP-MinD), 1 μM MinE, Alexa647-streptavidin). Experiments were performed independently three (b) or two (a) times under similar or identical conditions. Scale bars: 50 μm



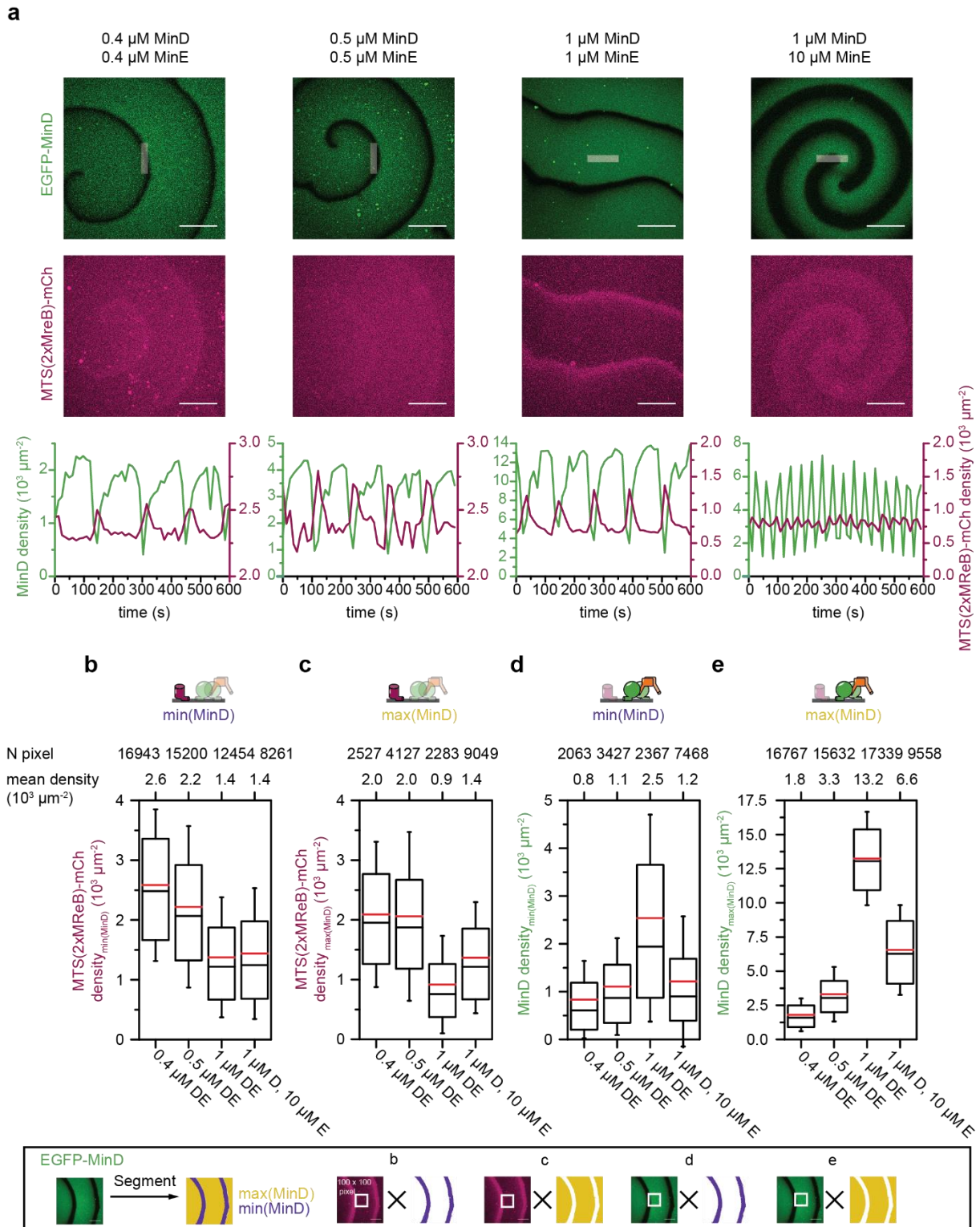
Supplementary Figure 10: Positioning of model membrane proteins by MinDE is independent of MinC. a) Representative images and kymograph of MinDE regulating mCh-MTS(BsD) in the presence or absence of MinC (1 μ M MinD (30 % EGFP-MinD), 1 μ M MinE, with and without 0.05 μ M MinC, 1 μ M mCh-MTS(BsD)) b) Representative images and kymograph of MinDE positioning lipid-anchored streptavidin in the presence of MinC (1 μ M MinD (30 % EGFP-MinD), 1 μ M MinE, 0.05 μ M MinC, Alexa647-streptavidin). Experiments were performed independently three (a) or two (b) times under identical conditions. Scale bars: 50 μ m



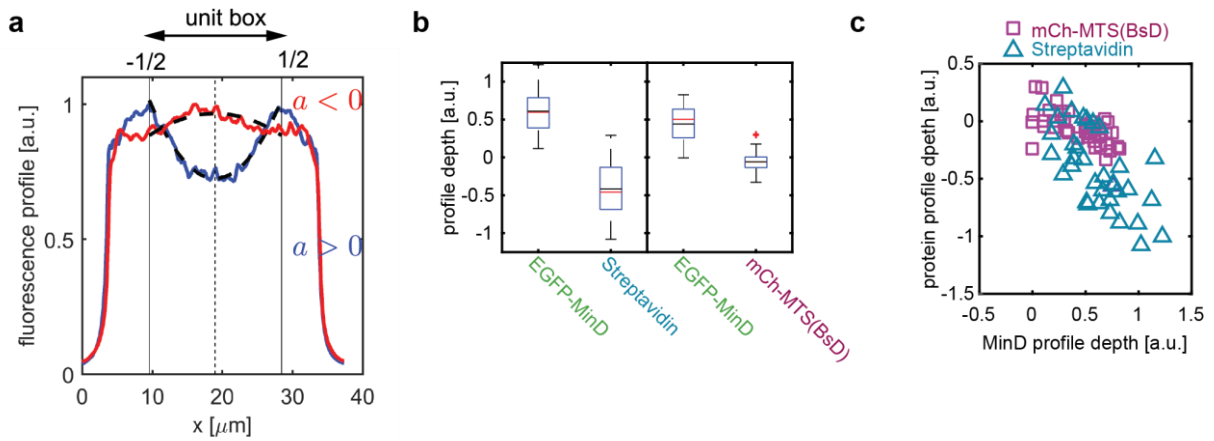
Supplementary Figure 11: Flowchart describing the Fluorescence Correlation Spectroscopy (FCS)-based image calibration performed to obtain EGFP-MinD and MTS(2xMreB)-mCh densities on the membrane.



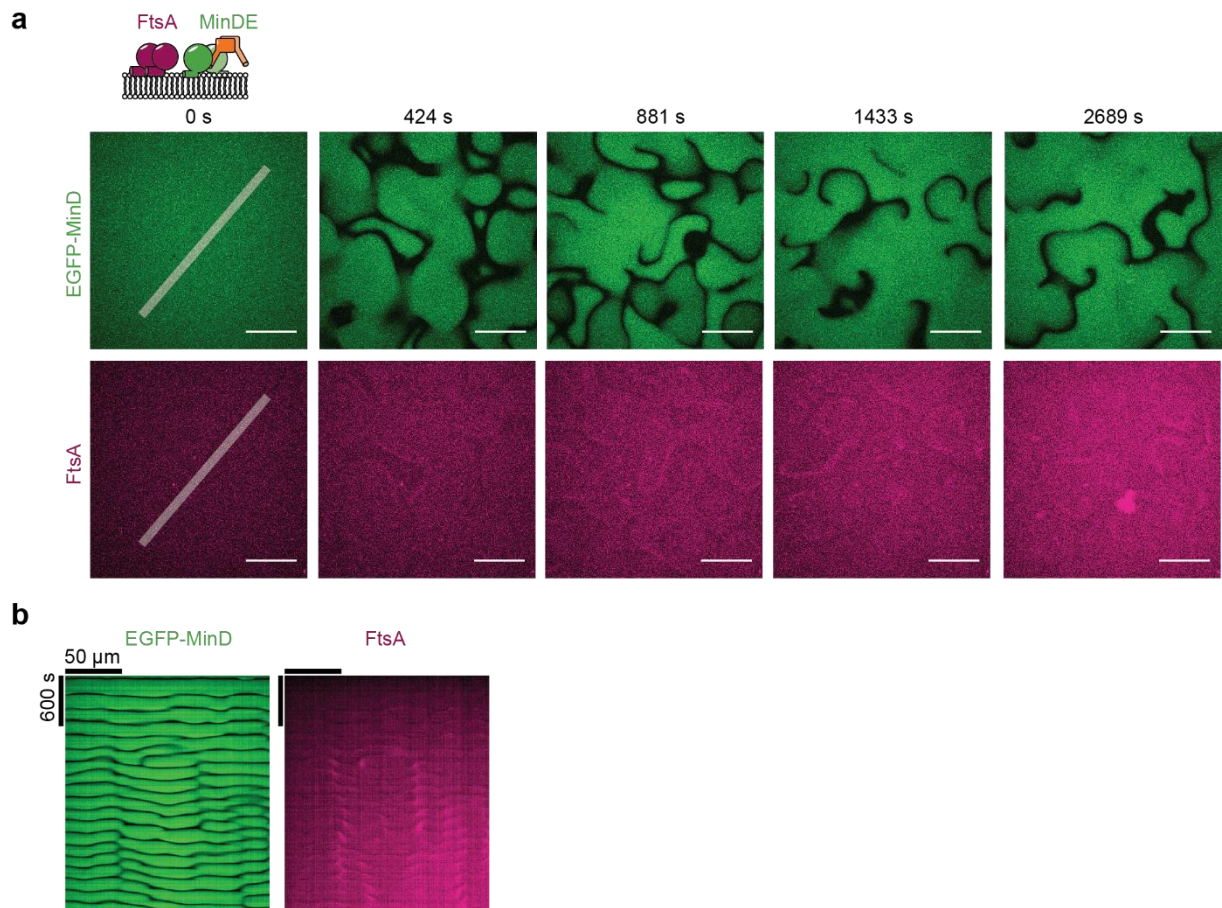
Supplementary Figure 12: Validation of the FCS-based quantification of surface densities. a) Representative autocorrelation curves for varying concentrations of streptavidin labeled with Alexa Fluor 488 freely diffusing in 3D. The experimental autocorrelation curves were fitted by a 3D diffusion model with a triplet contribution. b) The particle numbers obtained from the fit in a) are related to the corresponding fluorescence signal (black circles, mean \pm std) of a separately taken 100x100 pixel image (1 pixel corresponds to 420 nm). This data set is fitted by a line through the origin, yielding a calibration line, which relates the fluorescence signal in one pixel to the number of particles in the respective detection volume. Note the double-logarithmic scales. The linear relation adequately describes the experimental data over at least two orders of magnitude. The particle number N is easily translated into a 3D concentration via the relation $c_{3D} = N \left(\pi^2 w_0^3 S \right)^{-1}$, where w_0 and S are obtained from the initial calibration experiment on freely diffusing dye (compare step 1 in Supplementary Fig. 11). To validate the approach outlined in Supplementary Fig. 11, we imaged SLBs containing varying fractions of biotinylated lipids, which recruit the fluorescently labelled streptavidin. From the molar fraction of these lipids, their density and the streptavidin-biotin valency¹ the mean number of particles in the detection volume can be estimated (here 7.8, 78, and 778 particles per detection volume). A 100x100 pixel image (1 pixel corresponds to 420 nm) of the SLB was taken, and the pixel values divided by $\sqrt{2}$ (compare Supplementary Fig. S11). The corresponding pairs of fluorescence signal (mean \pm std) and the expected particle number (blue squares) were superimposed on the calibration curve, showing good agreement, and thus validate the proposed approach.



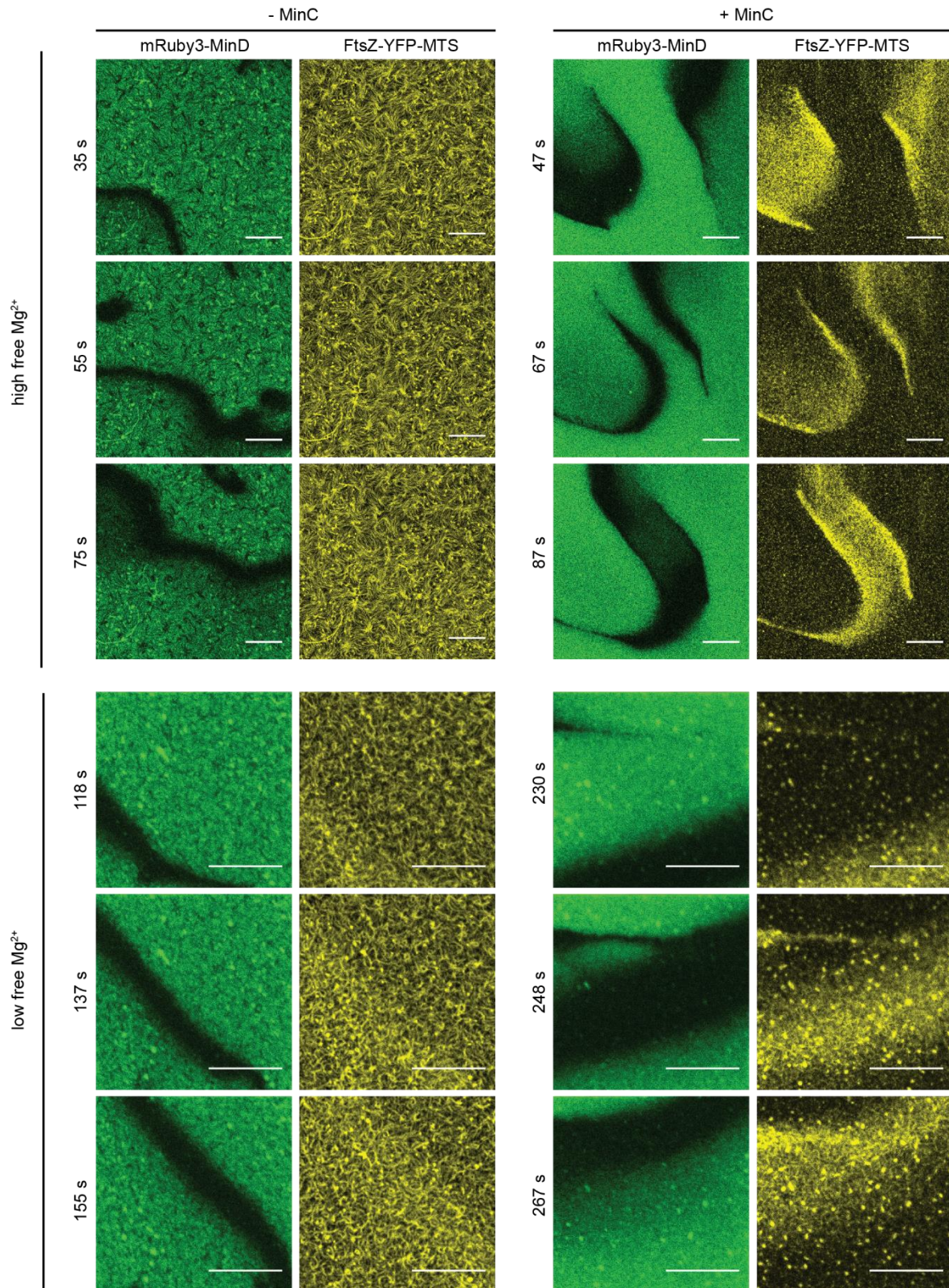
Supplementary Figure 13: MinDE waves spatiotemporally regulate MTS(2xMreB)-mCh at MinD densities on the order of magnitude occurring *in vivo*. a) Representative images used for density quantification (upper panels), temporal density profiles along the 20 by 100 pixel selection shown in the images. Scale bars: 50 μm b) Boxplots of density values in a 100 by 100 pixel region in the center of all images for b) MTS(2xMreB)-mCh in the MinD minimum, c) MTS(2xMreB)-mCh in the MinD maximum, d) MinD in the MinD minimum, e) MinD in the MinD maximum. Box limits are quartiles 1 and 3 and whiskers are standard deviation, median is shown as a black line, mean is shown as a red line. Data from two independent FCS/image calibrations.



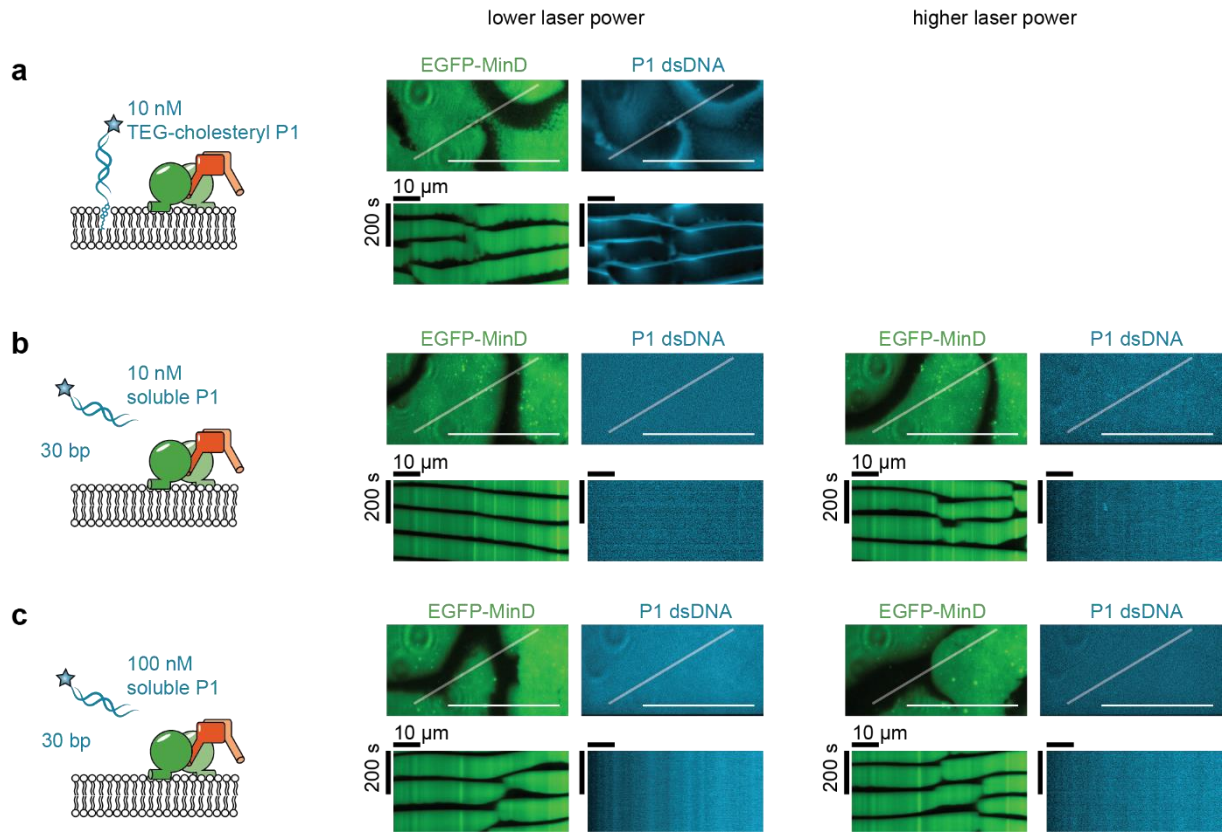
Supplementary Figure 14: Quantification of time-averaged fluorescence intensity profiles. a) Normalized, time-averaged fluorescence intensity profiles of EGFP-MinD (blue) and streptavidin (red). Vertical lines indicate the maxima of the EGFP-MinD profile that define the edges of the unit box, i.e. a box of length 1. Thus, every profile is projected from its physical extent onto the unit box, ranging from $-1/2$ to $1/2$. Dashed lines indicate the quadratic function fit to the profiles in the unit box to determine the profile depth. The curvature a is a direct measure for the depth of the profile. b) Box plot of the depth of the fluorescence intensity profile for mCh-MTS(BsD) and streptavidin with the respective EGFP-MinD one. Box limits are quartiles 1 and 3 and whiskers are $1.5 \times \text{IQR}$, median is shown as a black line, mean is shown as a red line, points are outliers. (Data from three independent experiments with mCh-MTS(BsD) = 45 and streptavidin = 35 individual microcompartments). c) Depths of individual fluorescence intensity profiles of mCh-MTS(BsD) and streptavidin plotted against the depth of the EGFP-MinD fluorescence intensity profile. mCh-MTS(BsD) profile depth is close to zero independent of EGFP-MinD profile depth. Streptavidin profile depth of individual fluorescence intensity profiles is correlated with EGFP-MinD profile depth, indicating a strong regulation of membrane-anchored proteins by MinDE.



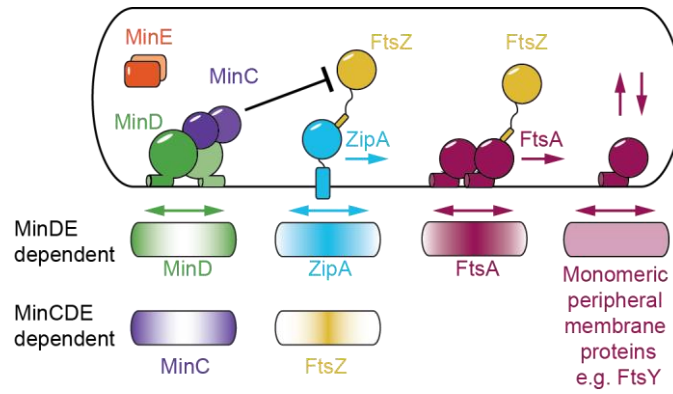
Supplementary Figure 15: MinDE spatiotemporally regulates FtsA. a) Representative images of time series of MinDE self-organization in the presence of FtsA (0.4 μM Cy5-FtsA, 1 μM MinD (30 % EGFP-MinD), 1 μM MinE). ATP is added at $t=0$ s to start self-organization. Scale bars: 50 μm . b) Kymograph along the line selection shown in a). Experiment was performed independently two times under similar or identical conditions. Scale bars: 50 μm and 600 s



Supplementary Figure 16: MinDE cannot move filaments and dynamic rings of FtsZ-YFP-MTS laterally. Representative images of MinDE self-organization in the presence of FtsZ-YFP-MTS with high and low free Mg^{2+} and with and without MinC (1 μ M MinD (30 % EGFP-MinD), 1 μ M MinE, 0.5 μ M FtsZ-YFP-MTS, with and without 0.05 μ M MinC) at high magnification. Brightness/contrast settings are not comparable between images. For low Mg^{2+} conditions images were acquired with a line average of 4 for better resolution. Scale bars: 10 μ m



Supplementary Figure 17: Binding of soluble P1 dsDNA fragment to MinD cannot be observed in TIRF. a) Spatiotemporal positioning of TEG-cholesterol anchored P1 DNA fragment by MinDE is clearly visible in TIRF microscopy images (1 μM MinD (30 % EGFP-MinD), 1 μM MinE, 10 nM TEG-cholesterol dsP1). No modulation in the fluorescence intensity signal of soluble P1 dsDNA fragment can be observed for b) 10 nM or c) 100 nM P1 dsDNA, when added to MinDE self-organization assays (1 μM MinD (30 %E GFP-MinD), 1 μM MinE, 10 or 100 nM soluble P1). Images were acquired at two different laser powers. Experiments were performed independently two times under identical conditions. Scale bars: 50 μm



Supplementary Figure 18: Schematic model of how the MinCDE system could influence positioning of major divisome proteins FtsZ, ZipA and FtsA. MinC, antagonist of FtsZ assembly, whose time-averaged concentration is highest at the cell poles confines FtsZ polymerization to midcell. MinDE oscillations might establish a time-averaged concentration gradient of the transmembrane protein ZipA and the oligomerized FtsA that is maximal at midcell. MinDE might establish counter-oscillations of monomeric peripheral membrane proteins decreasing protein abundance on the membrane.

Supplementary Table 1

List of observations possibly linked to MinDE-mediated regulation of membrane proteins

Possible target	Observation	study
FtsY, UspE, PfkA, Pkg, YciG	Abundance of peripheral membrane proteins is decreased in the presence of MinCDE as compared to a $\Delta minCDE$ strain	²
ZipA	ZipA and MinCDE counteroscillations; no counteroscillation in a $\Delta minCDE$ strain	³
ZipA	ZipA although essential in <i>E. coli</i> can be bypassed by mutations in other divisome proteins and thus has been suggested to enhance cell division.	⁴⁻⁷
Differential regulation of FtsA, FtsA*	FtsA mutant (FtsA*) impaired for self-interaction can bypass ZipA. Monomeric FtsA has been suggested to recruit other divisome proteins.	^{6,7}
FtsZ anchors, ZipA and FtsA	Slow FtsZ oscillations on the timescale of MinDE oscillations; no detectable slow FtsZ oscillations in a $\Delta minCDE$ strain	⁸
FtsZ anchors, ZipA and FtsA	Similar FtsZ dynamics for WT and $\Delta minC$ strains, but altered dynamics in a $\Delta minCDE$ strain	⁹
<i>B. subtilis</i> membrane-bound division proteins	<i>E. coli</i> MinDE oscillate in <i>B. subtilis</i> and impair sporulation by inhibiting polar septum formation in the absence of both <i>E. coli</i> and <i>B. subtilis</i> MinC	¹⁰
TnaA, GroES, YqjD	Polar localization of three foci-forming inner membrane associated proteins is disrupted in $\Delta minCDE$ strain	¹¹
chromosome	Abnormal nucleoid distribution and anucleate rod-shaped cells in MinCDE mutants	¹²⁻¹⁴
chromosome	Strains deleted for the histone-like protein HU acquire secondary mutations in <i>minCDE</i>	¹⁵
chromosome	Overexpression of MinE impairs nucleoid segregation	¹⁶
chromosome	Disturbed chromosome segregation in $\Delta minCDE$ strains	¹⁷

Supplementary Table 2

List of plasmids

Vector	Protein name	Reference or Source
pET28a-His-MinD_MinE	MinD	18
pET28a-His-EGFP-MinD	EGFP-MinD	19
pET28a-His-MinE	MinE	18
pML60	Sumo-Gly5-FtsA	20
pLVX-mCherry-C1		Clontech
pCoofy1-mCherry	His-mCh	Lei Kai
pET28a-BsMTS-mCherry-His	BsMTS-mCherry	This study
pET28a-mCherry-GGBsMTS	mCh-MTS(BsD)	This study
pET28a-MreBN-mCherry-His	MTS(1xMreB)-mCh	This study
pET28a-2xMreBN-mCherry-His	MTS(2xMreB)-mCh	This study
pET28a-mCherry_FtsA	mCh-MTS(FtsA)	This study
pET28a-FtsY_mCherry	MTS(FtsY)-mCh	This study
pET28a-mCherry_EcMTS	mCh-MTS(1xMinD)	This study
pET28a-mCherry_2xEcMTS	mCh-MTS(2xMinD)	This study
pET28a-mCherry-Jun-EcMTS	mCh-Jun-MTS(1xMinD)	This study
pET28a-mRuby3-MinD	mRuby3-MinD	21
pET11b-FtsZ-YFP-MTS	FtsZ-YFP-MTS	22

Supplementary Table 3

List of primers

Primername	Sequence 5' to 3'
21_YFP_for	ATGGTGAGCAAGGGCGAG
22_YFP_rev	CTTGTACAGCTCGTCCATGC
23_YFP_MinD_for	CATGGACGAGCTGTACAAGGAATTCGCACGCATTATTGTTG
24_pET_YD_rev	CTCGCCCTTGCTCACCATGGATCCGCGACCCATTTG
64_BsMTS-mCH_fw	AATCAAATCTTTCTTCGGTCTTCTGGTCTTCTGGTATGGTGAGCAAGG GCGAG
65_BsMTS-pET_rev	GAACCGAAGAAAGATTTGATTTTAGCCATCATACCTTTACTGCTGCCCAT GGTATATCT
68_His-mcherry_rev	TGGTGGTGGTGGTGGTCTCGACTCCAGATCCACCCTTGTACAGCTCGTCCAT G
pET28a_fw	GTCGAGCACCACCACCA
19_mCherry_fw	TCAGGTGGAAGTCCTAGGATGGTGAGCAAGGGCGAG
20_pET28a_rev	CCTAGGACTTCCACCTGAA
50_BsMTS-pET	GTATGATGGCTAAAATCAAATCTTTCTTCGGTGTTCGTTCTTAAAAGCTT GCGGCCGCA
61_BsMTS_mCh_rev	ATTTGATTTTAGCCATCATACCTTTGCCAGATCCCTTGTACAGCTCGTCCA TGCC
80_MreBN-mCherry_fw	AAATTCCGTGGTATGTTCCGTGGTCTGGTCTTCTGGTCTTCTGGT
81_MreBN-pET_rev	ACGGAACATACCACGGAATTTTTTCAGCATGGTATATCTCCTTCTTAAAG TTAAA
78_MreBN2x-pEt28a_rev	CAGAACCACCGAACATACCACGGAATTTTTTCAGCATGGTATATCTCCTT CTTAAAGTTAAA

79_MreBN2x-mCherry_fw	AACAGCAGCTGAAAAAATCCGTGGTATGTTCCGTGGTCTGGTCTTCT GGTCTTCTGGT
BR200_mCherry_FtsA_for	ATTGAGTCGCTTGATCCACGAGCCGCCAGATCCCTTGACAGC
p11_MTSftsA_rev	AGTTGGCTGCGAAAAGAGTTTTAAGGATCCGGCTGCTAACAAAG
BR201_fw_FtsY_mCherry	CCTGTAAAAACCAAAGAAAATCTCGGTCGTGGTCTGGTCTTCTGGTT
BR202_FtsY_mCherry_rev	CTGCGTTTCAGGCGCGGAACATGGTATATCTCCTTCTTAAAGTTAAAC
BR234_tandemMinD_fw	TAAAAGCTTGCGGCCGCACTC
BR235_tandemMinD_rev	TCCTCCGAACAAGCGTTTGAGGAAGCCTTCTTCTTCTTCAATagatccg ccTCCTCCGAACAAGCGTTTGAGGA
43_mut_Kan_fw	TGAAACATGGCAAAGGTAGCGT
93_mCh-EcMTS_fw	AGCTGTACAAGGGATCTGGCATTGAAGAAGAGAAGAAAGGCTTCTC
94_GSG_mCh_rev	GCCAGATCCCTTGACAGCTCG
44_mut_Kan_rev	GCTACCTTGCCATGTTTCAGAAA
472_Lin-RV	GCCAGATCCCTTGACAGC
473_Lin-FW	ATTGAAGAAGAGAAGAAAGGC
474_Jun-FW	CTGTACAAGGGATCTGGCCGTATCGCTCGTCTGGAA
475_Jun-RV	TTTCTTCTTCTTCAATAGAACCTCCTCCACCGTAGTTCATAAC
LP2_fw	CGCCATTAACCTGATGTTCTGGGG
FW_P1_30bp_chol	GAATCAGCGCCATTTATCACAGAATAGACT-CHOLESTEROL
FW_P1_30bp_sol	GAATCAGCGCCATTTATCACAGAATAGACT
RV_P1_30bp_Al647	AGTCTATTCTGTGATAAATGGCGCTGATTC-ALEXA647
BR215_Cy5_tetO_lambda_fw	AGACATCCCTATCAGTGATAGAGACGCGGGTTTTCGCTATTTATGAAAAT TTTC
BR120_5'BiotinTEG_l300_rev	TAAAGCACCTCATTACCCTTGCCAC
BR122_5'BiotinTEG_l2000rev	ATCGTCGTGGCGGCC

Supplementary Note 1

In vivo MinDE densities. MinD and MinE concentrations in *E. coli* have been determined to be about 2000-3000 molecules per cell by western-blotting^{23,24}. Assuming that almost all proteins bind to the membrane and do so only at one pole at a time, and an average inner membrane area of about $6 \mu\text{m}^2$, the density of MinD on the membrane can be estimated to about $1 \times 10^3 \mu\text{m}^{-2}$. Furthermore, a large fraction of the total membrane surface in vivo is occupied (~60%) by transmembrane proteins²⁵, further reducing the available membrane area and potentially increasing the local MinDE density.

Supplementary Note 2

MinDE change the physical properties of membranes. The MTS of both MinD and MinE are amphipathic helices, known to change the physical properties of membranes²⁶. They insert into the membrane leading to deformation of liposomes²⁷⁻²⁹, change the membrane viscosity in vitro³⁰, preferentially bind to anionic lipids³¹⁻³³ and can stabilize lipid domains³⁴. Interestingly, stains for membrane properties, such as cardiolipin density, resemble the MinD localization at cell poles and nascent septa^{35,36}, which led to the suggestion that MinDE self-organization relies on certain lipid distributions as a spatial cue³⁷. However, this hypothesis has been disproved by showing that geometry sensing is an intrinsic property of the MinDE system^{31,38-40}.

Supplementary Methods

Estimation of protein surface densities

We estimated the surface concentration from confocal fluorescence images based on a multistep procedure, as outlined in Supplementary Fig. 11. In essence, this approach relies on a combined confocal Fluorescence Correlation Spectroscopy (FCS)^{41–43} and imaging-based calibration, which relates the pixel values to the number of particles in this pixel. Similar approaches have been introduced before.^{44–46}

In an initial step (box 1 in Supplementary Fig. 11), the effective detection volume $V_{\text{eff}} = \pi^{\frac{3}{2}} w_0^3 S$ was calibrated based on the diffusion coefficient of a known dye, which has spectral properties similar to the fluorescent tag whose density needs to be determined later. Here, w_0 is the lateral width of the Gaussian detection volume $\Omega(x, y, z) = \Omega_0 \exp\left(-2 \frac{x^2 + y^2}{w_0^2}\right) \exp\left(-2 \frac{z^2}{(S w_0)^2}\right)$ and S is the structure parameter, which describe the elongation of this volume. In this work, ATTO488-COOH and Alexa Fluor 546-NHS freely diffusing in water were used to calibrate the detection volumes for measurements on EGFP and mCherry, respectively. The corresponding diffusion coefficients at 25°C are $D = 405 \mu\text{m}^2 \text{s}^{-1}$ for ATTO488 (unpublished data) and $D = 364 \mu\text{m}^2 \text{s}^{-1}$ for Alexa Fluor 546.⁴⁷ The temperature at the objective was monitored by a thermocouple and the diffusion coefficient was corrected for the respective temperature T using the Stokes-Einstein-Smoluchowski relation $D \propto T/\eta(T)$.^{48–50} The acquired autocorrelation curves were fitted by a model function for combined 3D diffusion and blinking:

$$G(\tau) = N^{-1} \left(1 + \frac{f}{1-f} \exp\left(-\frac{\tau}{\tau_T}\right)\right) \left(1 + \frac{\tau}{\tau_D}\right)^{-1} \left(1 + \frac{\tau}{S^2 \tau_D}\right)^{-\frac{1}{2}} \quad (1)$$

Here, f is the fraction of molecules in a dark state, e.g. triplet, and τ_T is the associated characteristic decay time. As $\tau_D = \frac{w_0^2}{4D}$ and S are obtained from the fit, V_{eff} can be readily calculated. Moreover, the number of fluorescent particles N in the detection volume is obtained. This calibration was performed on a daily basis and for each spectral channel separately.

Next (boxes 2-5 in Supplementary Fig. 11), a relation between image brightness and the number of particles in one pixel, which corresponds to one detection volume, was determined. Therefore, a solution of the protein of interest was prepared, e.g. EGFP-MinD or mCh-MTS above a non-charged supported lipid bilayer (100 mol % DOPC). In a first step, another FCS measurement in solution was performed. From the autocorrelation curve and its fit (eq. 1), the number of particles N was obtained and corrected for uncorrelated background.⁵¹ Subsequently, a fluorescence image was taken in solution and background corrected. Thus, the mean signal I in this image was connected to a number of particles N . This approach was repeated for several concentrations to map the relation N vs. I , which was fitted by a linear function (compare Supplementary Fig. 11). Importantly, the imaging settings were identical for the FCS measurements, the corresponding imaging and all subsequent images, which relied on the determined relation N vs. I .

To estimate surface concentrations, the sample of interest, e.g. MinDE forming patterns on an SLB, was prepared and imaged with the membrane being in focus. To determine the effective background of fluorescently labelled protein that was not membrane bound, we took another image in solution far above the membrane. For a simplified system with no axial concentration gradient, the signal measured in solution corresponds to twice the background signal of an image taken on the membrane, because in this scenario, only the upper half of the detection volume collects fluorescence from the solution. The resulting pixel values cannot directly be translated into particle numbers via the previously determined relation N vs. I , because particles that are on the membrane have a higher average apparent brightness \bar{Q} than identical particles diffusing in 3D. This effect results from the restriction to two dimensions, which implies that all particles are always perfectly in focus, i.e. in the axial maximum of the 3D Gaussian Ω . Consequently, the average apparent brightness \bar{Q} in 2D and 3D reads:

$$\bar{Q}_{2D} \propto \frac{1}{V_{\text{eff}}} \int dx \int dy \exp\left(-2 \frac{x^2 + y^2}{w_0^2}\right) \exp\left(-2 \frac{z^2}{(Sw_0)^2}\right)$$

$$\bar{Q}_{3D} \propto \frac{1}{V_{\text{eff}}} \int dx \int dy \int dz \exp\left(-2 \frac{x^2 + y^2}{w_0^2}\right) \exp\left(-2 \frac{z^2}{(Sw_0)^2}\right)$$

$$\frac{\bar{Q}_{2D}}{\bar{Q}_{3D}} = \sqrt{2}$$

Thus, the membrane-bound particles appear a factor of $\sqrt{2}$ brighter than in solution. After correction for this factor, the previously determined relation N vs. I was applied to determine the particle number in each pixel. Since w_0 was initially determined, the obtained N in each pixel can be converted into a surface concentration $C = \frac{N}{\pi w_0^2}$. Further, this surface concentration was corrected for the fluorescent fraction of proteins used (box 13 Supplementary Fig. 11). To validate this approach, we determined Alexa488-streptavidin densities bound to SLBs containing different amounts of biotinylated lipids (70 mol % DOPC, 30 mol % DOPG, 0.01/0.1/1 mol % Biotinyl-CAP-PE), prepared in the same way as described in the methods section (Supplementary Fig. 12). To determine the densities of MTS(2xMreB)-mCh and EGFP-MinD on the membrane, the images were first calibrated as described above. We further generated the binary masks of the MinDE wave from the original EGFP-MinD as described (Analysis of mean fluorescence intensities in MinDE wave minima and maxima). The calibrated images were multiplied with the binary masks and all zero values were removed. All pixels located in a centered 100 x 100 pixel region from all images of one condition were pooled to obtain the box plot and average protein densities on the membrane in the MinDE minima ((MTS(2xMreB)-mCh density_{min(MinD)}/MinD density_{min(MinD)}) and maxima ((MTS(2xMreB)-mCh density_{max(MinD)}/MinD density_{max(MinD)}).

Cloning methods

For cloning all plasmids were propagated in *E. coli* OneShot TOP10 (Invitrogen, Thermo Fisher Scientific, Waltham, USA). We used seamless assembly for the cloning of larger DNA fragments into vectors. DNA fragments and vector backbones were amplified by PCR with primers that contained 15-

20 bp overlaps between adjacent fragments. The PCR products were then combined using GeneArt Seamless Cloning and Assembly Enzyme Mix (Thermo Fisher Scientific, Waltham, USA) according to manufacturer's instruction.

We used blunt end cloning for the introduction of point mutations or small peptide sequences. The entire vector was amplified with two primers extended by the sequence to be introduced. After PCR the product was digested with DpnI to remove plasmid template. The blunt ends of the PCR products were phosphorylated using T4 Phosphokinase and subsequently ligated with T4 DNA Ligase (Thermo Fisher Scientific).

The plasmids for the purification of His-MinD¹⁸, His-EGFP-MinD¹⁹, His-MinE¹⁸ and FtsA (pML60)²⁰ have been described previously.

pET28a-BsMTS-mCherry-His encodes the N-terminal fusion of the *Bacillus subtilis* MTS (KGMMMAIKSFFGSSGSSG (AA 254-265 of *B. subtilis* MinD) to mCherry and a C-terminal His-Tag. The coding region for mCherry was amplified by PCR from the plasmid pLVX-mCherry-C1 (Clontech, Mountain View, CA, USA) using the primers 64_BsMTS-mCH_fw/68_His-mcherry_rev and the backbone was amplified from pET28a using the primers pET28a_fw/65_BsMTS-pET_rev. The two PCR products overlap and were assembled using seamless assembly. pET28a-mCherry-GGBsMTS encodes for the C-terminal fusion of the *B. subtilis* MinD MTS (GSGKGMMMAIKSFFGVRS; AA 254-268 of *B. subtilis* MinD) to mCherry and an N-terminal His-Tag (mCh-MTS(BsD)). mCherry coding region was amplified from pLVX-mCherry-C1 (Clontech) using primers 19_mCherry_fw/61_BsMTS_mCh_rev and the backbone was amplified from pET28a with the primers 20_pET28a_rev/50_BsMTS-pET. PCR products were combined using seamless assembly. pET28a-MreBN-mCherry-His encodes for the N-terminal fusion of the *E. coli* MreB MTS (MLKKFRGMFRGSGSSGSSG; AA 1-9 of *E. coli* MreB) of mCherry with a C-terminal His-Tag (MTS(1xMreB)-mCh). The construct is designed analogously as the MreB-MTS fusion of EGFP in pFE356⁵². mCherry coding region was amplified from pET28a-BsMTS-mCherry-His with primers 68_His-mcherry_rev/80_MreBN-mCherry_fw and the backbone was amplified from

pET28a with primers pET28a_fw/81_MreBN-pET_rev. Both PCR products were subsequently combined using Seamless Assembly. pET28a-2xMreBN-mCherry-His encodes for an N-terminal fusion of two copies of the *E. coli* MreB MTS (MLKKFRGMFEGGSEQQLKKFRGMFRGSGSSGSSG) to mCherry with a C-terminal His-Tag (MTS(2xMreB)-mCh). The construct was analogously constructed to the 2xMreB-MTS fusion of EGFP in plasmid pJS111.⁵² The plasmid was amplified from pET28a-MreBN-mCherry-His with primers 78_MreBN2x-pEt28a_rev/79_MreBN2x-mCherry_fw and ligated using blunt end cloning. pET28a_mCherry_FtsA codes for a C-terminal fusion of the FtsA MTS to mCherry with an N-terminal His-Tag (mCh-MTS(FtsA)) (GSGGSWIKRLNSWLRKEF; AA 406-420 of *E. coli* FtsA) analogously to the GFP-FtsA-MTS fusion in plasmid pSEB295.⁵³ The mCherry coding regions from plasmid pET28a-mCherry-GGBsMTS were amplified with primers BR200_mCherry_FtsA_for/p11_MTSftsA_revA and subsequently religated using blunt end cloning. pET28a_FtsY_mCherry encodes the N-terminal fusion of the FtsY-MTS to mCherry with a C-terminal His-Tag (MTS(FtsY)-mCh) (MFARLKRSLKTKENLGRGSGSSGSSG; AA 196-211 of *E. coli* FtsY) and was designed analogously to the NG+1-Trx fusion.⁵⁴ It was constructed by amplification of the mCherry coding region from pET28a-MreBN-mCherry-His using primers BR201_fw_FtsY_mCherry/BR202_FtsY_mCherry_rev and recombined with blunt end cloning. pET28a-mRuby3-MinD was cloned from a sequence-optimized, custom-ordered mRuby3⁵⁵ DNA fragment that was inserted in place of EGFP on pET28a-EGFP-MinD using primers 21_YFP_for, 22_YFP_rev, 23_YFP_MinD_for and 24_pET_YD_rev and Seamless Assembly. pET28a_mCherry_EcMTS codes for a C-terminal fusion of the *E. coli* MinD MTS to mCherry (mCh-MTS(1xMinD)) with an N-terminal His-tag (GSGIEEEKKGFLKRLFGG; AA 256 – 270 of *E. coli* MinD) analogously to the fusion to GFP in plasmid in pTS14⁵⁶. It was constructed by amplification of the mCherry coding region from plasmid pET28a-mCherry-GGBsMTS using primers 94_GSG_mCh_rev/44_mut_Kan_rev and of the *E. coli* MTS sequence from plasmid pET28a-EGFP-MinD using primers 43_mut_Kan_fw/93_mCh-EcMTS_and assembly using seamless assembly.

pET28a_mCherry_2xEcMTS codes for a C-terminal fusion of two copies of the *E. coli* MinD MTS to mCherry (mCh-MTS(2xMinD)) with an N-terminal His-tag

(GSGIEEEKKGFLKRLFGGGSIEEEKKGFLKRLFGG; AA 256 – 270 of *E. coli* MinD) analogously to the fusion to GFP in plasmid in pSLR92⁵⁶. It was constructed by amplification of the mCherry coding region from pET28a_mCherry_EcMTS using primers BR234_tandemMinD_fw/BR235_tandemMinD_rev and recombined using blunt end cloning. pET28a-mCherry-Jun-EcMTS encodes for C-terminal fusion of the *E. coli* MinD MTS to an mCherry Jun leucine zipper fusion construct (mCh-Jun-MTS(1xMinD)) with an N-terminal His-tag (GGGGSIEEEKKGFLKRLFGG; AA 256 – 270 of *E. coli* MinD) analogously to pTS37⁵⁶. It was constructed by amplification of the mCherry coding region from plasmid pET28a_mCherry_EcMTS using primers 472_Lin-RV/473_Lin-FW and the coding region Jun from a custom ordered gene sequence using primers 474_Jun-FW/475_Jun-RV that were combined using seamless assembly.

Supplementary References

1. Dubacheva, G. V. *et al.* Controlling Multivalent Binding through Surface Chemistry: Model Study on Streptavidin. *J. Am. Chem. Soc.* **139**, 4157–4167 (2017).
2. Lee, H.-L. *et al.* Quantitative proteomics analysis reveals the Min system of Escherichia coli modulates reversible protein association with the inner membrane. *Mol. Cell. Proteomics* **15**, 1572–1583 (2016).
3. Bisicchia, P., Arumugam, S., Schwille, P. & Sherratt, D. MinC, MinD, and MinE drive counter-oscillation of early-cell-division proteins prior to Escherichia coli septum formation. *MBio* **4**, e00856-13 (2013).
4. Hale, C. A. & De Boer, P. A. J. Direct binding of FtsZ to ZipA, an essential component of the septal ring structure that mediates cell division in E. coli. *Cell* **88**, 175–185 (1997).
5. Geissler, B., Elraheb, D. & Margolin, W. A gain-of-function mutation in ftsA bypasses the requirement for the essential cell division gene zipA in Escherichia coli. *Proc. Natl. Acad. Sci. U. S. A.* **100**, 4197–4202 (2003).
6. Pichoff, S., Shen, B., Sullivan, B. & Lutkenhaus, J. FtsA mutants impaired for self-interaction bypass ZipA suggesting a model in which FtsA's self-interaction competes with its ability to recruit downstream division proteins. *Mol. Microbiol.* **83**, 151–167 (2012).
7. Pichoff, S., Du, S. & Lutkenhaus, J. The bypass of ZipA by overexpression of FtsN requires a previously unknown conserved FtsN motif essential for FtsA-FtsN interaction supporting a model in which FtsA monomers recruit late cell division proteins to the Z ring. *Mol. Microbiol.* **95**, 971–987 (2015).
8. Thanedar, S. & Margolin, W. FtsZ Exhibits Rapid Movement and Oscillation Waves in Helix-like Patterns in Escherichia coli. *Curr. Bio* **14**, 1167–1173 (2004).
9. Yang, X. *et al.* GTPase activity–coupled treadmilling of the bacterial tubulin FtsZ organizes

- septal cell wall synthesis. *Science* **355**, 744–747 (2017).
10. Jamroškovič, J., Pavlendová, N., Muchová, K., Wilkinson, A. J. & Barák, I. An oscillating Min system in *Bacillus subtilis* influences asymmetrical septation during sporulation. *Microbiology* **158**, 1972–1981 (2012).
 11. Li, G. & Young, K. D. Isolation and identification of new inner membrane-associated proteins that localize to cell poles in *Escherichia coli*. *Mol. Microbiol.* **84**, 276–295 (2012).
 12. Jaffé, A., D’Ari, R. & Hiraga, S. Minicell-forming mutants of *Escherichia coli*: production of minicells and anucleate rods. *J. Bacteriol.* **170**, 3094–3101 (1988).
 13. Mulder, E., El’Bouhali, M., Pas, E. & Woldringh, C. L. The *Escherichia coli* minB mutation resembles gyrB in defective nucleoid segregation and decreased negative supercoiling of plasmids. *Mol. Genet. Genomics* **221**, 87–93 (1990).
 14. Åkerlund, T., Bernander, R. & Nordström, K. Cell division in *Escherichia coli* minB mutants. *Mol. Microbiol.* **6**, 2073–2083 (1992).
 15. Jaffé, A., Vinella, D. & D’Ari, R. The *Escherichia coli* histone-like protein HU affects DNA initiation, chromosome partitioning via MukB, and cell division via MinCDE. *J. Bacteriol.* **179**, 3494–3499 (1997).
 16. Åkerlund, T., Gullbrand, B. & Nordström, K. Effects of the Min system on nucleoid segregation in *Escherichia coli*. *Microbiology* **148**, 3213–3222 (2002).
 17. Jia, S. *et al.* Effect of the Min system on timing of cell division in *Escherichia coli*. *PLoS One* **9**, e103863 (2014).
 18. Loose, M., Fischer-Friedrich, E., Ries, J., Kruse, K. & Schwille, P. Spatial Regulators for Bacterial Cell Division Self-Organize into Surface Waves in Vitro. *Science* **320**, 789–792 (2008).
 19. Zieske, K., Schweizer, J. & Schwille, P. Surface topology assisted alignment of Min protein

- waves. *FEBS Lett.* **588**, 2545–2549 (2014).
20. Loose, M. & Mitchison, T. J. The bacterial cell division proteins FtsA and FtsZ self-organize into dynamic cytoskeletal patterns. *Nat. Cell Biol.* **16**, 38–46 (2014).
 21. Glock, P. *et al.* Optical Control of a Biological Reaction–Diffusion System. *Angew. Chemie Int. Ed.* **57**, 2362–2366 (2018).
 22. Osawa, M., Anderson, D. E. & Erickson, H. P. Reconstitution of contractile FtsZ rings in liposomes. *Science* **320**, 792–794 (2008).
 23. Shih, Y. L., Fu, X., King, G. F., Le, T. & Rothfield, L. Division site placement in E.coli: Mutations that prevent formation of the MinE ring lead to loss of the normal midcell arrest of growth of polar MinD membrane domains. *EMBO J.* **21**, 3347–3357 (2002).
 24. de Boer, P. A., Crossley, R. E., Hand, A. R. & Rothfield, L. I. The MinD protein is a membrane ATPase required for the correct placement of the Escherichia coli division site. *EMBO J.* **10**, 4371–4380 (1991).
 25. Devaux, P. F. & Seigneuret, M. Specificity of lipid-protein interactions as determined by spectroscopic techniques. *Biochim. Biophys. Acta - Rev. Biomembr.* **822**, 63–125 (1985).
 26. Cornell, R. B. & Taneva, S. G. Amphipathic helices as mediators of the membrane interaction of amphitropic proteins, and as modulators of bilayer physical properties. *Curr. Protein Pept. Sci.* **7**, 539–552 (2006).
 27. Zhou, H. & Lutkenhaus, J. Membrane binding by MinD involves insertion of hydrophobic residues within the C-terminal amphipathic helix into the bilayer. *J. Bacteriol.* **185**, 4326–4335 (2003).
 28. Hu, Z., Gogol, E. P. & Lutkenhaus, J. Dynamic assembly of MinD on phospholipid vesicles regulated by ATP and MinE. *Proc. Natl. Acad. Sci. U. S. A.* **99**, 6761–6766 (2002).

29. Shih, Y.-L. L. *et al.* The N-Terminal Amphipathic Helix of the Topological Specificity Factor MinE Is Associated with Shaping Membrane Curvature. *PLoS One* **6**, e21425 (2011).
30. Mazor, S. *et al.* Mutual effects of MinD-membrane interaction: I. Changes in the membrane properties induced by MinD binding. *Biochim. Biophys. Acta - Biomembr.* **1778**, 2496–2504 (2008).
31. Vecchiarelli, A. G., Li, M., Mizuuchi, M. & Mizuuchi, K. Differential affinities of MinD and MinE to anionic phospholipid influence Min patterning dynamics in vitro. *Mol. Microbiol.* **93**, 453–463 (2014).
32. Mileykovskaya, E. *et al.* Effects of phospholipid composition on MinD-membrane interactions in vitro and in vivo. *J. Biol. Chem.* **278**, 22193–22198 (2003).
33. Renner, L. D. & Weibel, D. B. MinD and MinE interact with anionic phospholipids and regulate division plane formation in Escherichia coli. *J. Biol. Chem.* **287**, 38835–38844 (2012).
34. Mazor, S. *et al.* Mutual effects of MinD-membrane interaction: II. Domain structure of the membrane enhances MinD binding. *Biochim. Biophys. Acta - Biomembr.* **1778**, 2505–2511 (2008).
35. Mileykovskaya, E. & Dowhan, W. Visualization of Phospholipid Domains in Escherichia coli by Using the Cardiolipin-Specific Fluorescent Dye 10-N-Nonyl Acridine Orange. *J Bacteriol* **182**, 1172–1175 (2000).
36. Fishov, I. & Woldringh, C. L. Visualization of membrane domains in Escherichia coli. *Mol. Microbiol.* **32**, 1166–1172 (1999).
37. Dowhan, W., Mileykovskaya, E. & Bogdanov, M. Diversity and versatility of lipid-protein interactions revealed by molecular genetic approaches. *Biochim. Biophys. Acta - Biomembr.* **1666**, 19–39 (2004).
38. Zieske, K. & Schwille, P. Reconstitution of self-organizing protein gradients as spatial cues in

- cell-free systems. *Elife* **3**, e03949 (2014).
39. Schweizer, J. *et al.* Geometry sensing by self-organized protein patterns. *Proc. Natl. Acad. Sci. U. S. A.* **109**, 15283–15288 (2012).
 40. Wu, F., van Schie, B. G. C., Keymer, J. E. & Dekker, C. Symmetry and scale orient Min protein patterns in shaped bacterial sculptures. *Nat. Nanotechnol.* **10**, 719–726 (2015).
 41. Magde, D., Elson, E. & Webb, W. W. Thermodynamic fluctuations in a reacting system measurement by fluorescence correlation spectroscopy. *Phys. Rev. Lett.* **29**, 705–708 (1972).
 42. Rigler, R., Mets, Ü., Widengren, J. & Kask, P. Fluorescence correlation spectroscopy with high count rate and low background: analysis of translational diffusion. *Eur. Biophys. J.* **22**, 169–175 (1993).
 43. Eigen, M. & Rigler, R. Sorting single molecules: application to diagnostics and evolutionary biotechnology. *Proc. Natl. Acad. Sci.* **91**, 5740–5747 (1994).
 44. Weidemann, T. *et al.* Counting nucleosomes in living cells with a combination of fluorescence correlation spectroscopy and confocal imaging. *J. Mol. Biol.* **334**, 229–240 (2003).
 45. Digman, M. A., Dalal, R., Horwitz, A. F. & Gratton, E. Mapping the number of molecules and brightness in the laser scanning microscope. *Biophys. J.* **94**, 2320–2332 (2008).
 46. Politi, A. Z. *et al.* Quantitative mapping of fluorescently tagged cellular proteins using FCS-calibrated four-dimensional imaging. *Nat. Protoc.* **13**, 1445–1464 (2018).
 47. Petrášek, Z. & Schwille, P. Precise measurement of diffusion coefficients using scanning fluorescence correlation spectroscopy. *Biophys. J.* **94**, 1437–1448 (2008).
 48. Einstein, A. Über die von der molekularkinetischen Theorie der Wärme geforderte Bewegung von in ruhenden Flüssigkeiten suspendierten Teilchen. *Ann. Phys.* **322**, 549–560 (1905).
 49. von Smoluchowski, M. Zur kinetischen Theorie der Brownschen Molekularbewegung und der

- Suspensionen. *Ann. Phys.* **326**, 756–780 (1906).
50. Sutherland, W. LXXV. *A dynamical theory of diffusion for non-electrolytes and the molecular mass of albumin. Philos. Mag. Ser. 6* **9**, 781–785 (1905).
 51. Thompson, N. L. in *Chemistry and Physics of Lipids* (ed. Lakowicz, J. R.) **50**, 337–378 (Springer US, 1999).
 52. Salje, J., van den Ent, F., de Boer, P. & Löwe, J. Direct Membrane Binding by Bacterial Actin MreB. *Mol. Cell* **43**, 478–487 (2011).
 53. Pichoff, S. & Lutkenhaus, J. Tethering the Z ring to the membrane through a conserved membrane targeting sequence in FtsA. *Mol. Microbiol.* **55**, 1722–1734 (2005).
 54. Parlitz, R. *et al.* Escherichia coli signal recognition particle receptor FtsY contains an essential and autonomous membrane-binding amphipathic helix. *J. Biol. Chem.* **282**, 32176–32184 (2007).
 55. Bajar, B. T. *et al.* Improving brightness and photostability of green and red fluorescent proteins for live cell imaging and FRET reporting. *Sci. Rep.* **6**, 20889 (2016).
 56. Szeto, T. H., Rowland, S. L., Habrukowich, C. L. & King, G. F. The MinD membrane targeting sequence is a transplantable lipid-binding helix. *J. Biol. Chem.* **278**, 40050–40056 (2003).

Switching Protein Patterns on Membranes

A review of the recent literature concerning the manipulation of biological patterns. Specifically, manipulation of the PAR system in *C. elegans*, the Cdc42 system in *S. cerevisiae* and the Min system in an *in vitro* context are described.

Reprinted with permission from Elsevier.

Full citation: P. Glock and P. Schwille, “Switching protein patterns on membranes,” *Current Opinion in Colloid & Interface Science*, vol. 38, pp. 100–107, nov 2018

Source online: <https://doi.org/10.1016/j.cocis.2018.10.004>

Switching protein patterns on membranes

Philipp Glock and Petra Schwille



Abstract

Intracellular protein patterns govern many fundamental processes in all living cells. Recently, researchers have started to actively perturb the mechanisms forming these patterns in real time. With exciting new developments in guiding intracellular flows, in optogenetics and in chemical biology, it is becoming feasible to change self-organized protein pattern formation. This review provides a survey of the approaches that have so far been used to control fundamental processes such as polarization, development of multicellular organisms and bacterial cell division, with a focus on membrane-assisted processes. Already in the limited set of published results on this topic to date, there is big diversity in the designs. The different established starting points for switching reaction-diffusion systems are therefore described and further complemented by future perspectives.

Addresses

Max Planck Institute of Biochemistry, Am Klopferspitz 18, 82152 Martinsried, Germany

Corresponding author: Schwille, Petra. (schwille@biochem.mpg.de)

Current Opinion in Colloid & Interface Science 2018, 38:100–107

This review comes from a themed issue on **Biological Colloids 2018**

Edited by **Martin Malmsten** and **Stephan Zauscher**

For a complete overview see the [Issue](#) and the [Editorial](#)

<https://doi.org/10.1016/j.cocis.2018.10.004>

1359-0294/© 2018 Elsevier Ltd. All rights reserved.

Keywords

Protein patterns, Optogenetics, Reaction-diffusion, Min system, Cdc42, PAR proteins, Photoswitch, membranes, Pattern formation.

Introduction

Patterns are among the key hallmarks of life across all scales. From vegetation patches in arid ecosystems [1] including the development of animals [2] to bacterial cell division [3] - pattern formation is sometimes a consequence, but more often prerequisite for forming and sustaining life forms. While the pattern forming units on the larger scale can be groups of organisms, tissues or cells [4], patterns on the smallest, intracellular scale have to be established by spatiotemporal dynamics of molecules. There are examples of maternally deposited gradients of RNA in egg cells that determine the

ensuing pattern [5], but in most cases the molecules forming intracellular patterns are proteins.

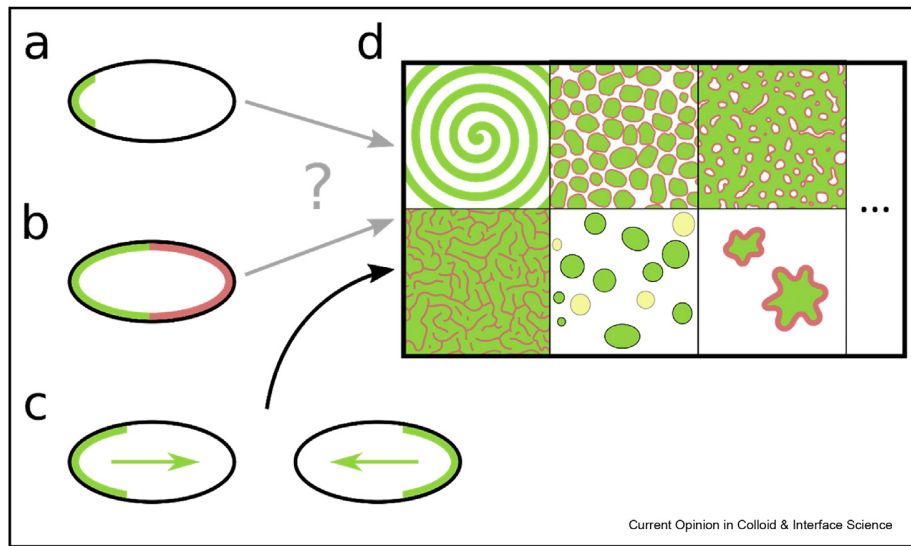
Due to the limited space within a single cell, the types of patterns one can expect to observe are restricted in their complexity. The simplest case of an intracellular pattern is polarization, meaning that one region of the cell is selected and locally enriched in a patterning molecule (Figure 1a). A bipolar pattern can result from reaction-diffusion, curvature-sensing or the molecule's dependence on additional factors such as lipid composition [6,7] (Figure 1b). Finally, systems have been described that show a time-dependent switching of patterns, such as a regular pole-to-pole oscillation of protein concentrations in cells [3] (Figure 1c). One should note however, that self-organized pattern forming systems can be reconstituted without the boundaries of a natural cell, which can greatly expand the range of patterns formed [8,9] (Figure 1d).

Except for cases where patterns arise from prepositioned agents, or where curvature or membrane changes are sensed, intracellular pattern formation generally depends on reaction-diffusion (R-D) mechanisms to form and sustain the pattern. These mechanisms, in the context of biological patterns and morphogenesis first described by Alan Turing [10], often rely on a large difference between diffusion coefficients of the proteins involved, or between multiple conformational states of proteins [11]. All of the systems discussed herein feature a membrane-bound state of one or more of the involved proteins, due to membrane-diffusion being orders of magnitude slower than free diffusion in the cytosol. Other options to achieve this difference intracellularly are binding to DNA [12] or, mostly in eukaryotic cells, binding to specific organelles or the cytoskeleton. An important similarity between all reaction-diffusion systems is the nonlinearity introduced by positive feedback or negative feedback regulation [13].

If we assume the very simple case of a mass-conserving system consisting of one protein, existing in two states A and B, which both diffuse and can be interconverted, we could write down the following rate equations (Figure 2).

Herein, a and b depict the local concentrations, D_a and D_b the diffusion constants for the soluble (e.g. A) and

Figure 1



Protein patterns formed by reaction-diffusion systems. a) Polarized pattern e.g. displayed by the cell polarity factor Cdc42. b) Anterior/posterior polarization as formed by the eukaryotic PAR system. c) Dynamic reaction-diffusion system showing a pole-to-pole oscillation, e.g. the Min system of *E. coli*. d) New patterns emerge when these reaction-diffusion systems are reconstituted without the confinement of the cell on a flat 2D membrane. This effect has been shown for the *E. coli* Min protein system, but is equally conceivable for many other systems. For the Min system spiral waves and travelling waves have been described, among other patterns that emerge under specific conditions.

Figure 2

$$\frac{\partial a(\vec{x}, t)}{\partial t} = D_a \nabla^2 a + f(a, b; p)$$

$$\frac{\partial b(\vec{x}, t)}{\partial t} = D_b \nabla^2 b - f(a, b; p)$$

Rate of concentration change Molecular diffusion Reaction of b to a external modulation p(x, t)

Example of rate equations for a simple one-protein reaction-diffusion system.

membrane-bound form (e.g. B) and the nonlinear function f comprises all interconversion steps. Additionally, p contains any means of externally manipulating the pattern, as in the applications discussed in this review. In all of the biological systems described to date, the complexity is higher than this example, with a minimum of two proteins interacting in multiple conformations and states. We therefore encourage the interested reader to start with the following references [11,13–17] or consult textbooks on nonlinear dynamics, e.g. Refs. [18,19].

For the reasons highlighted above, theoretical models are many times not yet capable of describing the full complexity and predicting exact spatial pattern distribution produced by real-world reaction-diffusion systems [11]. For example, the length scale of the Min system’s travelling waves reproducibly differs by more than one order of magnitude between in vivo and in vitro experiments although the same proteins, at the same concentrations, react on similar matrices. From an experimentalist’s point of view, it is tempting to manipulate the formed patterns for multiple reasons. Firstly, the phenomena regulated by intracellular pattern formation are generally of great interest to cell biologists. By manipulating the underlying pattern forming system, new insights can be gained into the physiological role of the system. Secondly, manipulating pattern forming systems may open up new applications and avenues for research, especially in synthetic biology. These systems are unique in their ability to de novo pattern or polarize a cell or compartment. Lastly, reaction-diffusion systems are fascinating subjects of study, both theoretically and experimentally. While the theory to comprehensively describe the behavior of manipulated patterns may still be missing, new avenues can already be explored experimentally. In the past years, several groups have succeeded in manipulating pattern formation on membranes, and we are sure to see more such endeavors in the future.

Switching polarity by using light: Cdc42 under optical control

Cdc42 is a small GTPase of the Rho family and is known as one of the central factors for eukaryotic cell polarization [20]. There is a complex interplay between Cdc42 and the cytoskeleton, and in higher organisms there are many more factors involved. But in essence, the Cdc42 GTPase has an active, membrane-bound GTP-state and an inactive, cytosolic GDP-state. In yeast, local positive feedback is provided by recruitment of Bem1, a scaffold protein, and the Cdc24 GEF (guanosine nucleotide exchange factor). Negative feedback is realized via the interaction with GAPs (GTPase activating proteins). Thus, while there are many more components involved in the mechanism, in its core it is a reaction-diffusion system [21]. In *Saccharomyces cerevisiae* (baker's yeast), cells polarize at a specific point in the cell cycle to specify where the daughter cell, which emerges as a bud from its mother cell, is placed. *S. cerevisiae* usually relies on landmark cues to find the next bud site, but will spontaneously polarize if the gene *Rsr1* is deleted [22].

In a recently published work, Witte et al. achieved control over this process by employing an optogenetics strategy [23]. They realized their polarization switch by introducing a membrane-bound target protein and fusing either Bem1 or Cdc24 to a blue-light-activated binder, thereby recruiting Bem1 or Cdc24 to a specified region on the membrane with blue light. Their experiments confirmed that there is indeed positive feedback. Both the Bem1 construct and the Cdc24 construct successfully recruited endogenous Bem1 and Cdc24 on top of activating Cdc42 locally. Light-activated recruitment of either protein at the right time was sufficient to selectively determine the next bud site. However, they also found that successful activation is highly dependent on the cell cycle, and identified a second, so far not described positive feedback loop. The well-described tripartite positive feedback involving Bem1, Cdc24 and Cdc42 can be externally activated by recruiting Bem1 to the membrane, but only if the cell is non-polarized. On the other hand, optogenetic recruitment of Cdc24 to the membrane leads to Cdc42 and Cdc24 accumulation both in polarized and in non-polarized cells. Therefore, there are two interlinked positive feedback loops. The aforementioned interplay between the actin cytoskeleton and Cdc42 polarization was shown to play a rather subordinate role. When actin was inhibited by Latrunculin A (a small molecule that binds monomeric actin and prevents polymerization), optogenetic recruitment of Bem1 or Cdc24 still reproducibly led to polarization. The authors then went further towards artificial pattern formation by simultaneously photo-activating two areas, recruiting either Bem1 or Cdc24 to the membrane areas. In either case, only one of the activated regions developed to form a bud. These experiments revealed that polarization of only one site is enforced via negative feedback, and that this negative feedback is too strong

to be overcome by optogenetic Bem1-or Cdc24-recruitment.

Overall, this study outlines a promising strategy for controlling reaction-diffusion patterns in vivo. While optogenetic approaches have long been used in neurobiology to disentangle functions of specific neurons, cell biology has just started picking up these tools, and there remains much to be discovered by artificially positioning proteins by optical cues with great spatial and temporal precision [24,25].

Switching protein patterns in higher organisms: PAR proteins of *C. elegans*

Partitioning defective (PAR) proteins are highly conserved polarity factors found in all animals, which control asymmetric cell divisions and define polarity axes [26]. In the model organism *Caenorhabditis elegans* (a small worm belonging to the nematode phylum), the very first division of the egg after fertilization is asymmetric and the ensuing polarity of the embryo is controlled by PAR proteins [27]. As with Cdc42, there are many factors contributing to the decoration of the anterior portion of the cell membrane with anterior PARs (aPARs), and the posterior half with posterior PARs (pPARs), respectively. The presence of mutual inhibition of pPARs and aPARs, as well as self-recruitment within the two groups puts the PAR system in the vicinity of reaction-diffusion systems. And indeed, after verifying diffusive properties of some components, the PAR system has been successfully described and modeled as a reaction-diffusion system [27,28].

It has been established in the literature that cortical flows involving the actin cortex contribute to the polarity of *C. elegans* zygotes [27,29]. Thanks to technical advances, the flows inside the fertilized egg can now be manipulated in a precise manner [30]. Mittasch et al. developed a technique they call focused-light-induced cytoplasmic streaming (FLUCS), which allows to non-invasively induce directed cytoplasmic flows with the help of an infrared laser. When they induced a cytoplasmic flow towards the posterior pole, as naturally happens in the zygote, the loading of pPARs on the posterior side was enhanced. When they employed FLUCS to induce a rotational movement of the cytoplasm, they could reposition the polar zones formed by the PAR proteins. However, when rotating by less than 90°, the following division would always happen in the original plane, reverting back to the anterior-posterior organization before FLUCS manipulation. This shows that the zygote has inbuilt stability versus perturbations in the orientation of polar zones. Only when they induced a shift of the PAR zones by more than 90°, the entire polarity inverted, with aPARs occupying the cell half previously occupied by pPARs,

and vice versa. On top of the impressive polarity switching enabled by their technique, FLUCS could in the future be used on other reaction-diffusion systems to control flows externally, thereby influencing the patterns.

The Min system of *Escherichia coli*: advanced control over self-organized patterns

The Min system plays a major role in ensuring that cell division takes place in the middle of the cell in *Escherichia coli* and many other bacteria [31–33]. It does so by dynamically positioning MinC, an inhibitor of the primary division ring constituent FtsZ. Thus, if the Min system is deleted or malfunctioning, divisions are no longer constrained to the cell middle, leading to aberrant cell divisions, especially near the poles. The genetic locus (*minB*) and the encoded proteins, were therefore named after the chromosome-less *minicells* that form when the Min system is deactivated [31]. The Min proteins show a regular oscillation between the cell poles, whereby a new polar zone is always growing from the pole towards midcell, and is dissolved from midcell towards the poles. This leads to a time-averaged concentration minimum of Min proteins at midcell, inhibiting the formation of division rings everywhere else.

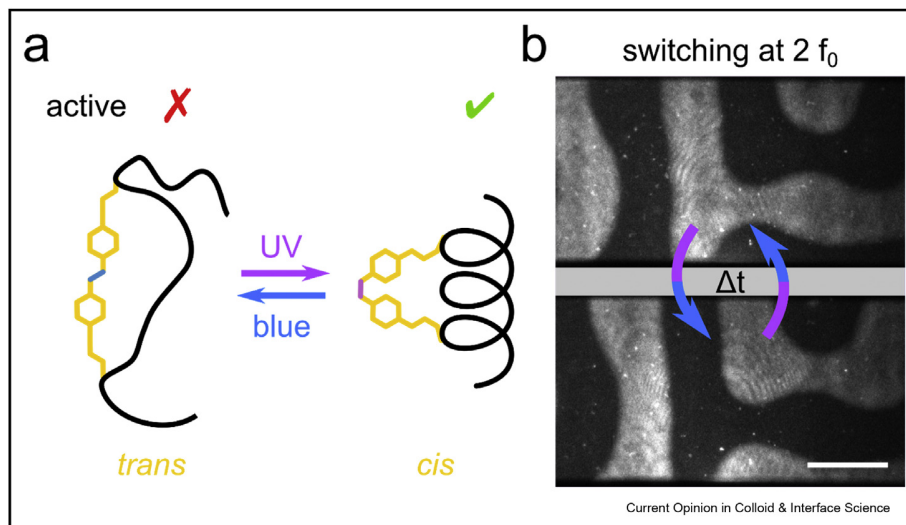
The three proteins of the Min system are called MinC, MinD and MinE, and their respective functions have been determined in great detail [34–37]. MinD is an ATPase that dimerizes upon ATP binding. This switch, in conjunction with a protein sequence near MinD's C-terminus, a membrane binding amphipathic helix, constitutes the core of the Min system. MinD monomers carry a single membrane targeting sequence (MTS), thus remain cytosolic. MinD dimers, on the other hand, carry two MTS and can bind to negatively charged lipid bilayers. It is important to note that MinD's intrinsic ATPase activity is very low, and therefore dimers are rather long-lived. The second protein of the Min system, MinE, activates the ATPase activity of MinD [38]. MinE can switch its conformation from a latent form, with a structural core of 6 beta sheets, to an active conformation. In the active conformation two of the beta sheets rearrange their secondary structure to form an alpha helix that senses and contacts MinD, and an MTS [36,37]. These features allow MinE to provide long-ranged negative feedback, as well as enhancing its processivity on MinD polar zones [37,39,40]. MinC, as mentioned above, is an inhibitor of FtsZ ring formation, and binds to MinD, piggybacking on the regular Min oscillations.

Since the Min system's ability to self-organize only depends on two proteins (MinD and MinE), a negatively charged membrane and ATP as the energy source, the system can easily be reconstituted in vitro [8,9]. Depositing the proteins and ATP on supported lipid

bilayers (SLB) in either a well setup [9] or a flow-cell [8] has revealed that the system is capable of forming large-scale surface waves and multiple other patterns. Reconstitution enabled detailed studies on the influence of membrane composition [41], geometry [42–44], single-molecule behavior [39] and many more. Notably, the limited phenotypes observed with mutated or partially deleted Min system in vivo translate into a rich phenomenology when reconstituted in vitro. This allows for an in-depth analysis of the changes induced by certain mutations [45,46]. Especially in combination with mathematical modeling [11,46,47] and innovative experiments in vivo [48], we have gained many insights into this fascinating model system for biological reaction-diffusion. Owing to the fact that only MinDE are necessary, and that these can be modified in many ways, the Min system is also a promising candidate as a pattern formation system in bottom-up synthetic biology [49].

In a recent publication, we developed and applied a photo switch for the Min system that enables control over pattern formation with great spatial and temporal precision [50]. The photoswitch was designed to locally enhance ATP hydrolysis by MinD, thereby monomerizing it and subsequently detaching it from the membrane. To do so, the aforementioned contact helix, with which MinE enhances MinD's ATPase activity, was modified and produced by solid-phase peptide synthesis. We incorporated two cysteines into the sequence, to which we covalently crosslinked an azobenzene crosslinker [51]. The azobenzene can be switched between a stretched trans configuration and a bent cis configuration by applying blue light (470 nm) or UV-light (365 nm), respectively (Figure 3a). This switch impacts the peptide's conformation in a way that it becomes more alpha-helical when UV-light is applied and loses helicity upon illumination with blue light or if left in the dark. Pattern formation by the Min system could be reversibly turned off by activating the photoswitch to release MinD from the membrane. Switching back to the trans configuration reinitiated pattern formation, which turned out to be chaotic at first. Over time, waves re-align to reproduce regular travelling waves as observed before switching. Unlike optogenetic tools, the azobenzene offers a very fast and reversible switching in both directions. Therefore, we could apply regular pulses of alternating UV- and blue light to entrain the Min system with an external forcing frequency. Intriguingly, the system responds to certain frequencies with characteristic new patterns. Most strikingly, when forcing at approximately twice the endogenous frequency, the travelling waves turn into a standing wave with precise spatial memory (Figure 3b). As long as external forcing continues, the memory is retained by the system, and even persists for a few cycles after external forcing is stopped.

Figure 3



Photoswitching patterns formed by the Min system with an azobenzene-crosslinked MinE derived peptide. a) Crosslinking two cysteines within a small MinE peptide with an azobenzene linker turns it into a switch for alpha-helicity. In this case, UV-light switches the azobenzene to cis, thereby promoting helicity and rendering the peptide active. Blue light reverses the conformation of the azobenzene to trans, thus inhibiting the alpha-helical conformation. b) Periodically activating the photoswitch at twice the endogenous frequency f_0 produces a standing wave, with precise memory of the two MinD distributions (taken by TIRF microscopy, scale bar: 30 μm).

Unfortunately, azobenzenes are not as easily genetically encoded as optogenetic proteins, and therefore the application *in vivo* is currently not feasible. The photoswitch could, however, be combined with efforts to encapsulate the Min system, e.g. in droplets or vesicles [52]. Additionally, building a closed loop with spatially heterogeneous intensities of UV- or blue light, based on a camera readout, would enable sophisticated spatial and temporal control over this reaction-diffusion system. We are, moreover, convinced that the full spectrum of patterns formed by the Min system is yet to be reported, and a means of externally controlling the local MinD concentration will be valuable in the future.

Further advances towards switching protein patterns on membranes

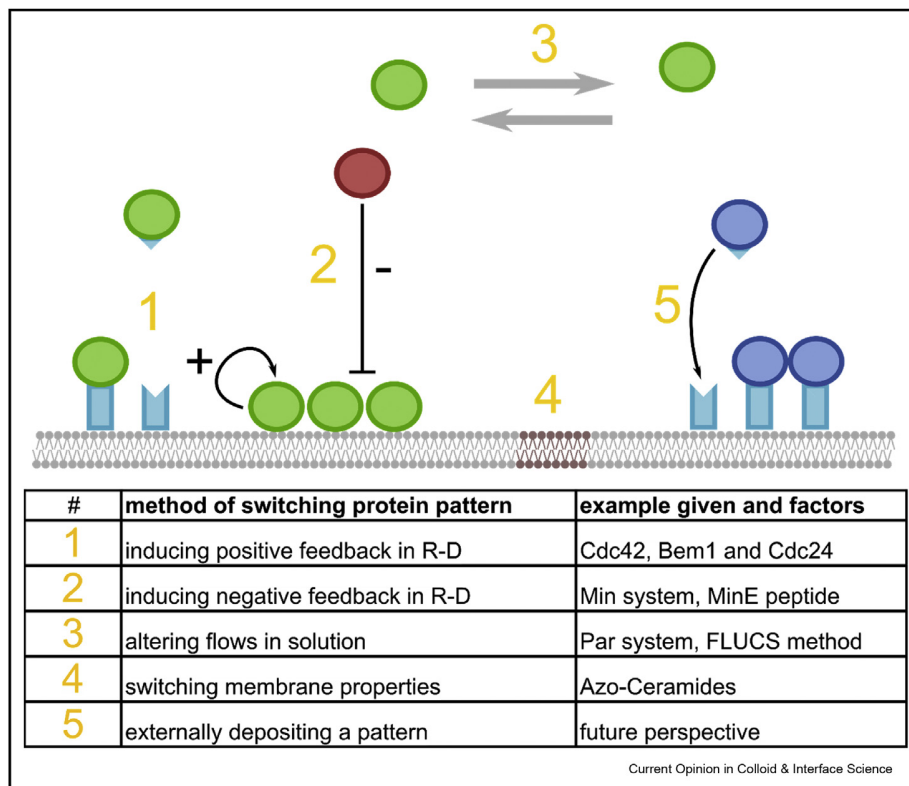
While we have discussed several systems where proteins self-organize to form patterns, there are cases of protein pattern formation as a consequence of non-proteinaceous factors. A prominent example of such patterns are membrane domains formed by sphingolipids and cholesterol (lipid rafts) in eukaryotic cells [53]. But also in prokaryotes, lateral membrane inhomogeneities seem to be important [54]. While the dynamic nature and small sizes of lipid rafts has made *in vivo* research difficult, larger and stable domains are easily formed on model membranes *in vitro*. By incorporating artificial photoswitchable ceramide lipids, Frank et al. have recently shown that lipid domains can

be controlled with light [55]. This approach could be combined with proteins that bind preferentially to the domains, such as GPI-anchored proteins or many signaling components [53]. Controlling the size and shape of the lipid domains would then also impact the distribution of proteins on the membrane.

Another path to future work on controlling or establishing protein patterns could lie in optogenetics, as employed with Bem1 and Cdc24 in the Cdc42 patterning [23]. By anchoring a binder to a membrane and supplying a fusion with the second, light-switchable, partner in solution, spatially inhomogeneous membrane distributions of almost any protein could be achieved by spatially selective light activation. While cells are usually too small for sophisticated patterns, we expect this approach to also be applicable on model membranes *in vitro*. This approach becomes even more powerful if recent findings about phase separation by proteins are taken into account, potentially enabling the localization of complex microenvironments and functionalities, such as ribonucleoprotein particles [56] and T-cell signaling [57].

Lastly, reaction-diffusion systems can in many cases be modified by fusing one of the proteins involved in patterning with another, unrelated protein. This is most often done with fluorescent proteins to visualize the pattern formed by system [3]. However, if the size of the fusion is within limits, other functional proteins

Figure 4



Multiple ways of switching protein patterns on membranes Schematic illustrating the presented methods of switching patterns. Patterns can be influenced by optogenetically recruiting proteins, leading to locally enhanced positive feedback (1). Alternatively, reaction-diffusion patterns can be controlled via negative feedback (2). FLUCS as a new method allows to bias the flows within the cytoplasm (3). Proteins that attach preferentially to lipid microdomains can be differentially positioned by switching the properties of the lipid bilayer (4). Finally, patterns could be created de novo by using an optogenetic approach and membrane-attached adaptors (5).

could be dynamically positioned together with their pattern forming partner. A recent example shows that, if sufficiently high densities of one of the interacting proteins are achieved, reaction-diffusion systems can even induce dynamic patterns in unrelated proteins binding to the same matrix [58].

Conclusions and perspective

To conclude, in recent years there have been many advances towards switching protein patterns on membranes. The reaction-diffusion systems, which are most often responsible for protein pattern formation, can be externally altered by inducing positive or negative feedback, as shown for Cdc42 and the Min system (Figure 4). A more broadly applicable way of changing intracellular patterns is by applying alternating flows in solution, e.g. via FLUCS, or by locally changing the membrane properties, as shown with photoactivatable ceramides. Finally, future efforts could induce patterns de novo, without the need or the benefit of self-organization. We are positive that many insights will yet be gained by altering pattern formation on

membranes, and that these efforts will move us closer to understanding important cellular mechanisms as well as pattern formation itself.

Acknowledgements and Funding

The authors thank Tamara Heermann for comments on the manuscript and Fridtjof Brauns for helpful discussions. P.G. is supported by “GRK2062 - Molecular Principles of Synthetic Biology” and the International Max Planck Research School for Molecular Life Sciences (IMPRS-LS).

References

Papers of particular interest, published within the period of review, have been highlighted as:

- * of special interest
- ** of outstanding interest

1. Klausmeier CA: **Regular and irregular patterns in semiarid vegetation.** *Science* 1999, **284**:1826–1828, <https://doi.org/10.1126/science.284.5421.1826>.
2. Johnston DS, Nüsslein-Volhard C: **The origin of pattern and polarity in the Drosophila embryo.** *Cell* 1992, **68**:201–219, [https://doi.org/10.1016/0092-8674\(92\)90466-P](https://doi.org/10.1016/0092-8674(92)90466-P).
3. Raskin DM, de Boer P a: **Rapid pole-to-pole oscillation of a protein required for directing division to the middle of Escherichia coli.** *Proc Natl Acad Sci U S A* 1999, **96**:4971–4976, <https://doi.org/10.1073/pnas.96.9.4971>.

4. Scholes NS, Isalan M: **A three-step framework for programming pattern formation.** *Curr Opin Chem Biol* 2017, **40**:1–7, <https://doi.org/10.1016/j.cbpa.2017.04.008>.
 5. Anderson KV, Nüsslein-Volhard C: **Information for the dorsal-ventral pattern of the Drosophila embryo is stored as maternal mRNA.** *Nature* 1984, **311**:223–227, <https://doi.org/10.1038/311223a0>.
 6. Ramamurthi KS, Losick R: **Negative membrane curvature as a cue for subcellular localization of a bacterial protein.** *Proc Natl Acad Sci U S A* 2009, **106**:13541–13545, <https://doi.org/10.1073/pnas.0906851106>.
 7. Renner LD, Weibel DB: **Cardiolipin microdomains localize to negatively curved regions of Escherichia coli membranes.** *Proc Natl Acad Sci U S A* 2011, **108**:6264–6269, <https://doi.org/10.1073/pnas.1015757108>.
 8. Ivanov V, Mizuuchi K: **Multiple modes of interconverting dynamic pattern formation by bacterial cell division proteins.** *Proc Natl Acad Sci U S A* 2010, **107**:8071–8078, <https://doi.org/10.1073/pnas.0911036107>.
 9. Loose M, Fischer-Friedrich E, Ries J, Kruse K, Schwille P: **Spatial regulators for bacterial cell division self-organize into surface waves in vitro.** *Science* 2008, **320**:789–792, <https://doi.org/10.1126/science.1154413>.
 10. Turing AM: **The chemical basis of morphogenesis.** *Philos Trans R Soc B Biol Sci* 1952, **237**:37–72, <https://doi.org/10.1098/rstb.1952.0012>.
 11. Halatek J, Brauns F, Frey E: **Self-organization principles of intracellular pattern formation.** *Philos Trans R Soc Lond B Biol Sci* 2018, **373**, <https://doi.org/10.1098/rstb.2017.0107>.
- Comprehensive review of current quantitative models for intracellular pattern formation on membranes.
12. Schumacher D, Bergeler S, Harms A, Vonck J, Huneke-Vogt S, Frey E, et al.: **The PomXYZ proteins self-organize on the bacterial nucleoid to stimulate cell division.** *Dev Cell* 2017, **41**, <https://doi.org/10.1016/j.devcel.2017.04.011>. 299–314. e13.
 13. Kondo S, Miura T: **Reaction-diffusion model as a framework for understanding biological pattern formation.** *Science* 2010, **329**:1616–1620, <https://doi.org/10.1126/science.1179047>.
- Review of reaction-diffusion, especially Turing patterns and their described occurrences in biological systems.
14. Trong PK, Nicola EM, Goehring NW, Kumar KV, Grill SW: **Parameter-space topology of models for cell polarity.** *New J Phys* 2014, **16**:065009, <https://doi.org/10.1088/1367-2630/16/6/065009>.
 15. Otsuji M, Ishihara S, Co C, Kaibuchi K, Mochizuki A, Kuroda S: **A mass conserved reaction-diffusion system captures properties of cell polarity.** *PLoS Comput Biol* 2007, **3**, e108, <https://doi.org/10.1371/journal.pcbi.0030108>.
 16. Goryachev AB, Pokhilko AV: **Dynamics of Cdc42 network embodies a Turing-type mechanism of yeast cell polarity.** *FEBS Lett* 2008, **582**:1437–1443, <https://doi.org/10.1016/j.febslet.2008.03.029>.
 17. Mori Y, Jilkine A, Edelstein-Keshet L: **Wave-pinning and cell polarity from a bistable reaction-diffusion system.** *Biophys J* 2008, **94**:3684–3697, <https://doi.org/10.1529/biophysj.107.120824>.
 18. Strogatz SH: *Nonlinear dynamics and chaos: with applications to physics, biology, chemistry, and engineering.* CRC Press; 2018.
 19. Murray JD. *Mathematical biology II*, vol. 18. New York: Springer-Verlag; 1993, <https://doi.org/10.1007/b98869>.
 20. Etienne-Manneville S: **Cdc42—the centre of polarity.** *J Cell Sci* 2004, **117**:1291–1300, <https://doi.org/10.1242/jcs.01115>.
- Overview of Cdc42-governed polarization and its involvement in many cellular pathways.
21. Savage NS, Layton AT, Lew DJ: **Mechanistic mathematical model of polarity in yeast.** *Mol Biol Cell* 2012, **23**:1998–2013, <https://doi.org/10.1091/mbc.E11-10-0837>.
 22. Park HO, Kang PJ, Rachfal AW: **Localization of the Rsr1/Bud 1 GTPase involved in selection of a proper growth site in yeast.** *J Biol Chem* 2002, **277**:26721–26724, <https://doi.org/10.1074/jbc.C200245200>.
 23. Witte K, Strickland D, Glotzer M: **Cell cycle entry triggers a switch between two modes of Cdc42 activation during yeast polarization.** *Elife* 2017, **6**:1–27, <https://doi.org/10.7554/eLife.26722>.
- Optogenetic control over Cdc42-guided cell polarization via the proteins Bem1 and Cdc24.
24. Niopek D, Benzinger D, Roensch J, Draebing T, Wehler P, Eils R, et al.: **Engineering light-inducible nuclear localization signals for precise spatiotemporal control of protein dynamics in living cells.** *Nat Commun* 2014, **5**:4404, <https://doi.org/10.1038/ncomms5404>.
 25. van Bergeijk P, Adrian M, Hoogenraad CC, Kapitein LC: **Optogenetic control of organelle transport and positioning.** *Nature* 2015, **518**:111–114, <https://doi.org/10.1038/nature14128>.
 26. Hoegge C, Hyman AA: **Principles of PAR polarity in Caenorhabditis elegans embryos.** *Nat Rev Mol Cell Biol* 2013, **14**: 315–322, <https://doi.org/10.1038/nrm3558>.
- Comprehensive review of PAR polarity in the model system *C. elegans*.
27. Goehring NW, Trong PK, Bois JS, Chowdhury D, Nicola EM, Hyman AA, et al.: **Polarization of PAR proteins by advective triggering of a pattern-forming system.** *Science* 2011, **334**: 1137–1141, <https://doi.org/10.1126/science.1208619>.
 28. Goehring NW, Hoegge C, Grill SW, Hyman AA: **PAR proteins diffuse freely across the anterior–posterior boundary in polarized C. elegans embryos.** *J Cell Biol* 2011, **193**:583–594, <https://doi.org/10.1083/jcb.201011094>.
 29. Hird SN, White JG: **Cortical and cytoplasmic flow polarity in early embryonic cells of Caenorhabditis elegans.** *J Cell Biol* 1993, **121**:1343–1355, <https://doi.org/10.1083/jcb.121.6.1343>.
 30. Miittasch M, Gross P, Nestler M, Fritsch AW, Iserman C, Kar M, et al.: **Non-invasive perturbations of intracellular flow reveal physical principles of cell organization.** *Nat Cell Biol* 2018, **20**: 344–351, <https://doi.org/10.1038/s41556-017-0032-9>.
- New and innovative technology to change intracellular flows, applied to PAR polarity.
31. Adler HI, Fisher WD, Cohen A, Hardigree AA: **Miniature Escherichia coli cells deficient in DNA.** *Proc Natl Acad Sci U S A* 1967, **57**:321–326.
 32. de Boer PA, Crossley RE, Rothfield LI: **Isolation and properties of minB, a complex genetic locus involved in correct placement of the division site in Escherichia coli.** *J Bacteriol* 1988, **170**:2106–2112, <https://doi.org/10.1128/jb.170.5.2106-2112.1988>.
 33. Shih Y-L, Zheng M: **Spatial control of the cell division site by the Min system in Escherichia coli.** *Environ Microbiol* 2013, **15**: 3229–3239, <https://doi.org/10.1111/1462-2920.12119>.
- Comprehensive review of the Min system of *E. coli* and its role in bacterial cell division.
34. Cordell SC, Anderson RE, Löwe J: **Crystal structure of the bacterial cell division inhibitor MinC.** *EMBO J* 2001, **20**: 2454–2461, <https://doi.org/10.1093/emboj/20.10.2454>.
 35. Cordell SC, Löwe J: **Crystal structure of the bacterial cell division regulator MinD.** *FEBS Lett* 2001, **492**:160–165.
 36. Park KT, Wu W, Battaile KP, Lovell S, Holyoak T, Lutkenhaus J: **The min oscillator uses MinD-dependent conformational changes in MinE to spatially regulate cytokinesis.** *Cell* 2011, **146**:396–407, <https://doi.org/10.1016/j.cell.2011.06.042>.
 37. Park K-T, Villar MT, Artigues A, Lutkenhaus J: **MinE conformational dynamics regulate membrane binding, MinD interaction, and Min oscillation.** *Proc Natl Acad Sci Unit States Am* 2017, **114**:201707385, <https://doi.org/10.1073/pnas.1707385114>.
 38. Hu Z, Lutkenhaus J: **Topological regulation of cell division in E. coli: spatiotemporal oscillation of MinD requires stimulation of its ATPase by MinE and phospholipid.** *Mol Cell* 2001, **7**: 1337–1343, [https://doi.org/10.1016/S1097-2765\(01\)00273-8](https://doi.org/10.1016/S1097-2765(01)00273-8).

39. Loose M, Fischer-Friedrich E, Herold C, Kruse K, Schwille P: **Min protein patterns emerge from rapid rebinding and membrane interaction of MinE.** *Nat Struct Mol Biol* 2011, **18**:577–583, <https://doi.org/10.1038/nsmb.2037>.
40. Vecchiarelli AG, Li M, Mizuuchi M, Hwang LC, Seol Y, Neuman KC, *et al.*: **Membrane-bound MinDE complex acts as a toggle switch that drives Min oscillation coupled to cytoplasmic depletion of MinD.** *Proc Natl Acad Sci Unit States Am* 2016, **113**:E1479–E1488, <https://doi.org/10.1073/pnas.1600644113>.
41. Vecchiarelli AG, Li M, Mizuuchi M, Mizuuchi K: **Differential affinities of MinD and MinE to anionic phospholipid influence Min patterning dynamics in vitro.** *Mol Microbiol* 2014, **93**:453–463, <https://doi.org/10.1111/mmi.12669>.
42. Zieske K, Schwille P: **Reconstitution of pole-to-pole oscillations of min proteins in microengineered polydimethylsiloxane compartments.** *Angew Chem Int Ed* 2013, **52**:459–462, <https://doi.org/10.1002/anie.201207078>.
43. Schweizer J, Loose M, Bonny M, Kruse K, Monch I, Schwille P: **Geometry sensing by self-organized protein patterns.** *Proc Natl Acad Sci Unit States Am* 2012, **109**:15283–15288, <https://doi.org/10.1073/pnas.1206953109>.
44. Caspi Y, Dekker C: **Mapping out Min protein patterns in fully confined fluidic chambers.** *Elife* 2016, **5**:1–53, <https://doi.org/10.7554/eLife.19271>.
45. Kretschmer S, Zieske K, Schwille P: **Large-scale modulation of reconstituted Min protein patterns and gradients by defined mutations in MinE's membrane targeting sequence.** *PLoS One* 2017:1–16. <https://doi.org/10.1371/journal.pone.0179582>; 2017.
46. Denk J, Kretschmer S, Halatek J, Hartl C, Schwille P, Frey E: **MinE conformational switching confers robustness on self-organized Min protein patterns.** *Proc Natl Acad Sci U S A* 2018, **115**:4553–4558, <https://doi.org/10.1073/pnas.1719801115>.
47. Halatek J, Frey E: **Rethinking pattern formation in reaction–diffusion systems.** *Nat Phys* 2018, **14**:507–514, <https://doi.org/10.1038/s41567-017-0040-5>.
48. Wu F, Halatek J, Reiter M, Kingma E, Frey E, Dekker C: **Multi-stability and dynamic transitions of intracellular Min protein patterns.** *Mol Syst Biol* 2016, **12**:873, <https://doi.org/10.15252/msb.20156724>.
49. Kretschmer S, Schwille P: **Toward spatially regulated division of protocells: insights into the E. coli min system from in vitro studies.** *Life* 2014, **4**:915–928, <https://doi.org/10.3390/life4040915>.
50. Glock P, Broichhagen J, Kretschmer S, Blumhardt P, Mücksch J, Trauner D, *et al.*: **Optical control of a biological reaction–diffusion system.** *Angew Chem Int Ed* 2018, **57**:2362–2366, <https://doi.org/10.1002/anie.201712002>.
This report applies a novel photoswitch that was built using a chemical biology approach to the in vitro Min system.
51. Kumita JR, Smart OS, Woolley GA: **Photo-control of helix content in a short peptide.** *Proc Natl Acad Sci Unit States Am* 2000, **97**:3803–3808, <https://doi.org/10.1073/pnas.97.8.3803>.
52. Zieske K, Chwastek G, Schwille P: **Protein patterns and oscillations on lipid monolayers and in microdroplets.** *Angew Chem Int Ed* 2016, **55**:13455–13459, <https://doi.org/10.1002/anie.201606069>.
53. Lingwood D, Simons K: **Lipid rafts as a membrane-organizing principle.** *Science* 2010, **327**:46–50, <https://doi.org/10.1126/science.1174621>.
54. Bramkamp M, Lopez D: **Exploring the existence of lipid rafts in bacteria.** *Microbiol Mol Biol Rev* 2015, **79**:81–100, <https://doi.org/10.1128/MMBR.00036-14>.
55. Frank JA, Franquelim HG, Schwille P, Trauner D: **Optical control of lipid rafts with photoswitchable ceramides.** *J Am Chem Soc* 2016, **138**:12981–12986, <https://doi.org/10.1021/jacs.6b07278>.
56. Banani SF, Lee HO, Hyman AA, Rosen MK: **Biomolecular condensates: organizers of cellular biochemistry.** *Nat Rev Mol Cell Biol* 2017, **18**:285–298, <https://doi.org/10.1038/nrm.2017.7>.
57. Su X, Ditlev JA, Hui E, Xing W, Banjade S, Okrut J, *et al.*: **Phase separation of signaling molecules promotes T cell receptor signal transduction.** *Science* 2016, **352**:595–599, <https://doi.org/10.1126/science.aad9964>.
58. Ramm B, Glock P, Mücksch J, Blumhardt P, García-Soriano DA, Heymann M, *et al.*: **The MinDE system is a generic spatial cue for membrane protein distribution in vitro.** *Nat Commun* 2018, **9**:3942, <https://doi.org/10.1038/s41467-018-06310-1>.

Outlook

3.1 Manuscript: Building minimal biochemical interaction networks for pattern formation

In this unsubmitted manuscript, we explore the possibility of building minimal networks consisting of MinD and MinE-derived peptides. The networks are analyzed via linear stability analysis, but also experimentally realized.

This is a research project in close collaboration with Fridtjof Brauns, a theoretical physicist in the group of Prof. Erwin Frey (LMU physics). We share authorship and responsibilities, but the final author list and contributions will be determined when we are ready for submission.

Building minimal biochemical interaction networks for pattern formation

Philipp Glock^{1†}, Fridtjof Brauns^{2†}, Jacob Halatek², Erwin Frey^{2*}, Petra Schwille^{1*}

*For correspondence:

frey@lmu.de (EF);
schwille@biochem.mpg.de (PS)

[†]These authors contributed equally to this work

¹Max-Planck-Institute of Biochemistry, D-82152 Martinsried; ²Ludwigs-Maximilians University of Munich, D-80799 Munich

Abstract Despite many advances, pattern formation by proteins is still mostly unexplored. Many descriptions are incomplete because proteins show complex interactions. Here, we show that the Min system of *Escherichia coli* can be turned into minimal biochemical interaction networks by reducing the complexity of MinE. Adding back modular subsystems such as membrane binding or dimerization enables pattern formation via two distinct mechanisms. We analyze these minimal systems using quantitative modeling and linear stability analysis and reveal the underlying principles of protein pattern formation.

Introduction

Patterns are a defining characteristic of all living beings, and are found throughout the kingdoms of life. In the last years, it is becoming more apparent that patterns formed by reaction-diffusion systems are responsible for many phenomena previously thought to be regulated without the involvement of self-organization (*Green and Sharpe, 2015*). Reliance on such mechanisms allows organisms and cells to achieve robust patterning based on basic physical principles. However, the complex biomolecular interactions of proteins make complete theoretical models hard to achieve. Furthermore, all biological systems to date come with many unknown rates and morphogen properties. A fairly well-understood biological reaction-diffusion system is the Min system of *Escherichia coli*. In the bacterial cell, it biases the localization of FtsZ, a crucial component of the division ring, towards mid-cell. It does so by performing a rapid oscillation between the cell poles, governed by the proteins MinD and MinE. On time average, the ATPase MinD spends longer at the poles and less time at mid-cell. MinE facilitates membrane release of MinD by stimulating its ATPase. Piggybacking on MinD is the protein MinC, which directly inhibits FtsZ polymerization. This system serves as a simple model system for biological pattern formation, since the components are all known, only two proteins are needed to form a pattern (MinD and MinE), and the system has been successfully reconstituted in an easily modifiable *in vitro* system (*Loose et al., 2008*).

Even though the Min system seems simple at first glance, there is much complexity within the protein domain sequence and structure, and hence in the interaction between proteins. MinD is an ATPase which is believed to dimerize upon ATP-binding, raising its membrane affinity via the C-terminal membrane targeting sequence (MTS). MinE, although only 88 amino acids in length, incorporates many functions: The protein is found as a dimer in two distinct conformations (*Pichoff et al., 1995; Park et al., 2011*). While diffusing in the cytoplasm, a structure with 6 beta-sheets is formed, which sequesters both an N-terminal MTS and the sequence directly interacting with MinD more closely into the structure. Upon sensing membrane-bound MinD, it restructures into a 4

41 beta-structure allowing the MTS to contact the membrane and the anti-MinD sequence to fulfill its
42 function. In summary, MinE therefore carries four functions – activating MinD's ATPase, binding
43 to the membrane, dimerization and switching between an active and a closed conformation. In a
44 previous study, colleagues of ours investigated the importance of MinE's switch both experimentally
45 and in the context of a mathematical model. They found that MinE switching is not essential for
46 pattern formation, but opens up the parameter space in which patterns are achieved considerably,
47 thereby unlocking a high E/D-ratio regime (*Denk et al., 2018*). From other previous work, it is
48 known that also membrane binding by MinE is not essential to form patterns (*Kretschmer et al.,*
49 *2017*). Both of the previous studies retained most of the structure of MinE, predominantly mutating
50 single residues. Here, we find and analyze minimal systems for pattern formation. We show that
51 systems in which MinE is replaced by peptides that emulate core features of MinE are capable of
52 pattern formation in vitro. We thereby identify the essential features of MinE. Moreover, we provide
53 evidence that features inherent to MinE do not need to be provided by native parts of MinE, but can
54 be substituted with foreign sequences.

55 Results and Discussion

56 To reduce the complexity of MinE in the Min system, we removed all sequences not in direct contact
57 with MinD, and therefore kept only 19 amino acids (13-31). While the full in vitro Min system,
58 consisting of MinD and full-length MinE, forms spiral patterns, travelling waves and stationary
59 reaction-diffusion patterns on supported lipid bilayers (SLBs), this minimal version of MinE is not
60 capable of inducing pattern formation, at least under all conditions that we examined. We then
61 tried to rescue pattern formation capability by re-introducing features of MinE. Firstly, we added
62 back the MTS found in native MinE (residues 2-12) to the N-terminus of the peptide. This construct,
63 contrary to published results (*Vecchiarelli et al., 2016*), forms patterns with MinD. The observed
64 patterns are dynamic waves several orders of magnitude larger than those reported for the native in
65 vitro Min system (Figure 2). Patterns are sustained over many hours within our assay. Secondly, we
66 introduced dimerization back into the minimal peptide by synthetically fusing it with well-described
67 human leucine-zippers (Fos, Jun and GCN-4) (*Szálóki et al., 2015; O'Shea et al., 1989*). Interestingly,
68 also this modification enabled sustained pattern formation in the system. While the length scale
69 of patterns formed with the dimerized peptides were still larger than native Min patterns, the
70 difference was not as drastic as the MTS case. Notably, while full-length MinE forms patterns with
71 MinD in a big concentration range, the range for minimal peptides is much more limited and they
72 enable patterns only at low E/D ratios, as expected based on previous theoretical and experimental
73 work (*Halatek and Frey, 2012; Denk et al., 2018*).

74 Combining the approaches and adding both the MTS and a dimerizer to the MinE peptide
75 resulted in stationary or very slowly moving patterns and the outcome depended heavily on the
76 starting conditions of the assay (Supplementary Figure X). In general, patterns formed by our
77 minimal networks do not show the same degree of order as patterns formed by the wild-type Min
78 proteins or MinD and His-MinE. Specifically, the wavelength is much less uniform, and the defined
79 spirals or stationary patterns observed in the wild type Min system are sometimes replaced by
80 chaotic centers (Figure 2 last panel). The chaotic behavior is especially pronounced at high MinD
81 concentrations (in this case with a minimal MinE plus MTS and sfGFP) (Supplementary Video X).

82 We suspect that the minimization of MinE peptides could be taken even further by shortening
83 the peptide. Especially at the C-terminus we expect that several residues do not contribute to
84 function, since they are not visible in a crystal structure of MinE(13-31) with MinD (*Park et al.,*
85 *2011*). Additionally, the peptide still retains residues required for the dual function in the context
86 of the MinE switch. Therefore, an optimized and further reduced peptide could be screened
87 for. Additionally, our experiments with minimal peptides added to a superfolder GFP show that
88 unrelated proteins can be attached. This opens the possibility to couple the spatiotemporal pattern
89 to a different protein system. In principle, any protein can act as a minimal MinE if a peptide can be
90 added internally or at either terminus of the protein.

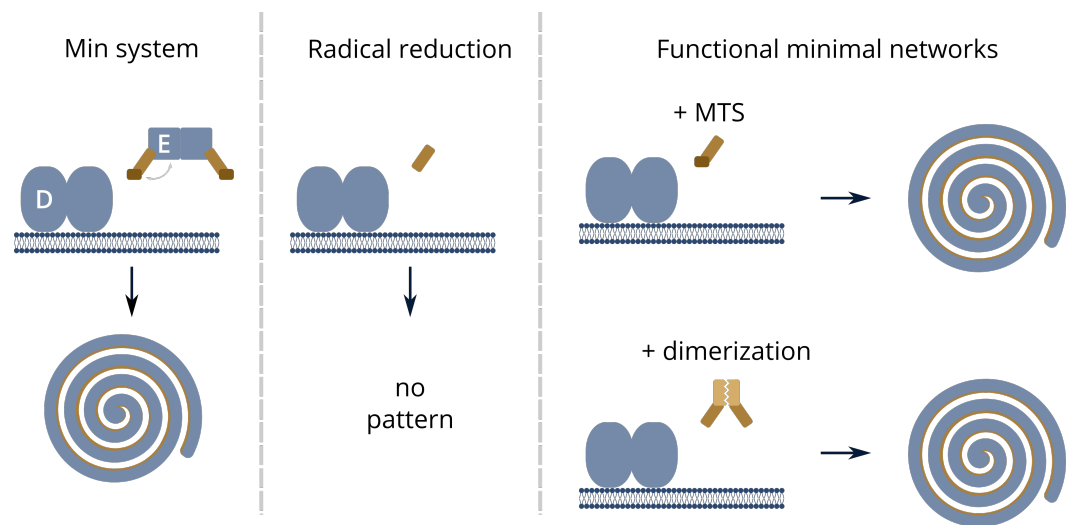


Figure 1. Steps for rebuilding minimal pattern formation in the Min system. Schematic representation of our approach to form a minimal system for pattern formation. The full Min system, consisting of MinD (blue) and MinE (blue, brown) was reduced to MinD and only a small peptide directly interacting with MinD. Pattern formation could be restored by either adding the MinE MTS to the peptide or by dimerizing it.

91 Since we relate the lack of pattern formation to the recruitment rate of MinE(13-31), it may be
 92 possible to alter MinE recruitment by changing the buffer conditions such as salt concentration, type
 93 of ions (e.g. Sodium instead of Potassium), viscosity or pH. We can only speculate here, however,
 94 since screening a vast amount of conditions was not in the scope of the present study. Studies
 95 done on the wild type Min system using different buffer conditions showed some impact on pattern
 96 formation (*Vecchiarelli et al., 2014*).

97 Although we have not tested this prediction, we expect that the native MTS of MinE could
 98 be replaced with another MTS in our minimal peptides to restore pattern formation. It would
 99 be interesting to exchange the native MTS for a quantitatively described, diverse set of MTS to
 100 determine the required strength of membrane anchors needed for minimal MinE pattern formation.
 101 However, no such set or even just quantitative data on binding strength of multiple MTS is available
 102 at the moment.

103 The networks that were established experimentally were modelled in silico based on the skeleton
 104 network (*Halatek and Frey, 2012*). MinE recruitment by MinD and MinE membrane binding were
 105 systematically altered to determine a phase diagram (Figure 3 a). Interestingly, we found that
 106 the parameter regime, namely the concentrations and rates, and not just the network topology,
 107 have a major impact on the ability to form patterns. The concentrations and rates furthermore
 108 determine the underlying mechanism of Min pattern formation. Here, we found that the respective
 109 mechanisms have different characteristics, e.g. in their ability to sense geometry. Coming back to
 110 the biochemical origin of these constructs, additional protein domains can apparently move the
 111 entire system to a different regime, as we have shown in the case of elevated MinE recruitment via
 112 dimerization of the peptide. Raising the MinE recruitment by MinD via dimerization transitioned
 113 the system into a recruitment-driven regime that enabled pattern formation (Figure 3). Adding
 114 membrane targeting to the peptide unlocked a new pathway and lead to sustained patterns via
 115 membrane recombination. This study therefore complements previous work targeted towards
 116 the MinE-switch (*Denk et al., 2018*), where another regime is unlocked by addition of the switch,
 117 namely the high E/D-ratio regime. Compared to other model systems for reaction-diffusion, the
 118 concept of protein domains adds an entire dimension to the Min system. Now, defined modules
 119 can be added, subtracted and interchanged, or the MinE component of the system can be added as
 120 a small peptide tag of 18 amino acids to any target protein, inheriting any properties which affect

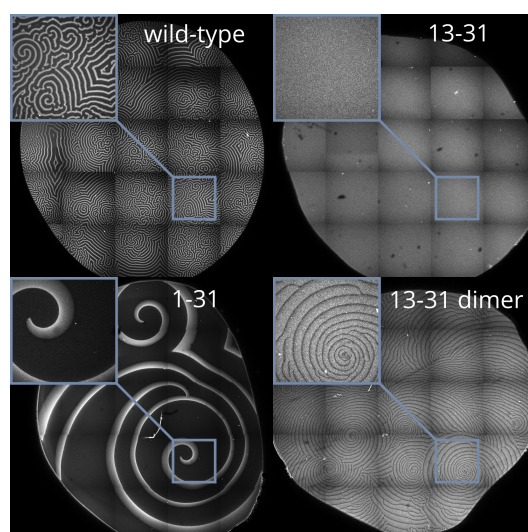


Figure 2. Examples of patterns formed by the networks presented here. The specific concentrations used were: wild type (1 μM MinD, 6 μM MinE-His), 13-31 (1.2 μM MinD, 50 nM MinE(13-31)), 1-31 (1.2 μM MinD, 50 nM MinE(1-31)), 13-31 dimer (1 μM MinD, 100 nM MinEs-Fos). Top left box in each subpanel shows zoom-ins (2.4x) of the connected blue square in the main image.

121 the pattern.

122 Taken together, we have found in a combined theory/experiment study that the two protein
123 Min system can be reduced to a small peptide taken from MinE and one protein, MinD. Patterns will
124 be formed if mechanisms driven either by recombination on the membrane or recruitment from
125 the bulk are enabled by adding the respective functionalities.

126 **Methods and Materials**

127 Most experimental methods used in this publication were exhaustively described in text and video
128 in a recent publication (*Ramm et al., 2018*). We therefore describe these techniques only in brief.

129 **Membranes**

130 SLBs were prepared from DOPC and DOPG (ratio 2:1) small unilamellar vesicles in Min buffer (25
131 mM Tris-HCl pH 7.5, 150 mM KCl, 5 mM MgCl₂) by adding them (at 0.53 mg/ml) on top of a charged,
132 cleaned glass surface. The solution was diluted after one minute by addition of 150 ml Min buffer.
133 After a total of 3 minutes, membranes in chambers were washed with 2 ml of Min buffer.

134 **Assay chamber**

135 Assay chambers were assembled from piranha-cleaned coverslips and a cut 0.5 ml plastic reaction
136 tube by gluing the tube upside down onto the cleaned and dried surface using UV-curable adhesive.

137 **In vitro self-organization assay**

138 The buffer volume in an assay chamber containing an SLB was adjusted to yield a final volume of
139 200 μl including protein solutions and ATP. Proteins, peptides and further reactants were added
140 and the solution was mixed by pipetting.

141 **Peptides**

142 Peptides were synthesized using Fmoc chemistry by our in-house Biochemistry Core Facility. MinE(2-
143 31)-KCK-Atto488 was expressed as a SUMO fusion in *E. coli*, the SUMO tag was cleaved using SenP2
144 protease and the remaining peptide was labelled using Atto488-maleimide to site-specifically target
145 the cysteine residue. Labelling was done as described below.

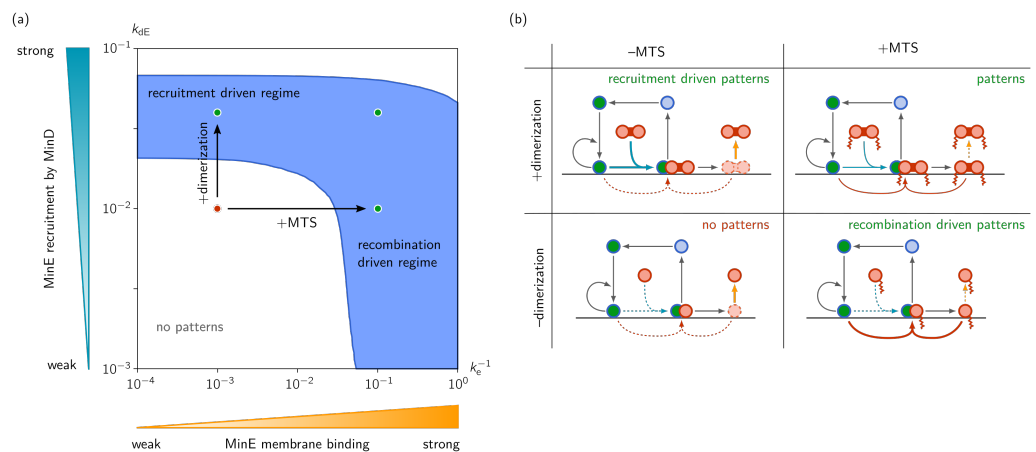


Figure 3. a) Phase diagram obtained by linear stability analysis, showing the pattern formation capabilities of the MinDE-system in dependence of MinE- and MinD-recruitment rates. The red circle represents MinE(13-31), which does not facilitate self-organized pattern formation. b) Schematic detailing the network topologies of the different minimal MinE-MinD systems studied here.

146 Protein design and purifications

147 Detailed information about cloning procedures and design of proteins can be found in the supplementary information. Protein concentration measurements Protein concentrations were determined by using a modified, linearized version of the Bradford assay in 96-well format (*Ernst and Zor, 2010*).

151 Labelling

152 Atto 488-maleimide in 5 -7 μ l DMSO (about three molecules of dye per protein) was added dropwise to 0.5 ml of protein solution in storage buffer (50 mM HEPES pH 7.25, 300 mM KCl, 10% glycerol, 0.1 mM EDTA, 0.4 mM TCEP) in a 1.5 ml reaction tube. The tube was wrapped in aluminium foil and incubated at 4 $^{\circ}$ C on a rotating shaker for two to three hours. Free dye was separated from proteins first by running the solution on a PD-10 buffer exchange column equilibrated with storage buffer. Then, remaining dye was diluted out by dialysis against storage buffer overnight. The labelling efficiency was measured by recording an excitation spectrum of the labelled protein and measuring the protein concentration as described above. We then calculated the resulting labelling efficiency using the molar absorption provided by the dye supplier (Atto 488: $9.0 \times 10^4 \text{ M}^{-1} \text{ cm}^{-1}$).

161 Imaging

162 Microscopy was done on commercial Zeiss LSM 780 microscopes with 10x air objectives (Plan-Apochromat 10x/0.45 M27 and EC Plan-Neofluar 10x/0.30 M27). Tile scans with 25 tiles (5x5) at zoom level 0.6 were stitched to obtain overview images of entire assay chambers and resolve the large-scale patterns formed.

166 Acknowledgments

167 We thank the MPIB Biochemistry Core Facility, especially Stefan Pettera, for synthesizing peptides used in this study.

169 References

170 **Denk J**, Kretschmer S, Halatek J, Hartl C, Schwille P, Frey E. MinE conformational switching confers robustness on self-organized Min protein patterns. *Proceedings of the National Academy of Sciences of the United States of America*. 2018 may; 115(18):4553–4558. <http://www.pnas.org/lookup/doi/10.1073/pnas.1719801115http>:

- 173 <http://www.ncbi.nlm.nih.gov/pubmed/29666276><http://www.pubmedcentral.nih.gov/articlerender.fcgi?artid=PMC5939084>, doi: 10.1073/pnas.1719801115.
- 174
- 175 **Ernst O**, Zor T. Linearization of the Bradford Protein Assay. *Journal of Visualized Experiments*. 2010 apr;
176 (38):1–6. <http://www.jove.com/index/Details.stp?ID=1918><http://www.ncbi.nlm.nih.gov/pubmed/20386536><http://www.pubmedcentral.nih.gov/articlerender.fcgi?artid=PMC3164080>, doi: 10.3791/1918.
- 177
- 178 **Glock P**, Broichhagen J, Kretschmer S, Blumhardt P, Mücksch J, Trauner D, Schwille P. Optical Control of a
179 Biological Reaction-Diffusion System. *Angewandte Chemie International Edition*. 2018 feb; 57(9):2362–
180 2366. <http://doi.wiley.com/10.1002/anie.201712002><http://www.ncbi.nlm.nih.gov/pubmed/29266672>, doi:
181 10.1002/anie.201712002.
- 182 **Glock P**, Ramm B, Heermann T, Kretschmer S, Schweizer J, Mücksch J, Alagöz G, Schwille P. Stationary patterns
183 in a two-protein reaction-diffusion system. *ACS Synthetic Biology*. 2018; p. acssynbio.8b00415. <http://pubs.acs.org/doi/10.1021/acssynbio.8b00415>, doi: 10.1021/acssynbio.8b00415.
- 184
- 185 **Green JBA**, Sharpe J. Positional information and reaction-diffusion: two big ideas in developmental biology combine. *Development*. 2015 apr; 142(7):1203–1211. <http://dev.biologists.org/cgi/doi/10.1242/dev.114991><http://www.ncbi.nlm.nih.gov/pubmed/25804733>, doi: 10.1242/dev.114991.
- 186
- 187
- 188 **Halatek J**, Frey E. Highly Canalized MinD Transfer and MinE Sequestration Explain the Origin of Robust MinCDE-
189 Protein Dynamics. *Cell Reports*. 2012; 1(6):741–752. <http://dx.doi.org/10.1016/j.celrep.2012.04.005>, doi:
190 10.1016/j.celrep.2012.04.005.
- 191 **Kretschmer S**, Zieske K, Schwille P. Large-scale modulation of reconstituted Min protein patterns and gra-
192 dients by defined mutations in MinE's membrane targeting sequence. *PLoS ONE*. 2017; p. 1–16. doi:
193 <https://doi.org/10.1371/journal.pone.0179582>.
- 194 **Loose M**, Fischer-Friedrich E, Ries J, Kruse K, Schwille P. Spatial regulators for bacterial cell division self-organize
195 into surface waves in vitro. *Science (New York, NY)*. 2008; 320(5877):789–792. doi: 10.1126/science.1154413.
- 196 **O'Shea E**, Rutkowski R, Stafford W, Kim P. Preferential heterodimer formation by isolated leucine zippers from
197 fos and jun. *Science*. 1989 aug; 245(4918):646–648. <http://www.sciencemag.org/cgi/doi/10.1126/science.2503872><http://www.ncbi.nlm.nih.gov/pubmed/2503872>, doi: 10.1126/science.2503872.
- 198
- 199 **Park KT**, Wu W, Battaile KP, Lovell S, Holyoak T, Lutkenhaus J. The min oscillator uses MinD-dependent
200 conformational changes in MinE to spatially regulate cytokinesis. *Cell*. 2011; 146(3):396–407. <http://dx.doi.org/10.1016/j.cell.2011.06.042>, doi: 10.1016/j.cell.2011.06.042.
- 201
- 202 **Pichoff S**, Vollrath B, Touriol C, Bouché JP. Deletion analysis of gene minE which encodes the topological
203 specificity factor of cell division in *Escherichia coli*. *Molecular microbiology*. 1995; 18(2):321–329.
- 204 **Ramm B**, Glock P, Schwille P. In Vitro Reconstitution of Self-Organizing Protein Patterns on Supported Lipid Bilay-
205 ers. *Journal of Visualized Experiments*. 2018 jul; (137):e58139. <https://www.jove.com/video/58139>[https://www.jove.com/video/58139https://www.jove.com/video/58139/in-vitro-reconstitution-self-organizing-protein-patterns-on-supported](https://www.jove.com/video/58139/in-vitro-reconstitution-self-organizing-protein-patterns-on-supported), doi:
206 <https://www.jove.com/video/58139/in-vitro-reconstitution-self-organizing-protein-patterns-on-supported>, doi:
207 10.3791/58139.
- 208 **Szalóki N**, Krieger JW, Komáromi I, Tóth K, Vámosi G. Evidence for Homodimerization of the c-Fos Tran-
209 scription Factor in Live Cells Revealed by Fluorescence Microscopy and Computer Modeling. *Mol Cell Biol*. 2015; 35(August):3785–3798. <http://mcb.asm.org/content/35/21/3785.abstract>{%}5Cnalsdb.org, doi:
210 10.1128/MCB.00346-15.
- 211
- 212 **Vecchiarelli AG**, Li M, Mizuuchi M, Hwang LC, Seol Y, Neuman KC, Mizuuchi K. Membrane-bound MinDE complex
213 acts as a toggle switch that drives Min oscillation coupled to cytoplasmic depletion of MinD. *Proceedings of the National Academy of Sciences*. 2016 mar; 113(11):E1479–E1488. <http://www.pnas.org/lookup/doi/10.1073/pnas.1600644113>, doi: 10.1073/pnas.1600644113.
- 214
- 215
- 216 **Vecchiarelli AG**, Li M, Mizuuchi M, Mizuuchi K. Differential affinities of MinD and MinE to anionic phos-
217 pholipid influence Min patterning dynamics in vitro. *Molecular Microbiology*. 2014; 93(3):453–463. doi:
218 10.1111/mmi.12669.

219 **Appendix 1**

220 **Protein design and cloning** Several instances of MinE(2-31)-sfGFP were cloned, expressed
221 and tested.. We started with a construct carrying a His-tag on the N-terminus His-(MinE-2-
222 31)-sfGFP. Then, we became concerned about dimerization of the fluorescent protein and
223 introduced a mutation (V206K) to make His-MinE(2-31)-msfGFP. Then, we discovered that
224 N-terminal tagging influences the properties of our minimal constructs and wt MinE and
225 changed the construct to carrying a C-terminal His-tag (MinE(1-31)-msfGFP-His). The methio-
226 nine residue was re-introduced here as a start codon, and is cleaved in E. coli. Additionally,
227 we prepared MinE(13-31)-sfGFP and confirmed that without MTS, no patterns are formed.

228 The first construct, His-MinE(2-31)-sfGFP was cloned as follows: A fragment containing
229 the pET28a vector-backbone and the start of His-MinE was amplified from pET28a-His-MinE
230 using primers PG073+PG074. The sfGFP fragment was amplified from pVRB18-XX-sfGFP
231 using primers PG069+PG070. The two fragments were recombined in E. coli to yield pET28a-
232 His-MinE(2-31)-sfGFP. His-MinE(13-31)-sfGFP was assembled from three fragments. The
233 sfGFP fragment was generated as described above. A second fragment containing the vector
234 backbone and compatible overhangs was generated from pET28a-His-MinE using primers
235 PG073+PG077. Finally, the MinE(13-31) fragment was amplified from pET28a-His-MinE using
236 primers PG072+PG016, then a second PCR reaction was run on this fragment with primers
237 PG076+PG074. All three fragments were recombined in E. coli.

238 His-MinE(2-31)-msfGFP was generated from His-MinE(2-31)-sfGFP by recombining two
239 fragments generated by PCR with primers PG087+PG043 and PG088+PG044, respectively.

240 MinE(1-31)-msfGFP-His was recombined from two fragments. the MinE(1-31)-msfGFP
241 was amplified from pET28a-His-MinE(2-31)-msfGFP using primers PG090+PG091. The vector
242 fragment was generated from pET28a-BsMTS-mCherry-His using primers PG089+PG007.

243 Custom DNA sequences were ordered for GCN-4, c-Jun and c-Fos. DNA fragments con-
244 sisting of a linker sequence, the respective leucine zipper and another linker sequence were
245 amplified via PCR using primers PG103+PG104 (GCN4), PG105+PG106 (Jun) or PG107+PG108
246 (Fos). Similarly, FKBP and FRB were amplified using primers PG110+PG111 (FKBP) and
247 PG112+PG113 (FRB). A fragment of MinE(13-31) containing compatible overlaps was gen-
248 erated from PCR on pET28a-MinEL-msfGFP-His using primers PG109+PG102. The vector
249 containing MinE(1-31) and compatible overhangs was amplified from pET28a-MinE-His using
250 primers PG007 and PG102. For the three-fragment assemblies, the vector was created via
251 PCR from BsMTS-mCherry-His (Ramm et al.) using primers PG007+PG089. The desired
252 construct vectors were then created via three-fragment homologous recombination in E. coli
253 TOP10, or two-fragment in case of MinE(1-31) constructs. In an additional step, the protein
254 sequence KCK was inserted into the MinE(13-31) constructs by amplifying two halves of
255 the vector. The first half was amplified using primers PG114+PG43, the second half using
256 primers PG115+PG44. After DpnI digest (done for all fragments amplified from functional
257 vectors), the fragments were transformed in to E. coli TOP10 and selected on kanamycin
258 LB plates for homologous recombination. All constructs' integrity was verified via Sanger
259 sequencing.

260 SUMO-MinE(1-31)-KCK-His and SUMO-MinE(13-31)-KCK-His were generated via homolo-
261 gous recombination of two fragments each. For the construct with MTS, one fragment was
262 amplified from pET28M-SUMO1-GFP using primers PG043+PG116. The second fragment
263 was amplified from pET28M-SUMO1-MinE (*Glock et al., 2018b*) using primers PG044+PG117.
264 Fragments for the construct without MTS were amplified from the recombined vector de-
265 scribed above using primers PG043+PG118 and from pET28M-SUMO1-GFP using primers
266 PG044+PG119.

Purification of proteins: MinD, MinD-KCK-Alexa647, mRuby3-MinD, His-MinE and MinE-

267
268
269
270
271
272
273
274
275
276
277
278
279
280
281
282
283
284
285
286
287
288
289
290
291
292
293
294

His were purified as previously described (*Ramm et al., 2018; Glock et al., 2018a,b*). MinE(13-31)-Fos, MinE(13-31)-Jun and MinE(13-31)-GCN4 were purified as described for MinE-His (*Glock et al., 2018b*). MinE(2-31)-Fos, MinE(2-31)-Jun and MinE(2-31)-GCN4 were highly insoluble and therefore fully found in the pellet fraction after cell lysis and centrifugation. The supernatant was discarded and the pellet re-solubilised in lysis buffer U (8M Urea, 500 mM NaCl, 50 mM Tris-HCl pH 8) by pipetting, vortexing and submerging the vial in a sonicator bath. The residual insoluble fraction was pelleted by centrifugation at 50000 g for 40 minutes. The supernatant was incubated with Ni-NTA agarose beads (2ml per 400 ml initial culture) for 1 h at room temperature on a rotating shaker. Agarose beads were pelleted at 400 g, 4 min and the supernatant was discarded. Purification was continued at RT since proteins were unfolded and kept in 8 M Urea. Agarose beads were loaded on a glass column and washed three times with 10 ml of above lysis buffer U. Further washes (3x) were performed with wash buffer U (8 M Urea, 500 mM NaCl, 20 mM imidazole, 50 mM Tris-HCl pH 8). The protein was eluted with elution buffer U (8 M Urea, 500 mM NaCl, 300 mM imidazole, 50 mM Tris-HCl pH8) and fractions with the highest protein content (Bradford, by eye) were pooled. Re-folding of the pooled eluate was done by dialyzing in multiple steps. In a first step, the solution was dialyzed against buffer D1 (6 M Urea, 500 mM NaCl, 50 mM Tris-HCl pH 8, 10% glycerol) over night. In a second step, against buffer D2 (4 M Urea, 500 mM NaCl, 50 mM Tris-HCl pH8, 10% glycerol) for 2 h, then against buffer D3 (2 M Urea, 500 mM NaCl, 50 mM Tris-HCl pH8, 10% glycerol) for further 2 h. The final dialysis was done against storage buffer (300 mM KCl, 50 mM HEPES pH 7.25, 10% glycerol, 1 mM TCEP, 0.1 mM EDTA). To separate the re-folded protein from aggregates, the protein solution was ultracentrifuged for 40 min at 50000 g, 4° C. Protein concentration was then determined as described in the methods section. MinE(13-31)-KCK-His-Atto 488 and MinE(2-31)-KCK-His-Atto 488 were expressed and purified as described for MinE-His. SUMO-peptide fusions were then added into 1:100 (protease:protein) of SenP2 protease and dialyzed against storage buffer. Labelling was performed as described in the methods section.

Primers used in this study:

PG007: AC-pET_for	GTCGAGCACCACCACCA
PG016: B-pET-MinE_rev	GTGCGGCCGCAAGCTTTTAGCGACGGCGTTCAGCAA
PG043: mut_KanR_fw	TGAAACATGGCAAAGGTAGCGT
PG044: mut_KanR_rev	GCTACCTTTGCCATGTTTCAGAAA
PG073: sfGFP-pET_fw	CATGGATGAGCTCTACAAATAAAAGCTTGCGGCCGCAC
PG074: sfGFP-li-MinE31_rev	AAAGTTCTTCTCTTTGCTCACAGAACCAGAAGAACCAGAAGAGCGACGGCGTTCAGCAAC
PG075: sfGFP-MinE_L_fw	CATGGATGAGCTCTACAAAGCATTACTCGATTCTTCTCTCGC
PG076: E-pET-MinEs_fw	GGGTCGCGGATCCGAATTCAAAAACACAGCCAACATTGCAA
PG077: lolipET_rv	GAATTCGGATCCGCGACC
PG087: sfGFP_V206K_fw	TACCTGTCGACACAATCTAAGCTTTCGAAAGATCCCAAC
PG088: sfGFP_V206K_rev	GTTGGGATCTTTCGAAAGCTTAGATTGTGTGCGACAGGTA
PG089: pET28a-start_rev	CATGGTATATCTCTTCTTAAAGTTAAACAA
PG090: pET-MinEL_fw	TAAGAAGGAGATATACCATGGCATTACTCGATTCTTCTCTCGC
PG091: pET-msfGFP_rev	TGGTGGTGGTGGTCTCGACTCCAGATCCACCTTTGTAGAGCT
PG103: GCN4_fw	TCTTCTGGTTCTTCTGGTTCTCGTATGAAACAGCTGGAAGACAA
PG104: GCN4_rev	GTGCTCGACTCCAGATCCACCACGTTACCAACCAGTTTTTTC
PG105: Jun_fw	TCTTCTGGTTCTTCTGGTTCTCGTATCGCTCGTCTGGAAGA
PG106: Jun_rev	GTGCTCGACTCCAGATCCACCCTAGTTTCATACTTCTGTTTCAGCTG
PG107: Fos_fw	TCTTCTGGTTCTTCTGGTTCTCTGACCGACACCCTGCAG
PG108: Fos_rev	GTGCTCGACTCCAGATCCACCCTAAGCAGCCAGGATGAATTCC
PG109: pET-MinEs_fw	TAAGAAGGAGATATACCATGAAAAACACAGCCAACATTGCAAAAG
PG110: FKBP_fw	TCTTCTGGTTCTTCTGGTTCTGGTGTTCAGGTCGAAACTATCTCTC
PG111: FKBP_rev	GTGCTCGACTCCAGATCCACCTTCCAGTTTCAGCAGTTCAACG
PG112: FRB_fw	TCTTCTGGTTCTTCTGGTTCTGAAATGTGGCATGAGGGTCTC
PG113: FRB_rev	GTGCTCGACTCCAGATCCACCCTGTTTAGAGATGCGACGAAAGAC
PG114: li-KCK_fw	GGATCTGGAGTCGAGAAATGCAAAACACCACCACCACCAC
PG115: li-KCK_rev	GTGGTGGTGGTGGTGTTCATTCTCGACTCCAGATCC
PG116: KCK-pET_fw	GTTCTTCTGGTAAATGCAAATGAAAGCTTGCGGCCG
PG117: EL_li_rev	TTTGATTACCAGAAGAACCAGAACCAGCGACGGCGTTTCAGC
PG118: SUMO-Es-fw	ACCAGGAACAAACCGGTGGATCAAAAAACACAGCCAACATTGCAAA
PG119: SUMO_rev	TCCACCGGTTTGTCTCTGG

295

296

Discussion

To summarize the results, I have worked towards establishing the *in vitro* Min system as the primary biological RD system. I have developed and applied a photoswitch for the Min system using a chemical biology approach. I have further discovered that the Min system can form stationary patterns, which closely mimic natural patterns and can be applied in synthetic biology. The described way of building minimal biochemical interaction networks based on the Min system expands the ways in which both theoreticians and experimentalists can modify the Min system. Lastly, publishing detailed protocols in open access facilitates future reconstitution experiments also by other groups.

In an ideal model system for RD, it would be possible to modify both reaction rates and diffusion of the morphogens. 1) Diffusion in a solution of viscosity η_v is given by the Stokes-Einstein relationship (equation 4.1).

$$D = \frac{k_B T}{6\pi\eta_v R_h} \quad (4.1)$$

Herein, R_h is the hydrodynamic radius of the diffusing molecule. While this property is not linearly correlated with the molecular mass, adding additional domains or large chemicals such as dextrans, polyethylene glycol (PEG) etc. will increase the hydrodynamic radius. It is therefore relatively easy to alter the diffusion of proteins and peptides in solution, while diffusion of small-molecule morphogens cannot be individually altered. 2) To modify the second term in RD equations, namely the reaction component, is harder. In purely chemical systems, the reaction rate depends on the constituent morphogens and on the temperature. Altering the temperature, however, will also impact diffusion (see equation 4.1). Biological systems offer more freedom here. However, designing proteins of defined activity is an unresolved problem. This relates back to one of the major challenges of biology, namely that a protein's 3D-structure and function cannot be derived from its primary amino acid sequence. Therefore, activity cannot be engineered in a predictable way. However, for most systems that have been studied *in vivo*, naturally occurring mutations are described that alter protein activity. This is also true for the Min system, where many MinE mutants have been studied both *in vivo* and in recent years also *in vitro* [32, 33]. Therefore, there are great advantages to using a biological system such as the *in vitro* Min system for studying pattern formation by RD. Using proteins or peptides as morphogens provides unmatched opportunities to tune both reaction and diffusion.

The overarching objective of this thesis, namely improving and establishing the Min system as the staple model system for RD research has been greatly helped by the creation of the peptide photoswitch as presented in section 2.1. All established model systems for RD profited from development of some means of direct control. This is especially evident in the case of the BZ reaction, where applications going towards RD computation have been developed [54]. I therefore expect great utility improvements by this tool. However, while the global activation shown in the publication uncovered new system behavior, activation selective in space and time should provide even more flexibility. Some easy activation schemes can be carried out by the scanning laser of a confocal microscope, as was shown in the supplement of section 2.3. But more advanced applications would require light patterns to be projected in quicker succession and with more control. Such devices are already available, but are so far only economically justifiable for groups focusing on optogenetics, especially if UV-light is needed as in our peptide photoswitch case. Another limitation of the peptide photoswitch is that it can only be applied *in vitro*. Unfortunately, the peptide does not permeate into living cells efficiently, as determined in preliminary experiments. Of course, engineering the sequence for membrane permeation, treating the cells with heat shock or chemicals, or adding specific tags such as sugars that can be transported may help. But on the other hand, optogenetic approaches may yield quicker results and here the proteins can be made *in situ*. A few such approaches have already been tested by me before the azobenzene strategy was implemented (see section A.1). However, they were so far not successful with purified proteins. Both blocking the MinE-MinD interface with a light-inducible MinC-bound dimerizer on ligand-bound MinD [55], and photocaging of the MinE peptide in a LOV domain protein have been tried. However, a dimerization approach based on PhyB/PIF [56] would be more promising, since it allows reversible photoswitching, much like the developed photoswitch peptide.

Complementary to controlling the pattern locally using light, I have found a way of globally changing the type of pattern that is formed by an *in vitro* Min reaction, as outlined in section 2.3. Even simplified mathematical models, such as the Gray-Scott model [57], show stationary and oscillatory cases when parameters are systematically changed. Likewise, in the BZ reaction stationary patterns have long been reported in addition to the dynamic concentration waves originally observed in thin films of BZ reagents [11]. Being able to study both pattern types is crucial for establishing Min as a model system, since stationary patterns formed by RD are very prominent in nature, e.g. in animal skin patterns. By using such an adaptable system as Min as an *ex vivo* model, it may even be possible to relate changes in the observed phenotype *in vivo*, e.g. in related species of patterned fish with vastly different patterns, to mutations in animal morphogens. It is furthermore unexplored whether stationary RD patterns play a role in the spatial organization of microorganisms, since they are much harder to spot than oscillatory cases. In addition to helping us understand biological RD, the newly discovered stationary patterns formed by the Min system offer great potential for synthetic biology applications. Firstly, the stationary distributions obtained here can be used to position other proteins

of interest in a self-organized fashion. This can be done either by a recently discovered phenomenon of MinD excluding other membrane-interacting factors from highly occupied areas [52] or by attaching the factor of interest to a fraction of MinD proteins. Using the first approach, permanently membrane-anchored proteins can even achieve a static distribution established and sustained by a stationary Min pattern (see supplement section 2.4.1). Combining these experiments with the peptide photoswitch would even allow defined changes to the protein distribution. Possible candidate proteins to be reconstituted in such a hybrid system includes for example eukaryotic cytoskeletal proteins like actin and tubulin, for which many organizing and accessory proteins exist which could be positioned in a self-organized manner. As mentioned in section 2.3, a spot pattern with a surplus of MinE renders the spots very sparse, thus turning it into an interesting candidate system. Secondly, another so far entirely unexplored aspect is the interaction of the stationary system with patterned supports. While this has been explored extensively in 2D for His-MinE [58, 46, 45], stationary patterns have only been reconstituted on flat supports. Using gold- or chromium-patterned glass slides, alignment or extraneous definition of stationary patterns may be possible. Additionally exploring interactions of stationary as well as dynamic Min patterns with supports structured in three dimensions is certainly going to have an impact in the future. One can imagine if the support were shaped by a “wave pattern“, with higher and lower areas, this would limit buffer availability in “dents“, while raising it in “bumps“. Thereby, most likely the pattern could be influenced and positioned. In turn, these studies could serve to test predictions and improve mathematical models capable of recapitulating stationary Min patterns, which are currently being developed.

The unpublished study presented in the Outlook (section 3.1) introduces exciting new possibilities to study RD with biological agents. But at the same time, many new questions arise from it. The peptides used in this study are derived from sequence segments of *E. coli*. While this approach stays as close to the *in vivo* situation as possible, improvements to the peptide sequence are likely possible. A comparison of the respective sections in homologous proteins shows some evolutionary divergence in the sequence. Based on this divergence, a consensus peptide could be designed and tested. However, all natural MinE proteins described thus far maintain MinE’s protein structure at the same time as keeping the peptide functional. This maintenance includes upkeep of MinE-switching between latent and active conformation, which directly involves residues within the peptide [30, 29]. Therefore an ideal peptide would have degrees of freedom in some residues that were not sampled by evolution, because the MinE switch had to stay intact. Computational design of an artificial peptide-MinD interface based on key residues taken from MinE would be a promising approach to improve activity and stability of the peptide, but has not been tried so far. The results of such a study would be very valuable to improve the peptide photoswitch (section 2.1) as well. Especially removing propensity to aggregate could enable higher photoswitch concentrations in small volumes and thus facilitate switching of the Min system inside microcompartments or vesicles. Likewise, tuning the strength of MinE action on MinD by altering residues in the peptide that change the degree of α -helicity or tone down the strength of ATPase activation would add an interesting new dimension to the

resulting RD-system by enabling comparisons of phase diagrams where only MinE activity has been altered in an otherwise identical system.

The MinD-depletion zones between oscillating RD waves can be explained by rapid rebinding of membrane proximal MinE [31] and may additionally involve a certain period in which the ADP to ATP exchange happens within individual MinD proteins. Likewise, stationary patterns can be envisioned to depend on the same two properties. However, the large scale patterns formed by minimal peptides prompt some questions. Here, large membrane areas stay in a low-MinD state for many minutes. Curiously, the fluorescence intensity of the minimal MinE construct is also very low in these areas, excluding the possibility that MinE stays in membrane proximity to ensure that the spot remains in a low-MinD state. ATP turnover by MinD is known to be faster than this [38], which suggests that there is another mechanism involved. A follow-up experiment would be to measure the residence times of MinD in high and low MinD areas, complemented by similar measurements for the minimal MinE species. This could be done by single-molecule tracking or surface-integrated fluorescence correlation spectroscopy (SI-FCS) [59], since the time between high-MinD and low-MinD states is much longer than for the wild-type system.

Intriguingly, MinE(13-31) has a similar ability to stimulate ATPase activity of MinD as a dimerized peptide (e.g. E(13-31)-Fos). However, the former has never been observed to form patterns, while the latter readily self-organizes with MinD into large-scale patterns. Analysis of theoretical models suggests that higher MinE recruitment by MinD could be responsible for this difference. Other parameters, such as ionic strength of the buffer, pH-value or the presence of crowding agents or other additives, are known to influence protein-protein interactions. Therefore, it would be interesting in the scope of simplifying biological pattern formation to systematically search for conditions in which a truly minimal MinE(13-31) would form patterns with MinD. This could not be done so far due to the vast parameter space to be sampled, but will be addressed in future experiments.

Similarly, it is intuitive to also minimize MinD after showing how much MinE can be simplified. However, MinD's specific function as a membrane-switch and ATPase makes any efforts to modify the protein extremely difficult. Here, the strength of MinD's membrane targeting sequence is finely tuned to allow membrane binding upon dimerization. Changing this balance by e.g. adding more turns to the amphipathic helix is possible, as Simon Kretschmer has shown recently (unpublished). However, reducing the membrane affinity by shortening or removing the helix would just render MinD incapable of pattern formation. Likewise, reducing the size of the main protein significantly would disable the ATPase function and thereby also abolish self-organization. Therefore, no efforts have been made towards a "minimal MinD" so far. In the future, computational design of proteins may become powerful enough to attempt a minimization of MinD.

Any means of dimerization seems to be sufficient to allow pattern formation by minimal MinE. In our experiments, both a Rapamycin-inducible system and human leucine-zipper sequences were successful. Further ideas that could be followed are to add two MinE(13-31) peptides together in a single chain, possibly with variable linker size between them, and fusing MinE(13-31) directly to MinD. The latter idea would certainly increase recruitment via proximity, but might also lead to a system deficient of pattern forming capabilities,

because MinD might not be able to utilize its positive feedback. Experiments with the leucine-zipper sequences showed that patterns are formed independent of the strength of the interaction (estimated K_D of strongest (GCN4 ~ 8 nM) vs weakest (Fos ~ 6.7 μ M) dimerizer) [60, 61]. It would be intriguing to explore the possibility of using this system as an assay for dimerization. However, more experiments with even weaker interactions would be necessary to confirm the practicality. This application could be beneficial in many cases, since unspecific interactions which commonly lead to false-positives in established interaction screens would not yield a coherently patterned assay. Purifying both interaction partners with a MinE peptide attached is a big hurdle, which might be overcome by producing the peptide with functional groups for direct attachment to e. g. the N-terminus of proteins.

While research on the Min system has been performed for decades *in vivo* and is now well-established *in vitro*, some fundamental questions remain, and some new ones arise with every new study. One crucial question concerns the positive feedback introduced by MinD membrane attachment. It is understood that the dimerization of MinD-ATP triggers membrane attachment. However, positive feedback requires that this initial membrane binding by a single dimer promotes further MinD dimers to bind to adjacent membrane areas. This would imply another interaction in MinD besides the dimer interface. Furthermore, the study presented in section 2.4 shows that the MinD zones on a membrane are dense enough to spatially regulate other proteins and thereby induce direct net transport in oscillating cases. This supports the requirement for additional interaction between MinD dimers. Uncovering the basis of this secondary interaction will require new ideas and innovative experiments, since the primary ATP-dependent dimerization has to be accounted for.

Another question that arose in the investigations leading to both the discovery of stationary patterns in Min and the minimal peptides is the nature of the effect N-terminal attachments have on MinE. As verified in the publication via quartz crystal microbalance with dissipation monitoring (QCM-D) (section 2.3), membrane binding by MinE is not changed by adding an N-terminal large linker and His-tag. But at the same time, the ATPase stimulation with linker is higher. A systematic study employing varying linker length, charge and structure would give more insight into the changes induced. For now, we can only speculate that the switch from the active to the latent conformation of MinE is slower when additional residues are present at the N-terminus.

Overall, the work presented here is a big step towards achieving the main objective, namely establishing the Min system as the primary biological RD model system. I have introduced a new tool, the peptide photoswitch, to control self-organization *in situ* using light. In terms of pattern diversity, I have found that removing a purification tag and linker from MinE and reconstituting the system with sufficient bulk volume gives access to stationary patterns in addition to the well-studied travelling waves. Thereby, the Min system can act as a model for many more processes of biological relevance. Additionally, we have shown how the Min system can serve as a basis for a simplified pattern forming system, and learned about the essential features of MinE. Finally, sharing our protocols

and resources, such as in the included JoVE publication, should enable researchers to more freely access the Min system and thus facilitate broader acceptance of Min as an RD-model.

Appendix

A.1 Discontinued approaches to photocontrol the Min system

The following approaches to achieve external control of the *in vitro* Min system were explored in the first year of my Thesis:

Firstly, I tried to combine published optogenetic dimerizers with the published detail that the binding site for MinE on a MinD dimer overlaps that of MinC [27]. I used systems based on light-oxygen-voltage domains (LOV), because the LOV domain and the engineered interactors are smaller than alternative optogenetic proteins and feature a relatively fast return to the ground state after illumination ceases. More details of the approach are described in Figure A.1. Dimerizers I tried include the TULIP system [55] and the iLID system [62]. Purifying the proteins already posed a major challenge, since most constructs were insoluble. Even after achieving reasonably pure proteins, no change in Min propagation could be invoked by illumination.

In a second approach, I tried to photocage a small MinE-derived peptide inside the LOV-domain as shown in Figure A.2. The LOV domains in use were taken from the same systems as above, TULIPs and iLID, with modifications in the caged region as well as some mutations to force the construct towards open or closed. While proteins were small and soluble, no change in activity upon illumination occurred. On a positive side-note, this approach sparked the idea for the photoswitch I eventually developed based on the same MinE-peptide and an azobenzene crosslinker.

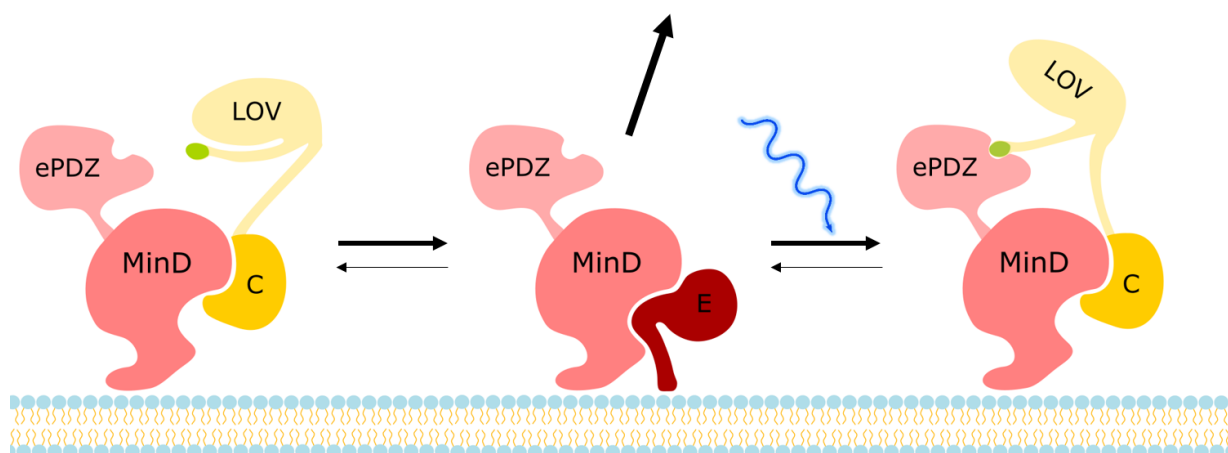


Figure A.1: Schematic of an unsuccessful approach to photocontrol the Min system. A hybrid construct containing the photoactivatable LOV-domain hybrid bound to MinC is complemented by a MinD-bound interaction domain (here ePDZ) when illuminated by blue light. This inhibits MinE-dependent release of MinD from the membrane. After return to the ground state, pattern formation by MinE should resume.

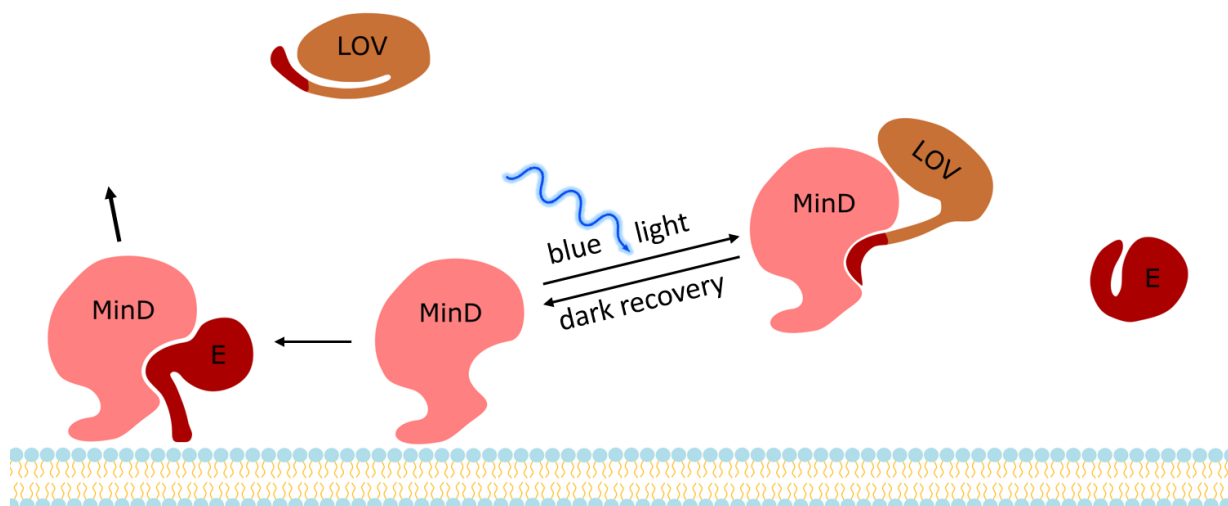


Figure A.2: Schematic of an unsuccessful approach to photocontrol the Min system. A MinE-derived peptide was incorporated into the mobile part of a LOV-domain. Illumination should release this part of the protein, enabling the MinE peptide to locally activate MinD's ATPase.

A.2 Programs and additional code

A.2.1 CoolLED-control

Custom python 3 software to run controlled timeseries on CoolLED illumination units (specifically made for pE-2 and pE-4000)

-Requires python 3.x, PyQt4, pyqtgraph-

Provides a GUI to enter sequences of LED-illumination and wait times(dark). Sequences can be saved and loaded or copy-pasted into the field to reproduce previous timeseries. Communicates with LED units by CoolLED via the USB connection (virtual COM port). A driver for Windows OS can be found on their homepage <http://www.coolled.com/product-detail/imaging-software/>

The full source-code of this program can be found on github: https://github.com/philglock/CoolLED_control

A.2.2 Visualization of spectra

This program displays a small GUI to load and select .CSV files generated by JASCO spectrometers.

Prerequisites:

- Python 3.x
- PyQt5
- pyqtgraph
- pandas
- numpy
- matplotlib
- FPDF
- time

Up to six spectra can be overlaid and individual line colors can be changed in a color picker. The displayed range can be adjusted both in x and in y. Additionally, a button sets the minimum of the curve = 0. "Create PDF output" generates a pdf with all the loaded curves and names assigned, plotted in matplotlib.

The full source-code of this program can be found on github: <https://github.com/philglock/SpectraViewerJasco>

A.2.3 ImageJ/Fiji code

Small macro to stitch LSM-780 5x5 tile scans. Simply edit the code if you want to stitch other tile types or create a dialog box asking for the size. Also works for time series of tile scans:

```
macro "Montage over time (newLSM) [F5]" {
    timepoints = nSlices/25;
    run("Stack to Image5D", "3rd=t 4th=z 3rd_dimension_size="+timepoints+"
    ↪ 4th_dimension_size=25 assign");
    run("Make Montage", "columns=5 rows=5 scale=1 first=1 last=25 increment=1
    ↪ border=0 displayed all output copy");
    run("Image5D to Stack");
}
```

A longer jython plugin to detect and label protein size markers in images of SDS-gels (copy the script into Fiji/plugins). Is currently set to detect the bands of Precision Plus Protein Dual Xtra Standard (Bio-Rad), but could easily be adapted for other marker brands (source code should be easy to modify). Select the region with marker with a rectangular ROI in a 16-bit TIFF image, then start the plugin. It will produce an error message in Fiji due to updates after I wrote it, but will still work if the range is set correctly (depends on image brightness):

```
'''
This program by Philipp Glock finds marker bands in a Coomassie-stained protein gel
and labels them with their respective kDa-values. So far, it is only designed for use
↪ with
BioRad Precision Plus dual Xtra marker. It will NOT find the 2kDa band.

Usage instructions:
Draw a rectangular selection over the marker lane. Start the plugin, it will now ask
↪ you for
a minimum value to identify bands. Depending on your staining and washing protocol, you
may have to play with the values in order to identify all bands.
The overlay is created automatically to the left of your selected lane.
If your gel is not destained properly (especially at the top end), identification of
↪ bands will go wrong!

'''

from ij import IJ
from ij import ImagePlus
from ij.gui import Roi
from ij.gui import TextRoi
from ij.plugin.frame import RoiManager
from java.awt import Color
from ij.gui import Overlay
from ij.process import ImageStatistics as IS
import sys
```



```
from ij.gui import GenericDialog

# this function grabs a value for the minimum darkness of a band from the user via a
↪ dialog
def getOptions():
    gd = GenericDialog("Select value")
    gd.addNumericField("Min band value: ", 150, 0)
    gd.showDialog()

    darkness = gd.getNextNumber()
    return darkness

# Grab the active image
imp = IJ.getImage()
if imp.type == ImagePlus.COLOR_RGB:
    print "ERROR: Please give me a grayscale image!"
    sys.exit("Please use on grayscale images only!")

# find the selection, create one ROI from it
# also make sure to note where it is in respect to the whole image

rm = RoiManager.getInstance()
if (rm==None):
    rm = RoiManager()
rm.reset()
rm.addRoi(imp.getRoi())

# create new image from selection and convert it to 8bit
IJ.run(imp, "Copy", "")
IJ.run("Internal Clipboard",)
marker = IJ.getImage()
marker.setTitle("gel_marker")
IJ.run(marker, "8-bit", "")

# run "find connected regions" on this new image -> creates yet another image
marker_opt = "allow_diagonal display_one_image display_results=0
↪ regions_for_values_over=" + str(getOptions()) + " minimum_number_of_points = 300
↪ stop_after=-1"
IJ.run(marker, "Find Connected Regions", marker_opt)
marker_c = IJ.getImage()
marker_c.setTitle("Colors")

marker_ip = marker_c.getProcessor()
options = IS.MIN_MAX
marker_stats = IS.getStatistics(marker_ip, options, marker_c.getCalibration())

if marker_stats.max > 11 or marker_stats.max < 8:
```

```
print "ERROR: Expected to find bands, found " , marker_stats.max , " regions
↳ instead. EXITING"
marker.changes = 0 # to keep it from prompting user every time.
marker.close()
marker_c.close()

# iterate over the pixels of the newest image. Find the first pixel with value 1 and
↳ the last pixel with value 1, 2, ...
one = []
two = []
three = []
four = []
five = []
six = []
seven = []
eight = []
nine = []
ten = []
eleven = []

# create the pixels to iterate on
ip = marker_c.getProcessor().convertToFloat()
pixels = ip.getPixels()

for i in xrange(len(pixels)):
    if pixels[i] == 1:
        one.append(i)
    elif pixels[i] == 2:
        two.append(i)
    elif pixels[i] == 3:
        three.append(i)
    elif pixels[i] == 4:
        four.append(i)
    elif pixels[i] == 5:
        five.append(i)
    elif pixels[i] == 6:
        six.append(i)
    elif pixels[i] == 7:
        seven.append(i)
    elif pixels[i] == 8:
        eight.append(i)
    elif pixels[i] == 9:
        nine.append(i)
    elif pixels[i] == 10:
        ten.append(i)
    elif pixels[i] == 11:
        eleven.append(i)

# find out and save the y-position of both first and last value (then find the middle)

mid = []
```

```

mid.append((one[0]+one[len(one)-1])/2)
mid.append((two[0]+two[len(two)-1])/2)
mid.append((three[0]+three[len(three)-1])/2)
mid.append((four[0]+four[len(four)-1])/2)
mid.append((five[0]+five[len(five)-1])/2)
mid.append((six[0]+six[len(six)-1])/2)
mid.append((seven[0]+seven[len(seven)-1])/2)
if eight:
    mid.append((eight[0]+eight[len(eight)-1])/2)
if nine:
    mid.append((nine[0]+nine[len(nine)-1])/2)
if ten:
    mid.append((ten[0]+ten[len(ten)-1])/2)
if eleven:
    mid.append((eleven[0]+eleven[len(eleven)-1])/2)

# roi_x, roi_y and roi_width now contain the x-value, y value and width of the initial
↪ ROI.

region = rm.getRoisAsArray()
roi_x = region[0].getXBase()
roi_y = region[0].getYBase()
roi_width = region[0].getFloatWidth()

# now calculate the actual y values of the bands

mid_y = [x/roi_width + roi_y for x in mid]

# close both images that were opened, go back to the original image

marker.changes = 0 # to keep it from prompting user every time.
marker.close()
marker_c.close()

# create an overlay that takes into account where the selection was and creates the
↪ description
# to the left of the selected region

marker_values = ["250", "150", "100", " 75", " 50", " 37", " 25", " 20", " 15", "
↪ 10", " 5"]

dummy = TextRoi(roi_x, roi_y, "")
dummy.setFont("SansSerif", 23, 0)
dummy.setColor(Color(0,0,0))
marker_overlay = Overlay(dummy)

kDa = TextRoi(roi_x - 70, mid_y[0] - 80, "kDa") # change - to + to label on the right,
↪ also below!
marker_overlay.add(kDa)

```

```
for count,band in enumerate(mid_y):
    label = TextRoi(roi_x - 70, band-dummy.getSize(), marker_values[count]) # change -
    ↪ to + here if label should be right of lane.
    marker_overlay.add(label)

imp.setOverlay(marker_overlay)
```

Bibliography

- [1] N. S. Scholes and M. Isalan, “A three-step framework for programming pattern formation.,” *Current opinion in chemical biology*, vol. 40, pp. 1–7, oct 2017.
- [2] S. Kondo and T. Miura, “Reaction-Diffusion Model as a Framework for Understanding Biological Pattern Formation,” *Science*, vol. 329, pp. 1616–1620, sep 2010.
- [3] L. Wolpert, “Positional Information and Pattern Formation,” in *Current Topics in Developmental Biology*, vol. 6, pp. 183–224, Academic Press, jan 1971.
- [4] D. S. Johnston and C. Nüsslein-Volhard, “The origin of pattern and polarity in the *Drosophila* embryo,” *Cell*, vol. 68, no. 2, pp. 201–219, 1992.
- [5] A. M. Turing, “The Chemical Basis of Morphogenesis,” *Philosophical Transactions of the Royal Society B: Biological Sciences*, vol. 237, pp. 37–72, aug 1952.
- [6] J. Halatek, F. Brauns, and E. Frey, “Self-organization principles of intracellular pattern formation.,” *Philosophical transactions of the Royal Society of London. Series B, Biological sciences*, vol. 373, may 2018.
- [7] G. Ertl, “Oscillatory kinetics and spatio-temporal self-organization in reactions at solid surfaces.,” *Science (New York, N.Y.)*, vol. 254, pp. 1750–5, dec 1991.
- [8] S. Nettesheim, a. von Oertzen, H. H. Rotermund, and G. Ertl, “Reaction diffusion patterns in the catalytic CO-oxidation on Pt(110): Front propagation and spiral waves,” *The Journal of Chemical Physics*, vol. 98, no. 12, p. 9977, 1993.
- [9] M. Kim, M. Bertram, M. Pollmann, A. von Oertzen, A. S. Mikhailov, H. H. Rotermund, and G. Ertl, “Controlling chemical turbulence by global delayed feedback: pattern formation in catalytic CO oxidation on Pt(110).,” *Science (New York, N.Y.)*, vol. 292, pp. 1357–60, may 2001.
- [10] A. N. Zaikin and A. M. Zhabotinsky, “Concentration wave propagation in two-dimensional liquid-phase self-oscillating system.,” *Nature*, vol. 225, pp. 535–7, feb 1970.
- [11] Q. Ouyang and H. L. Swinney, “Transition to chemical turbulence,” *Chaos*, vol. 1, no. 4, pp. 411–420, 1991.

- [12] V. Petrov, Q. Ouyang, and H. L. Swinney, "Resonant pattern formation in a chemical system," *Nature*, vol. 388, no. 6643, pp. 655–657, 1997.
- [13] V. Vanag, L. Yang, M. Dolnik, A. Zhabotinsky, and I. Epstein, "Oscillatory cluster patterns in a homogeneous chemical system with global feedback," *Nature*, vol. 406, no. 6794, pp. 389–91, 2000.
- [14] V. K. Vanag and I. R. Epstein, "Design and control of patterns in reaction-diffusion systems," *Chaos*, vol. 18, no. 2, 2008.
- [15] H. I. Adler, W. D. Fisher, A. Cohen, and A. A. Hardigree, "Miniature Escherichia coli cells deficient in DNA," *Proceedings of the National Academy of Sciences of the United States of America*, vol. 57, pp. 321–6, feb 1967.
- [16] D. W. Adams and J. Errington, "Bacterial cell division: assembly, maintenance and disassembly of the Z ring," *Nat Rev Micro*, vol. 7, no. 9, pp. 642–653, 2009.
- [17] J. Lutkenhaus, S. Pichoff, and S. Du, "Bacterial cytokinesis: From Z ring to divisome," *Cytoskeleton*, vol. 69, no. 10, pp. 778–790, 2012.
- [18] M. Vicente and A. I. Rico, "The order of the ring: Assembly of Escherichia coli cell division components," *Molecular Microbiology*, vol. 61, no. 1, pp. 5–8, 2006.
- [19] A. W. Bisson-Filho, Y.-P. Hsu, G. R. Squyres, E. Kuru, F. Wu, C. Jukes, Y. Sun, C. Dekker, S. Holden, M. S. VanNieuwenhze, Y. V. Brun, and E. C. Garner, "Treadmilling by FtsZ filaments drives peptidoglycan synthesis and bacterial cell division," *Science*, vol. 355, pp. 739–743, feb 2017.
- [20] L. J. Wu and J. Errington, "Nucleoid occlusion and bacterial cell division," *Nature Reviews Microbiology*, vol. 10, no. 1, pp. 8–12, 2011.
- [21] Z. Hu, a. Mukherjee, S. Pichoff, and J. Lutkenhaus, "The MinC component of the division site selection system in Escherichia coli interacts with FtsZ to prevent polymerization.," *Proceedings of the National Academy of Sciences of the United States of America*, vol. 96, no. 26, pp. 14819–14824, 1999.
- [22] J. Lutkenhaus and M. Sundaramoorthy, "MinD and role of the deviant Walker A motif, dimerization and membrane binding in oscillation," *Molecular Microbiology*, vol. 48, no. 2, pp. 295–303, 2003.
- [23] T. H. Szeto, S. L. Rowland, C. L. Habrukowich, and G. F. King, "The MinD membrane targeting sequence is a transplantable lipid-binding helix," *Journal of Biological Chemistry*, vol. 278, no. 41, pp. 40050–40056, 2003.
- [24] K. T. Park, W. Wu, K. P. Battaile, S. Lovell, T. Holyoak, and J. Lutkenhaus, "The min oscillator uses MinD-dependent conformational changes in MinE to spatially regulate cytokinesis," *Cell*, vol. 146, no. 3, pp. 396–407, 2011.

- [25] C. R. Zhao, P. a. de Boer, and L. I. Rothfield, "Proper placement of the Escherichia coli division site requires two functions that are associated with different domains of the MinE protein.," *Proceedings of the National Academy of Sciences of the United States of America*, vol. 92, no. 10, pp. 4313–4317, 1995.
- [26] L. Ma, G. F. King, and L. Rothfield, "Positioning of the MinE binding site on the MinD surface suggests a plausible mechanism for activation of the Escherichia coli MinD ATPase during division site selection," *Molecular Microbiology*, vol. 54, no. 1, pp. 99–108, 2004.
- [27] L. Y. Ma, G. King, and L. Rothfield, "Mapping the MinE site involved in interaction with the MinD division site selection protein of Escherichia coli," *Journal of Bacteriology*, vol. 185, no. 16, pp. 4948–4955, 2003.
- [28] A. G. Vecchiarelli, M. Li, M. Mizuuchi, L. C. Hwang, Y. Seol, K. C. Neuman, and K. Mizuuchi, "Membrane-bound MinDE complex acts as a toggle switch that drives Min oscillation coupled to cytoplasmic depletion of MinD," *Proceedings of the National Academy of Sciences*, vol. 113, pp. E1479–E1488, mar 2016.
- [29] K.-T. Park, M. T. Villar, A. Artigues, and J. Lutkenhaus, "MinE conformational dynamics regulate membrane binding, MinD interaction, and Min oscillation," *Proceedings of the National Academy of Sciences*, vol. 114, pp. 7497–7504, jul 2017.
- [30] S. H. Ayed, A. D. Cloutier, L. J. McLeod, A. C. Y. Foo, A. M. Damry, and N. K. Goto, "Dissecting the role of conformational change and membrane binding by the bacterial cell division regulator MinE in the stimulation of MinD ATPase activity.," *The Journal of biological chemistry*, vol. 292, pp. 20732–20743, dec 2017.
- [31] M. Loose, E. Fischer-Friedrich, C. Herold, K. Kruse, and P. Schwille, "Min protein patterns emerge from rapid rebinding and membrane interaction of MinE.," *Nature structural & molecular biology*, vol. 18, no. 5, pp. 577–583, 2011.
- [32] S. Kretschmer, K. Zieske, and P. Schwille, "Large-scale modulation of reconstituted Min protein patterns and gradients by defined mutations in MinE's membrane targeting sequence," *PLoS ONE*, pp. 1–16, 2017.
- [33] J. Denk, S. Kretschmer, J. Halatek, C. Hartl, P. Schwille, and E. Frey, "MinE conformational switching confers robustness on self-organized Min protein patterns.," *Proceedings of the National Academy of Sciences of the United States of America*, vol. 115, pp. 4553–4558, may 2018.
- [34] G. F. King, Y. L. Shih, M. W. Maciejewski, N. P. Bains, B. Pan, S. L. Rowland, G. P. Mullen, and L. I. Rothfield, "Structural basis for the topological specificity function of MinE.," *Nature structural biology*, vol. 7, no. 11, pp. 1013–1017, 2000.

- [35] H. Ghasriani, T. Ducat, C. T. Hart, F. Hafizi, N. Chang, A. Al-Baldawi, S. H. Ayed, P. Lundström, J.-A. R. Dillon, and N. K. Goto, “Appropriation of the MinD protein-interaction motif by the dimeric interface of the bacterial cell division regulator MinE.,” *Proceedings of the National Academy of Sciences of the United States of America*, vol. 107, no. 43, pp. 18416–18421, 2010.
- [36] A. Schmidt, K. Kochanowski, S. Vedelaar, E. Ahrné, B. Volkmer, L. Callipo, K. Knoop, M. Bauer, R. Aebersold, and M. Heinemann, “The quantitative and condition-dependent *Escherichia coli* proteome.,” *Nature biotechnology*, vol. 34, pp. 104–110, jan 2016.
- [37] X. Fu, Y. L. Shih, Y. Zhang, and L. I. Rothfield, “The MinE ring required for proper placement of the division site is a mobile structure that changes its cellular location during the *Escherichia coli* division cycle.,” *Proceedings of the National Academy of Sciences of the United States of America*, vol. 98, no. 3, pp. 980–985, 2001.
- [38] P. A. de Boer, R. E. Crossley, A. R. Hand, and L. I. Rothfield, “The MinD protein is a membrane ATPase required for the correct placement of the *Escherichia coli* division site.,” *The EMBO journal*, vol. 10, no. 13, pp. 4371–4380, 1991.
- [39] M. Loose, E. Fischer-Friedrich, J. Ries, K. Kruse, and P. Schwille, “Spatial regulators for bacterial cell division self-organize into surface waves in vitro.,” *Science (New York, N.Y.)*, vol. 320, no. 5877, pp. 789–792, 2008.
- [40] V. Ivanov and K. Mizuuchi, “Multiple modes of interconverting dynamic pattern formation by bacterial cell division proteins.,” *Proceedings of the National Academy of Sciences of the United States of America*, vol. 107, no. 18, pp. 8071–8078, 2010.
- [41] A. G. Vecchiarelli, M. Li, M. Mizuuchi, and K. Mizuuchi, “Differential affinities of MinD and MinE to anionic phospholipid influence Min patterning dynamics in vitro,” *Molecular Microbiology*, vol. 93, no. 3, pp. 453–463, 2014.
- [42] J. Halatek and E. Frey, “Highly Canalized MinD Transfer and MinE Sequestration Explain the Origin of Robust MinCDE-Protein Dynamics,” *Cell Reports*, vol. 1, no. 6, pp. 741–752, 2012.
- [43] J. Schweizer, M. Loose, M. Bonny, K. Kruse, I. Monch, and P. Schwille, “Geometry sensing by self-organized protein patterns,” *Proceedings of the National Academy of Sciences*, vol. 109, no. 38, pp. 15283–15288, 2012.
- [44] K. Zieske and P. Schwille, “Reconstitution of Pole-to-Pole Oscillations of Min Proteins in Microengineered Polydimethylsiloxane Compartments,” *Angewandte Chemie International Edition*, vol. 52, pp. 459–462, jan 2013.
- [45] K. Zieske and P. Schwille, “Reconstitution of self-organizing protein gradients as spatial cues in cell-free systems,” *eLife*, vol. 3, pp. 1–19, 2014.

- [46] Y. Caspi and C. Dekker, “Mapping out min protein patterns in fully confined fluidic chambers,” *eLife*, vol. 5, no. NOVEMBER2016, pp. 1–27, 2016.
- [47] P. Glock, B. Ramm, T. Heermann, S. Kretschmer, J. Schweizer, J. Mücke, G. Alagöz, and P. Schwille, “Stationary patterns in a two-protein reaction-diffusion system,” *ACS Synthetic Biology*, p. acssynbio.8b00415, 2018.
- [48] F. Wu, B. G. C. van Schie, J. E. Keymer, and C. Dekker, “Symmetry and scale orient Min protein patterns in shaped bacterial sculptures,” *Nature nanotechnology*, vol. 10, pp. 719–26, aug 2015.
- [49] K. Zieske, J. Schweizer, and P. Schwille, “Surface topology assisted alignment of Min protein waves,” *FEBS Letters*, vol. 588, no. 15, pp. 2545–2549, 2014.
- [50] B. Ramm, P. Glock, and P. Schwille, “In Vitro Reconstitution of Self-Organizing Protein Patterns on Supported Lipid Bilayers,” *Journal of Visualized Experiments*, p. e58139, jul 2018.
- [51] P. Glock, J. Broichhagen, S. Kretschmer, P. Blumhardt, J. Mücke, D. Trauner, and P. Schwille, “Optical Control of a Biological Reaction-Diffusion System,” *Angewandte Chemie International Edition*, vol. 57, pp. 2362–2366, feb 2018.
- [52] B. Ramm, P. Glock, J. Mücke, P. Blumhardt, D. A. García-Soriano, M. Heymann, and P. Schwille, “The MinDE system is a generic spatial cue for membrane protein distribution in vitro,” *Nature communications*, vol. 9, p. 3942, sep 2018.
- [53] P. Glock and P. Schwille, “Switching protein patterns on membranes,” *Current Opinion in Colloid & Interface Science*, vol. 38, pp. 100–107, nov 2018.
- [54] B. de Lacy Costello, R. Toth, C. Stone, A. Adamatzky, and L. Bull, “Implementation of glider guns in the light-sensitive Belousov-Zhabotinsky medium,” *Physical Review E*, vol. 79, p. 026114, feb 2009.
- [55] D. Strickland, Y. Lin, E. Wagner, C. M. Hope, J. Zayner, C. Antoniou, T. R. Sosnick, E. L. Weiss, and M. Glotzer, “TULIPs: tunable, light-controlled interacting protein tags for cell biology,” *Nature Methods*, vol. 9, no. 4, pp. 379–384, 2012.
- [56] A. Levskaya, O. D. Weiner, W. a. Lim, and C. a. Voigt, “Spatiotemporal control of cell signalling using a light-switchable protein interaction,” *Nature*, vol. 461, no. 7266, pp. 997–1001, 2009.
- [57] J. E. Pearson, “Complex Patterns in a Simple System,” *Science*, vol. 261, pp. 189–192, jul 1993.
- [58] J. Schweizer, M. Loose, M. Bonny, K. Kruse, I. Monch, and P. Schwille, “Geometry sensing by self-organized protein patterns,” *Proceedings of the National Academy of Sciences*, vol. 109, no. 38, pp. 15283–15288, 2012.

-
- [59] J. Mücksch, P. Blumhardt, M. T. Strauss, E. P. Petrov, R. Jungmann, and P. Schwille, “Quantifying Reversible Surface Binding via Surface-Integrated Fluorescence Correlation Spectroscopy,” *Nano Letters*, vol. 18, no. 5, pp. 3185–3192, 2018.
- [60] N. Szalóki, J. W. Krieger, I. Komáromi, K. Tóth, and G. Vámosi, “Evidence for Homodimerization of the c-Fos Transcription Factor in Live Cells Revealed by Fluorescence Microscopy and Computer Modeling,” *Mol Cell Biol*, vol. 35, no. August, pp. 3785–3798, 2015.
- [61] Y. Nikolaev, C. Deillon, S. R. Hoffmann, L. Bigler, S. Friess, R. Zenobi, K. Pervushin, P. Hunziker, and B. Gutte, “The leucine zipper domains of the transcription factors GCN4 and c-Jun have Ribonuclease Activity,” *PLoS ONE*, vol. 5, no. 5, 2010.
- [62] G. Guntas, R. a. Hallett, S. P. Zimmerman, T. Williams, H. Yumerefendi, J. E. Bear, and B. Kuhlman, “Engineering an improved light-induced dimer (iLID) for controlling the localization and activity of signaling proteins,” *Proceedings of the National Academy of Sciences*, vol. 112, no. 1, pp. 112–117, 2015.

Abbreviations

BZ reaction	Belousov-Zhabotinsky reaction
CIMA reaction	chlorite-iodide-malonic acid reaction
CO oxidation	Carbon monoxide oxidation on Pt(110) crystals
<i>E. coli</i>	<i>Escherichia coli</i>
FRAP	Fluorescence Recovery After Photobleaching
FRET	Foerster Resonance Energy Transfer
FtsZ	filamentous temperature sensitive Z
PDMS	polydimethylsiloxane
PEEM	photoemission electron microscopy
PEG	polyethylene glycol
QCM-D	quartz crystal microbalance with dissipation monitoring
RD	reaction-diffusion
SI-FCS	surface-integrated fluorescence correlation spectroscopy
SLB	supported lipid bilayer

Image Credits

Figure 1.1:

PAR proteins *C. elegans*:

<https://www.flickr.com/photos/thejcb/5686881261>

CC BY-NC-SA 2.0

Goehring et al. (2011) *J. Cell Biol.* 193, 583-594

doi: 10.1083/jcb.201011094

The Journal of Cell Biology

Drosophila fluorescence:

<https://academic.oup.com/bioinformatics/article/25/20/2670/192302>

CC BY-NC 2.5

Lee Zamparo, Theodore J. Perkins; Statistical lower bounds on protein copy number from fluorescence expression images, *Bioinformatics*, Volume 25, Issue 20, 15 October 2009, Pages 2670–2676,

<https://doi.org/10.1093/bioinformatics/btp415>

Dictyostelium aggregation:

<https://www.ncbi.nlm.nih.gov/pmc/articles/PMC3861886/>

CC BY 2.5

Dictyostelium: The Mathematician's Organism, A.J. Durston

Pufferfish:

https://upload.wikimedia.org/wikipedia/commons/4/4b/Tetraodon_mbu_-_5301.jpg

CC BY-SA 3.0, Wikimedia commons

Jaguar:

<https://www.publicdomainpictures.net/en/view-image.php?image=175359&picture=jaguar-resting>

CC0 1.0 Universal

Sand dune:

<https://www.pexels.com/photo/desert-sand-sand-dune-sand-dunes-785741/>

Isa Sebastião on Pexels

Figure 1.2:

BZ reaction:

<https://www.flickr.com/photos/nonlin/4297013382>

CC BY 2.0 Attribution

Stephen Morris on flickr

Please find the full description of the referenced licenses here: https://wiki.creativecommons.org/wiki/License_Versions#Licenses (accessed on 17.01.2019).

Acknowledgments

There are many people without whom this thesis would have been difficult, less enjoyable or would not even exist. First of all Petra Schwille, who gave me the opportunity to work very freely, develop my own ideas and grow as a scientist in her lab. Thank you, Petra, for this wonderful time, for providing the right environment, always having an open ear and for creating a lab with space for diversity and interesting people.

The members of my Thesis Advisory Committee, Prof. Dirk Trauner who made the Min photoswitch much cooler with his azobenzene-compounds, and Prof. Kirsten Jung for her scientific input and her role in GRK2062, but also for guiding me through the LMU bureaucracy. I would like to thank all members of the Schwille lab for making these four years such a pleasant experience. Simon, thank you for giving me such a good start in the lab and taking me along in my first weeks, as well as for sharing your exceptional knowledge of the literature and your editing skills. Bea, you started your PhD shortly after me, we learned so much from each other, struggled together through PhD times and collaborated on so many projects. Having you as a friend in the lab was always a pleasure! Tami, thank you for your friendship, for your proofreading and collaboration and for being a good part of the glue that lets us be a group of friends and not just PhD colleagues! A huge thank you to Philipp B., one of my go-to physicists and a true friend, who made the PhD-time really worthwhile. We are now ready to terminally confuse everybody one last time by almost finishing at the same time. Jonas, you are one funny child in a 14-year-old-girls-magnet body, and were always a pleasure to work with. A general shout-out to all the other people in the non-quiet office, Hiro, Sonal, Alena, etc. A special thank you to Leon and Kristina, two post-docs who brought a lot of expert knowledge to the lab and this thesis. This is also true for Henri, who furthermore helped a lot with establishing a photoswitching setup and knows and shares his great knowledge of membrane biophysics. A big thank you to Lei, who was extremely helpful with “all things protein“! Thanks also to Micha, who always encouraged me to start writing my projects up. Katharina deserves special mention for our joint musical efforts, but I am very thankful to all our technicians: Sigi, Brigitte, Kerstin, Michaela, Bea for everything they do for us!

Being a part of GRK2062 meant a lot to me, and I am grateful to all of you for stimulating discussions and suffering through late-night Garching meetings together, as well as to Beate Hafner for all her support and organization! Especially, I would like to thank Aurore, Karsten, Martin and Mona.

Thank you to the IMPRS-LS coordination office - Hans-Joerg, Ingrid, Maxi, Amy

and now Viktoria for all of their work, but also for insisting on timely TAC procedures and thereby somehow speeding me up! I am very grateful to the Max-Weber Programm Bayern for their generous support of my undergraduate studies, enabling me to go as far as Australia for my Thesis.

My past supervisors deserve a special mention for encouraging me to continue this scientific journey and for shaping my thoughts and methods, especially Wolfgang Droege-Laser and Christoph Weiste during my Bachelor's and Leann Tilley, Matt Dixon, Marion Hliscs and Christian Janzen during my Master's.

Last but not least, some personal words for my family: Ihr alle, Annegret und Bruno, Carolin & Florian mit Valentin, Thomas, Gretel, Trudel, Josef, Maria und Irmgard gebt mir viel Kraft und Unterstützung - Danke dafür! Meinen Eltern möchte ich dafür danken, dass sie mich und meine Ausbildung von Beginn an so unterstützt und gefördert haben, in jeder Hinsicht. Mama: Danke für Alles! Außerdem: Deinem Vorbild und auch Deinen Bemühungen ist es zu verdanken, dass mir trotz deutlicher naturwissenschaftlicher Neigung Sprache, Schreiben und Lesen immer nah geblieben sind! Papa: Deine Fähigkeit, Projekte zu planen und so viele Probleme durch Basteln und Bauen zu lösen sind und waren mir eine Inspiration - und oft macht man in der Doktorarbeit genau das! Meli, Dir verdanke ich den stärksten Rückhalt in allen Zeiten und die größte Motivation, mit dieser Arbeit fertig zu werden. Du bist die perfekte Partnerin! Gewidmet habe ich diese Thesis meinem Großvater Friedrich Busch, der mir dank seiner unendlichen Neugier und seinen modernen Ansichten immer ein großes Vorbild bleiben wird. Ich möchte schließen mit einem besonderen Gruß an meinen kleinen Neffen Valentin.

Lebenslauf

Philipp Glock

- 11.11.1988 geboren in Schwäbisch Hall
- 1999-2008 Besuch des Hohenlohe-Gymnasiums Öhringen
Abitur mit Gesamtnote 1,0
- 2008-2009 Zivildienst bei Evangelische Jugendhilfe Friedenshort GmbH
- 2009-2012 Bachelor-Studium Biologie an der Universität Würzburg
Bachelor of Science in Biologie (1,0)
- 2012-2014 Master-Studium Biologie an der Universität Würzburg
- 2013-2014 Master Thesis angefertigt am Bio21 Institute, University of Melbourne
Master of Science in Biologie (1,0)
- 2015-2019 Doktorarbeit am Max-Planck Institut für Biochemie, Martinsried